APPLICATION OF VERTICALLY ALIGNED ARRAYS OF METAL-OXIDE NANOWIRES IN HETEROJUNCTION PHOTOVOLTAICS

By

Muhammad Bello Ladan

Submitted in fulfillment of the requirements of the degree of PhD (Physics) in the Department of Physics and Astronomy, University of the Western Cape

Supervisor: Dr Franscious Cummings

Co-Supervisor: Dr Theophillus Muller

December 2020

To my beloved Family

ACKNOWLEDGEMENTS

I wish to sincerely show my appreciation to the following people for their guidance and assistance through this journey and without their advice this thesis would not have been possible.

Dr. Franscious Cummings (Electron Microscope Unit, Department of Physics, University of the Western Cape) who acted as supervisor and Dr Theophillus Muller (Department of Physics, University of the Western Cape), who acted as co-supervisor during this study, for their constant encouragement and interest in my progress.

The Head of Department, Prof Christopher Arendse and other staff of the Physics Department, University of the Western Cape, for their support and encouragement. Mrs Natasha Kensley, Natasha Peterson, Angela Adams, Anele Tshaka, Lionel Fourie, Ian Cupido, Norman Bowers, Siphelo Ngqoloda and Siphesihle Magubane for their help and friendship.

To my immediate, extended family and friends, for their encouragement and support: Firstly to my wife Amina Muhammad and children, Aisha, Hafsat, Aliyu, Salima and Muhammad, I would like to say thank you for your love, patience and understanding through this journey – I love you! To my late father, may Almighty Allah grant you paradise amin, and to my mother (Hajiya Ramatu Aliyu) and step mothers (Hasana Abubakar and Fatima Muhammad) for their believe in me and always inspiring me to greater things!

To the rest of my family – Ladan, Kasim, Ibrahim, Tayyib, Musa, Isah, Aliyu, Muhammad, Yahya, Abdullahi, Ahmad, Aisha, Maimuna, Fatima, Amina, Sadiyya, Saratu, to all my uncles and aunties and the rest of the family for being there in my time of need when your support was truly needed.

To my closest friends and colleagues, Umar Badeggi Muhammad, Jibrin Alhaji Yabagi, Tijjani Jimoh, Abdullah Saba Ahmad, Hassan Abdulazeez, Kasim Badmus and Isah Kimpa Muhammad – thank you for being very good friends. Not forgetting my senior colleagues, Alhaji Suleman Dalhatu, Muhammad Bello Aliyu, Nma Suleiman, Abubakar Muhammad Ndagi and others. Finally, i specially thank all the staff of Ibrahim Badamasi Babangida University Lapai and the school management in particular for my PhD Sponsorship through the Needs Assessment Intervention Fund, thank you.

To Almighty Allah my Creator!

Thank You!!

DECLARATION

I declare that

‘‘APPLICATION OF VERTICALLY ALIGNED ARRAYS OF METAL-OXIDE NANOWIRES IN HETEROJUNCTION PHOTOVOLTAICS”

is my own work, that it has not been submitted for any examination or degree in any other university, and that all the sources I have quoted or used have been indicated and acknowledged by means of complete references.

Muhammad Bello Ladan **December 2020**

Signature: …….

KEYWORDS

APPLICATION OF VERTICALLY ALIGNED ARRAYS OF METAL-OXIDE NANOWIRES IN HETEROJUNCTION PHOTOVOLTAICS

TiO_2 and ZnO Nanowires

Iron (Fe), Nitrogen gas (N_2)

Organic Solar Cells

Photovoltaics

Hydrothermal Synthesis

Nitrogen Plasma treatment

Doping

Renewable Energy

One dimensional Nanostructure

Materials Science

Opto-electronic Properties

Morphology

Electron Charge Transfer

Crystallinity

Charge transport

Conductivity

SYMBOLS

APPLICATION OF VERTICALLY ALIGNED ARRAYS OF METAL-OXIDE NANOWIRES IN HETEROJUNCTION PHOTOVOLTAICS

N_2 – Nitrogen

V- Vanadium

Cr – Chromium

Sn- Tin

Fe- Iron

ETL – Electron Transport Layer

HOMO – Highest Occupied Molecular Orbit

LUMO – Lowest Unoccupied Molecular Orbit

E_g – Optical Bandgap

VB – Valence Band

CB – Conduction Band

IPCE – Incident-Photon-Current-Conversion-Efficiency

AM 1.5 – Global Air Mass 1.5

T – Transmittance

R- Reflectance

HF- High Frequency

HP- High powered

λ– Wavelength

d – Interplanar spacing

ɵ - Bragg Angle

FWHM/Γ0/B – Full Width at Half Maximum

J_{sc} – Short circuit current density

I_{MP} – Maximum current point

Voc – Open circuit voltage

VMP – Maximum Voltage Point

FF – Fill Factor

P_{max} – Maximum Power Point

η, PCE – Photon-current Conversion Efficiency

I_{sat} – Saturation Current

e_0 – Electron Charge

k_B – Boltzmann Constant

I_{sc}- Current Short Circuit

V_{oc}- Voltage Open Circuit

Ag – Silver

ABSTRACT

APPLICATION OF VERTICALLY ALIGNED ARRAYS OF METAL-OXIDE NANOWIRES IN HETEROJUNCTION PHOTOVOLTAICS

Muhammad Bello Ladan

Ph.D. Thesis, Department of Physics and Astronomy, University of the Western Cape

The commercial need to improve the performance of low-cost organic solar cells has led to the idea for this research. The study discusses the synthesis of one dimensional TiO_2 and ZnO nanowire arrays synthesised using a hydrothermal autoclave method and their application in bulk heterojunction inverted organic solar cells. Previous literature has shown that the precise manipulation, positioning and assembly of 1D nanostructures remain one of the greatest challenges in the field of nanotechnology, with much of the difficulty arising primarily from the lack of size and scale of the materials as well as the inability to visualise the nanostructures. In particular, one dimensional metal-oxides such as TiO_2, ZnO and Fe_2O_3 have emerged as attractive alternatives to traditional semiconductor structures such as Si and GaAs as they are simple and inexpensive to manufacture, with research showing that application of ZnO nano-cones yield efficiencies of 8.4%, which is very attractive given the scope that exists in optimising the metal-oxide architecture. Much is still to be learned from the precise structural features of these materials and their influence on device performance. In this regard, this work largely focuses on this aspect of metal-oxide nanowires prior their application in organic solar cells. Understanding how these processes are influenced by the inherent opto-electronic properties potentially gives greater insights into the mechanisms that define device efficiency and performance. For example, although the 1D structure acts as atemplate for the manufacturing of radial, hetero-junction devices, the natural n-type character also allows metal-oxides to be used as charge-mediating material during operation, which leads to uncertainty in the exact role of the material during operation. This uncertainty, though, forms the basis of this study in that it offers the opportunity to investigate the performance of solar cells with natural n-type metal-oxide nanowires, as typically reported in literature, to co-doped nanowires to test the hypothesis of

charge transport in solar cells. A significant portion of the study is focused on understanding the doping mechanism and influence on the structure-property relationship prior to application in the well-researched regioregular poly(3-hexylthiophene-2,5-diyl) - [6,6]-Phenyl-C61-butyric acid methyl ester (P3HT-PCBM) polymer solar cells, or more commonly known as organic solar cells. Simple processing methods such as hydrothermal synthesis of the array of nanowires, spin-coating of the polymer-blends, cost-effective thermal evaporation and other common, low-cost lab-scale methods are employed to demonstate that effective devices can be manufactured without the use of expensive humidity controlled processing equipment such as glove-boxes and clean rooms. A novel approach explored in this study is the use of nitrogen plasma in combination with standard metal-doping strategies to introduce a controlled level of nitrogen dopants in the metal-oxide lattices of TiO_2 and ZnO to induce p-type doping, which in turn allows for improved electron transport during device operation.

To further investigate the performance of solar cells with natural n-type metal-oxide nanowires, as typically reported in literature, the co-doping of TiO_2 and ZnO nanowires with modifiers of Fe, V, Cr and Sn to test the hypothesis of charge transport in solar cells was also studied. Characterisation of the structural features of individual nanowires is achieved by electron microscopy and incident X-ray diffraction, with optical spectroscopy combined with X-ray photo-electron spectroscopy, electron energy loss spectroscopy and energy dispersive X-ray spectroscopy mapping give insights into the doping character, distribution of dopants and alteration of the electronic structure of the TiO2 and ZnO nanowires and their influence on the measured optical propertes. It will be shown that the use of plasma irradition morphologically causes a distortion of the vertical alignment of the nanowires due to a dissociation of the weak Van der Waals force clustering the nanowires, whereas optical spectroscopy studies show that plasma treatment increases the light transmission of TiO_2 arrays from 48% to 90%, with the ZnO arrays exhibiting an increase from 70% to 90% in the visible to UV range. The as-synthesised TiO_2 array has an indirect band gap of 3.13 eV, which reduces to 3.03 eV after N_2 treatment, with the ZnO equivalent decreasing from 3.20 to 3.17 eV post plasma exposure. A study of the 3d transition metal near edge fine structure of both Ti and Zn show that the N_2 plasma treatment of the nanowires results in nitrogen doping of both TiO_2 and ZnO lattices; this is confirmed by scanning transmission electron microscopy coupled with energy dispersive spectroscopy x-ray

maps collected of single nanowires, which show a clear distribution of nitrogen throughout the metal-oxide. Application of these structures in P3HT:PCBM polymer blends shows progressive improvement in the photoluminescence quenching of the photoactive layer when incorporating both undoped and nitrogen-doped nanowires. Inverted, hetero-junction organic solar cells are manufactured with as-prepared and nitrogen plasma irradiated nanowires, with device performance results showing that the plasma-assisted technique holding definite promise for improving the electron transport in organic solar cells. Photon-to-current conversion efficiency results show an increase from a poor performance of 0.167 for as-synthesised ZnO nanowire-based devices to a respectable value of 0.57% post plasma exposure. The TiO_2 based devices show overall better performance with an increase in efficiency of 15% from 1.7 for unmodified nanowire-based devices to 1.95% post irradiation.

TABLE OF CONTENTS

APPLICATION OF VERTICALLY ALIGNED ARRAYS OF METAL-OXIDE NANOWIRES IN HETEROJUNCTION PHOTOVOLTAICS

CHAPTER ONE

BACKGROUND AND LITERATURE REVIEW

1.1 Overview

Nanowires (NWs) are defined as metallic or semiconductor particles with high aspect ratio, having cross-sectional diameters less than 1 μm and length to the tune of tens of microns [1.1-1.2]. Of several known NWs, vertically and well-aligned one-dimensional (1D) NW arrays have been extensively investigated by researchers as a photoelectrode in solar energy conversion owing to its direct pathways and guarantee speedy collection of carriers generated throughout the device [1.3]. In addition, these structures have large junction areas and low reflectance which are favourable for internal light scattering and trapping [1.4]. Among the semiconductor based photovoltaic (PV) devices, excitonic solar cells such as organic and dye-sensitised solar cells show significant potential as a low cost alternative to the more common inorganic types.

In the last couple of years, the synthesis of metal oxide 1D materials and their applications in excitonic solar cells have attracted significant research due to their large surface areas and short diffusion length for minority carriers. Not only that, metal oxide 1D materials also represent a new class of photoelectrode with enormous prospect for photoelectrochemical (PEC) hydrogen generation applications in addition to PVs. To date, different varieties of metal oxide nanostructures including ZnO [1.5], TiO_2 [1.6], Fe_2O_3 [1.7], Nb_2O_5 [1.8], ZrO_2 [1.9], Al_2O_3 [1.10] and CeO_2 [1.11] have successfully been employed as photoelectrodes in different solar cell architectures. The inherent n-type nature of these materials has been widely exploited for use as an electron transport medium and originates from the large density of oxygen vacancies present on the surface of the 1D material. Nonetheless, these vacancies lead to electron trap-sites, causing electron-hole recombination and low electron mobility during operation of the device in addition to changing the material's chemical reactivity and stability [1.12-1.16]. To overcome this, nitrogen doping via chemical synthesis approaches [1.17], high temperature annealing in a nitrogen rich atmosphere [1.18], ion

implantation [1.19] and cathode magnetron sputtering [1.20] have been identified as viable strategies with different degree of success and repeatability.

Furthermore, two widely studied semiconductors namely TiO_2 and ZnO of well-known lattices and robust structural integrity with proven photovoltaic performances have been selected in this work due to their excellent chemical stability and light harvest and conversion potentials. The problem of high electron-hole recombination rate of the two materials limits their photovoltaic capacity. On the contrary, doping and co-doping of TiO_2 with selective metal [1.21-1.22] and non-metal ions [1.22-1.23] have shown to alter the electronic conductivity and optical bandgap of the TiO_2 host matrix under certain doping conditions, which are obviously beneficial for PV application. Similarly, the optoelectronic properties of ZnO are known to depend on its structural morphology [1.24], doping elements and concentration [1.25], as well as fabrication technique [1.26]. The similarities in ionic radius between O, Fe and N make the latter two elements, especially, suitable doping candidates in ZnO and TiO_2 lattices. Fe and N are known as p-type dopants in group II-VI semiconductors [1.27,1.28], and Fe and N impurities behave as donors and acceptors, respectively, or can be employed as co-dopants, thus acting as shallow donors to enhance the electrical properties in thin films of TiO_2 and ZnO [1.26, 1.29-1.30]. To appreciably minimise the disadvantages of surface oxygen vacancies, doping concentration exceeding 5 at% with either Fe or N, or both is required. The study focus on the irradiation of TiO_2 and ZnO NW arrays with radio frequency (RF) generated plasma nitrogen, followed by introduction of high concentration of substitutional nitrogen dopants onto the metal-oxide lattices, and then compared to more common chemical and high temperature annealing approaches often reported.

1.2 Doping of Semiconducting Material

Semiconductor crystals with no impurities are referred to as intrinsic semiconductors [1.31]. The process of introducing impurities, of a different element, into these pure materials is called *doping*. When any semiconductor is doped with impurities, it becomes an extrinsic semiconductor and new energy levels are introduced in the electronic structure. Figure 1.1 illustrates the principal of n and p-type doping of intrinsic silicon (Si). In Fig. 1.1 (a) the four valence electrons from phosphorous (P), a group V element, form covalent bonds with the

bordering nearest Si atoms; the fifth electron subsequently becomes a conduction electron which is donated to the conduction band; therefore. This material is referred to as an n-type donator due to the extra negative charge carrier, or just an *n-type* material. The situation is somewhat different in Fig. 1.1 (b), in which a Si atom is substituted by a group III atom such as boron (B). At this point the local lattice is deficient of one electron, and can receive an electron from one the nearest atom or a free conduction band electron. Therefore, the material is referred to as p-type acceptor (or just *p-type*) due to the released positive charge by the accepting electron.

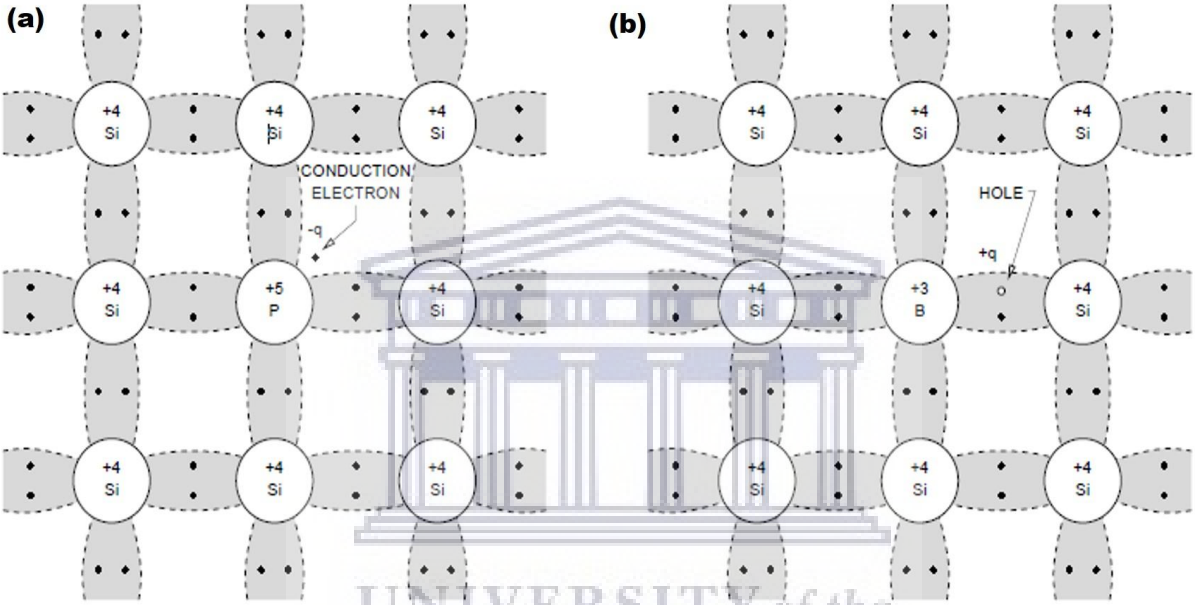

Fig. 1.1 (a) Si lattice with one of the atoms replaced by a group V atom, e.g. phosphor (b) the same lattice with one Si atom replaced by group III atom just like B. [1.31]

The conduction electrons in an n-type semiconductor are known as the majority carriers while conduction holes are minority carriers. In p-type materials, the situation is reversed in that conduction electrons become the minority carriers while conduction holes are the majority carriers. These two phenomena are schematically shown in Fig. 1.2 (a) and (b). The effect of introducing impurities and native defects plays a very important role in enhancing the optical and electrical properties of both ZnO and TiO_2 [1.32]. The n and p-type semiconductor nanowires have been achieved via different routes, including in-situ doping during growth [1.33], ion implantation [1.34], post-annealing [1.35] and high frequency (HF) plasma CVD. But, some of those methods have their inherent problems. For example, ion implantation leads to structural damage and high defect density, which results in a low

quality crystal structure and increased resistivity in nanowires [1.36]. Furthermore, post-annealing leads to a reduction in near band edge emission intensity due to dopant contamination of the nanowires [1.35]. Also, control of the doping concentration becomes obviously difficult to achieve, subsequently leading to inconsistent results upon device application. In comparing these techniques, HF plasma CVD yields better results in terms of delivering a controlled doping profile while maintaining the high quality nanowire structure [1.37].

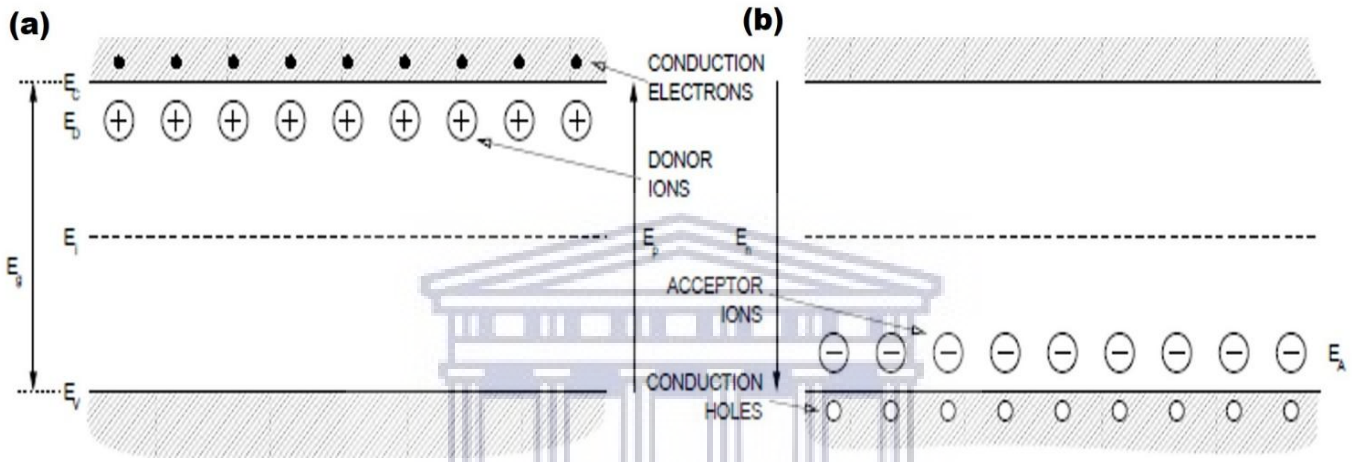

Fig. 1.2: Schematic illustration of the energy level diagram of (a) n-type and (b) p-type lattices [1.31].

1.3 Synthesis of ZnO Nanowires

ZnO nanowires can be grown on substrates or separately in powder form. For photovoltaic and photocatalytic applications, however, vertically aligned growth on a substrate has more benefits. The ZnO crystal structure anisotropy helps in the nanowire growth. The most prevalent polar surface is the basal plane (0001) with one end of the basal polar plane ending in partly positive Zn lattice points and the other ending in partly negative lattice points of oxygen. The nanowires anisotropic growth takes place along the c-axis in the direction [0002] [1.38]. The growth velocities (V) under hydrothermal conditions along the different directions follow the pattern $V(0001) > V(1011) > V(1010)$ [1.39]. The relative growth rate of these crystal faces determines final morphology and aspect ratio of the ZnO nanostructures. The ZnO nanowires synthesis techniques can primarily be categorised as phase vapour and phase solution synthesis.

1.3.1 Vapour Phase Synthesis. This synthesis route is arguably the most widely used approach to 1D nanostructure formation [1.40]. Typically vapour phase synthesis technique occurs in a gaseous closed chamber situation. Hence, the vapour species are primarily produced by evaporation, chemical reduction and gaseous reaction. Furthermore, the species are afterwards transmitted and condensed on top of a solid substrate surface. In general, the vapour phase synthesis method is performed at higher temperatures between 500 and 1500 °C to produce a high-quality nanowire. During vapour phase synthesis the standard method consists of the following: vapour liquid solid (VLS) growth [1.41], metal organic chemical vapour deposition (MOCVD) [1.42], chemical vapour deposition (CVD)[1.43], physical vapour deposition (PVD)[1.44], metal organic vapour epitaxy (MOVPE)[1.45], molecular beam epitaxy (MBE) [1.46], and pulsed laser deposition (PLD) [1.47]. VLS and MOCVD are two of the most significantly used methods for ZnO nanowires synthesis among all the other vapour phase synthesis techniques. Among these methods, the VLS approach has emerged as the most popular due to the easy set-up, inexpensive running costs and ability to grow ZnO on larger wafers [1.48]. The classical VLS process is characterised by the use of a nanosized liquid metal droplet as catalyst, gaseous reactants interacting with the nanosized liquid to facilitate nucleation and growth of single crystalline rods and wires. Au, Cu, Ni and Sn are typical metal catalysts used in the VLS process, with sapphire, AlGaN and GaN substrates the most utilised substrates [1.49]. During VLS growth, the quality, repeatability and growth behaviour of the nanowires are greatly influenced by chamber pressure, partial oxygen pressure and catalyst layer thickness [1.50, 1.51]. A specific highlight in this field is the work by Chu *et al.* [1.52] who reportedly synthesized well-aligned ZnO nanowires on a Si substrate using a chamber temperature ranging from 600 to 950 °C and 0.75 to 3 torr of pressure.

Over the last decade, catalyst-free MOCVD has emerged as a true rival to VLS techniques, due to the attractiveness of the catalyst-free approach that eliminates the possibility of catalytic impurity incorporation in the reactor chamber - a well-known disadvantage of VLS systems [1.42, 1.53]. This approach ensures the production of ZnO nanowires of high purity and at lower growth temperatures [1.54]. [1.40]. Zeng *et al.* [1.55] used catalyst-free MOCVD to prepare well-aligned ZnO nanowires on Si substrates using a high-purity diethyl zinc (99.999%) and N_2O (99.999%) zinc and oxygen sources, respectively, with N_2 as carrier gas and successfully synthesised the NWs at 650 °C. Similarly, the same group reported [1.56] the fabrication of ZnO nanowire arrays by PVD technique on Si substrates at a

comparatively low temperature of approximately 500 °C, with high-purity Zn powder as a source material placed in the middle of a horizontal tube furnace, using N_2 as feeder gas once more.

1.3.2 Solution Phase Synthesis. This method, when compared to vapour phase synthesis required no high-end vacuum and clean room facilities, and offer many benefits, including low cost, scalability, low temperature and ease of operation. When compared to the classical physical vapour methods, solution processing reactions generally take place at comparatively low temperatures (< 200 °C). Because of this, the solution synthesis methods cater for a greater selection of substrates, including both organic [1.57] and inorganic substrates [1.58]. It is should be mentioned that the growth process could be performed in solution phase synthesis in either an aqueous or organic solution or a combination of the two [1.59, 1.60].

1.3.3 Hydrothermal Synthesis. This solution phase synthesis is generally performed in an aqueous solution and is thus referred to as the *hydrothermal growth method* [1.61, 1.62]. ZnO nanowires grown hydrothermally have more crystalline defects than compared to those prepared using physical deposition methods, mainly due to oxygen vacancies [1.63]. However, the nanowires with intrinsic defects often exhibit visible light photocatalysis and act as electron transport media in photovoltaics, even without transition metal doping [1.64]. These oxygen vacancies are generally not ideal for PV application, as they lead to electron trap-sites, causing electron-hole recombination during operation of the device. In addition, the presence of vacancies also changes the material's chemical reactivity and stability [1.32], hence doping of NWs with metals and non-metals have been suggested as a viable option. The overall process for vertically aligned ZnO nanowire growth by hydrothermal synthesis on a substrate is shown schematically in Fig. 1.3. A thin layer of ZnO nanoparticles is seeded on a substrate, as required for a specific application. Although there are several methods used for the deposition of seed layers, including successive ionic layer adsorption and reaction (SILAR), spray pyrolysis, sputtering, CVD, dip coating, spin coating etc., the spin-coating method is generally the method of choice, due to its low-cost, easy handling and generally acceptably even thin films. The seed layer is typically deposited by spin-coating using a solution of poly(vinyl alcohol) (PVA) and zinc acetate ($Zn(Ac)_2$) salt onto the substrate at optimised conditions, followed by annealing. Due to the reduction of the thermodynamic barrier, the seeding layer encourages nucleation for the growth of the nanowires [1.65]. An

alkaline reagent such as sodium hydroxide (NaOH) or hexamethylenetetramine ($(CH_2)_6N_4$ or HMTA) and Zn^{2+} salt such as zinc nitrate ($Zn(NO_3)_2$) or zinc chloride ($ZnCl_2$) used as nanowire precursors are usually known as the growth solution. The seeded ZnO substrate is held at a specific temperature and time in the hydrothermal growth solution, followed by washing and drying. The chemical reactions leading to the formation of ZnO NWs can be summarised in equations 1.1 - 1.4 [1.66]. The different experimental stages usually followed to achieve a successful hydrothermal synthesis of ZnO NWs are displayed in Fig. 1.3:

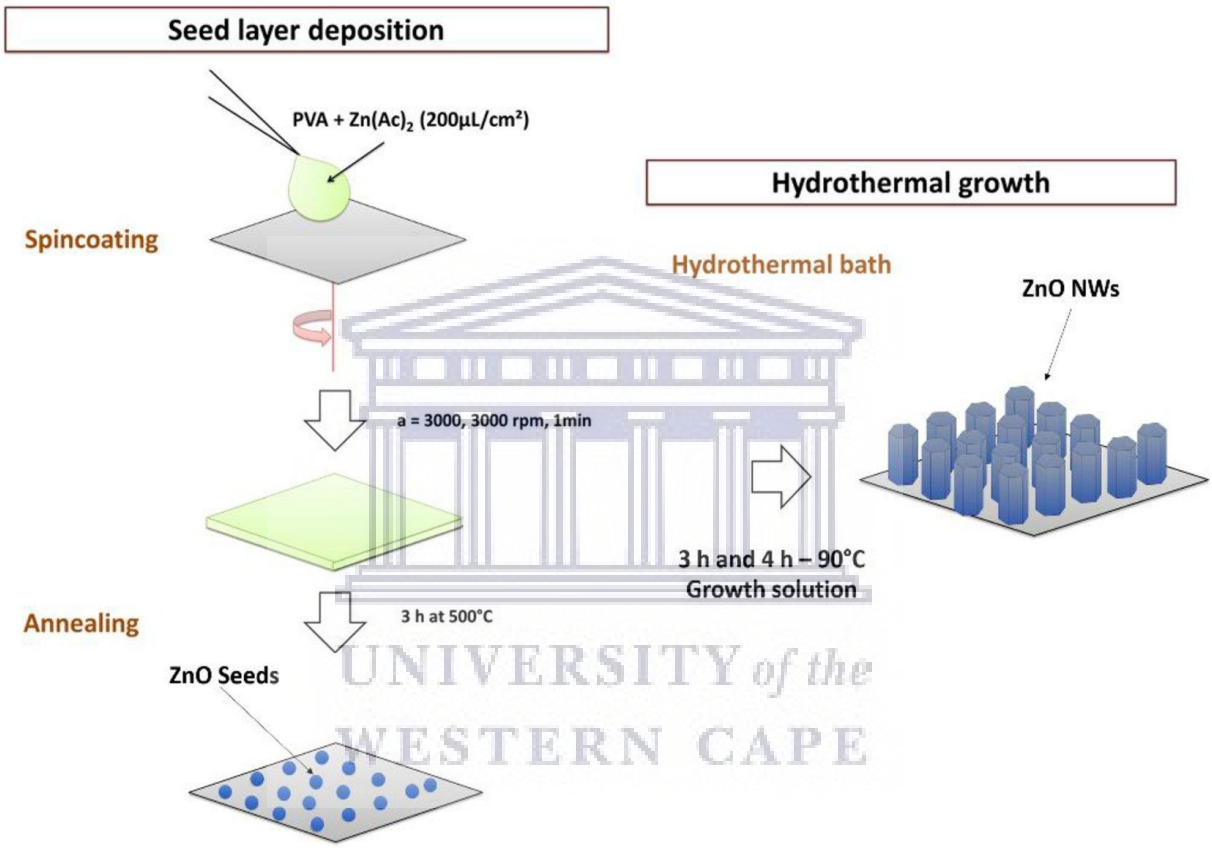

Fig. 1.3: Schematic diagram of a hydrothermal process for ZnO NWs growth [1.67]

Decomposition reaction:

$$(CH_2)_6N_4 + 6H_2O \rightarrow 6HCHO + 4NH_3 \qquad (1.1)$$

Hydroxyl supply reaction:

$$NH_3 + H_2O \longleftrightarrow NH_4^+ + OH^- \qquad (1.2)$$

Supersaturation reaction:

$$2OH^- + Zn^{2+} \rightarrow Zn(OH)_2 \quad (1.3)$$

ZnO nanowire growth reaction:

$$Zn(OH)_2 \rightarrow ZnO + H_2O \quad (1.4)$$

One of the main parameters for ZnO nanowires growth is controlling the super-saturation reactants. High concentrations of super-saturation favoured nucleation process while low concentrations of super-saturation promoted crystal growth [1.68]. If a lot of OH^- is produced in a short time, precipitate of Zn^{2+} ions would be obtained due to the high pH environment, and thus Zn^{2+} would contribute little to the growth of ZnO nanowire and ultimately result in quick nutrient intake and prohibit further ZnO nanowires growth [1.69]. Therefore, the concentration of OH^- in the solution should be regulated to keep low concentrations of super-saturation during the entire growth process.

1.4 Synthesis of TiO_2 Nanowires

Different approaches for synthesising TiO_2 nanowires have been developed and reported with the most researchers employing sol-gel, sonochemical and microwave-assisted approaches for wet-chemical synthesis, compared to the vacuum-assisted, physical vapor deposition methods are reviewed as follow (are discussed below). The last sub-section also focusses on the hydrothermal/solvothermal method as it related to growth kinetics of TiO_2 NWs

1.4.1 Sol-Gel Synthesis. The sol-gel method is widely used for the synthesis of hybrid materials of inorganic and organic compounds [1.70, 1.71]. The method involves the use of a colloidal suspension (or sol) produced via a typical sol-gel process from precursor hydrolysis and polymerisation reactions (usually inorganic metal salts or organic metal compounds) such as metal alkoxides. The solvent loss and complete polymerisation lead to transitional change from the liquid sol into solid gel phase. Vertically aligned TiO_2 nanowires are typically synthesised by hydrolysing a titanium precursor solution and subjecting it to a template during growth [1.72, 1.73]. Different researchers have employed this route to prepare titania NWs. For instance, Lei *et al*. [1.72] employed anodic alumina membranes (AAMs) to prepare highly ordered TiO_2 nanowires, where tetrabutyl titanate, ethanol, acetic acid and water served as the colloidal suspension. The AAMs were immersed into the sol,

followed by drying and annealing to obtain vertically aligned TiO_2 NWs. In addition, Miao *et al.* [1.73] innovatively prepared single crystalline nanowire arrays via an electrochemically induced sol-gel method by dissolving Ti powder in hydrogen peroxide (H_2O_2) and ammonia (NH_3), calcination at low temperature, followed by forming an electrolyte with the calcined powders and electrodeposition onto AAMs substrates.

1.4.2 Sonochemical Synthesis. Sonochemistry is the result of acoustic cavitation, a phenomenon that produces bubbles in liquid from sonic or ultrasonic waves. The cavitational collapse generates an intense local heating (~ 5000 K), at high pressure (~1000 atm) and vast heating and cooling (> 109 K/s). This method has been used in the preparation of different TiO_2 NWs structures. For instance, Zhu *et al*. [1.74] produced titanium whiskers and nanotubes by dissolving titania powder in a NaOH aqueous solution followed by sonication over an extended period of time. Because of the drastic temperature gradient close to the reaction sites, it was discovered that the sonication time played a significant part in accelerating the precursor reactions in addition to vertically aligning the TiO_2 crystal growth.

1.4.3 Microwave Assisted Methods. Microwave irradiation offers a distinctive progressive heating pattern that is particularly efficient for synthesis of colloidal nanomaterials. The conductive currents flowing within the material at lower microwave frequencies, owing to the movement of ionic constituents, transfer energy from the microwave field to the material. Furthermore, the energy absorption at higher frequencies is primarily owing to molecules with a permanent dipole, which tend to re-orientate under the control of a microwave electric field. As such, the microwave frequency plays a significant role in controlling the nanomaterial shape. Various researchers have applied microwave radiation to prepare TiO_2 nanowires. Jia *et al*. [1.75] have effectively synthesised TiO_2 nanorods (NRs) using a straightforward and low-cost microwave-assisted method where a tri-block copolymer was used as a stabilising agent and hydrolising $TiCl_4$, as metal precursor, in dilute hydrochloric acid (HCl), under the following applied conditions: room temperature to 300° C at a rate of 2.5°C min^{-1}, holding time of 8 hours, followed by cooling to room temperature for 7 days. The prepared material was then calcined in the furnace at 400°C for 3.5 hours. Small necklace-shaped NRs assembled initially and over time transformed into larger TiO_2 NRs. Ma *et al*. [1.76] reported high-quality TiO_2 rutile nanorods using a similar approach to that of Jia *et al*

[1.75], but discovered that the NRs developed along the c-axis of TiO_2 rutile and radially aggregated into secondary spherical nanoparticles (NPs).

1.4.4 Physical Vapour Deposition. The different types of PVD synthesis methods include thermal evaporation [1.77], ion implantation [1.78], ion plating [1.79], sputtering [1.80], laser surface alloying [1.81] and laser vaporisation [1.82]. However, thermal deposition remains the most popularly and widely used to fabricate TiO_2 nanowire arrays. Wu *et al.* [1.83] reported two-step thermal evaporation of Ti powders at 1050 ˚C on alumina substrates to form aligned TiO_2 nanowire, whereas Xiang et al [1.84] prepared TiO_2 arrays using thermal deposition method [1.84]. During this process Ti powder was evaporated at 850 ˚C under an argon stream for 3 h resulting in the formation of a layer of TiO_2 arrays aligned vertically on a Si wafer.

1.4.5 Chemical Vapour Deposition. Chemical vapour deposition is a process where vaporised precursor materials decompose or respond to particular surfaces of the substrate and condense to form a solid-phase material. Usually, the precursors are carried by an inert gas and the reaction takes place in a vacuum chamber. The method is called physical vapour deposition (PVD) if there are no chemical reactions involved during the deposition (as discussed in section 1.4.4 above); otherwise it is called CVD. Of the different CVD methods, metal-organic CVD has emerged as the most attractive owing to the repeatable results attainable. For instance, Pradhan *et al.* [1.85] reported the synthesis of TiO_2 nanorods on a WC-Co substrate using titanium tetra-isopropoxide (TTIP, $Ti(OC_3H_7)_4$) as a precursor during MOCVD and found that the TiO_2 NR orientation can be aligned with corresponding crystal lattices by introducing single-crystalline substrates. Elsewhere, also using TTIP as a precursor, Chen *et al.* [1.86] reported the synthesis of well aligned rutile TiO_2 NRs on (100) oriented sapphire substrates and showed that the NRs were very high in real density, with a preferred growth direction along [001]. Using a less common technique to MOCVD, Shi *et al.* [1.87] reportedly grew rutile TiO_2 NWs using CVD in a controlled manner and observed split growth of TiO_2 NWs as either curvy or high-index surfaces.

1.4.6 Hydrothermal/Solvothermal Methods. Hydrothermal/solvothermal method is a commonly employed in the growth synthesis of nanomaterials via the use of aqueous or non-aqueous solutions. Typically, the synthesis is performed inside autoclaves where

crystallisation of inorganic metals occurs at high temperature and pressure in a precursor solution. Many research groups used this method to synthesise TiO_2 nanowires because of the easy configuration, facile operations, and desirable growth results. This will also be the synthesis method of choice in this study and will be discussed in greater detail in Chapter 2. Of the most prominent work in the field, Zhang *et al.* [1.88] used a straightforward hydrothermal approach to successfully fabricate single-crystalline anatase TiO_2 nanowires. The wires were prepared via a chemical process very similar to the one described by Kasuga *et al* [1.89]. The experiment involves preparing a 40 ml aqueous solution consisting of 1 gram anatase TiO_2 powders and 10 M NaOH in a Teflon-lined autoclave (capacity of 50 ml), sealing the autoclave in a stainless steel tank leaving it at 200°C for 24 h without any shaking or stirring. Post-synthesis and cooling the structures are washed in dilute HCl and absolute ethanol followed by drying at 70°C for 6 h to form soft, white fibrous powders. Fig. 1.4 shows the different experimental stages followed to achieve successful hydrothermal synthesis of TiO_2 NWs:

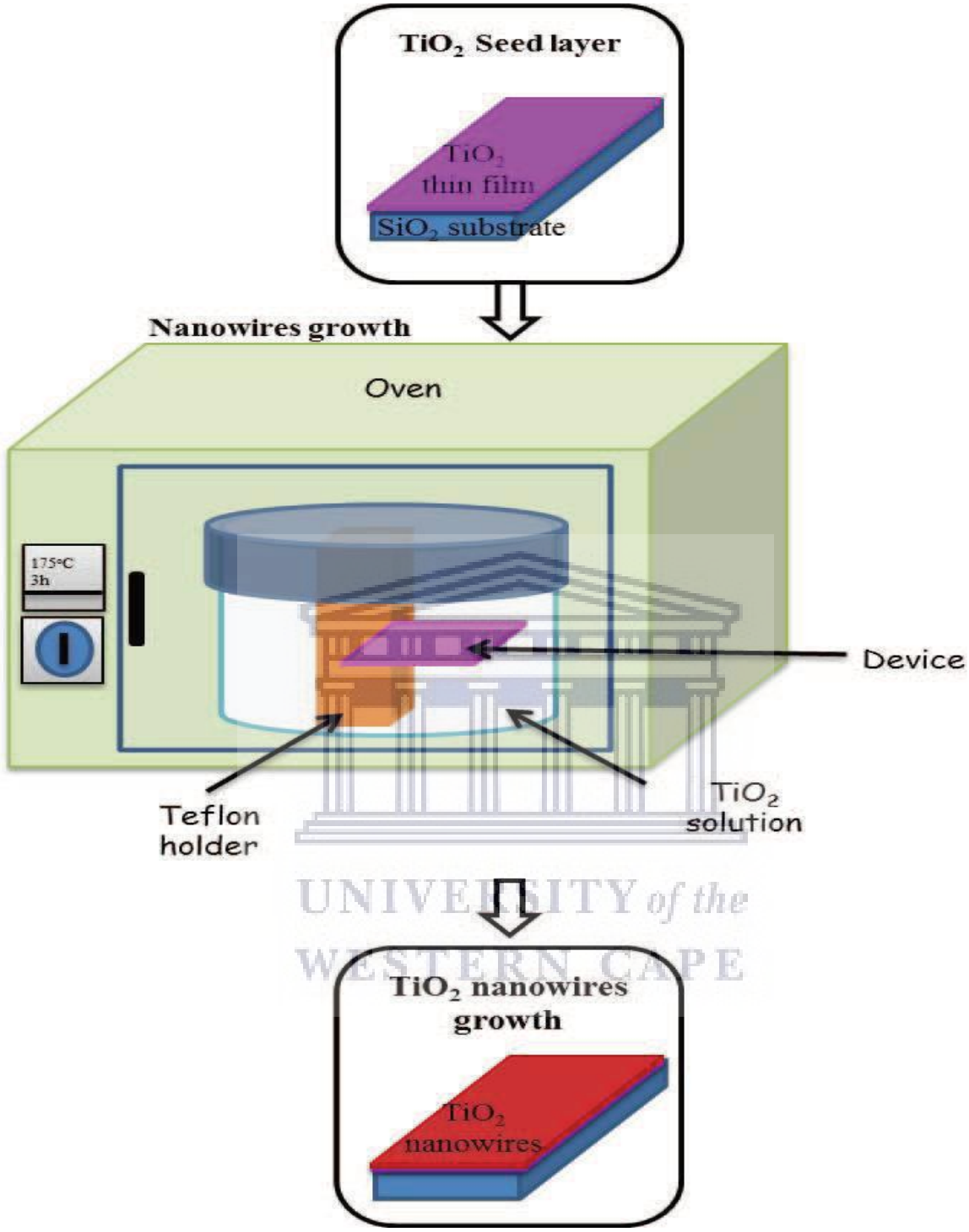

Fig. 1.4: Schematic diagram of hydrothermal process of TiO_2 NWs [1.90]

1.5 Hybrid Inverted Organic Solar Cells

Photovoltaics provide the most direct means of converting solar energy into electrical energy for household use. A basic PV device consists of an underlying photovoltaic (or solar) cell and peripheral devices, such as a battery, inverter, etc. The current high cost of producing electricity with PV technologies (compared to that generated from fossil fuels), combined with the relatively short life-time and low stability of the underlying solar cells, have seen PVs commercialised at a very small scale. However, the global energy demand is rapidly approaching the supply limit of fossil and crude oil technologies, meaning that renewable, and in particular PV technologies, must play a crucial role in the future global energy mix.

Over the last three decades, several research efforts have been devoted to the enhancement of the performance of low-cost, third generation photovoltaics; especially bulk heterojunction (BHJ) organic solar cells [1.91–1.93] and dye-sensitised solar cells (DSSCs) [1.94]. In addition to their relatively low cost compared to first and second generation semiconductor (e.g. Si and GaAs) PVs, these cells possess promising power conversion efficiency (PCE). In addition, these cells are easily fabricated by contact printing [1.95] and roll-to-roll processes [1.96, 1.97] for large area devices, and hold potential for small scale electronics, off-grid power connections and building integrated PV applications. Typical BHJ cells consist of conjugated derivatives of polymers and fullerenes, all of which are organic, which thus gives origin to its name as BHJ organic or just *organic solar cells* (OSCs). However, the fullerene derivatives are often substituted or mixed with inorganic materials such as CdS [1.98–1.99], TiO_2 [1.100–1.101], CdSe [1.102–1.103], ZnO [1.104–1.105], CuInS2 [1.106] SnO_2 [1.107] amongst others resulting in these devices being called *hybrid solar cells* (HSCs). Inorganic materials such as TiO_2 and ZnO have high dielectric constants, high electron affinity and mobility, and very strong thermal stability while their optoelectronic properties can be manipulated by adjusting the shapes and sizes of individual NPs; all of which could promote the design of high-performance HSCs [1.108–1.109].

Over the years, HSC research has developed rapidly and increased the understanding of the underlying physics during device operation. However, right selection of the conjugated polymer-inorganic dielectric mixture blend remains the most crucial aspects to optimum performance even though consideration may be given to the morphologies of the dielectric

metal-oxide nanoparticle or nanowires used. As such, this focus area remains one of the most intensely scrutinised photovoltaic research fields. More so, the present HSC PCEs are still considerably lower than that of traditional OSCs and DSSCs. A more attractive approach is the use of TiO_2 or ZnO thin films in HSCs as electron acceptors and conduction pathways, known as *electron transport layers* (ETLs), deposited directly onto transparent conducting oxide (TCO) substrates such as indium-tin oxide (ITO) or fluorine doped tin oxide (FTO) as part of the photo-active layer. Using this approach, the enhanced dielectric properties of the metal-oxide is still employed to the benefit of device performance. More recently, nanowire and nanorod arrays of ZnO and TiO_2 have been used as ETLs in HSCs as a further approach to improving the overall solar cell efficiency; this will be discussed in more detail in the following sections.

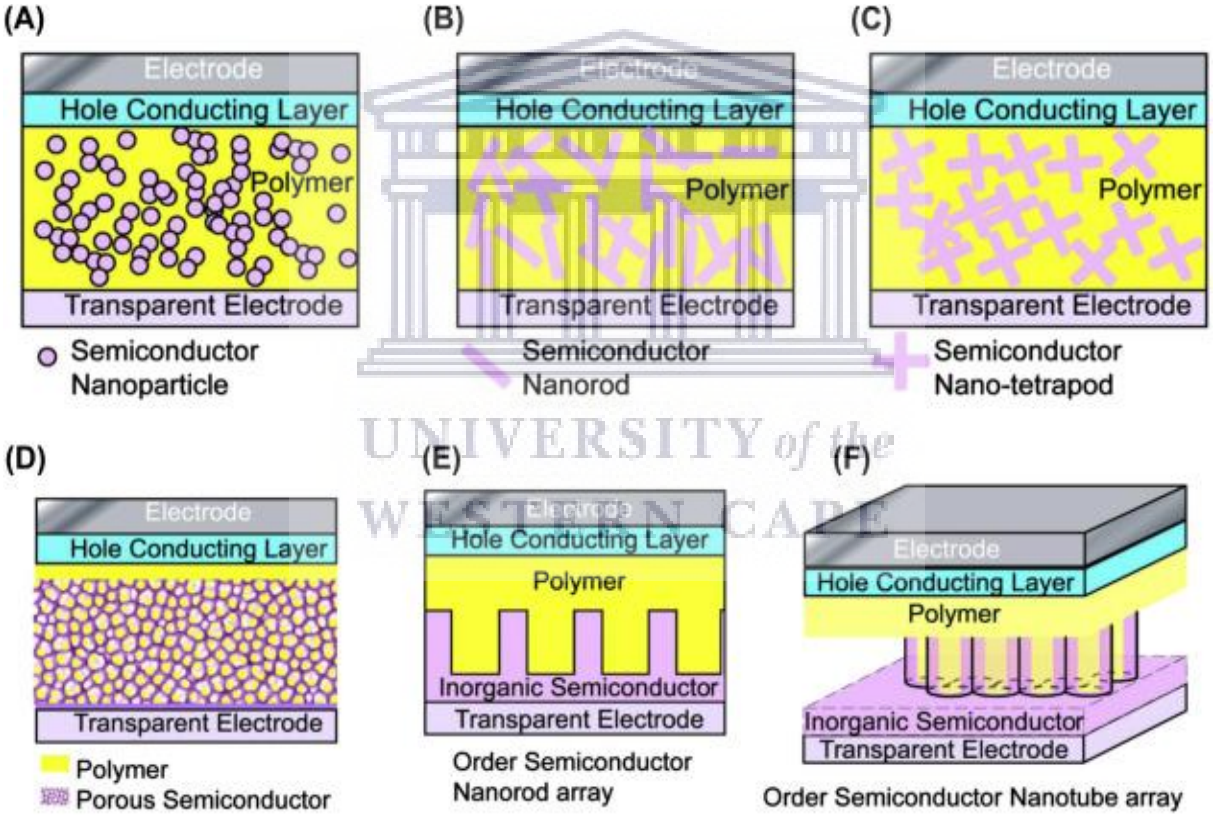

Fig. 1.5: Different possible BHJs when semiconductor materials are mixed with polymers in HSCs (a) nanoparticles (b) nanorods (c) nano-tetrapods (d) porous semiconductor layer (e) ordered nanorod array and (f) ordered nanotube array [1.110]

The use of BHJs in HSCs is an improvement over the previous use of a bilayer structure. By design the BHJ is a network of intermixed donor and acceptor materials, see Fig. 1.5 (a). Bulk heterojunction HSCs are fabricated either by infiltration of the polymer materials involving inorganic network, or using simultaneous deposition of the blend of polymer and inorganic nanocrystals. Various other types of hybrid heterojunctions are commonly employed, as shown in Fig. 1.5(b) to (d). If the BHJ is made up of ordered inorganic nanostructures, for example ordered nanorods, nanotubes, and nanowire arrays, it is also known as an *ordered heterojunction*; this is shown schematically in Fig. 1.5 (e) and (f). Ordered heterojunctions have recently emerged as the preferred morphology for HSCs, due to its direct charge pathway and tunable donor and acceptor (D/A) domain size, which are both essential for efficient charge dissociation and transport [1.111].

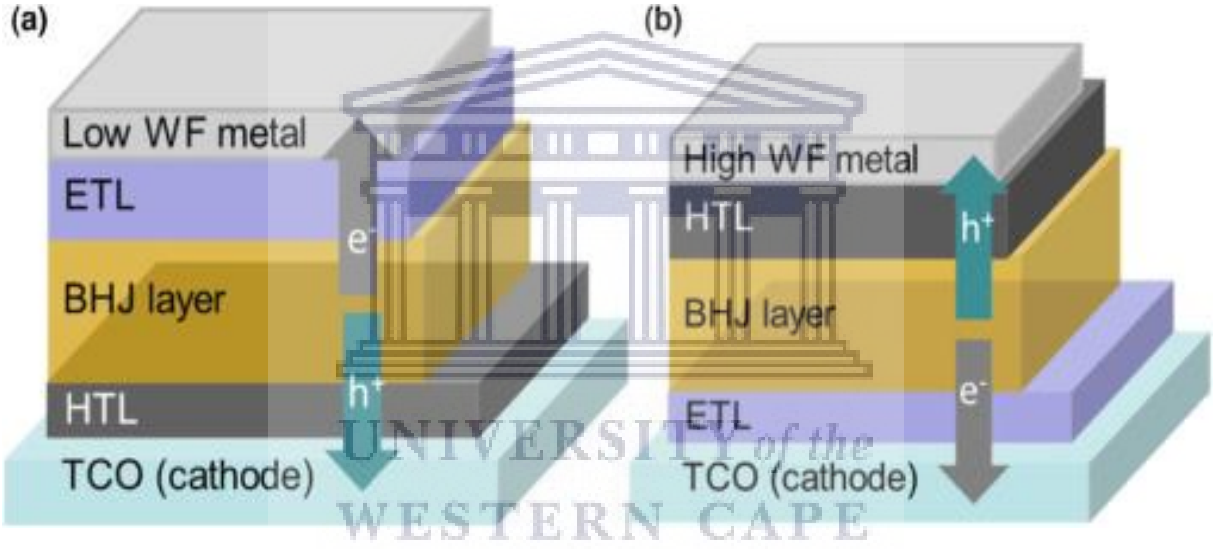

Fig. 1.6: Schematic diagram of a direct versus inverted BHJ solar cell [1.112]

Generally, there are two types of architectures to consider during fabrication of hybrid BHJ cells, namely direct and inverted device structures, as shown in Fig. 1.6. In a standard (direct) device the hole transporting layer (HTL), such as poly(3,4-ethylenedioxythiophene): poly(styrene sulphonate) (PEDOT:PSS) or molybdenum oxide (MoO_3) is deposited directly onto the TCO with a low work-function metal such as Al used as the top contact. This is reversed in the case of inverted devices where the ETL is deposited directly onto the TCO and a high work-function metal such as Au or Ag is used as top contact. Among several n-type metal oxides used in the inverted cells, ZnO and TiO_2 are promising candidates due to their relatively high electron mobility, environmental stability, and high transparency. The

operation principle and complete device structure will be discussed in greater detail in Chapter 2.

1.6 ZnO and TiO_2 Electron Transport Layers in Inverted Hybrid Solar Cells

During device operation, ZnO and TiO_2 served as the pathway through which the electrons move from the TCO/anode base to the top contact/cathode in the solar cell. This pathway is called the electron transport layer. Bak *et al* [1.113] reported that the mobility of electrons in TiO_2 is low (0.1 - 4 cm^2 Vs^{-1}) and thus affects the electron transport rate, which is the rate at which photo-generated electrons are transported from the photo-anode film to the external contact. This low mobility, owing to the large density of oxygen vacancies, leads to decrease in the collection efficiency of the device. On the other hand, ZnO is a well-known material that exhibits electron mobility of 200 - 300 cm^2 Vs^{-1} for bulk material and ~1000 cm^2 Vs^{-1} for single-crystal nanowires [1.114]. Although, the mobility of ZnO is orders of magnitude higher than TiO_2, it does not necessarily manifest in superior device performance compared to TiO_2. To understand this, the energy band diagrams of the two materials need to be compared (see Fig. 1.7). It can be noticed from Fig. 1.7 that the conduction band edge of ZnO sits slightly higher than that of TiO_2, which in turn offers slightly worse alignment with the lowest unoccupied molecular level (LUMO) of P3HT-PCBM blend (to be discussed in Chapter 2).

Feng *et al* [1.115] reported a noticeable increase in the photocurrent of OSCs upon incorporation of TiO_2 nanorods-nanoparticle composite as ETLs, compared to that of typical pristine TiO_2 films. This increase was ascribed to an enhanced charge extraction and charge density in the composite. Furthermore, the enhanced charge extraction in the nanoparticle–nanorod composite was found to be as a result of the electron accumulation in the nanoparticle layer under UV illumination. Hadar *et al* [1.116] demonstrated that ZnO interlayers deposited via ALD was better utilised as electron ETLs in BHJ OSCs than similar devices with solution deposited ZnO nanoparticle based ETLs. The authors further observed that OSCs with ALD-ZnO ETLs exhibited greater photocurrent densities and lower open circuit voltages. The low open circuit voltage was linked to the presence of pinholes and an

offset between the ALD-ZnO and $PC_{70}BM$ electron conducting states. This offset results from acceptor and traps sites generated during the low temperature ALD process.

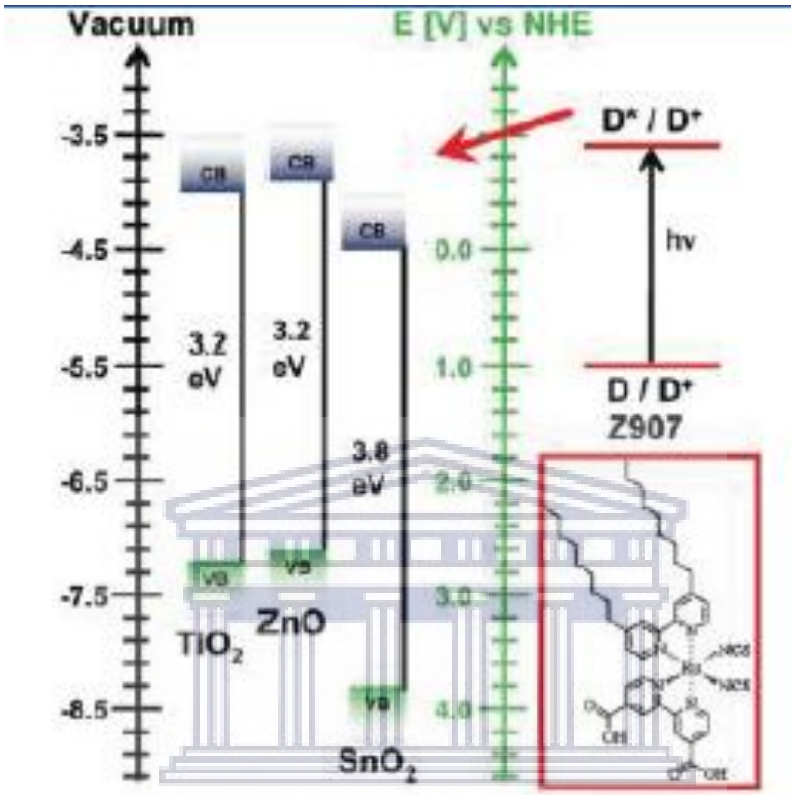

Fig. 1.7: Schematic diagram illustrating the energy levels of the conduction band (CB) and valence band (VB) of TiO_2, ZnO, and SnO_2 [1.114].

Fig. 1.8 represents the electron pathways between a thin film/nanoparticle ETL and a nanowire based ETL. The use of one-dimensional pathways have more efficient charge collection compared to zero dimensional pathways, due to the following reasons: (a) easy electron pathways (b) improved efficiency (c) faster electron recombination and reduction time [1.110]. Furthermore, the vertically aligned nanowires used as ETLs are better arranged and orderly electron pathways, when compared nanoparticle based ETLs. Thus, an ordered inverted/heterojunction with direct charge transport pathways is usually regarded as an ideal structure for HSCs. To demonstrate the electron pathways between one and zero dimensional electron ETLs, a schematic is shown in Fig. 1.8. As can be observed, because of the

discontinuous network of particles in a zero dimensional ETL, the electrons undergo multiple scattering during nanoparticle *hopping* before being collected by the TCO and exported through the external load. During these scattering events, the probability of recombination with nearby holes in the device is greatly increased. In contrast, the scattering probability and subsequent recombination with holes are minimised during transport in the continuous, one dimensional ETL network, potentially leading to more efficient charge collection at the TCO.

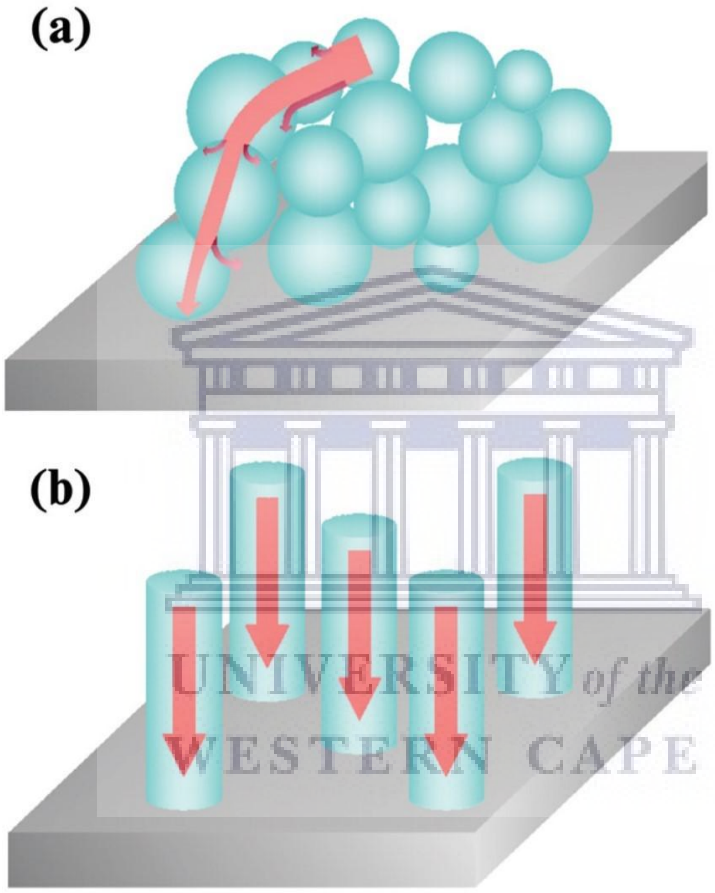

Fig. 1.8: Schematic comparison between one and zero dimensional electron pathways [1.110].

In addition, exciton separation efficiency is affected directly by the interfacial donor-acceptor area (to be discussed in Chapter 2) and the contact between the organic and inorganic components. As such, nanowires, tubes and array-based systems, which have higher surface areas, perform better, when compared with NR array-based systems with similar sizes. Hence for the development of hybrid solar cells, it is very important to choose proper components

by considering their energy-level arrangement at the interfaces. It is also vital to use nanostructures with large interfaces, for example long NWs, NRs, NTs, porous networks or branched nanopods, whereas considering the structural design for better improved charge transportation through the connection of each component. In that regard, ordered NWs, NR, and NT arrays are considered excellent candidates. [1.110].

1.7 ZnO Nanowires in Hybrid Inverted Solar Cells

Generally, ZnO nanowire based OSCs have PCEs lower than traditional BHJ devices, largely because of the inconsistent nanostructure architecture of the nanowire array. Liu *et al.* [1.119] used ZnO NWs, instead of thin films, as ETLs in inverted devices as shown in Fig. 1.9. In Fig. 1.9 (c) a schematic is shown of the structure of a hybrid OSC incorporating the nanowire arrays - from this sketch it becomes obvious that the morphology of the ZnO nanowires and the thickness of organic layer are very important factors in determining device performance.

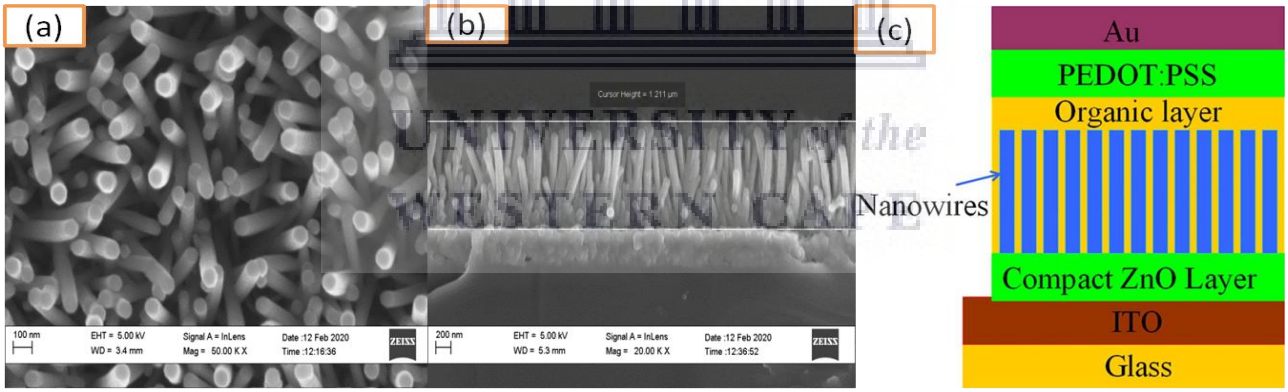

Fig. 1.9: (a) Plan-view (b) cross-sectional FESEM images of an aligned ZnO nanowire array on ITO substrates with a 40 nm ZnO seed layer; (c) schematic representation of the hybrid OSC incorporating the synthesised nanowires [1.119]

In the study [1.19], it was observed that the PCE increases with decrease in dimensions (diameter and length) of ZnO nanowires, with maximum performance achieved with a nanowire diameter of 20 nm and length of 100 nm. This performance characteristic was

attributed to the large space available, which allowed for the organic layer to infiltrate the space between the ZnO nanowires, thereby creating increasing the bulk heterojunction area. However, a maximum device efficiency of only 0.5% was attained using this approach. Similarly, fabrication of hybrid P3HT/nanostructured oxide devices via solution-based methods with efficiencies not much higher than 0.5% was achieved by Olson *et al.* [1.120]. The Manca group [1.121], used PCE of ZnO-NWs/P3HT BHJ SCs and reported that post-annealing of devices at the P3HT melting temperature for a short time of about 1min, can largely improve the PCE, this result is believed to be from an improved crystallinity of the P3HT. But annealing the devices for a longer period was found to reduce device performance. However the best device they obtained is with optimal thickness of the electron/ hole blocking layers and ZnO NWs length exhibited a PCE of 0.76%.

1.8 TiO_2 Nanowires in Hybrid Inverted Solar Cells

Similar to ZnO based devices, the application of TiO_2 nanowires in OSCs have yielded mixed performance results. Shankar *et al.* [1.122] demonstrated the use of a single heterojunction solid-state solar cell by sensitising anodic TiO_2 nanowire arrays with a P3HT derivative, however the device revealed poor performance because of poor contact between the active layer and electrode. This was eliminated by infiltrating both PCBM and P3HT into TiO_2 nanowire arrays to form double heterojunction solar cells, with a 1% PCE achieved. Kuo *et al.* [1.123] used vertically aligned TiO_2 nanowires used to fabricate HSC with P3HT but only 0.12 % PCE was obtained. Interestingly Chang *et al.* [1.124] used a ligand exchange technique, resulting in an improvement from 0.4 to 1.14% of PCE with P3HT as donor. Elsewhere, Lin *et al.* [1.125] modified the surface of TiO_2 nanowires using interface modifiers to obtain the PCE of 2.2 %. Furthermore, Tepavcevic et al. [1.126] reportedly found that when the polymer was in situ polymerised in the TiO_2 nanowires arrays, the device showed a much stronger photocurrent density, than that of device fabricated with ex-situ synthesised polymer only. Mor *et al.* [1.127] reportedly demonstrated an efficient TiO_2 nanowire array/dye/P3HT device structure, where the dye accounted for the absorption of the red and near-infrared portion of the solar spectrum, while the P3HT absorbed the higher energy photons and served as hole transport material. Yodyingyong *et al.* [1.128] synthesised highly oriented TiO_2 nanowires using a ZnO nanowire template and reported 3.32 %

efficiency for HSCs fabricated by infiltrating P3HT/PCBM into the TiO_2 matrix. This technique seems to be a promising way to prepare large area, low cost and efficient HSCs. From these studies it can be seen that the ordered heterojunction is most effective when infiltrating conjugated polymers into the vertically aligned nanostructures of the inorganic nanocrystals, an approach that will be followed in this study. Fig. 1.10 (c) shows a schematic structure of a hybrid OSC incorporating the nanowire arrays - from this sketch it becomes obvious that the TiO_2 nanowires lengths play a very important role in organic layer and in determining the device performance.

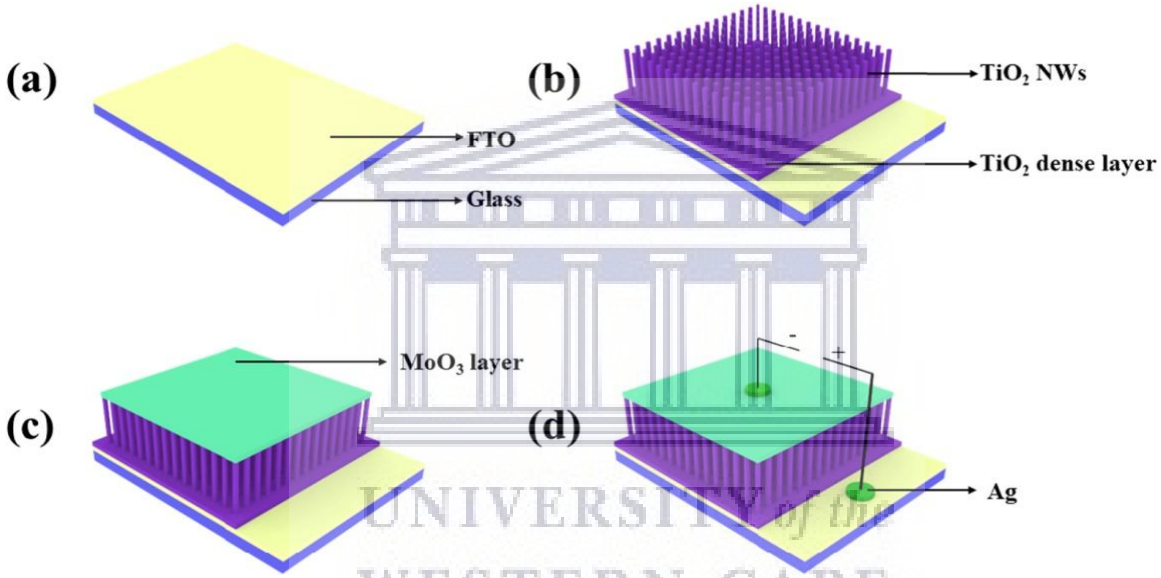

Fig. 1.10: Schematic structure of a hybrid organic PV based on TiO_2 nanowires arrays [1.129].

1.9 Plasma-assisted Doping of ZnO Nanowires

Plasma treatment is a multipurpose method used for processing material surfaces for cleaning of hydrocarbon contamination from atmosphere, adhesion promotion and improvement in surface stoichiometry on the sub-micron scale [1.130]. Felten *et al* [1.131] reported irradiation of multi-wall carbon nanotubes (CNT) with oxygen RF plasma and demonstrated

an improved uniformity in the distribution of surface defects and consequently dispersion of metallic nanoparticles. Elsewhere, excellent electrochemical contact between enzymes and carbon nanotubes was obtained via nitrogen plasma treatment of as-grown CNTs; the improved adhesion was ascribed to changing from hydrophobic to hydrophilic nature of the surface [1.132]. These approaches have led researchers to consider nitrogen plasma as an effective surface treatment method for use in photovoltaics. To this end, Le *et al* [1.133] used N_2 plasma to treat the hydrothermally synthesised ZnO NWs as ETLs as it was motivated that the ionic radius of nitrogen is close to O and hypothesised that the nitrogen will act as deep acceptor and compensator during device operation [1.134]. Reddy *et al* [1.135] reported a considerable improvement in the crystalline quality of thermo chemically grown ZnO NWs with the treatment of high intensity N_2 plasma. These studies paved the way for further investigation of nitrogen doping of ZnO as the scope for study is still broad with many lingering questions.

1.10 Plasma-assisted Doping of TiO_2 Nanowires

Rankin *et al* [1.137] used a microwave-assisted plasma CVD system to dope N atoms in mesoporous TiO_2. Elsewhere [1.39], glow-discharge plasma with RF power was used as a simpler technique compared to that reported in [1.137]. In both instances, however, the nitrogen doped TiO_2 could illustrate considerable absorption in the visible light region and improvement of the photocatalytic efficiency. Pertaining to PVs, both N_2 and O_2-plasma-treated TiO_2 thin films revealed to decrease surface recombination by reducing the amount of oxygen vacancies in TiO_2 material when used in hybrid organic solar cells [1.140]. By using 1D nanostructured TiO_2 and altering the TiO_2 surface by plasma treatment, the electrical conversion performance of a hybrid cell can be further, significantly enhanced. For example, Ahn *et al.* [1.141] reported the growth of TiO_2 NRs on FTO/glass substrates through a straightforward hydrothermal process and found that the TiO_2 NR wettability, surface morphologies, and chemical bonding states after plasma treatment improved, using reactive gasses such as O_2, N_2 and H_2. Wang *et al* [1.142] made a comparative study of plasma application using hydrogen, oxygen and nitrogen sources to ascertain which gas is the most appropriate for improvement in DSSC efficiency and found that nitrogen and oxygen show respectively 13% and 5% enhancement in the overall efficiency compared to the sample

without treatment, whereas hydrogen exposure causes a 15% reduction in inefficiency, making NP the best gas for plasma application and improved efficiency in solar cells.

1.11 Motivation, Aims and Thesis Outline

The literature reviewed thus far shows the scope to improve the electron transport properties of 1D nanowire arrays of TiO_2 and ZnO nanowires, if they are to be used as ETLs in hybrid organic solar cells. This is especially important if their full potential as fast, direct transport materials are to be realised. The major issue affecting this is, as highlighted, the presence of surface oxygen vacancies and trap sites in the lattice of the metal-oxides. Elemental doping with nitrogen has been identified as a simple solution to this problem with various studies already validating this approach. In this work, this approach will be explored further by developing a simple plasma irradiation technique, using highly kinetic RF generated plasma species of nitrogen.

To achieve the overall goal of the study, the intermediate tasks and milestones will be divided as follow:

- Optimisation of the hydrothermal growth synthesis method: A requirement of ordered bulk-heterojunction OSCs is that the ZnO and TiO_2 nanowires, for use as ETLs, should be vertically aligned to the TCO substrate; with NWs diameter thicknesses of between 40 and 80 nm and lengths ranging between 500 and 800 nm

A major drawback of using hydrothermally grown ZnO and TiO_2 nanowires in OSCs is the formation of the initial seed layer at the bottom of the nanowires, which if not accurately achieved, can prevent the incident light from reaching the photo-active layer, thereby significantly reducing solar cell performance. To overcome this:

- N_2 Plasma treatment of grown ZnO and TiO_2 nanowires will be performed with the aim of improving the optical properties of the ETLs incorporating these structures
- Deposition of optimised blends of P3HT (donor) and PCBM (acceptor) materials onto the plasma treated ZnO and TiO_2 ETLs: This part of the study will focus on deposition of the active layer using spin coating process to form a good medium for exciton dissociation.

- Developing optimised processes for the thermal deposition of hole transport and top contact layers and repeatable testing of the new devices

The outline of the thesis is as follows:

Chapter One Summarised the use of ZnO and TiO_2 nanowires and their importance as electron transport layers in the inverted/hybrid/ hetero-junction organic solar cells. The chapter gives a detailed introduction into the use of different metal-oxides as electron transport layer in different types of solar cells and motivation for the choice of ZnO and TiO_2 as ETLs. The chapter also discussed the doping and its effects on NWs prior to application in hybrid solar cells.

Chapter Two will discuss the physics and chemistry underpinning the experimental techniques that were used to during the course of the study. Specifically, the growth model during hydrothermal synthesis of ZnO and TiO_2 NWs on top of TCO substrates will be explored. In addition, the chapter will also discuss the physics involved in generation of plasmas and their use as a surface treatment technique. The chapter will conclude by giving a detailed discussion of the operating principle of organic solar cells and the steps used to fabricate inverted devices followed in this study.

Chapter Three will focus on the characterisation techniques used to perform the desired investigations such as the electron microscopy, light and electron spectroscopy, x-ray diffraction and the current-voltage characterisation used for PV testing.

Chapters Four to Six will discuss the most important results produced by this study. The results of each of these three chapters have been published in peer-reviewed journals as follow:

- **Chapter Four:** Bello Ladan Muhammad and Franscious Cummings, *"Nitrogen plasma treatment of ZnO and TiO_2 nanowire arrays for polymer photovoltaic applications"* Surfaces and Interfaces 17 (2019) 100382 https://doi.org/10.1016/j.surfin.2019.100382
- **Chapter Five:** B.L. Muhammad, N.V. Peterson, L. Kotsedi, F.R. Cummings, *"RF nitrogen plasma irradiation of metal-doped TiO_2 nanowire arrays as an effective*

technique for improved light transmission and optical bandgap manipulation", Chemical Physics 538 (2020) 110922 https://doi.org/10.1016/j.chemphys.2020.110922

- **Chapter Six:** Bello Ladan Muhammad and Franscious Cummings, *"Nitrogen plasma irradiation of Fe doped ZnO nanowire arrays for improved optical properties"*, Materials Today: Proceedings (2020), Article In Press https://doi.org/10.1016/j.matpr.2020.04.684

Chapter Seven will present the findings of the current-voltage characterisation of the completed organic solar cells, whereas the final **Summary** chapter will review the major findings of the study and provide details on possible future studies.

Appendix A contains supplementary data to the results presented in Chapter Five. **Appendix B** summarise work recently completed on kesterite based inorganic solar cells incorporating ZnO nanowires synthesised in the study, which will perform the basis of future research. **Appendix C** presents the cover pages of the manuscripts published from this work.

References

[1.1] S. Barth, F. Hernandez-Ramirez, J.D. Holmes, A. Romano-Rodriguez, Progress in Material Science 55 (2010) 563-627.

[1.2] V.N.T.K. Satyanarayana, A.S. Karakoti, B. Debasis S. Seal, Progress in Material Science 52 (2007) 699-913.

[1.3] Y.B. Tang, Z.H. Chen, H.S. Song, C.S Lee, H.T Cong, H.M Cheng, W.J Zhang, I. Bello, S.T. Lee, Nano Lett. 8 (2008) 4191-4195.

[1.4] O.L Muskens, J.G Rivas, R.E Algra, E.P.A.M. Bakkers, A Lagendijk, Nano Lett. 8 (2008) 2638-2642.

[1.5] G. Yanfeng, N. Masayuki, C. Tien-Cheng, S. Jing-Jong, Cryst. Growth Des. 7 (2007) 2467-2471.

[1.6] S. Shiva, M. Raheleh, I. Azam, T. Nima, Material Letters 159 (2015) 273-275.

[1.7] S.S. Shinde, R.A Bansode, C.H. Bhosale, K.Y. Rajpure, J. of Semiconductors 32 (2011) 013001.

[1.8] L. Xufeng, Y. Jianyu, L. Dongyang, W. Yongjie, Z. Yannan, S. Chen, W. Haihua, J. Feng, J. Feng, W. Fupeng, S. Guozheng, T. Xun Z. Jaiwei, L. Shengzhong (Frank), L. Zhike, M. Wanli, ACS Appl. Mater. Interfaces 9 (2017) 23181-23188.

[1.9] M.H Abdulmenan, V.I. Anastasiia, T.K. Ranjit, A.L. Brain, V,S. Rajesh, Energy Reports 4 (2018) 56-64.

[1.10] P. Chaiya, T.H. Joseph, J. Phys. Chem. Lett. 10 (2010) 1611-1615.

[1.11] H. Gui, W. Min, L. Danyang, B. Jingyi, D. Guowang, Solar Energy Material and Solar Cells 160 (2017) 54-59.

[1.12] G. Chiarello, V. Fabio, D. W. Boukhvalov, A. Politano, Chem. Commun. 55 (2019) 8607-8610.

[1.13] A. Politano, G. Chiarello, R. Samnakay, G. Liu, B. Gürbulak, S. Duman, A.A. Balandin, D.W. Boukhvalov, Nanoscale 8 (2016) 8474.

[1.14] A. Politano, M.S. Vitiello, L. Viti, D.W. Boukhvalov, G. Chiarello, Flat Chem. 1 (2017) 60-64.

[1.15] A. Politano, G. Chiarello, C. Kuo, C.S. Lue, R. Edla, P. Torelli, V. Pellegrini, D.W. Boukhvalov, Adv. Funct. Mater. 28 (2018) 1706504.

[1.16] Y.Liu, C.R. Gorla, S. Liang, N. Emanetoglu, Y. Lu, H. Shen, M. Wraback . Journal of Elec Materi. 29 (2000) 69.

[1.17] X. Cheng, X. Yu, Z. Xing, J. Wan, Energy Procedia 16 (2012) 598-605.

[1.18] R. Rahimi, S.S. Moghaddam, M. Rabbani, J. Sol-Gel Sci. Technol. 64 (2012) 17–26.

[1.19] H. Tsuchiya, J.M. Macak, A. Ghicov, P. Schmuki, Nano Lett. 7 (2006) 888-91.

[1.20] K. Yamada, H. Yamane, S. Matsushima, H. Nakamura, T. Sonoda, S. Miura, K. Kumada, Thin Solid Films 516 (2008) 7560-7564..

[1.21] S.S. Soni, M.J. Henderson, J.F. Bardeau, A. Gibaud, Adv. Mater. 20 (2008) 1493−1498.

[1.22] R. Asahi, T. Morikawa, T. Ohwaki, K. Aoki, Y. Taga, Science 293 (2001) 269−271.

[1.23] L. Jinlong, M. Xinxin, S. Mingren, X. Li, S. Zhenlun, Thin Solid Films 519 (2010) 101−105.

[1.24] W.Z. Lin, J. Phys. Condens. Matter 16 (2004) 829–858.

[1.25] R. Kobayashi, T. Kishi, Y. Katayanagi, T. Yanoa, N. Matsushita, RSC Adv. 8 (2018) 23599-23605.

[1.26] B.T. Adekore, J.M. Pierce, R.F. Davis, D.W. Barlage, J.F. Muth, J. Appl. Phys. 102 (2007) 024908.

[1.27] E. Alves, N. Franco, N.P. Barradas, F. Munnik, T. Monteiro, M. Peres, J. Wang, R. Martins, E. Fortunato, Vacuum 83 (2009) 1274–1278.

[1.28] L.C. Chao, Y.R. Shih, Y.K. Li, J.W. Chen, J.D. Wu, C.H. Ho, Appl. Surf. Sci. 256 (2010) 4153–4156.

[1.29] D.C. Look, J. Elect. Mater 35 (2006) 1299–1305.

[1.30] A. Kobayashi, O.F. Sankey, J.D. Dow, Phys. Rev. B 28 (1983) 946–956

[1.31] S. K. Tewksbury, West Virginia University Morgantown, WV 26506 (1995) 293-6371

[1.32] B.L. Muhammad, F. Cummings, Surfaces and Interfaces 17 (2019) 100382.

[1.33] J. Shi, X. Wang, Cryst. Growth Des. 11 (2011) 949 –954.

[1.34] Q. Zhang, L. Gao. Langmuir 19 (2003) 967 – 97

[1.35] Y.X. Zhang, G.H. Li, Y.X. Jin, Y. Zhang, J. Zhang, L.D. Zhang, Chemical Physics Letters 365 (2002) 300 – 304.

[1.36] X. Feng, K. Shankar, O.K. Varghese, M. Paulose, T.J. Latempa, C.A. Grime, Nano Lett. 8 (2008) 3781-3786.

[1.37J. Y. Kim, J. W. Cho, S.H. Kim, Materials Letters 65 (2011) 1161–1164.

[1.38]. S. Baruah, J. Dutta, Journal of Crystal Growth 311 (2009) 2549–2554.

[1.39] Z. Zhang, J. Mu, Journal of Colloid and Interface Science 307(2007) 79–82.

[1.40] G.C. Yi, C. Wang, W.I. Park, Semicond. Sci. Tech. 20 (2005) 22–34.

[1.41] E.W. Petersen, E.M. Likovich, K.J. Russell, V. Narayanamurti, Nanotechnology 20 (2009) 405603.

[1.42] S. Ashraf, A.C. Jones, J. Bacsa, Chemical Vapor Deposition 17 (2011) 45–53.

[1.43] L.N. Protasova, E.V. Rebrov, K.L. Choy Catalysis Science and Technology 1 (2011) 768–777.

[1.44] L. Wang, X. Zhang, S. Zhao, G. Zhou, Y. Zhou, J. Qi, Applied Physics Letters 86 (2005) 024108.

[1.45] K. Kitamura, T. Yatsui, M. Ohtsu, G.C. Yi, Nanotechnology 19 (2008) 175305.

[1.46] J.S. Wang, C.S. Yang, P.I. Chen, Applied Physics A 97 (2009) 553–557.

[1.47] L.C. Tien, S.J. Pearton, D.P. Norton, F. Ren, Journal of Materials Science 43 (2008). 6925–6932.

[1.48] D.I. Suh, C.C. Byeon, and C.L. Lee, Applied Surface Science 257 (2010) 1454–1456.

[1.49] X. Wang, J. Song, P. Li, Journal of the American Chemical Society 127 (2005) 7920–7923.

[1.50] J. Song, X. Wang, E. Riedo, Z. L.Wang, Journal of Physical Chemistry B 109 (2005) 9869–9872.

[1.51] X. Wang, J. Song, C.J. Summers, Journal of Physical Chemistry B 110 (2006) 7720–7724.

[1.52] F.H. Chu, C.W.Huang, C.L.Hsin Nanoscale 4 (2012) 1471–1475.

[1.53] S. Ashraf, A.C. Jones, J. Bacsa Chemical Vapor Deposition 17 (2011) 45–53.

[1.54] M.H. Huang, Y.Y. Wu, H. Feick, N. Tran, E. Weber, P.D. Yang, Advanced Materials 13 (2001) 113–116.

[1.55] Y.J. Zeng, Z.Z. Ye, W.Z. Xu, L.P. Zhu, B.H. Zhao, Applied Surface Science 250 (2005) 280–283.

[1.56] B. Zhang, S. Zhou, B. Liu, H. Gong, X. Zhang, Science in China, Series E 52 (2009) 883–887.

[1.57] M.A. Malik, M.Y. Wani, M.A. Hashim, 1st Nano Update. Arabian Journal of Chemistry 5 (2012) 397-417.

[1.58] C. Yoshina-Ishii, T. Asefa, N. Coombs, M.J. MacLachlan, G.A. Ozin. Cem Commun. (1999) 2539-2540.

[1.59] B. Liu, H.C. Zeng, Journal of the American Chemical Society 125 (2003) 4430–4431.

[1.60] G. An, Z. Sun, Y. Zhang, Journal of Nanoscience and Nanotechnology 11 (2011) 1252–1258.

[1.61] J.Y. Kim, J.W. Cho, S.H. Kim, Materials Letters 65 (2011) 1161–1164.

[1.62] J. Song, S. Baek, H. Lee, S. Lim, Journal of Nanoscience 9 (2009) 3909-3913.

[1.63] S. Baruah, M. Abbas, M. Myint, T. Bora, J. Dutta, Beilstein Journal of Nanotechnology 1 (2010) 14–20.

[1.64] S. Baruah, J. Dutta, Science and Technology of Advanced Materials 10 (2009) 013001.

[1.65] Y.X. Zhang, G.H. Li, Y.X. Jin, Y. Zhang, J. Zhang, L.D. Zhang. Chemical Physics Letters 365 (2002) 300 – 304.

[1.66] M. Ladanov, M.K. Ram, G. Matthews, A. Kumar, Langmuir 27 (2011) 9012–9017.

[1.67] M. Erfan, M. Gnambodoe-Capochichi, M. Le pivent, F. Marty, Y.M. Sabry, Y. Leprince-Wang, T. Bourouina, Proceedings Volume 10919, Oxide-based Materials and Devices X 1091922 (2019).

[1.68] B. Weintraub, Z. Zhou, Y. Li, Y. Deng, Nanoscale 2 (2010) 1573–1587.

[1.69] S. Xu, C. Lao, B. Weintraub, Z.L. Wang, Journal of Materials Research 23 (2008) 2072–2077.

[1.70] D.M. Antonelli, J. Y. Ying, Angewandte Chemie International Edition 34 (1995) 2014 – 2017.

[1.71] J. Yu, X. Zhao, Q. Zhao, Thin Solid Films 379 (2000) 7 – 14.

[1.72] Y. Lei, L.D. Zhang, G.W. Meng, G.H. Li, X.Y. Zhang, C.H. Liang, W. Chen, S.X. Wang. Applied Physics Letters 78 (2001) 1125 –1127.

[1.73] Z. Miao, D. Xu, J. Ouyang, G. Guo, X. Zhao, Y. Tang, Nano Letters 2 (2002) 717 – 720

[1.74] Y. Zhu, H. Li, Y. Koltypin, Y. R. Hacohen, A. Gedanken, Chemical Communications (2001) 2616 – 2617.

[1.75] X. Jia, W. He, X. Zhang, H. Zhao, Z. Li, Y. Feng, Nanotechnology 18 (2007) 075602/1 – 075602/7.

[1.76] G. Ma, X. Zhao, J. Zhu, International Journal of Modern Physics B 19 (2005) 2763 – 2768.

[1.77] R.S. Dariani, Z.N Qaleh, Thin Solid Film 542 (2013) 192-198

[1.78] H. Tsuchiya, J.M. Macak, A. Ghicov, P. Schmuki, Nano Lett. 7 (2006) 888-891

[1.79] K. Guenther, B. Loo, D. Burns, J. Edgell, D. Windham, K. Muller. Journal of Vacuum Science & Technology A **7** (1989) 1436

[1.80] J.C. Dhar, A. Mondal, S. Bhattacharya, N.K. Singh, C. Ngangbam, K.K. Chattopadhvav. Journal of Nanoscience and Nanotechnology 15 (2015) 3951-3955.

[1.81] R. Nechache, M. Ncklaus, N. Diffalah, A Ruediger, F. Rosei. Applied Surface Science 313 (2014) 48-52

[1.82] S. Hong, H. Lee, J. Yeo, S. Hwanko. Review Digital selective laser methods for nanomaterials: From synthesis to processing nanotoday 11 (2016) 547-564.

[1.83] J.M. Wu, H.C. Shih, W.T. Wu, Y.K. Tseng, I.C. Chen, Journal of Crystal Growth 281 (2005) 384 – 390.

[1.84] B. Xiang, Y. Zhang, Z. Wang, X.H. Luo, Y.W. Zhu, H.Z. Zhang, D.P. Yu, Journal of Physics D: Applied Physics 38 (2005) 1152 – 1155.

[1.85] S.K. Pradhan, P.J. Reucroft, F. Yang, A. Dozier. Journal of Crystal Growth 256 (2003) 83 – 88.

[1.86] C.A. Chen, Y.M. Chen, A. Korotcov, Y.S. Huang, D.S. Tsai, K.K. Tiong. Nanotechnology 19 (2008) 075611/1 – 075611/5.

[1.87] J. Shi, X. Wang, Crystal Growth and Design 11 (2011) 949 –954.

[1.88] Y.X. Zhang, G.H. Li, Y.X. Jin, Y. Zhang, J. Zhang, L.D. Zhang, Chemical Physics Letters 365 (2002) 300 – 304.

[1.89] T. Kasuga, M. Hiramatsu, A. Hoson, T. Sekino, K. Niihara, Adv. Mater. 15 (1999) 1307.

[1.90] S. Nadzriha, U. Hashim, T. Adams, Fifth International Conference on Intelligent Systems, Modelling and Simulation (2014).

[1.91] B.C. Thompson, J.M.J Frechet, Angew. Chem. Int Edit. 47 (2008) 58–77.

[1.92] G. Dennler, M.C. Scharber, C.J Brabec, Adv Mater. 21 (2009) 1323–1338.

[1.93] C.J. Brabec, S, Gowrisanker, J.J.M. Halls, D. Laird, S.J Jia, S.P. Williams, Adv Mater. 22 (2010) 3839–3856.

[1.94] A. Hagfeldt, G. Boschloo, L.C. Sun, L. Kloo, H. Pettersson, Chem Rev. 110 (2010) 6595–6663.

[1.95] S. Chen, P. Comte, M.K. Nazeeruddin, P. Liska, P. Pechy, M. Gratzel, Prog Photovoltaics 15 (2007) 603–612. .

[1.96] F.C. Krebs, S.A. Gevorgyan, J. Alstrup, J Mater Chem. 19 (2009) 5442–5451.

[1.97] F.C. Krebs, T. Tromholt, M. Jorgensen, Nanoscale 2 (2010) 873–886.

[1.98] Y. Kang, D. Kim, Sol. Energy Mater Sol C 90 (2006) 166–174.

[1.99] L. Wang, Y.S. Liu, X. Jiang, D.H. Qin, Y. Cao, J. Phys Chem. C 111 (2007) 9538–9542.

[1.100] K.M. Coakley, X.Y. Liu, M.D. McGehee, K.L. Frindell, G.D. Stucky, Adv Funct. Mater. 13 (2003) 301–306.

[1.101] K.M. Coakley, M.D. McGehee, Appl Phys Lett. 83 (2003) 3380–3382.

[1.102] W.U. Huynh, J.J. Dittmer, A.P. Alivisatos, Science 295 (2002) 2425–2427.

[1.103] B.Q. Sun, E. Marx, N.C. Greenham, Nano Lett. 3 (2003) 961–963.

[1.104] W.J.E. Beek, M.M. Wienk, R.A.J. Janssen, Adv Mater. 16 (2004) 1009–1013.

[1.105] W.J.E Beek, L.H. Slooff, M.M. Wienk, J.M. Kroon, R.A.J. Janssen, Adv Funct. Mater. 15 (2005) 1703–1707.

[1.106] E. Arici, N.S. Sariciftci, D. Meissner, Adv Funct. Mater. 13 (2003) 165–171.

[1.107] J.A Ayllon, M. Lira-Cantu, Appl Phys A Mater. 95 (2009) 249–255.

[1.108] W.J.E Beek, M.M. Wienk, R.A.J. Janssen, Mater. Chem. 15 (2005) 2985–2988.

[1.109] C. Sanchez, B. Julian, P. Belleville, M. Popall, J. Mater. Chem. 15 (2005) 3559–3592.

[1.110] N. Aism, M. Mohammad, M. Badiei, Nanomaterials for Green Energy (2018) 227-277.

[1.111] J. Weickert, R.B. Dunbar, H.C. Hesse, W. Wiedemann, L. Schmidt-Mende Adv Mater. 23 (2011) 1810–1828.

[1.112] S.O. Oseni, G.T. Mola, Solar Energy Material and Solar Cells 160 (2017) 241- 256.

[1.113] T. Bak, M. K. Nowotny, L. R. Sheppard, J. Nowotny, J. Phys. Chem. C 122 (2008) 12981–12987.

[1.114] P. Tiwana, P. Docampo, M.B. Johnston, H.J. Snaith, L.M. Herz, ACS Nano 5 (2011) 5158–5166

[1.115] F. Xie, C.H.C. Wallace, E.I. Wei, D. Zhang, S. Zhang, X. Li, C.L.J. Hou, Energy & Environmental Science. The Royal Society of Chemistry 11 (2013)

[1.116] F. Hadar, C.Z. Leng, M.D. Losego, G.L. Frey, Organic Electronics 64 (2019) 37-46.

[1.117] M. Wright, A. Uddin, Sol. Energy Mater. Sol. Cell. 107 (2012) 87e111.

[1.118] K. Shankar, G.K. Mor, M. Paulose, O.K. Varghese, C.A. Grimes, J. Non-cryst. Solids 354 (2008) 2767e2771.

[1.119] J. Liu, S. Wang, Z. Bian, M. Shan, C. Huang, Applied Physics Letters 94 (2009) 173107

[1.120] D.C. Olson, J. Piris, R.T. Collins, S.E. Shaheen, D.S. Ginley, Thin Solid Films 496 (2006) 26-29.

[1.121] L. Baeten, B. Conings, H.G. Boyen, J. D'Haen, A. Hardy, M. D'Olieslaeger, J.V. Manca, M.K. Van Bael, Adv. Mater. 23 (2011) 2802–2805.

[1.122] K. Shankar, G.K. Mor, H.E. Prakasam, O.K. Varghese, C.A. Grimes, Langmuir 23 (2007) 12445–12449.

[1.123] C.Y. Kuo, W.C. Tang, C. Gau, T.F. Guo, D.Z. Jeng, Appl Phys Lett. 93 (2008) 033307

[1.124] C.H. Chang, T.K. Huang, Y.T. Lin, Y.Y. Lin, C.W. Chen, T.H. Chu, W.F. Su, J Mater Chem. 18 (2008) 19.

[1.125] Y.Y. Lin, T.H. Chu, S.S. Li, C.H. Chuang, C.H. Chang, W.F. Su, C.P. Chang, M.W. Chu, C.W. Chen, J Am Chem Soc. 131(2009) 3644–3649.

[1.126] S. Tepavcevic, S.B. Darling, N.M. Dimitrijevic, T. Rajh, S.J. Sibener, Small 5 (2009) 1776–1783.

[1.127] G.K Mor, S. Kim, M. Paulose, O.K. Varghese, K. Shankar, J. Basham, C.A. Grimes, Nano Lett. 9 (2009) 4250–4257.

[1.128] S. Yodyingyong, X.Y. Zhou,Q.F. Zhang, D. Triampo, J.T. Xi, K. Park, B. Limketkai, G.Z. Cao, J. Phys Chem C. 114 (2010) 21851–21855.

[1.129] B. Yin, Y. Zhang, K. Li, J. Zhou, C. Liu, M. Zhang, S. Ruan. Nanotechnology 30 (2019) 465501.

[1.130] M.A. Lieberman, A.J. Lichtenberg, 2nd edn. (Wiley Interscience, Hoboken, NJ: Wiley (2005) 2859.

[1.131] A. Felten, J. Ghijsen, J.J. Pireaux, R.L. Johnson, C.M. Whelan, D. Liang, G.V. Tendeloo, C. Bittencourt, J. Phys. D Appl. Phys. 40 (2007) 7379.

[1.132] H. Muguruma, T. Hoshino, Y. Matsui, ACS Appl. Mater. Interfaces 3 (2011) 2445.

[1.133] H.Q. Le, S. Tripathy, S. Chua, Appl. Phys. Lett. 92 (2008) 141910–141911.

[1.134] C.M. Reddy, C.C. Amato-Wierda, Electrochem. Soc. Pennington, New Jersey, USA (2001) 396

[1.135] N. K. Reddy, M. Devika Y.Hahn, Nano Convergence 1 (2014) 1-26.

[1.136] S.M Sze, John Wiley & Sons, New Jersey 1985.

[1.137] S.Z. Islam, A. Reed, N. Wanninayake, D.Y. Kim, S.E. Rankin, J. Phys. Chem. C 120(2016)14069.

[1.138] J. Wang, N. Tafen, J.P. Lewis, Z. Hong, A. Manivannan, M. Zhi, M. Li, N. Wu, J. Am. Chem. Soc. 131 (2009) 12290.

[1.139] X. Liu, Z. Liu, J. Zheng, X. Yan, D. Li, S. Chen, W. Chu, J. Alloys Compd. 509 (2011) 9970.

[1.140] Y. Kim, B. Y. Yoo, R. Vittal, Y. Lee, N. G. Park, and K. J. Kim, J. Power Sources 175 (2008) 914.

[1.141] K. Ahn, H. Lee, S. Jeong, J. Kim, J. S. Jin, H. Ahn, H. Kim, C. Cho, J. Nanosci. Nanotechnol. 12 (2012).

[1.142] W. Wang, J. Chen, J. Luo, Y. Zhang, L. Gao,Y. Liu, J. Sun. Applied Surface Science 324 (2015) 143–151.

CHAPTER TWO

PROCESSING METHODS

In this chapter an overview of the underlying physics and chemistry determining the growth of ZnO and TiO_2 nanowire structures during the hydrothermal synthesis technique will be given, including the physics of plasma generation and their use during surface treatment of the samples. Also, a discussion of the operating principles of organic solar cells and the theory of the processing methods used to fabricate the different layers comprising a complete cell, Complete experimental details of the steps involved during nanowire growth, plasma irradiation and solar cell fabrication will also be documented.

2.1 Hydrothermal Synthesis

2.1.1 Background. Hydrothermal is a Greek term derived from the words hydro meaning (water) and thermos (heat). Sir Roderick Murchison (1792–1871), a British geologist was the first person to use the word hydrothermal to describe the reaction of water at higher temperature and pressure, to bring about a change in the earth's crust, leading to the formation of various rocks and minerals [2.1]. All over the world, researchers in the field of material science have developed special interest in the use of hydrothermal techniques for the synthesis of different types of nanomaterials. Rappa and Yoshimura [2.2] defined hydrothermal as any homogeneous or heterogeneous chemical reaction in the presence of a solvent (whether aqueous or non-aqueous) took place above room temperature and a pressure greater than 1 atmosphere in a closed system. Hydrothermal techniques offer advantages such as accelerated interactions between fluid and solid species, provide an easy route towards achieving a homogeneous and pure phase material. It also enhances reaction kinetics and can be used to facilitate mass transport of materials while providing higher dissolving power. In addition, these processes are also both chemically and environmentally friendly. Hydrothermal synthesis has been used in the formation of hydroxides, carbonate silicates, sulphides, phosphate tellurides, selenides, tellurides and metal oxides in both particle and nanostructure forms like nanowires, nanotubes nanopillars, nanorods amongst others. In

recent times, the technique has become an industrial scale processing choice because it requires very little energy, with no or very small solid waste, gas or liquid by-products [2.3]. Fig. 2.1 presents a schematic drawing of the cross-section and components of a Parr Instruments® General Purpose Pressure Vessel (45 ml) used during this study; the Teflon cup (256 AC) is generally referred to as a liner and is the central chamber in which all reactants are mixed. The bottom and upper plates, corrosion disc, cover and spring assembly help prevent overspill of reagents during synthesis and to maintain high pressure. The liner and plate assembly are placed inside the stainless steel body and screwed tight with the steel screw cap. This fully assembled vessel is then placed in a controlled oven at a desired temperature and time to initiate synthesis.

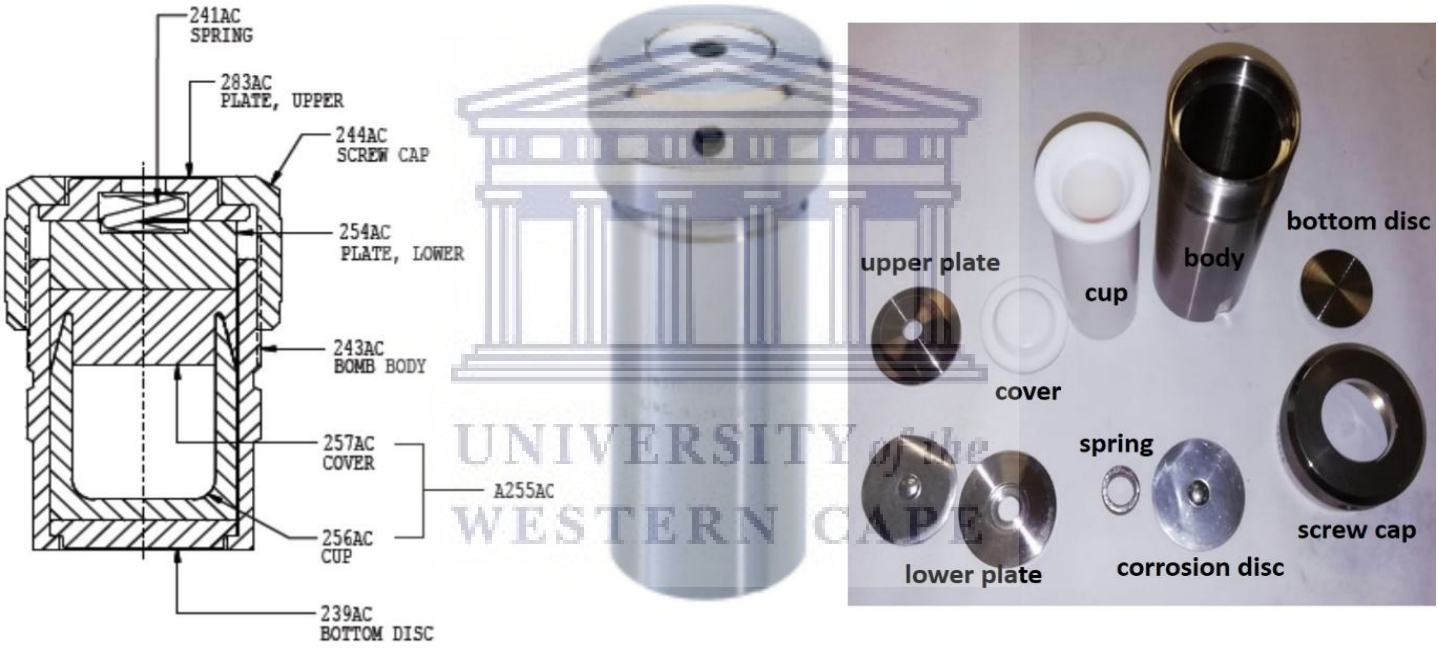

Fig. 2.1: Schematic of a fully assembled Parr Instruments® autoclave high pressure vessel (45 ml) with all components

2.1.2 The Significance of Hydrothermal Synthesis in Nanotechnology. Nanostructures have been synthesised using different processes involving the conversion of solid to solid, liquid to solid and gas to solid approaches. Recently, the use of solution techniques like hydrothermal autoclave synthesis has become one of the most valuable tools in industrial scale fabrication of nanostructures, due to high quality of product. It also makes easy to synthesise self-assembly structures (like one dimensionals) using a perfect dispersion of nanoparticles in a

given solvent. On the other hand, the knowledge on the self-assembly, crystallisation, nucleation and growth mechanism of the crystals in hydrothermal solution media are quite complicated and still not well understood. This largely emanates from the fact that the hydrothermal method has an exceptional characteristic of generating unexpected reactions at the beginning of the synthesis which sometimes lead to the formation of nanoscopic morphological features that is not commonly observed in other classical reactions. The nanoscopic morphologies can be controlled by changing the parameters in the reaction system, such as the rate of time, choice of solvents, solution concentration and reaction temperature [2.4]. The most popular reactors used for synthesis are the Morey [2.5] autoclave, Batch type reactors [2.6], Tuttle- Roy type reactors [2.7] and General Purpose autoclave [2.8]. The General Purpose autoclave was used for this research work as shown in Fig. 2.1.

2.1.3 Growth Mechanism of TiO_2 Nanowires. The relative growth of different faces bonding the crystals are mainly responsible for the growth characteristics of TiO_2 nanowires during hydrothermal synthesis, where factors such as concentration of precursors, temperature, pH of the solution and duration of the experiment greatly affect the final morphology. However, the synthesis conditions can be adjusted to obtain the required minimum surface energy after different optimisation. In the case of rutile TiO_2, every Ti atom is surrounded by six oxygen atoms oxygen to form a TiO_6 octahedral, which shares a pair of opposite edges with another nearest octahedral resulting in the formation of a chain like structure, as shown in Fig. 2.2 [2.4].

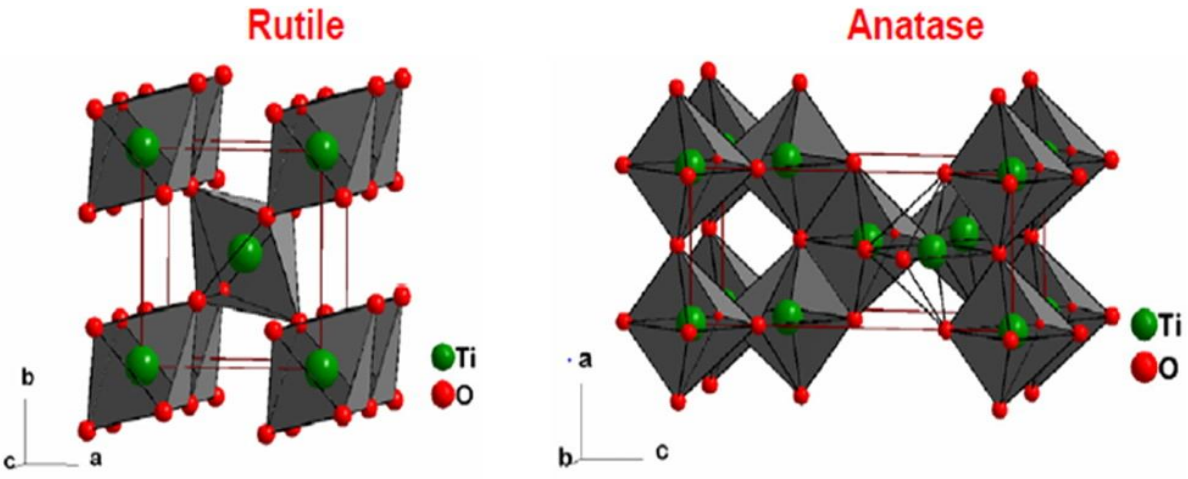

Fig. 2.2: Coordination of Ti and O atoms in the rutile and anatase TiO_2 unit cell [2.9].

Though the numbers of edges and corners are responsible for the coordination polyhedral availability; the growth rate of different crystal faces differs and follows the sequence (110) < (100) < (101) < (001) [2.10]. The formation of the growth units and their incorporation into crystal lattice are responsible for the growth of TiO_2 in aqueous solution. The ligand and acidity in a solution are very critical to the nature of the growth units, which are made up of Ti (IV) complex ions. In the present experimental reaction conditions, the TiO_2 is formed in accordance with the following reactions:

$$TiCl_4 + H_2O + HCl + Ti(IV)\ \text{complex dehydration} \qquad (2.1)$$

$$2Ti(IV) \xrightarrow{\text{dehydration}} TiO_2 \qquad (2.2)$$

The growth unit supply is significantly restricted due to the presence of an excess amount of H^+ from the hydrochloric acid, however this growth mechanism is used to determine the morphology. As stated earlier, the growth of the rutile TiO_2 is in the [001] direction, which is the utmost result in the growth of steady C-elongated anisotropic crystals displaying (110) faces. Also, the Cl-ions presence is well known to limit the growth of the (110) faces but surprisingly enhanced the growth along (001) direction [2.11]. At closer inspection of TiO_2 nanowire growth during hydrothermal synthesis comprises the formation of nano-sized *fingers,* which have recently become a topic of intense debate.

Kalb *et al* [2.12] provided a concise and in-depth review of the finger formation during growth as summarised in Fig. 2.3. According to this model, rutile TiO_2 nanorods reached their final size while two physical processes were competing; one being the chemical reaction converted $TiCl_4$ molecules into solid and crystalline TiO_2 as explained by equations (2.1) and (2.2) and the other which was the minimisation of the surface energy for a given volume resulted to the Wulff shape of the crystal [2.13]. Due to a fast conversion of $TiCl_4$ into TiO_2 on the (001) (001) faces of the fingers (green regions), their dimensions differ from the Wulff shape (purple region). Due to the fast growth in the [001] direction, the fingers would have to grow much faster in the [110] direction to fit the dimensions of the Wulff construction (left construction). To reduce the surface energy, additional fingers are attached to the central finger, which may be considered a seed. The bunching of the fingers subsequently matches

the Wulff construction, with the outermost fingers being slightly expanded due to better precursor supply (right construction). A further model ascribing the nano-finger formation to crystal defects is presented by Wisnet *et al* [2.14], which will be discussed in greater detail in Chapter 5.

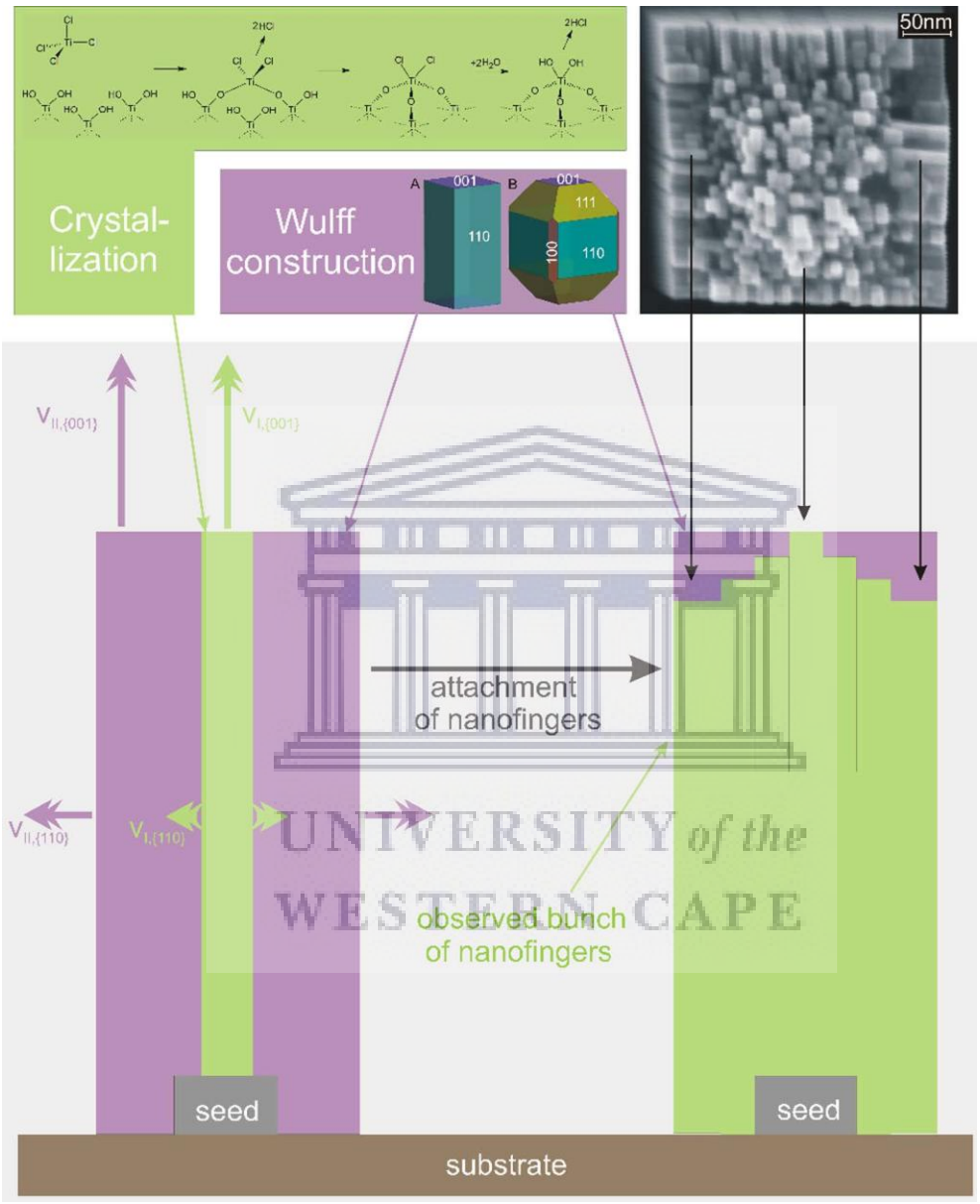

Fig. 2.3: Schematic of the non-equilibrium growth model of TiO_2 nanowires during hydrothermal synthesis as proposed by Kalb *et al* [2.11]

2.1.4 Growth Mechanism of ZnO Nanowires. ZnO crystallises in two main forms, namely the hexagonally coordinated Wurtzite and tetragonal zinc blende structure as shown in Fig 2.4 [2.15]. Wurtzite is the most common and thermodynamically stable ZnO structure at

ambient conditions and also the preferred crystal orientation of ZnO nanowires during hydrothermal growth. An elegant nanowire growth model has been presented by Chevalier-César *et al* [2.16]. The chemical reactions governing the nanowire structure formation are as discussed in Chapter 1.3.3. According to the Chevalier-César model, two main routes of synthesis are generally employed during growth, both requiring ZnO seeds or a seed layer covering the entire substrate. In the first method (way 1), the substrate coated with the seed layer is dipped into the growth solution only when the desired temperature is reached. During Way 2 the coated substrate is submerged in the growth solution at room temperature, the autoclave is sealed and placed in the heating system.

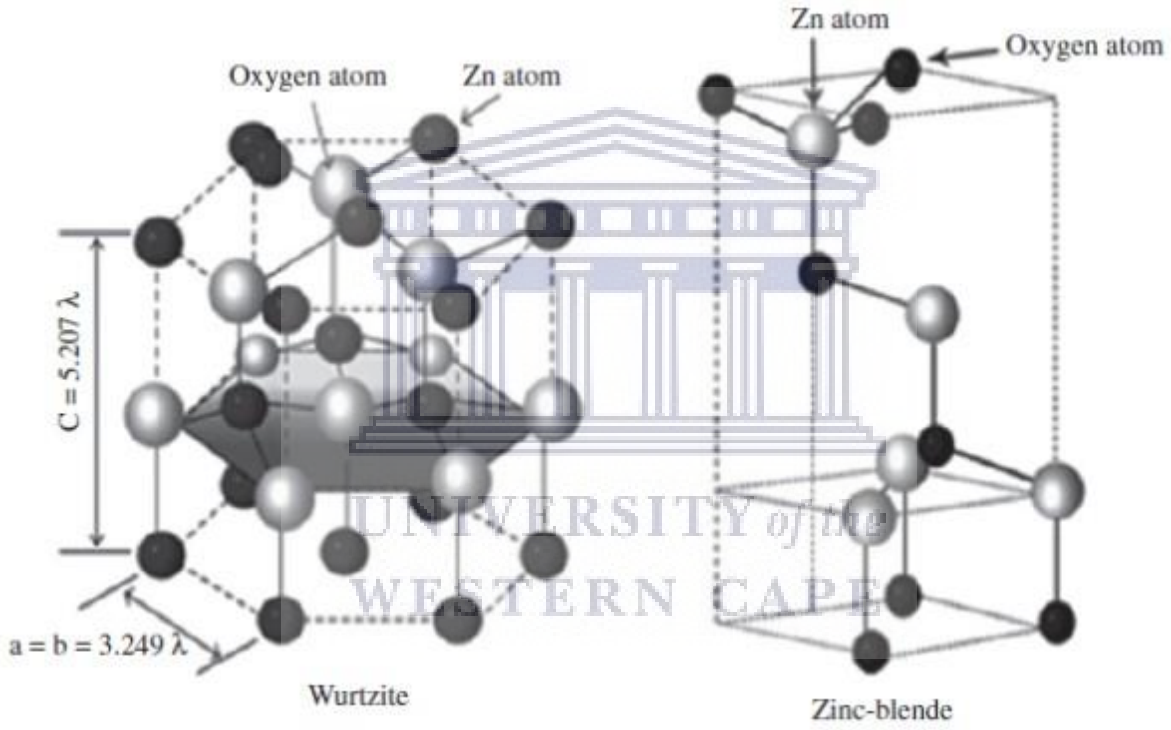

Fig. 2.4: Crystal structures of ZnO [2.15]

These two routes are schematically shown in Fig. 2.5. The nanowires obtained by the first route generally possess a narrow diameter size distribution with the diameter also appearing uniform along the nanowire length, as shown in Fig. 2.6 (a). Conversely, the nanowires synthesised via the second approach have a wider diameter size distribution and display a slightly cone-shaped in nature as shown in Fig 2.6 (b). The diameter variation can be ascribed to the rise in temperature of the ZnO seeds inside the high pressure vessel. During the temperature rise from room temperature to the minimum required growth temperature (about

60 °C), the ZnO seeds firstly coalesce, leading to the formation of the larger seed clusters, which ultimately control the nanowire diameter size. For the cone-shaped form there are two influencing parameters, namely the temperature and the concentration of reactants: at low temperatures (60 °C to 80 °C), both lateral and axial growth are promoted, while at higher temperatures the axial growth dominates. As the temperature increases toward the desired growth temperature (90 °C for example), the concentration of reactants changes: the concentration is usually higher at the beginning than the end of the synthesis.

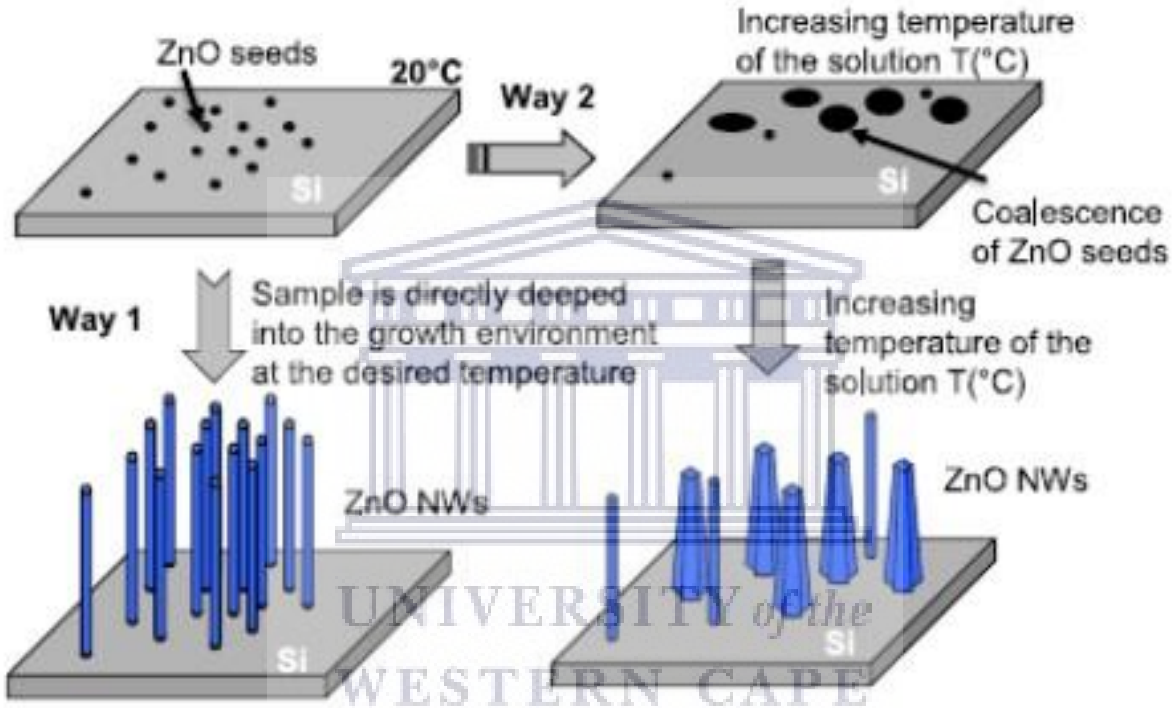

Fig. 2.5: Schematic diagram of the two possible routes for ZnO nanowire growth as proposed by Chevalier-César *et al* [2.16].

This can be seen by studying the chemical reactions (1.1) to (1.4) of Chapter 1. At higher temperatures the *decomposition rate* (equation 1.1) dominates the growth, subsequently leading to a rapid decline in the *hydroxyl supply* (equation 1.2) and ultimately quick *supersaturation* (equation 1.3). Over time, this leads to smaller diameter formation and explains the conical shape shown in Fig 2.6 (b). As such, important experimental considerations are the temperature, concentration of reactants, pH of the growth solution and time of synthesis. For ZnO nanowires, the target parameters are temperature ranging between 60 and 110 °C, chemical concentrations of 1mM of each reactant, neutral pH of 7 and time of

synthesis wide ranging between 1 and 24 hours. In general, the synthesis time controls the nanowire length, however, this is also dependent on reagent concentrations as well temperature.

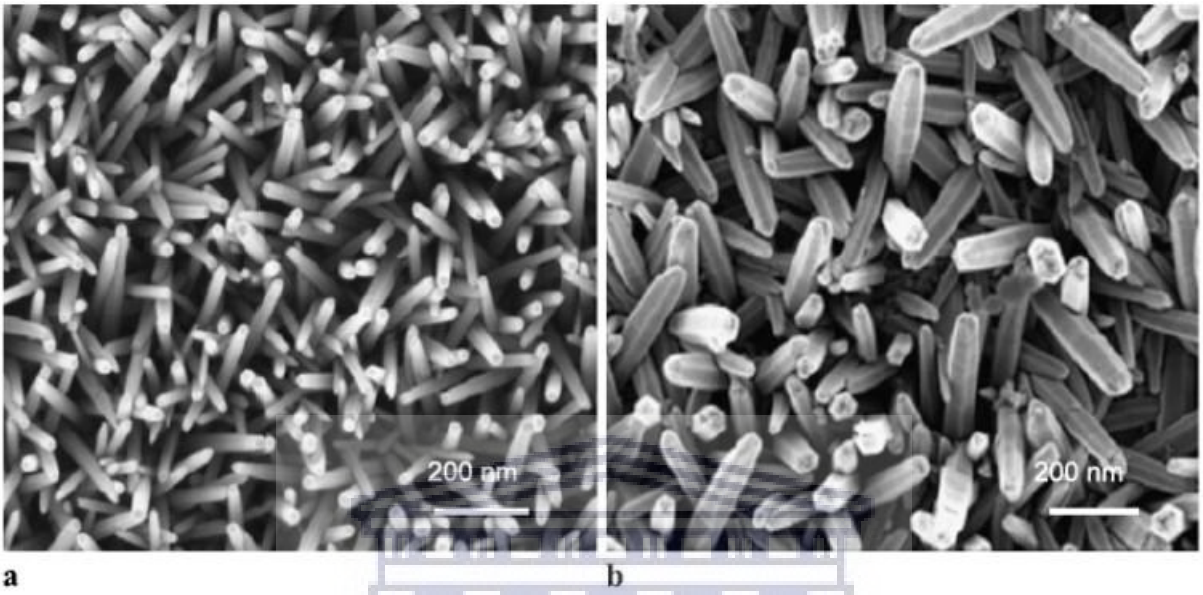

Fig. 2.6: Scanning electron micrographs of the ZnO nanowires resulting from (a) way 1 and (b) way 2 synthesis routes [2.16]

2.1.5 Experimental Procedure: TiO_2 and ZnO Nanowire Synthesis. FTO coated soda lime glass substrates (F:SnO_2, MSE Supplies USA, 12-15 Ω per square) were initially cut into 2 x 1.5 cm^2 sizes, followed by successive ultrasonic bath cleaning in 2 vol% Hellmanex®-deionsed water solution and 100% isopropanol for 5 min at 70 ºC. The cleaned substrates were then dried in an Argon stream and stored under vacuum until processing. During synthesis of the TiO_2 NWs arrays, a nutrient solution containing 12 ml of deionised water, 0.25 ml of tetrabutyl titanate and 10.5 ml of hydrochloride acid (37 wt %) was prepared and magnetically stirred for 10 minutes at ambient conditions. The solution was subsequently transferred to the Teflon liner and placed inside General Purpose Acid Digestion Vessel with the FTO substrates placed upright inside the liner during synthesis. A growth temperature and time of 150 ˚C and 4 hours, respectively, yielded the most consistent nanowire structures and used as the optimum growth conditions. The lattice matching of the rutile F:SnO_2 substrate and rutile TiO_2 phase allows for the direct growth of the nanowires on the FTO substrates.

However, for use as an ETL in organic-inorganic solar cells, a compact layer, directly grown atop the FTO layer, is required [2.17] prior to nanowire synthesis. In this work this was achieved by spin-coating 35 μl of a solution comprising of 0.35 ml titanium isopropoxide dissolved in 5 ml ethanol, with 0.1 ml of 2 M hydrochloric acid (37 wt %) added as mediator. The final solution was stirred for 3 hours at room temperature, then spin-coated for 30 seconds at 4000 rpm and sintered at 500 ˚C for one hour. The metal-doped NWs were synthesised by adding 0.1 M of vanadium trichloride (VCl3), chromium trichloride hexahydrate ($CrCl_3.6H_2O$) and tin tetrachloride ($SnCl_4$) to the TiO_2 precursor solution.

For ZnO NW array growth on FTO substrates, the lattice mismatch between the rutile FTO and stable hexagonal Wurzite phase of ZnO meant that a seed layer was first required on the FTO substrate. This seed layer also acted as hole blocking layer and consisted of a sol-gel solution, prepared using 0.7 M Zinc acetate dihydrate and 0.7 M ethanolamine in 25 ml ethanol and stirred for 10 minutes at room temperature, spin-coated at 3000 rpm for 40 seconds, followed by curing at 250 ˚C for 10 minutes to evaporate the solvent and improve ZnO particle adhesion to the substrate. The ZnO nanowires were then vertically grown by placing the seeded FTO/glass substrate upside down in the Teflon liner containing 25 mM zinc nitrate hexahydrate ($Zn(NO_3)_2.6H_2O$) and hexamethyleneteramine (HTMA) in 20 ml deionised water, which was mixed for 20 minutes at room temperature. Synthesis occurred at optimised temperature and time of 90 ˚C and 4 hours, respectively. The growth of Fe doped ZnO NWs was carried out in a nutrient solution containing 25 mM zinc nitrate ($Zn(NO_3)_2$), 12.5 mM of hexamethylenetetramine (HMTA) and 0.25 mM of iron (III) chloride ($FeCl_3$). For both TiO_2 and ZnO structures, upon completion of the growth time, the autoclave vessels are removed from the oven and evaporatively cooled to room temperature before the removal of the substrate from the nutrient solution. This method allows for faster and more controlled ceasing of the nanowire growth. Once done, the samples were thoroughly washed in deionised water and dried under an argon stream followed by storing under vacuum for further processing.

2.2 Spin Coating

2.2.1 Background. One of the most common techniques for applying thin films on the substrates is spin coating. The technique is widely used in various sectors and offers the advantage of quick and inexpensive processing of uniform films, requiring no high-end vacuum or clean room facilities. Recently, there has been widespread use of spin coating techniques in both organic electronics and nanotechnology research and development and the technique is also central to lab-scale manufacturing of small sized solar cells. Fig. 2.7 shows the low-cost, multi-purpose spin-coater, requiring no vacuum sealed chuck assembly, used during this work; purchased from Ossila, United Kingdom.

Fig. 2.7: Spin coater used for spin-coating of thin film precursors (Ossila, United Kingdom).

2.2.2 Theory. Generally, spin coating refers to the application of thin film thicknesses of a few nanometres up to a few micrometres, that are homogeneously distributed across the

surface of a substrate. This involves coating (casting) a solution of the desired material in a solvent while the substrate is rotated at high revolutions per minute (RPM). The high rotation speed [usually >10 rotations per seconds = 600rpm] implies that the centripetal force, in combination with the surface tension of the solution, pulls the liquid coating into an even covering. During this time the solvent evaporates to leave the desired material on the substrate in an even homogeneous layer.

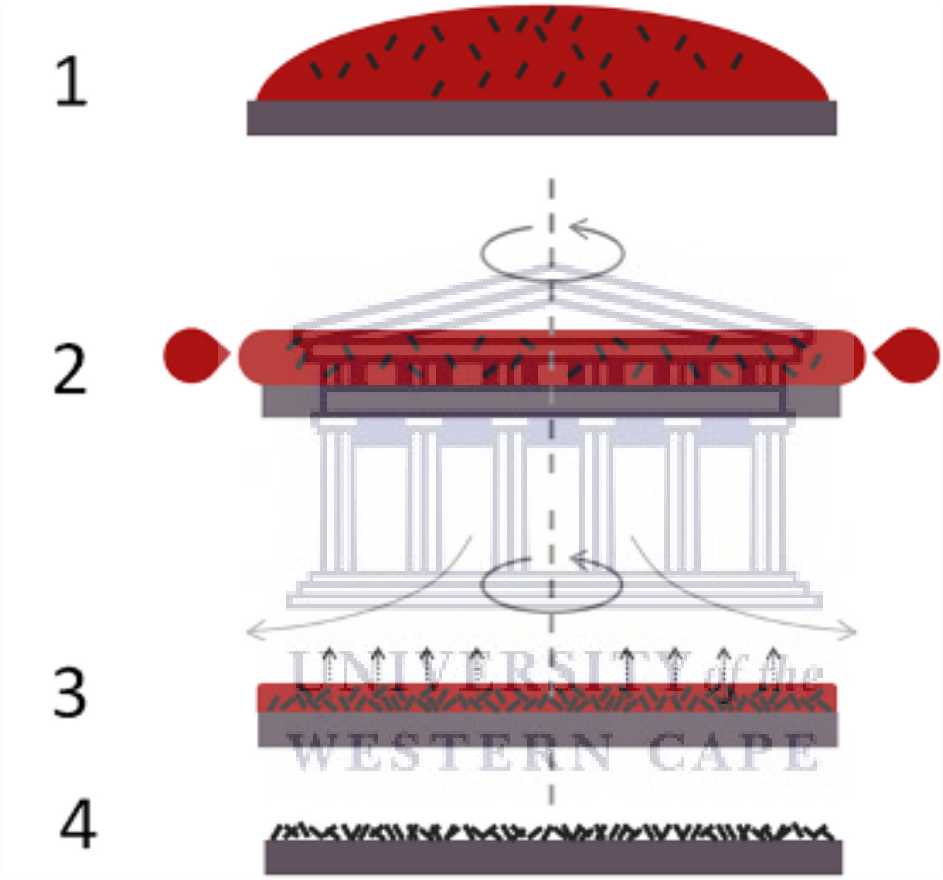

Fig. 2.8: Spin coating process of a droplet of precursor solution [adapted from Ossila, UK; (2.18)].

Fig. 2.8 summarises the simple route to spin coating. The process can be summarised as follows: During step 1 the substrate is coated with the already prepared solution ink. The substrate is thereafter rotated at high speed with the majority of the ink flung off the side (step 2). Airflow then evaporates the majority of solvent, leaving a plasticised thin film (step 3). During step 4 the film completely dries to leave the desired molecules on the surface.

One the major drawback of the technique is that it uses essentially batch (single substrate) process, which results in a very low output performance when compared to roll-to-roll processes [2.19]. The fast drying times have direct effects on some particular nano-technologies, due to the fact that they require more time for self-assembly and/or crystallisation, thus resulting in lower output performance. In addition, as shown, during the coating process, roughly 80 to 90% of the material is flung off, leaving only 10% or less on the substrate. Though this is not an issue to the researchers, it is a clear wastage for the manufacturing sector. Despite these advantages, spin coating remains the best starting point and a benchmark for both the academic and industrial sectors for thin and homogenous coating.

2.2.3 Annealing of Substrates After Spin Coating. There are many known heat treatment processes, of which some are peculiar to steels only, while others can be applied to other different alloys. Heat treatment processes can be classified into four categories: hardening, surface hardening, miscellaneous and annealing [2.20]. Annealing is a heat treatment process which allows for easy and quick alteration of the microstructures of a spin-coated material on glass or even change its mechanical or electrical properties [2.20]. This procedure is advised immediately after spin coating of the samples to remove the residual organic constituents, by quick drying the spin coated layer on the glass. During the formation of ZnO seed layers, 250˚C was applied to the substrates for 10 minutes to obtain the desired morphology. Meanwhile, for the TiO_2 blocking layer, the samples are sintered at 500˚C for an hour before the layer was formed. Furthermore, during the formation of absorber layer of P3HT:PCBM the substrates were annealed at stages, initially the samples were annealed at 90˚C for 30 minutes cool down for 10 minutes, then 120˚C for 20 minutes cool down 20 minutes and finally annealed at 150˚C for 20 minutes, these procedure is to completely remove all the unwanted organic residual constituents on the substrates and gave the better seeded layer morphology of the samples. This will be discussed in this section. Fig.2.9 shows a schematic of a hot-plate capable of magnetic stirring at high temperature. Most magnetic stirrer hot-plates only provide curing upt to roughly 150 °C, however the Corning® PC-4000 high temperature hot-plate used during this study is capable of achieving high temperature (up to 600 °C) open air annealing, post spin-coating.

Fig. 2.9: (left) schematic of one of the magnetic stirrer hot-plates used during this study; (right) Corning PC-4000 hot-plate used for high temperature curing of ZnO and TiO_2 seed layers (Corning, United States)

2.3 Plasma Physics

2.3.1 Background. Plasma, the fourth state of matter, is usually associated with the intense temperatures of matter found in the sun. Non-thermal plasmas are more manageable in comparison to these extreme temperatures observed in thermal plasmas. Non-thermal plasmas are commonly used in laboratories and manufacturing around the globe. Plasma is made up of electrons, neutrals, radicals and ions, and all together are quasi-neutral. The relative temperatures and densities of each of these species distinguish different kinds of plasmas. For thermal plasmas, electron temperatures (T_e) are in equilibrium with neutral (T_n) and ionic (T_i) species temperatures, whereas in non-thermal plasmas, T_e values are far greater than T_n. The experiments described in this thesis, use non-thermal low pressure plasmas of 10^{-6} mbar base pressure and deposition pressure of 10^{-2} mbar that are generated electrically by induction [2.21], using an alternating current of 2.16 A, 2.5 V and stabilisation/oscillating frequency of 13.56 MHz, with a forward biased operating power of 500 W.

2.3.2 Theory. A plasma is a system of charges that are coupled and collide with one another through self-consistent electric and magnetic fields. If electromagnetic wave and magnetic field interaction is ignored, then in principle we solve 6N basic coupling equations that are associated with what happens inside the plasma chamber [2.22] as follows:

$$F = m\ddot{a} = m_i \frac{d^2 \boldsymbol{r}_i}{dt^2} = q_i \boldsymbol{E}(\boldsymbol{r}_i) \tag{2.3}$$

$$E(\boldsymbol{r}_i) = \sum_j \frac{q_j}{|\boldsymbol{r}_i - \boldsymbol{r}_j|^3}(\boldsymbol{r}_i - \boldsymbol{r}_j) \tag{2.4}$$

where m_i q_i and $\boldsymbol{r}_i$ are the mass, charge and position of the i^{th} particle, and the electrostatic field is **E**. However, this is obviously a doubtful approach, if a nontrivial number of charges are considered. But luckily, simplification is achievable if collision-less behaviour is considered. The electric field may be split into two fields ($\boldsymbol{E_1}$ and $\boldsymbol{E_2}$), each having special spatial scales. $\boldsymbol{E_1}$ field has spatial differences on a scale length much less than the electron Debye length; this is the length over which the field of an individual charge is protected by the response of the surrounding charges. The $\boldsymbol{E_1}$ field represents the fast fluctuating micro-field, because of the multiple and random collisions between the discrete charges. In comparison, $\boldsymbol{E_2}$ signifies the field owing to deviations from charge neutrality over space scales much more than or comparable to the Debye length. This produces a collective or coherent motion of the charges. A natural separation into collective and collisional behaviour is thus achieved. The collisional behaviour becomes insignificant when the number of electrons in a sphere/chamber with a radius equal to the electron of Debye length, then electron of Debye length becomes very large. To motivate this, simple ions scattering calculation of the electron must be solved.

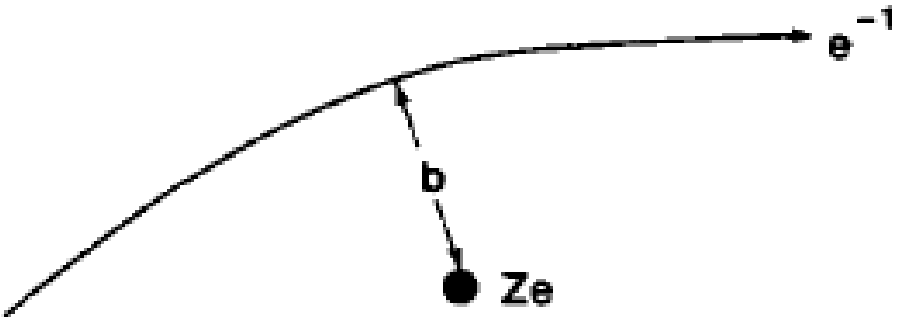

Fig. 2.10: Schematic representation of an electron being deflected as it streams past an ion [2.23].

As illustrated in Fig. 2.10, consider an electron with velocity υ, mass m and charge e streaming past an ion with charge Ze [2.22, 2.23]. The distance of closest approach is b. The electron experiences a change in velocity $\Delta\upsilon$ which is approximately

$$\Delta\upsilon = \frac{\boldsymbol{Ze^2}}{mb^2}\left(\frac{2b}{\upsilon}\right) \tag{2.5}$$

which is the maximum electrostatic force multiplied by the interaction time (~ *2b/v).* Assuming several randomly spaced ions, then $(\Delta\upsilon = 0)$, where the brackets denote an average. Though, there is a change in the mean square velocity. Thus, this average rate of change is given by$(\Delta\upsilon)^2$ multiplied by the rate of encounters, which is given by $n_i\,\boldsymbol{\sigma}\,\boldsymbol{\upsilon}$**.** At this point n_i is the ion density and $\boldsymbol{\sigma}$ is the cross-section of the impact. Summation of the all encounters gives

$$\frac{d}{dt}\langle(\Delta\upsilon)^2\rangle = \int 2\pi b\, db\, n_i\upsilon\,(\Delta\upsilon)^2\,. \tag{2.6}$$

Now substituting for $\Delta\upsilon$ and integrating over the impact parameters, we obtain

$$\langle(\Delta\upsilon)^2\rangle = \frac{8\pi\, n_i Z^2 e^4 \ln\Lambda}{m^2\upsilon}\mathrm{t}\,, \tag{2.7}$$

where Λ is the ratio between the minimum and maximum impact parameters (b_{min} and b_{max}).

The maximum impact parameter is approximately the electron Debye length, as other electrons in the plasma shield over this distance outweigh the Coulomb potential. However, the minimum impact parameter is the bigger of either the classical distance of closest approach ($b_{min} \approx Ze^2/m\upsilon^2$) or the De Broglie wavelength of the electron ($b_{min} \approx \hbar/m\upsilon$), where ħ is the Planck's constant. Using the first assumption, the distance of closest approach, we have $\Lambda \approx 9N_D/Z$, here N_D is the number of electrons in a Debye sphere. Above all $N_D = \frac{4}{3}\pi\, n_e\lambda_{De}^3$, here n_e is the electron density and λ_{De} is the electron Debye length. Though, this vital length will be derived later in this section [2.22-2.25]. It is suitable to define a ninety-degree deflection time (t_{90°) by the condition that the root-mean-square change in velocity becomes as large as the velocity, therefore

$$t_{90^\circ} = \frac{m^2 v^3}{8\pi\, n_i Z^2 e^4 \ln \Lambda} \tag{2.8}$$

Averaging over a Maxwellian distribution of velocities, a suitable measure of the mean rate ($\upsilon_{90^\circ} \equiv 1/t_{90^\circ}$) upon which electron-ion collisions scatter electrons through a large angle is obtained as

$$\upsilon_{90^\circ} = \frac{8\pi\, n_i Z^2 e^4 \ln \Lambda}{6.4 m^2 \upsilon_e^3} \tag{2.9}$$

where $\upsilon_e = \sqrt{\theta_e/m}$ is the electron thermal velocity and θ_e is the electron temperature.

Note that:

$$\frac{\upsilon_{90^\circ}}{\omega_{pe}} \simeq \frac{Z \ln \Lambda}{10} \frac{1}{N_D}, \tag{2.10}$$

where the electron plasma frequency is given by ω_{pe}, which is a frequency characteristic of collective electron motion. On this fine scale, collisional interactions can be neglected to the zero[th] order in the parameter $\frac{1}{N_D}$. Hence, if the electron density is expressed in $cm^{-3}$and the electron temperature in eV, then

$$N_D = 1.7 * 10^9 (\theta_e^3 / n_e)^{1/2} \tag{2.11}$$

N_D can be incredibly large even in a rather dense plasma, as long as the electron temperature is high. For instance, if $n_e = 10^{21} cm^{-3}$ and $\theta_e = 1\ keV$,$N_D \approx 1700$.. However, in the collisionless limit($N_D \to \infty$), the fine scale fluctuating microfields related with discrete charges are totally negligible. The behaviour of the plasma can be investigated by solving for the motion of charges in the smooth or coarse-grained fields resulting from the collective motion of large numbers of charges. For collective behaviour two parallel levels of description may be developed, namely analytical and numerical description. Analytical descriptions are characterised by the Vlasov equation, which is a set of moment (fluid-like) differential equations describing the electrons and ions by finding the averages over the velocities of the charges. This supposed two-fluid description will subsequently be used expansively to describe a wide range of laser or high frequency plasma interactions. In the

second, numerical description the use of simulations of particles are extensively used. Such simulations are a powerful tool for investigating nonlinear and kinetic effects (effects based on the details of particles velocity distribution) [2.22, 2.26].

2.3.3 The Vlasov Equation. The use of the Vlasov equation is a normal starting point to explain the evolution collision-less plasmas. Firstly, the phase distribution function $f_j(x, v, t)$ is introduced. This is basically the function that characterises the position of j particles in phase at space (x, v) as a function of time. By understanding the laws of motion, an expression for $f_j(x, v, t)$ can be derived. However, because particles are assumed to be neither destroyed nor created when they move from one position to another in phase space (no ionisation or recombination), $f_j(x, v, t)$ must follow the equation of continuity:

$$\frac{\partial f_j}{\partial t} + \frac{\partial}{\partial x} . \left(\boldsymbol{x} f_j\right) + \frac{\partial}{\partial v} . (\boldsymbol{v} f_j) = 0 \ . \tag{2.12}$$

Thus, from the laws of motion,

$$\dot{\mathrm{x}} = \boldsymbol{v}$$

$$\frac{\partial \boldsymbol{v}}{\partial \boldsymbol{t}} = \frac{\boldsymbol{q_j}}{m_j} \left(\boldsymbol{E} + \frac{\boldsymbol{vXB}}{C} \right), \tag{2.13}$$

Here q_j and m_j are the charge and mass of the j^{th} species and where **E** and **B** are the coarse-grained fields related to the collective behaviour. Taking note that x and v are independent variables and substituting equation (2.13) into (2.12), the famous Vlasov equation is obtained as:

$$\frac{\partial f_j}{\partial t} + \boldsymbol{v} . \frac{\partial f_j}{\partial \boldsymbol{x}} . + \frac{\boldsymbol{q_j}}{m_j} \left(\boldsymbol{E} + \frac{\boldsymbol{vXB}}{C} \right) . \frac{\partial \boldsymbol{f_j}}{\partial \boldsymbol{v}} = 0 \tag{2.14}$$

The equation basically means that the term $f_j(\boldsymbol{x}(t), \boldsymbol{v}(t), t$ is a constant; and after a dynamic trajectory, the phase space density is conserved. Thus, such an equation relates to each charge species in the plasma. The Vlasov equation is improved with Maxwell's equations for an absolute description of collision-less plasma behaviour. In reality, a more complete description is required which can be achieved by averaging the individual velocities of the particles. This can be achieved by deriving equations for the evolution in space and time of

density, pressure, and mean velocity of each species by taking different velocity moments of the Vlasov equation. Each moment leads to the next higher moment, creating an infinite set of moment equations. Fortunately, this can be truncated by adding heat flow assumptions [2.22, 2.23-2.24].

2.3.4 The Moment Equations. The moment equations and their truncation must be motivated. At first, the mean velocity (u_j), density (n_j) and pressure tensor ($\boldsymbol{P}_j$) are calculated by averaging the different moments of phase space distribution function over velocity:

$$n_j = \int f_j(\boldsymbol{x}, \boldsymbol{v}, t) d\boldsymbol{v} \tag{2.15}$$

$$n_j \boldsymbol{u}_j = \int \boldsymbol{v} f_j(\boldsymbol{x}, \boldsymbol{v}, t) d\boldsymbol{v} \tag{2.16}$$

$$\boldsymbol{P}_j = m_j \int (\boldsymbol{v} - \boldsymbol{u}_j)(\boldsymbol{v} - \boldsymbol{u}_j) f_j(\boldsymbol{x}, \boldsymbol{v}, t) d\boldsymbol{v} \tag{2.17}$$

If the subscript j is suppressed when deriving the moment equations, it becomes clear that these equations will apply to each charge species [2.22, 2.27-2.29]. Therefore, taking the average velocity, the Vlasov equation yields:

$$\int \boldsymbol{dv} \left[\frac{\partial f_j}{\partial t} + \boldsymbol{v}. \frac{\partial f_j}{\partial \boldsymbol{x}} . + \frac{\boldsymbol{q_j}}{m} \left(\boldsymbol{E} + \frac{\boldsymbol{vXB}}{c} \right) . \frac{\boldsymbol{\partial f_j}}{\boldsymbol{\partial v}} \right] = 0 . \tag{2.18}$$

The first two terms in equation (2.18) give:

$$\int \boldsymbol{dv} \, \frac{\partial f}{\partial t} = \frac{\partial n}{\partial t}$$

$$\int d\boldsymbol{v} \, \boldsymbol{v} . \frac{\partial f}{\partial \boldsymbol{x}} = \int d\boldsymbol{v} \sum_i v_i \, \frac{\partial f}{\partial x_i} \tag{2.19}$$

$$= \frac{\partial}{\partial \boldsymbol{x}} . (n. \boldsymbol{u}) .$$

The term in equation (2.18) thus vanishes after the integration by parts and also as $f \rightarrow 0 \; as |v| \rightarrow \infty$. The first moment of the Vlasov equation therefore gives the continuity equation for the particle density:

$$\frac{\partial n}{\partial t} + \frac{\partial}{\partial \boldsymbol{x}}.(n.\boldsymbol{u}) = 0. \tag{2.20}$$

This leads to the next moment of the Vlasov equation:

$$\int \boldsymbol{dv}\, \boldsymbol{v}\left[\frac{\partial f}{\partial t} + \boldsymbol{v}.\frac{\partial f}{\partial \boldsymbol{x}}\right. . + \frac{q}{m}\left(\boldsymbol{E} + \frac{\boldsymbol{v}\, X\, \boldsymbol{B}}{C}\right).\left.\frac{\partial f}{\partial \boldsymbol{v}}\right].\frac{\partial f}{\partial \boldsymbol{v}} \;\; = 0\,. \tag{2.21}$$

The first term of equation (2.21) can be rewritten as

$$\int \boldsymbol{dv}\, \boldsymbol{v}\, \frac{\partial f}{\partial t} \;=\; \frac{\boldsymbol{\partial}}{\boldsymbol{\partial t}}\, n\boldsymbol{u}.$$

and similarly the second term as

$$\int d\boldsymbol{v}\, \boldsymbol{v}\, \boldsymbol{v}.\frac{\partial f}{\partial x} = \frac{\partial}{\partial x}\,.\int d\boldsymbol{v}\, \boldsymbol{vv}\, \boldsymbol{f}$$

$$= \frac{\partial}{\partial x}\,.\left(\frac{\boldsymbol{P}}{m} + n\boldsymbol{uu}\right).$$

Equation (2.21) can now be rewritten as:

$$\int d\boldsymbol{v}\,(\boldsymbol{v} - \boldsymbol{u} + \boldsymbol{u})(\boldsymbol{v} - \boldsymbol{u} + \boldsymbol{u})f \;= \frac{\boldsymbol{P}}{m} + n\,\boldsymbol{u}\,\boldsymbol{u} \tag{2.22}$$

However, since the term $\int (v - u)\, f\, dv = 0$, the last evaluation of equation (2.21) gives

$$\int d\boldsymbol{vv}\, \frac{q}{m}\left(\boldsymbol{E} + \frac{\boldsymbol{v}\, X\, \boldsymbol{B}}{C}\right).\frac{\boldsymbol{\partial} f}{\boldsymbol{\partial v}} = -\,\frac{nq}{m}\left(\boldsymbol{E} + \frac{\boldsymbol{u}\, X\, \boldsymbol{B}}{C}\right) \tag{2.23}$$

After integration by parts and collecting the above terms together, we obtain an expression for a charged fluid as:

$$\frac{\partial}{\partial t}\,(n\,\boldsymbol{u}) + \frac{\boldsymbol{\partial}}{\boldsymbol{\partial x}}\,.(n\,\boldsymbol{u}\,\boldsymbol{u}) = \frac{nq}{m}\left(\boldsymbol{E} + \frac{\boldsymbol{u}\, X\, \boldsymbol{B}}{C}\right) - \frac{\partial}{\partial x}\,.\frac{\boldsymbol{P}}{m}. \tag{2.24}$$

Thus, it is suitable to rewrite the first two terms of equation (2.24) with the continuity equation and assuming the pressure is isotropic i.e, $\mathbf{P} = \mathbf{I_P}$ where **I** is the unit dyad. This yields:

$$n\frac{\partial u}{\partial t} + n\,\boldsymbol{u}.\frac{\partial \boldsymbol{u}}{\partial \boldsymbol{x}} = \frac{nq}{m}\left(\boldsymbol{E} + \frac{\boldsymbol{u}\,X\,\boldsymbol{B}}{C}\right) - \frac{1}{m}\frac{\partial p}{\partial x} \qquad (2.25)$$

Note that each moment takes in the next, higher one. For the density, the continuity equation involves the mean velocity; the force equation for the velocity brings in the pressure. The subsequent moment term gives an equation for the pressure (energy density) which includes the heat flow, leading to an infinite set of combined equations, which are hardly a practical description. Fortunately, by making different assumptions regarding the heat flow, the moment equations can be truncated yielding the so-called equation of state.

The simplest assumption is that the heat flow is so rapid that the temperature of the charged fluid is a constant. In this case, the isothermal equation of state: $P = n\,\theta$, with a constant temperature θ is obtained. This equation of state, plus the force and continuity equations for the fluid, and the Maxwell's equations form a closed description. But, if $\omega/k \ll v_t$, where ω and k are the characteristic frequency and wave number of the physical process being considered, while v_t is the thermal velocity of the particles, then isothermal equation of state is suitable. However, in the opposite limit ($\omega/k \gg v_t$) the heat flow may be discarded [2.27-2.29]. This hypothesis results in an adiabatic equation of state. To obtain an equation for the pressure, the Vlasov equation must be multiplied by the kinetic energy and averaged over velocity as follows:

$$\int \frac{m\boldsymbol{v^2}}{2}\boldsymbol{dv}\left[\frac{\partial f}{\partial t} + \boldsymbol{v}.\frac{\partial f}{\partial \boldsymbol{x}} . + \frac{q}{m}\left(\boldsymbol{E} + \frac{\boldsymbol{v}\,X\,\boldsymbol{B}}{C}\right).\frac{\partial f}{\partial \boldsymbol{v}}\right] = 0\,. \qquad (2.26)$$

Considering one-dimension to simplify the algebra, the first term can be written as

$$\frac{m}{2}\frac{\partial}{\partial x}\int f\,(v-u+u)^2\,dv = \frac{1}{2}\frac{\partial}{\partial t}(P + nmu^2) \qquad (2.27)$$

The next term in equation (2.26) gives

$$\frac{m}{2}\frac{\partial}{\partial x}\int f\,(v-u+u)^2\,dv = \frac{\partial Q}{\partial x} + \frac{3}{2}\frac{\partial}{\partial x}(up) + \frac{m}{2}\frac{\partial}{\partial x}(nu^3), \qquad (2.28)$$

where $Q \equiv \left(\frac{m}{2}\right)\int (v-u)^3\, f dv$. The last term in equation (2.26) is simply

$$\frac{\boldsymbol{q}}{\boldsymbol{2}}\int \boldsymbol{v^2}\,\boldsymbol{E}\frac{\boldsymbol{\partial f}}{\boldsymbol{\partial v}}\,\boldsymbol{dv} = -\boldsymbol{n}\,\boldsymbol{q}\,\boldsymbol{u}\,\boldsymbol{E} \qquad (2.29)$$

Adding all terms, the final moment expression is obtained as

$$\frac{1}{2}\frac{\partial}{\partial t}\left(P + n\,m\,u^2\right) + \frac{3}{2}\frac{\partial}{\partial x}\left(up\right) + \frac{1}{2}\frac{\partial}{\partial x}\left(n\,m\,u^3\right) + \frac{\partial Q}{\partial x} = q\,n\,uE. \quad (2.30)$$

2.3.5 Nitrogen Plasma Treatment of ZnO and TiO_2 Nanowires. Fig. 2.11 shows the CADAR (Cluster Apparatus for Device Application Research) system housed in the Department of Physics and Astronomy at the University of the Western Cape, used to plasma treat the nanowire structures used in this work.

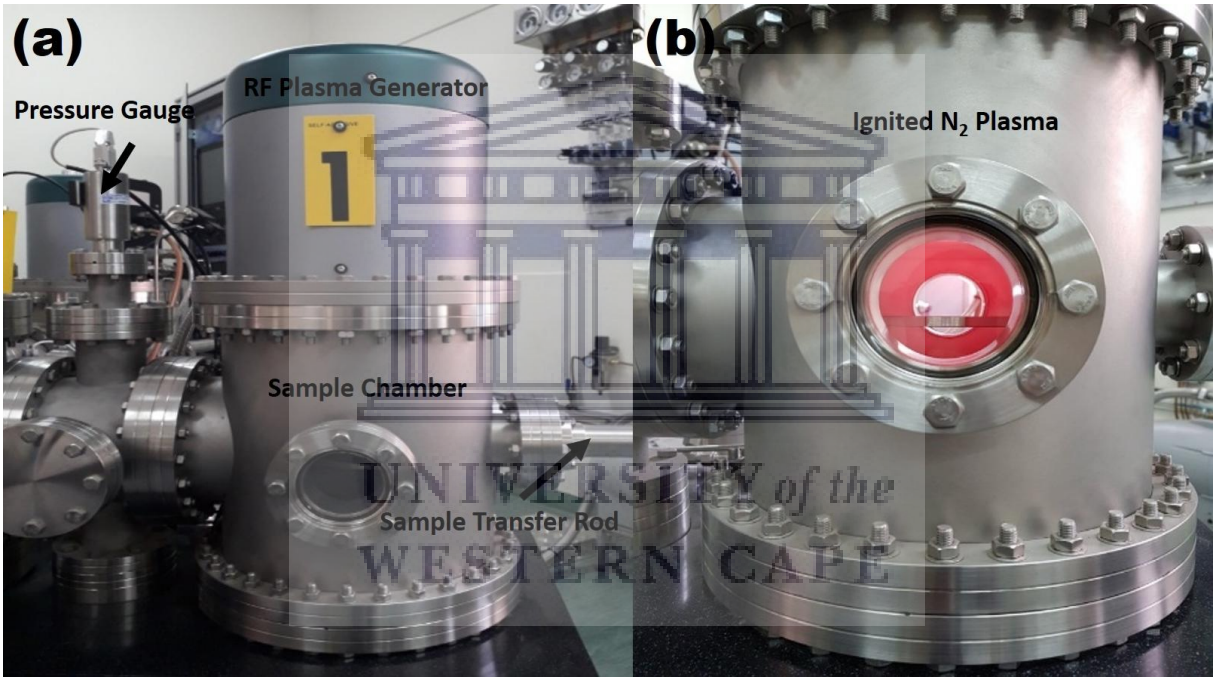

Fig. 2.11: (a) Components of the CADAR system used for plasma irradiation of the nanowire structures; (b) chamber with a fully ignited N_2 plasma

Fig. 2.12 shows a schematic representation of the experimental approach used to obtain N_2 plasma treated TiO_2 and ZnO NW arrays. The nanowire arrays were placed in a custom-built plasma-enhanced chemical vapour deposition chamber at a base and treatment pressure of 1.5×10^{-6} and 7×10^{-2} mbar, respectively. Prior to treatment, the plasma power was fine-tuned in a N_2:Ar gas mixture, controlled by keeping a constant gas flow rate of 100:100 sccm mixture. Based on previous optimisation experiments, an optimum plasma power of 500W (plasma power supply = 5 V; 1.25 A) yields the most consistent and significant changes in

the opto-electronic behaviour of both TiO_2 and ZnO structures. Once set, the Ar flow was reduced to 0 sccm, allowing for the red glowing N_2 plasma (see Fig. 2.11) to interact with the specimen; this point also signalled the time of exposure, set for a total of 10 min. Herein after the N_2 plasma treated TiO_2 and ZnO NW films will be referred to as N_2-TiO2 and N_2-ZnO, respectively, the metal-doped N_2 treated TiO_2 denoted as metal:TiO_2 – N_2 and Fe:ZnO – N_2 will be the sample code for the Fe doped ZnO NWs treated with plasma.

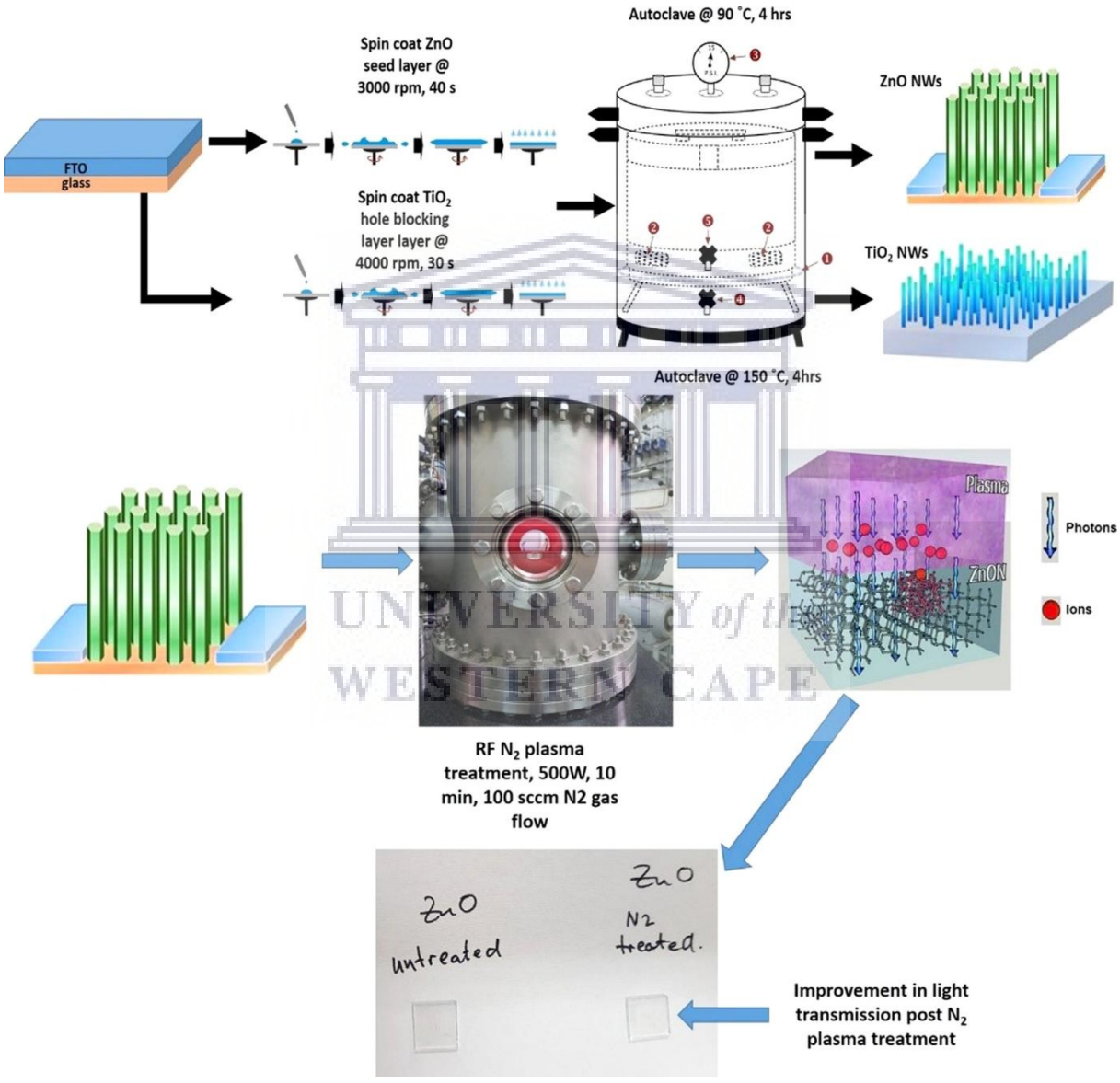

Fig. 2.12: Schematic representation of the (top row) hydrothermal synthesis; (middle row) N_2 plasma irradiation; (bottom row) optical image of a glass/FTO/compact layer/ZnO NW array before and after N_2 plasma exposure

2.4 Solar Cell Fabrication

2.4.1 Overview of Device Architecture. The schematics of the organic solar cell architectures fabricated in this study are shown in Fig. 2.13. For both TiO_2 and ZnO based devices, the hybrid inverted device architecture (as discussed in Chapter 1.5), with the electron transport layer deposited on the TCO substrate, is employed during fabrication.

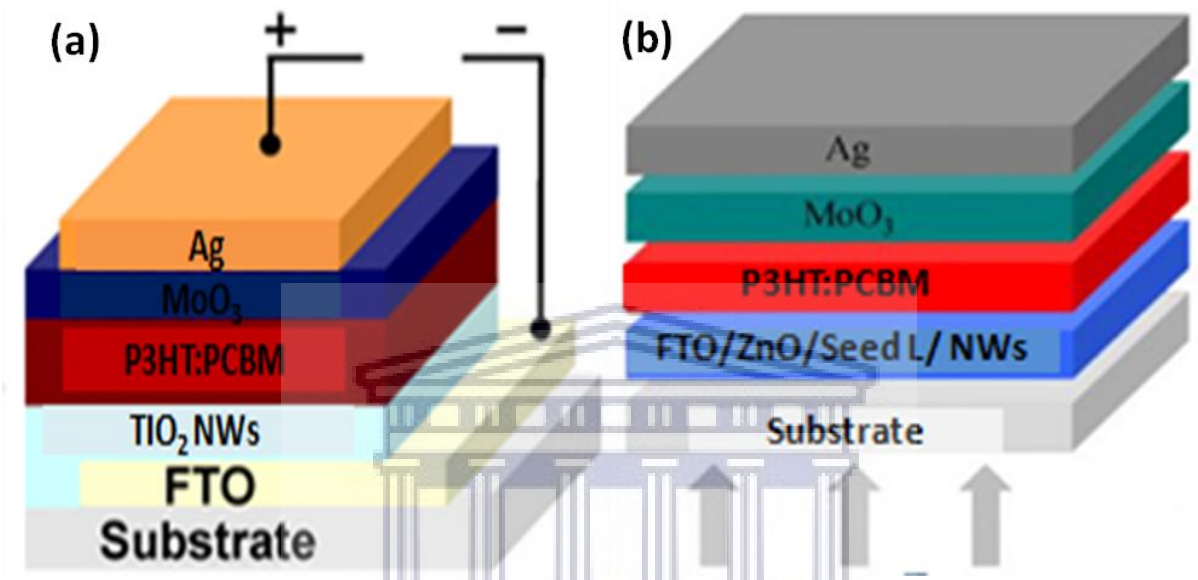

Fig. 2.13: Schematic diagram of inverted organic solar cell devices incorporating (a) TiO_2 and (b) ZnO NW arrays

These device structures allow for the light to be illuminated from the substrate side. The anode consists of semi-transparent oxide layers, usually FTO or ITO, which have two very important functions during device operation. In the first instance, the TCO *must* allow photons to pass through towards the photo-active layer and secondly serves as an electron collector passing on electrons from the active layer through the exterior load. A layer of the conductive ZnO and TiO_2 nanowires are synthesised between the TCO anode and the photoactive layer to serve as an enhanced electron transport layer. The light absorbing photoactive layer consists of the donor and acceptor material (P3HT:PCBM in general) which is sandwiched between two electrodes as shown in Fig 2.13. A thin molybdenum oxide (MoO_3) layer of between 7 and 10 nm thin, is deposited on top of the photoactive layer by thermal evaporation process and serves as a hole transport layer (HTL). The MoO_3 layer also acts as a sealing layer protecting the active polymer layer from oxidation, and prevents the cathode material (Au or Ag) from diffusing into the active layer, which can lead to trap sites

[2.30]. Fig 2.14 shows a complete solar cell incorporating either TiO_2 or ZnO NWs, as fabricated in this study, along with a schematic depicting the operation of the device under illumination.

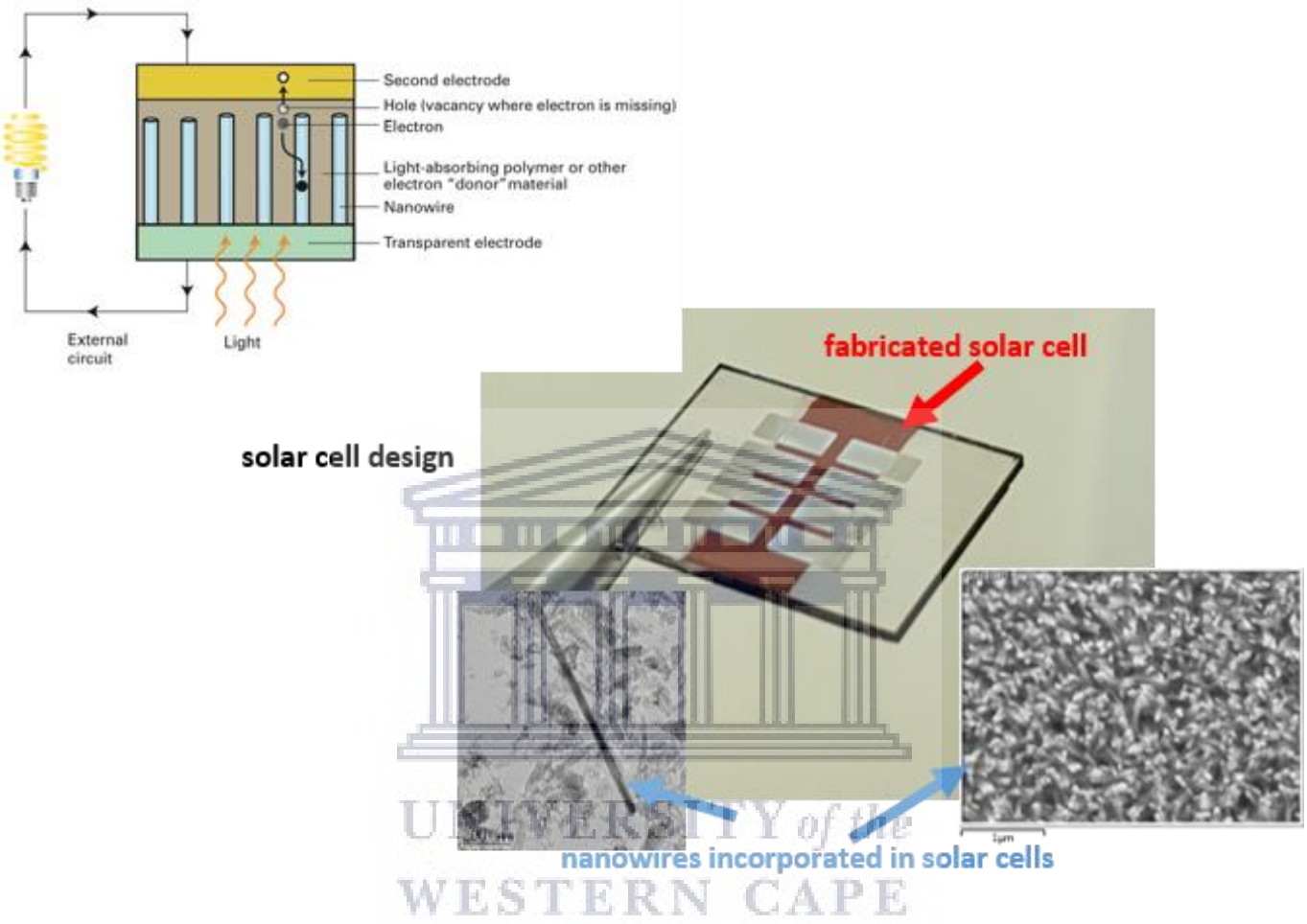

Fig. 2.14: Schematic representation of the device operation and image of a fully assembled device, fabricated during the course of this study.

2.4.2 Solar Cell Operating Principle. Since the basic properties of organic semiconductors vary from those of their inorganic counterparts, the operation of OPV devices is dissimilar from that of silicon solar cells. Incident photons split the covalent bonds in a silicon solar cell, which form electron – hole pairs. Because of the silicon's crystalline nature, charge carrier generation requires only a minimal interaction force. Thus silicon absorption leads to free charge carriers effectively. The Coulombic force of attraction between electrons and holes are very high, due to the low dielectric constant (ε~3) in semiconducting polymer

materials [2.31, 2.32]. This means that unlike inorganic semiconductors, where photo-excitation typically produces a free electron and hole, excited states form bound electron – hole pairs in semiconducting polymers. This bound electron – hole pair is known as exciton. The excitonic binding energy needs to be overcome by a driving force so that the free charge carriers can be produced and transported throughout the device. In organic solar cells the excitons formed in the donor material can be dissociated at the donor–acceptor (D–A) interface. Organic solar cells are categorised by whether the electron donor (D) and acceptor (A) layers form a planar heterojunction or are intermixed to form a bulk-heterojunction (BHJ) or planar-heterojunction (PHJ), as illustrated in Fig. 2. 15. In BHJs, the donor and acceptor are intermixed during fabrication (Fig. 2.15 (b)), whereas for PHJs the semi-conductor layers are deposited in sequence as shown in Fig. 2.15 (a).

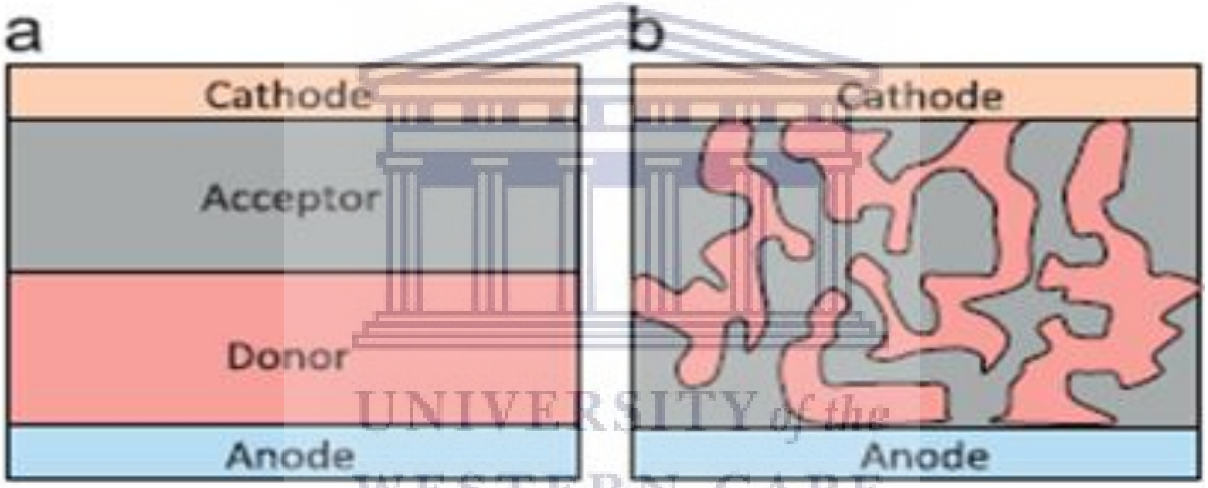

Fig. 2.15: Schematic cross-section of the different layers of (a) planar-heterojunction and (b) bulk-heterojunction OSC [2.33]

Fig. 2.16 displays an OSC energy band diagram, representative of either PHJ or BHJ. Excitons formed in the donor material are dissociated at the D–A interface, with the force required to overcome the exciton binding energy provided by the energy level offset of the lowest unoccupied molecular orbital (LUMO) of the donor polymer and the conduction band edge, E_g, of the acceptor material. This energy off-set is shown as ΔE_{ES} in Fig. 2.16. The energy offset of the acceptor's highest occupied molecular orbital (HOMO) and donor material's HOMO is needed to dissociate excitons formed in the acceptor material. Excitonic dissociation due to this energy offsets occurs at the donor-acceptor phase interface, so the

arrangement of the two materials in the active layer is essential to the device's successful operation. Based on this, it can be seen that a BHJ structure is much more efficient compared to a PHJ OSC. A device with such large dispersion of interfaces right through the photoactive layer requires smaller exciton diffusion distances, and consequently, a larger exciton dissociation yield is achieved. There exists an exchange between increasing interfacial area via the close dispersion of phases and the creation of efficient conductive pathways through which free electrons and holes may be transported. Therefore, this well dispersed interface of donor and acceptor materials also exposes the device to increased recombination of e-h pairs caused by material impurities, oxidation of the photo-active polymer layer (donor) and inter-diffusion of ions from the top metal contact. In this regard, the application of one-dimensional nanostructures of metal-oxides, as motivated in this study, hold much promise for improved charge transport within the device.

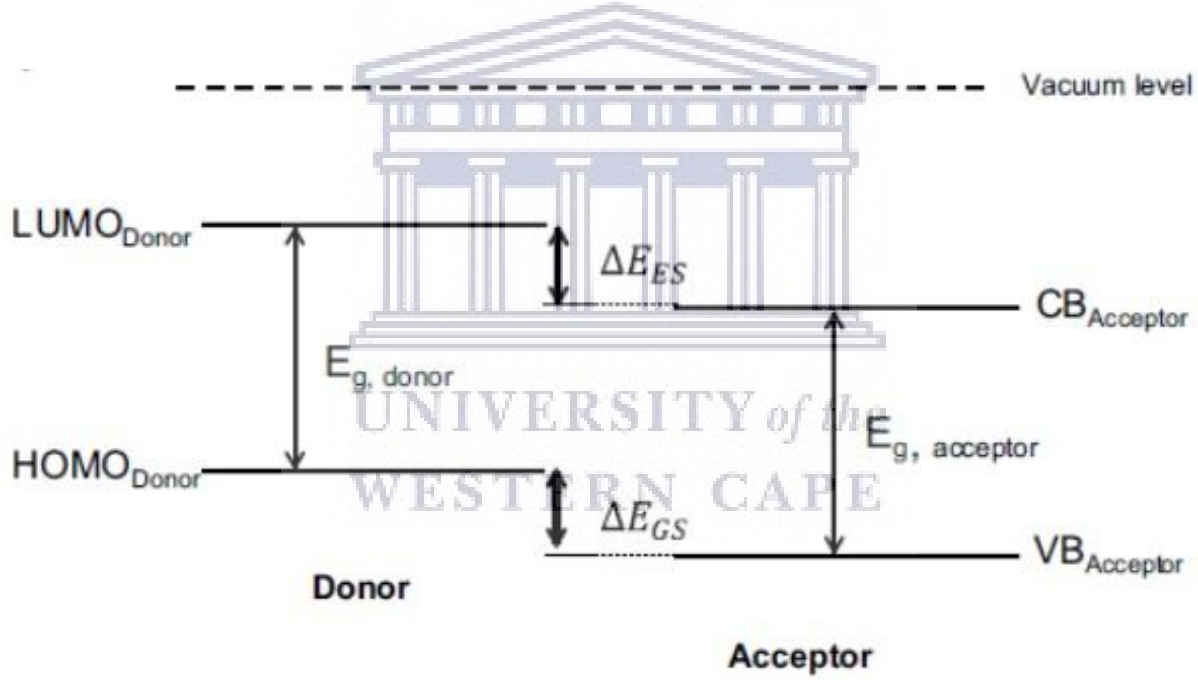

Fig. 2.16: Energy level diagram of the D-A interface of heterojunction devices [2.34].

2.8. Device Characterisation. The main parameters of a photovoltaic cell, which are obtained from a simple photo-current-voltage (I-V) curve, are the open circuit voltage (V_{oc}), the short-circuit current (I_{sc}), the power conversion efficiency (PCE) and the fill factor (FF) as shown in Fig. 2.17.

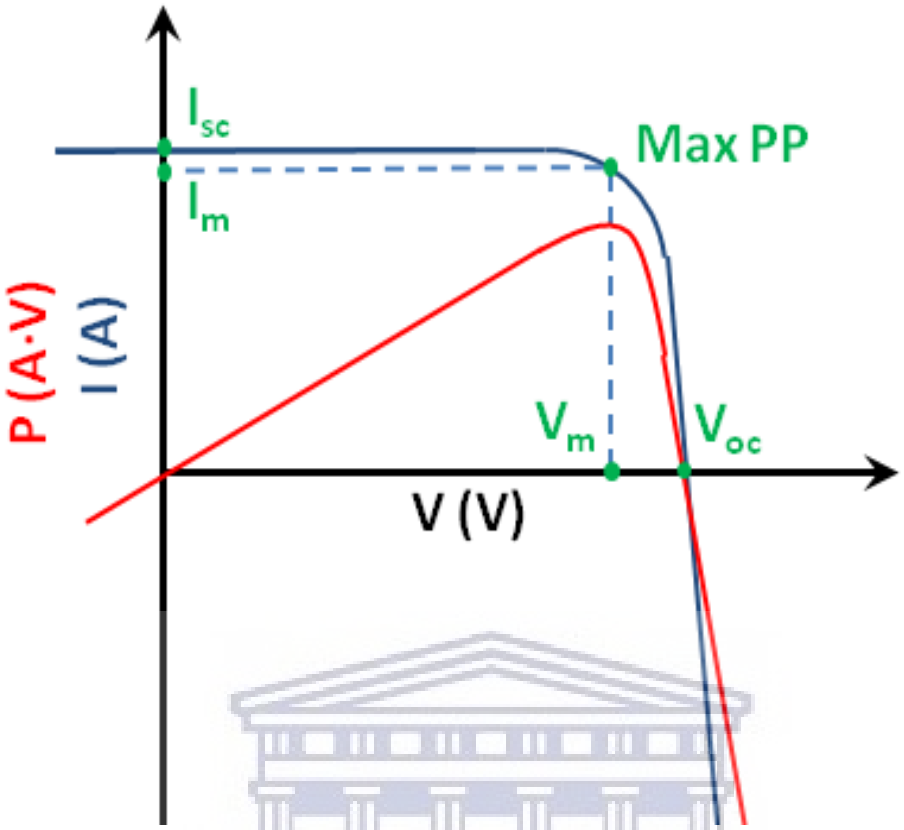

Fig. 2.17: Basic I-V curve of a solar cell under illumination [2.35]

The voltage at which no current flows through the solar cell is referred to as V_{oc}. Primarily, V_{oc} is determined by the band gap of the absorbing semiconductor for conventional single junction inorganic solar cells, although it is limited by the recombination of charge by radiative processes, as Shockley and Queisser first hypothesised in 1961 [2.36]. On the contrary, in BHJ organic PVs, charge separation at the D-A interface occurs effectively as discussed above. Because of this, as several studies have shown [2.37], the V_{oc} absolutely depends on the energy difference between the $HOMO_D$-$LUMO_A$ offset at the D-A interface of the cell, relative to the band gap. However, the experimental V_{oc} values can vary from those inferred from that disparity, depending on the morphology of the D-A blend and the morphology and nature of the electrode [2.38]. In fact, unlike the theory of Shockley and Queisser, since strict quenching of the excited states occurs through active charge separation processes at the D-A interface, charge losses occur primarily through non-radiative recombination pathways rather than radiative ones [2.39].

When V = 0, I_{sc} is the current that flows through the solar cell. Under a certain photon flux, I_{sc} depends primarily on the ability of the D material to absorb light and generate excitons, which in turn is electrical conductivity and morphology in the BHJ film. The maximum electric power produced by the illuminated OPV (P_{max}), which is obtained by plotting the maximum power curve (red curve in Fig. 2.17) against the photo-voltage (V). This value is primarily determined by the band gap and material absorption coefficient, the exciton diffusion at the donor/acceptor interface. Secondly, I_{sc} furthermore depends on the carrier mobility in the D and A phases, as well as, on their morphology and electrical conductivity in the BHJ film. The maximum electric power formed by the OPV cell under illumination is the maximum of the power curve (Pmax) and corresponds to the maximum power point (MPP) in the (I-V) curve. The cell generates a certain I_m under a voltage of V_m at the MPP. The ratio between the maximum power obtained by the cell ($I_m \cdot V_m$, or P_{max}) and the theoretical maximum power that could be obtained from the cell ($I_{sc} \cdot V_{oc}$) is referred to as the FF, calculated as:

$$FF = \frac{P_{max}}{I_{sc} * V_{oc}} \tag{2.31}$$

Therefore, the FF is a measure of a photovoltaic cell performance. This actually represents the deviation of the I-V behaviour of the cell from ideality. These variations are appreciably affected both by the ideality factor (ξ) of the cell and also by its electrical resistances, namely the series resistance (R_s) and the shunt resistance (R_p). Increasingly higher R_s and lower R_p lead to lower FF and thus lower cell efficiencies. Approaches for reducing contact resistance (hence lowering R_s) include the precise selection and processing of the electrodes (for example using of gold instead of silver or aluminium top contacts) and inserting buffer layers (e.g. MoO_3) between the photo-active layer and top metal contact. Strategies used to decrease shunt currents (R_p) include improving the morphology of the BHJ (for example introducing ordered vertically aligned inorganic nanowire structures as is the case in this study) as well as fine-tuning the energetic and kinetics involved in the charge separation process. Usually both of these approaches are used to maximise both FF and efficiency of the cells. The power conversion efficiency (PCE) of a solar cell is the ratio of the power output (P_{max}) of the cell to the incident power from the sun, or other illuminating species (P_L), measured in $W.m^{-2}$. This is summarised in equation (2.32) as:

$$PCE = \frac{P_{max}}{P_L} = \frac{J_{sc}.V_{OC}.FF}{P_L} \quad (2.32)$$

The PCE is measured under standard solar cell testing conditions of temperature = 25 °C, incident P_L = 1000 W.m^{-2} and air mass = 1.5 (AM1.5). The air mass refers to the thickness of the atmosphere; at the equator the air mass = 1, whereas in Europe it is approximately 1.5.

2.4.2 Device Fabrication – Patterned Substrate Preparation. ZnO nanowire based solar cells were fabricated on patterned ITO substrates (Ossila, UK), as shown schematically in Fig. 2.18 (a). The glass/ITO/ZnO NWs (synthesis discussed in Chapter 2.1.5) and subsequent plasma-irradiated ZnO NWs (Chapter 2.3.5) form the ETL in the final device architecture. For TiO_2 based devices, FTO coated substrates were used and etched into the patterns shown in Fig. 2.18 (b). The patterning was done by taping off the desired pattern on the FTO with 3M tape and placing zinc powder on the exposed areas. This was followed by carefully dropping hydrochloric acid on the zinc powder to initiate the etching process; the template was patterned for 30 seconds up to 1 minute depending on the completeness of the etching process. Once done, the substrates were rinsed immediately with deionised water to remove the acid residue. The final cleaning process was done in an ultrasonic bath for 5 minutes at temperature of 70˚C with Hellmanex solution, followed a final isopropanol clean under ultrasound agitation.

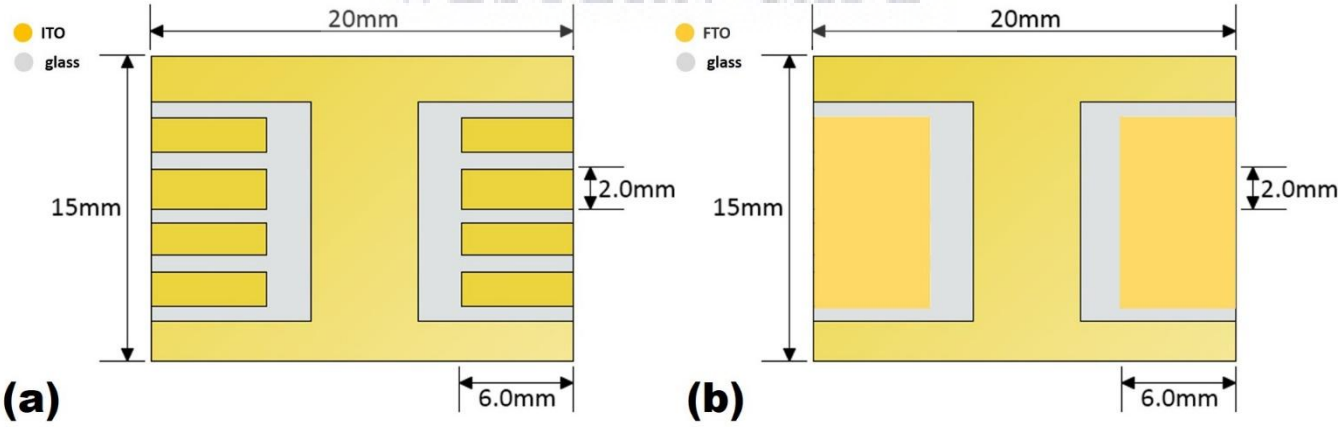

Fig. 2.18: Schematic of (a) the patterned ITO substrate used for ZnO based solar cells (Ossila, UK) and (b) in-house patterned FTO substrates.

2.4.3 Device Fabrication – Photoactive Layer Preparation. After the cleaning of the patterned substrates, hydrothermal synthesis and plasma irradiation of the nanowires, an optimised blend of P3HT to PCBM weight ratio of 1:1, as reported by Chirvase et al. [2.40] and Reyes-Reyes et al. [2.41], was prepared as follow. The precursor solution was prepared by stirring 15 mg.ml^{-1} P3HT and 15 mg.ml^{-1} PCBM in 1,2 dichlorobenzene at 70°C overnight using a Corning PC-4000 magnetic hot-plate stirrer at a rotational speed of 350 rpm. The as-prepared P3HT:PCBM blend was deposited on top of the glass/TCO/compact layer/NWs structure by spin coating a 30µl drop of the mixed semiconductor solution, delivered on the middle of the substrate, using a two-step process at 1000 rpm for 10 seconds, followed by 2000 rpm for 60s. The film was cured by drying the substrate at 90°C for 30 minutes, followed by natural cooling to room temperature, a second anneal at 120 °C for 20 minutes, another cool down to room temperature, before the final anneal at 150 °C for 20 minutes and cool down to room temperature. The resulting blended film was ~100 nm thick as established by profilometry.

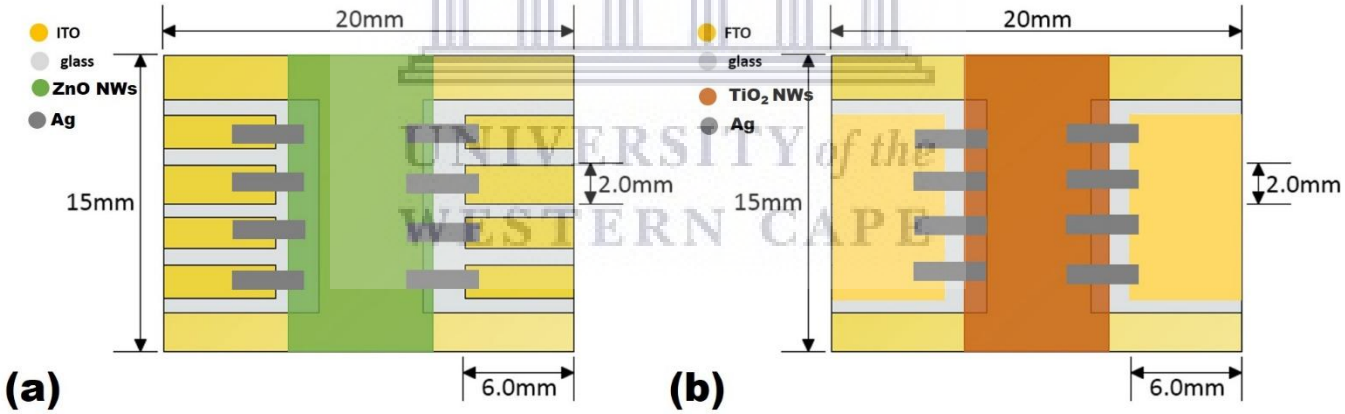

Fig. 2.19: Schematic representation of a fully assembled (a) ZnO NW and (b) TiO_2 NW based organic solar cell

2.4.4 Device Fabrication - Hole Transport Layer and Top Contact Synthesis. The deposition of the photoactive layer onto the nanowire arrays was proceeded by deposition of the HTL, consisting of a thin layer of molybdenum oxide (Mo_xO_y), by thermal evaporation. The device manufacturing was concluded by depositing a top silver (Ag) contact, also by thermal evaporation. Molybdenum (IV) oxide (MoO_2) powder, purchased from Sigma

Aldrich, was used for the fabrication of the MoOx HTL. The thin film of MoOx was deposited by placing about 10 mg of the MoO_2 powders in molybdenum boat and loading into the thermal evaporation chamber of the CADAR system. The chamber was pumped down to a base pressure of 6.5 × 10-6 mbar, before the evaporation started and throughout the process the working pressure was retained at 1×10^{-5} mbar. The evaporation rate of 0.5 $Å.s^{-1}$ was used for the deposition of the evaporated MoOx thin film, and nominal thickness of the deposited film of 10 nm achieved. The Veeco Dektak profilometer was employed to confirm this thickness and the results are in close conformity with the quartz-crystal monitor which is part of the CADAR system. Also, the distance between the source and the substrate was approximately 12 cm so as to obtain a homogeneous thin film. For the deposition of the Ag top contact, a deposition rate of 0.5 $Å.s^{-1}$ was maintained to obtain a 100 nm thickness at base pressure of 6.5×10^{-6} mbar. Hereafter the devices were ready for performance testing.

References

[2.1] K. Byrappa, S. Srikantaswamy, Progress in Crystal Growth and Characterisation of Materials 21 (1991) 199 – 254.

[2.2] K. Byrappa, M. Yoshimura, Handbook of hydrothermal. Technology, Noyes Publications, NJ, USA (2001).

[2.3] K. Byrappa, Journal of the Ceramic Society of Japan 117 [2009] 236-244

[2.4] A.F Wells, Structural inorganic chemistry, 4th ed. Clarendon Press: Oxford, U.K. 1975.

[2.5] J. Li, Q. Wu, J. Wu, Synthesis of Nanoparticles via Solvothermal and Hydrothermal Methods.In: Aliofkhazraei M. (eds) Handbook of Nanoparticles. Springer, Cham. (2016).

[2.6] C.C. Manole, C. Julcour-Lebigue, A. Wilhelm, H. Delmas, Ind. Eng. Chem. Res. 46 (2007) 8388-8396.

[2.7] S. Komarneni, K. Byrappa, Materials Research Innovations 15 (2010) 348-350.

[2.8] R.A Caroline, P. Luciano, B. Azevedo, Journal of Endodontics 34 (2008) 859-862.

[2.9] D.T. Cromer, K. Herrington, J. Am. Chem. Soc. 77 (1955) 4708 – 4709.

[2.10] H. Cheng, J. Ma, Z. Zhao, L. Qi, Chem. Mater. 7 (1995) 663-671.

[2.11] B. Liu, E.S. Aydil, J. Am. Chem. Soc. 131 (2009) 3985-3990.

[2.12] J. Kalb, A. Folger, C. Scheu, L. Schmidt-Mende, Journal of Crystal Growth 511 (2019) 8–14

[2.13] G.V. Wulff, Zeitschrift für Krystallographie und Mineralogie 34 (1901) 449–530

[2.14] A. Wisnet, S.B. Betzler, R.V. Zucker, J.A. Dorman, P. Wagatha, S. Matich, E. Okunishi, L. Schmidt-Mende, C. Scheu, Cryst. Growth Des. 14 (2014) 4658−4663.

[2.15] A. Ali, A.R. Phull, M. Zia, Nanotechnol. Rev. 7 (2018) 413–441.

[2.16] C. Chevalier-César, M. Capochichi-Gnambodoe, Y. Leprince-Wang, Appl Phys A: Mat Sci Process 115 (2014) 953 – 960

[2.17] X. Feng, K. Shankar, O.K. Varghese, M. Paulose, T.J. Latempa, C.A. Grime, Nano Lett. 8 (2008) 3781-3786

[2.18] [www.ossila.com] Site visited on the 9th August 2020.

[2.19] J. Chang, S. Lee, K.B. Lee, S. Lee, Y. T. Cho, J. Seo, S. Lee, G. Jo, Ki. Lee, H. Kong, S. Kwon, Review of Scientific Instruments 86 (2015) 055108

[2.20] T. Arai, G. Baker, C. Bates, B. Becherer, Heat Treating, Vol 4, ASM hand book, ASM international 1991.

[2.21]. J.V Daniel, Pulsipher, Investigating Plasma Modifications And Gas-Surface Reactions of TiO_2-Based Materials for Photoconversion, PhD Dissertation submitted to Colorado State University, Fort Collins, Colorado, 2012
[2.22] W. Kruer, The Physics of Laser Plasma Interaction published by CRC Press, 2003.
[2.23] L. Spitzer, Physics of Fully Ionized Gases, Inter-science Publishers, New York, 1962.
[2.24] J.M. Dawson, M.B. Gottlieb, Introduction to Plasma Physics, Lecture Notes, Princeton University, Princeton, 1964.
[2.25] F.F. Chen, Introduction to Plasma Physics, Plenum Press, New York, 1974.
[2.26] G. Schmidt, Physics of High Temperature Plasmas, Academic Press, New York, 1966.
[2.27] T.H. Stix, The Theory of Plasma Warns, McGraw-Hill, New York, 1962.
[2.28] J.M. Dawson, Phys. Fluids 5 (1962) 445.
[2.29] R.L Morse, C.W. Nielsen, Phys. Rev. Letters 23 (1969) 1087.
[2.30] B.H. Saunders. J. Colloid Interface Sci, 369 (2012) 164–169.
[2.31] W. Cai, X. Gong, Y. Cao, Solar Energy Mater Solar Cells 94 (2010) 114–127.
[2.32] G. Garcia-Belmonte, A. Munar, E.M. Barea, J. Bisquert, I. Ugarte, R. Pacios, Org Electron, 9 (2008) 847–851.
[2.33] R. Kisslinger, W. Hua, K. Shankar, Polymers 9 (2017) 35.
[2.34] M. Wright, A. Uddin, Solar Energy Materials and Solar Cells 107 (2012) 87–111
[2.35] G. Yu, J. Gao, J.C. Hummelen, I.F. Wudl, A. Heeger, Science 270 (1995) 1789–1791
[2.36] W. Shockley, H. Queisser, J. Appl. Phys. 32 (1961) 510.
[2.37] S. Yamamoto, A. Orimo, H. Ohkita, H. Benten, S. Adv. Energy Mater. 2 (2012) 229.
[2.38] J. C. Blakesley, D. Neher, *Phys. Rev. B*, 84 (2011) 075210.
[2.39] K. Vandewal, K. Tvingstedt, A. Gadisa, O. Inganäs, J. V. Manca, *Nat. Mater*. 8 (2009) 904.
[2.40] D. Chirvase, J. Parisi, J.C. Hummelen, V. Dyakonov, Nanotechnology 9 (2004) 1317.
[2.41] M. Reyes-Reyes, K. Kim, D.L. Carroll, Applied Physics Letters 8 (2005) 083506.

CHAPTER THREE

CHARACTERISATION TECHNIQUES

This chapter will centre on the physical principles behind the instruments used to characterise the nanowire arrays as well as the testing methodology of the fabricated solar cells. The characterisation of the nanowires can be classified into optical and structural, with the optical techniques comprising of ultraviolet-visible and photoluminescence spectroscopy, whereas the structural techniques encompass electron microscopy and x-ray diffraction. The third class of techniques probe the doping characteristics and consist of electron energy loss spectroscopy and x-ray photoelectron spectroscopy. The chapter will conclude by giving a brief overview of the instrumentation used to test the PV cells.

3.1 Optical Characterisation

3.1.1 Ultraviolet-Visible Spectroscopy. Fundamentally, the absorption edges of both semiconductors and insulators are either near-infrared, visible or ultraviolet spectral region. From the onset the optical transition across fundamental band gap (E_g) of any material is due to the existence of absorption edge. Thus, ultraviolet–visible (UV-vis) spectroscopy, aid in studying of the fundamental absorption edge situated in the in the UV to visible wavelength range. Fig. 3.1 presents a simple energy diagram of two separated bands in a solid. The band gap refers to the gap in energy between two bands. However, only the selection rule, permit the inter-band transitions across E_g. The lower band is normally known as the valence band, while the top band is referred to as the conduction band. Furthermore, the valence band edge is known as E_v and the conduction band edge is referred to as E_c. Normally, an electron jumps from the lower energy band to the higher energy band above it during transition by absorbing photons. This takes place only when there is an electron in the initial state in the lower band. Relating the law conservation of energy to the interband transition presented in Fig. 3.1 results in:

$$E_f = E_i + \hbar\omega \quad (3.1)$$

where E_i the energy of the electron is in the lower band, E_f is the energy of the final state in the upper band and $\hbar\omega$ is the photon energy occupied lower band and a final state at energy E_f in an empty upper band. Eg is the energy variation between the two bands [3.1].

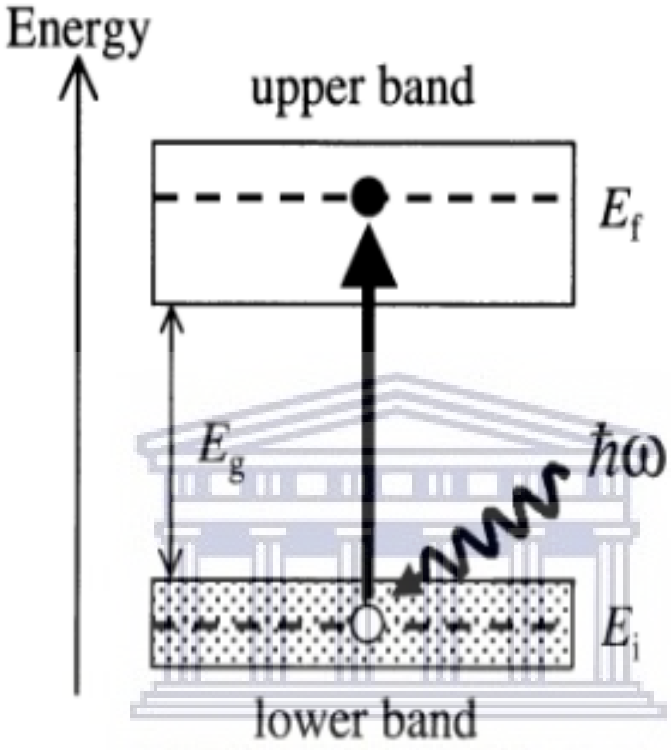

Fig. 3.1: The inter-band optical absorption sandwiched between an initial state of energy $\boldsymbol{E_i}$ in an occupied lower band and a final state at energy $\boldsymbol{E_f}$ in an empty upper band. The energy difference between the two bands is E_g [3.2]

The valence band of an initial state's energy E_i became unoccupied during electron excitation. This process of inter-band absorption results in the creation of a "hole" at the initial state and an electron in the final state; these may simply refer to as creation of an "electron–hole pairs". The band gap of a material is classified as either direct or indirect, as shown by the energy band diagram of Fig. 3.2.

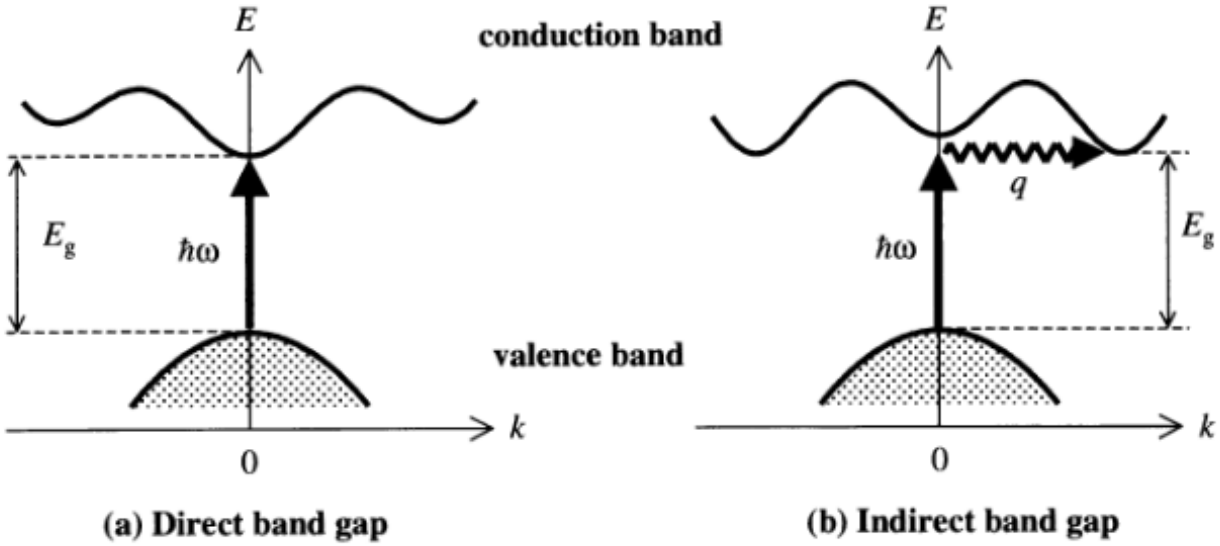

Fig. 3.2: Interband transitions in (a) direct band gap and (b) indirect band gap materials [3.2].

For a direct band gap material, the Brillouin centre at $k = 0$ is where the valence band maximum and conduction band minimum coincides, however, for the indirect band gap material, at $k = 0$ the maximum and minimum do not coincides, but do so at some value for k close to the zone edge.

However, during a photon absorption process, conservation of momentum takes place only when the electron wave vector, **k**, remains significantly the same. Furthermore, Fig. 3.2 (b) shows that in transiting from valence band to the bottom of the conduction in indirect band gap, the value of **k** must change significantly. Thus, it's impossible for transition by absorption to take place with only photon; a phonon must be engaged to conserve momentum. This is a clear distinction with direct band gap material, where the transition process may take place without involving a phonon.

3.1.1 (a) UV-vis Diffuse Reflectance Spectra. Diffuse reflectance spectroscopy (DRS) is a useful technique for optical characterisation of different types of materials that are not transmitting in the UV-vis- NIR spectral ranges [3.4] and is a measure of the change between incident and back scattered light intensity related to absorption and scattering process. The reflectance of a given sample at any particular wavelength is comprised of two components; either regular or specular (mirror) reflectance and or diffuse (volume or non-directional) reflectance. Thus, DRS depend mainly on the projection focus of the spectrometer beam on

the sample, wherever it reflects, scattered and transmitted through the sample, this diffusedly scattered light, alongside the back reflected light are collected by the accessory and finally directed to the detector of the spectrometer. But occasionally, the sample may absorb part of the incident light, this part of the incident beam undergoes scattering within the sample and return to the surface of the sample, this process referred to as diffuse reflectance. The component of specular reflectance in diffused reflectance light, may be contributed partly to change in bands shape and its relative intensity, these processes are in agreement with laws of geometrical optics. When a sample absorbs a light beam, it then follows Lambert-Beer absorption law [3.5]:

$$I = 10e^{-\alpha t} \tag{3.2}$$

where, 'I' is the transmitted radiation from an initial flux '10' passage through a layer of thickness 't' of a sample, which has an absorption (or extinction) coefficient 'α' measured in transmittance [3.6]. But if the sample size is smaller in respect to the beam cross section, and larger in relative to the wavelength of light, then there is a probability of optical diffraction. The NWs samples are such a small nano-sized structure of randomly distributed particles. Therefore, a part of the incident radiation returns back at all cost to the original point of radiation. Hence, this process of reflection aiding reflection, diffraction refraction and absorption by particles coming from all direction is referred to as diffused reflection [3.5, 3.6]. As the light falls on a glass sample, it reflects from virtually all directions due to variation of the NWs and surface reflection of the glass sample. Some portion of light reflected as it enter the glass surface with NWs, is scattered due to nature of the NWs, and also because of internal reflection, more so, reflection from the surface of the other NWs or repeated refractions. Furthermore, some of the scattered light goes back into the air medium. When the diffuse reflected light is transmitted through the glass, it becomes weaken and could be absorbed by the NWs [3.2]. Though diffuse reflected spectrum and transmission spectrum are similar, the K-M function ($F(R\infty)$) derived by Kubelka-Munk is used for comparison to transmission spectra or quantitative analysis [3.4].

$$F(R\infty) = \frac{(1-R\infty)^2}{2R\infty} = \frac{K}{S} \tag{3.3}$$

where $F(R\infty)$ is known as Kubelka-Munk (K-M) function or remission function, where the absolute reflectance is '$R\infty$', the absorption coefficient is 'K' and the scattering coefficient is 'S'. However, there is no difficulty in measuring the absolute reflectance '$R\infty$', the estimated band gap of material is obtained by the plotting of $((\frac{K}{S})\hbar\upsilon)^2$ versus $\hbar\upsilon$ (where $\hbar\upsilon$ is the photon energy) by extrapolating the graph to the x-axis.

3.1.1 (b) Band Gap Analysis. The band gap is obtained usually from the absorption edge energy, which is defined to be the minimum photon energy necessary to excite an electron from E_v to the E_c. Basically there are two types of transitions - direct and indirect. The optical band gap of the grown vertically aligned TiO_2 and ZnO NWs films are evaluated from the transmission spectra of the TiO_2 and ZnO NWs grown on the FTO substrates. The determination of the optical band gap is achieved by extrapolation of Tauc's plot [3.3] from

$$(\alpha h\upsilon)^{\frac{1}{n}} = B(h\upsilon - Eg) \tag{3.4}$$

From the equation above, when n=1/2 is for direct allowed transitions, but n=2 is for indirect allowed transitions, but B is a constant independent of energy and h is Planck's constant, while hυ is the photon energy, but α is the absorption coefficient. To obtain the bandgap by extrapolation of Tauc's plot, then the value of α must be known,

$$\alpha = \left(\frac{1}{t}\right) ln\left(\frac{1}{T}\right) \tag{3.5}$$

where t is the cross-section thickness of NWs and T is the transmittance. Meanwhile, the graph is plotted of (αhυ) 1/n versus (hυ), n = 1/2 for direct allowed transitions. While the extrapolation yields a good straight-line fit to the absorption edge and provides the optical band gap value on the hυ axis. In the case of opaque NWs structures, however, the absorption is determined from the K-M function and thus $F(R\infty)$ is substituted for α in equation 3.3. In this study, UV-Vis spectroscopy was performed with a Cecil Aurius UV-VIS-NIR Spectrophotometer Unit 2021, operated between 200 and 900 nm. The instrumentation is shown in Fig. 3.3 and is hosted by the Materials Research Division, iThemba LABS, Cape Town.

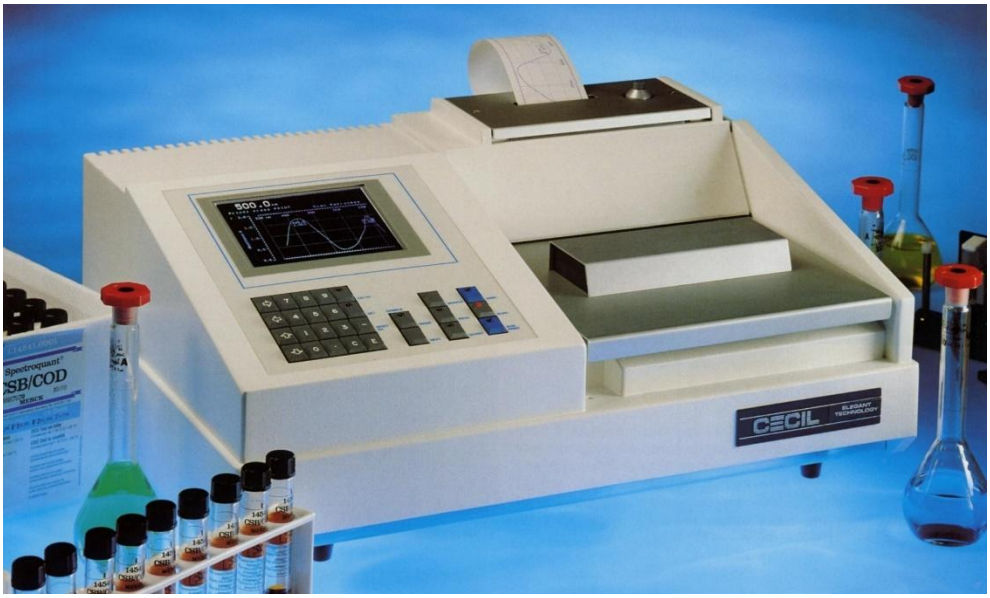

Fig. 3.3: Image of the Cecil Aurius UV-vis-NIR Spectrophotometer used to characterise the optical properties of the TiO_2 and ZnO NWs.

3.1.2 Photoluminescence. Photoluminescence (PL) spectroscopy refers to a physical process in which emission of light from a material occurs spontaneously under optical excitation or occurs when atom emits light by spontaneous emission, and the electrons in excited states drop down to a lower level by radiative transitions. The technique is non-destructive and sensitive making it a very useful method for probing the discrete electronic structure material without any electrical contact [3.7]. Furthermore, PL has also been proven to be a very important technique for characterisation of optical energy bands of materials and donor/acceptor states, study of surface states and also for structure-induced trapping states present within the band gap of material.

It is well known that the change in size of nanomaterials has a significant effect on PL spectra. The PL emission spectrum can be used to recognise the surface, interface, and also impurity levels in a nanomaterial. The information and quality of surfaces and interfaces depends on the intensity of the PL. The transient PL intensity offers the full information about the lifetime of non-equilibrium interface and bulk state through the use of pulsed excitation sources. Furthermore, the variation in the PL intensity with regards to the temperature depends on the thermal activities of the physical phenomenon in the material. The sample absorbs the incident light, while the excess energy is then used for photo-

excitation. The sample therefore releases the energy through light emission, or luminescence [3.8]. The electrons are lifted from the material due to the photo-excitation, and then moved into permissible excited states. These excited electrons return to their equilibrium states by releasing the excess energy in photon form. The electrons relaxation processes that form the excited to normal states are either radiative or non-radiative process, as shown in Fig. 3.3. In a radiative process, the emitted light's energy originates from the difference in levels of energy between the two electronic states. The radiative process has direct contribution on the amount of the emitted light, and different phenomena exist for each emission process. A photon of each individual wavelength is absorbed and immediately the same amount of photon energy is released in resonant radiation process, these occur within a time of 10 nanoseconds. However, during non-radiative processes, if a material went through internal energy transition processes before relaxing to its ground state by emitting photons, part of this absorbed energy is dissipated, such that the emitted light photons are of lower energy than those absorbed in fluorescence, with shorter lifetime (10^{-8} to 10^{-4}s). Fig. 3.4 presents a schematic diagram of PL emission of the samples.

If the band gap energy is less than the photon energy, the photon is can be absorbed, thus, raising an electron from the valence band to the conduction band transversely through the forbidden energy gap in a semiconductor material [3.8]. The electron may fall down after the photo-excitation process, and lost energy is converted back into a luminescent photon, thereby emitted from the material. The band gap energy is thus a direct measure of the photon emitted energy.

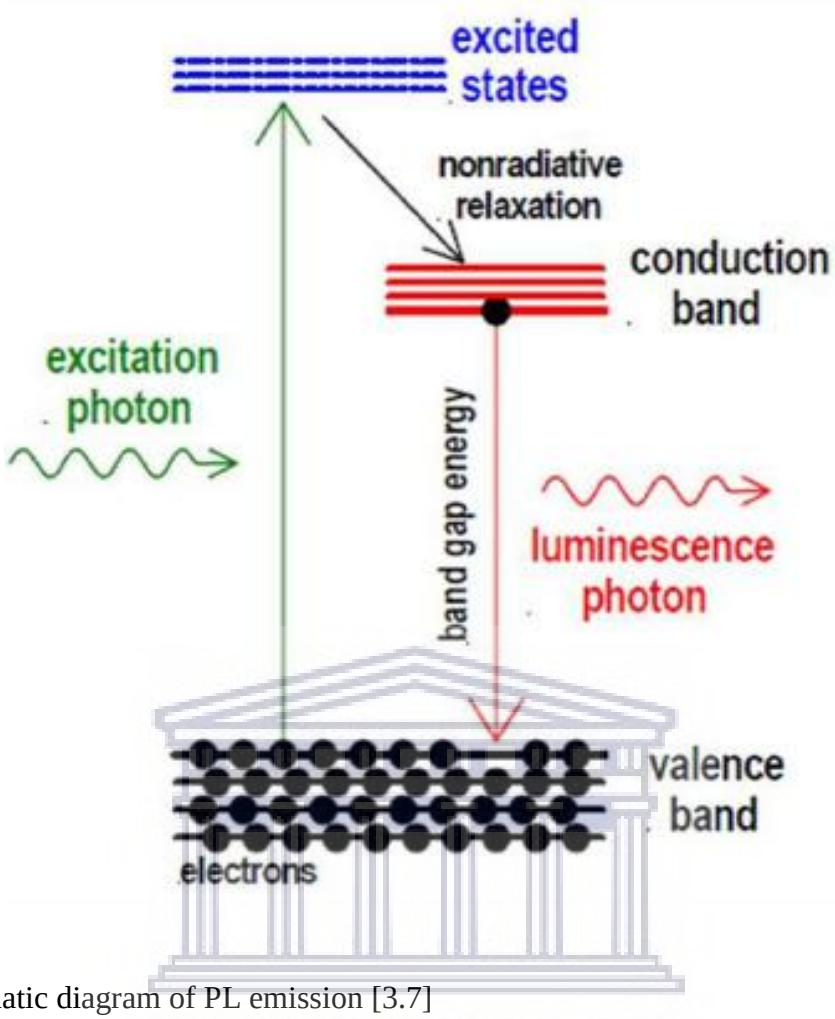

Fig. 3.4: Schematic diagram of PL emission [3.7]

In practical semiconductor materials, during an extrinsic optical process of applying an external light with energy $\hbar\upsilon \geq E_g$, denoting the band gap energy by E_g, and observing the re-emitting photons, the major photoluminescence measurement features are [3.10]:

- To investigate the recombination mechanism and identification of surface, interface and impunity level of material.
- To investigate the general radiative transitions in semiconductor occurring between states of conduction and valence bands, with E_g as the equivalent energy difference between then, and the PL techniques is then determined easily with band gap results of the semiconducting material.
- Also the amount of radiative recombination can be used to quantify the quality of material. Because the majority of the non-radiative recombination is connected to localised defect levels that are disadvantageous to the device performance.

Occasionally radiative also contributes to the take part of localised defect; the associated PL energy to the levels can be used to identifying the specific defects.

- Also, detail information about the material deep energy states are obtained, due to radiative transition giving a very wide and strong phonon coupling.

In the present work, room temperature PL of the samples was measured on Horiba Jobin Yvon Lab Ram HR system with Ar-ion laser (514.5 nm) as the excitation source, as shown in Fig. 3.5 and hosted by the Sensors Laboratories, Department of Chemistry, University of the Western Cape, Cape Town.

Fig. 3.5: Horiba Jobin Yvon photoluminescence system used to characterise the photo-electrodes developed in this study.

3.1.3 Photoluminescence Quenching. The atmosphere surrounding a P3HT:PCBM (chromophore) combination is of primary importance, as it can produce other decay channels inducing a decrease of the photoluminescence intensity (for instance the photoluminescence quantum yield). This phenomenon is usually called PL quenching, and it can be caused by a variety of different processes. The two common types of quenching are static, and collisional (dynamic) quenching. They can be caused, for instance, by impurities left by the synthesis of the conjugated system. However, in both cases the chromophore must come into closes contact with the quencher. The Collisional quenching takes place only when a chromophore

in the excited state comes into closes contact with a quencher. However, this process needs the quencher to diffuse toward the chromophore, while the latter is still in its excited state. As an example, we can use molecular oxygen. Actually, O_2 is one of the most renowned and studied quencher, and the almost certainly the mechanism is that as the oxygen causes intersystem crossing in the chromophore, which in tune diminishes the fluorescence quantum yield and then inducing phosphorescence that is typically absent at room temperature, which decreases the overall photoluminescence [3.9]. This is why most of the photoluminescence quantum yield measurements are done in N_2 atmosphere. However, the static quenching involves instead the formation of non-radiative complexes in the ground state between the quencher and the chromophore. In this case the quenching is not dynamic and does not depend on the life time of the excited state as for collisional quenching. Thus, we can imagine the quencher as a chemical compound added directly to the chromophore solution and so, the quenching intensity depends directly from the amount of quencher in the environment surrounding the chromophore.

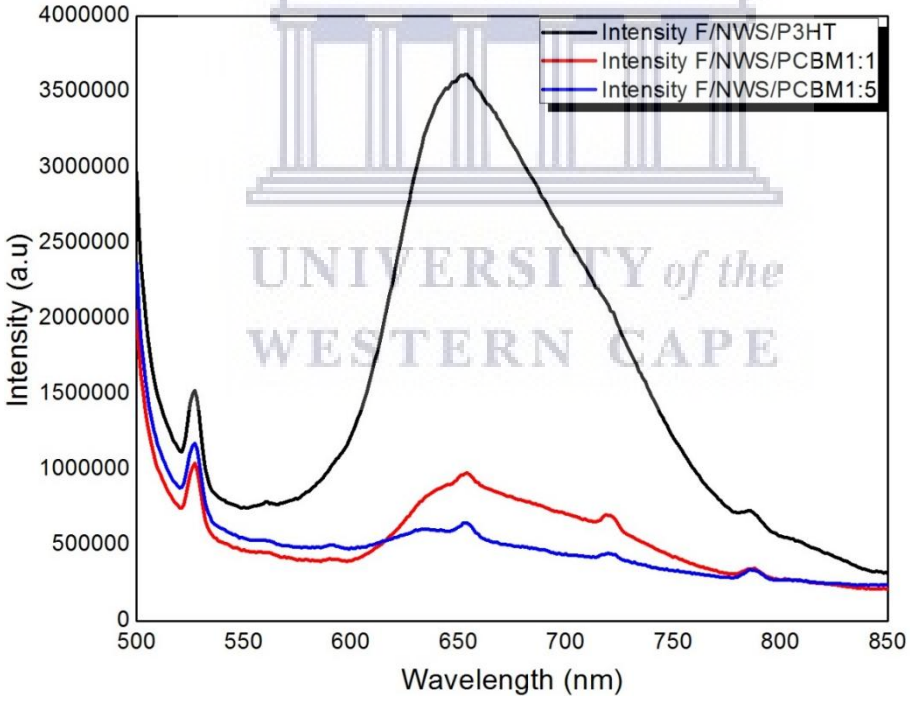

Fig. 3.6: PL showing different quenching behaviors of P3HT:PCBM blends with NWs as ETLs

So, both dynamic and static quenching requires the diffusion of the quencher toward the chromophore, i.e. they are common in solutions or liquid phases. But in solid state, both these

types of quenching are still present, but the diffusion range is very much lower than in a solution. Nonetheless, the effect of molecular aggregation (i.e. concentration quenching) is usually much stronger than in solution. Molecular aggregation is caused by intermolecular Van der Waals-like forces between the molecules and they exhibit distinct changes in the absorption and emission spectrum with respect to the monomer. Fig. 3.6 shows a typical PL spectrum with the different quenching behaviours due to photo-excitation in P3HT-PCBM layers, as will be discussed in Chapter Four.

3.2 Structural Characterisation – X-Ray Diffraction

3.2.1 Background. The XRD technique is a powerful non-destructive characterisation tool widely used in material science. The technique is used for both quantitative and qualitative phase identification. It is a fingerprint characterisation method used for the determining crystalline structure of the materials. Virtually all solid crystalline materials have their own unique characteristics, thus the identification of any particular material can be achieved with XRD patterns [3.10]. The crystal structures are one of the major information that can be obtained from the diffraction techniques others are how the atoms are placed in the crystalline states, the inter-atomic distance between the atoms and the angle between the atomic bonding. X-ray diffraction analysis is used to identify the state of chemical combination of the elements in a particular phase. Thus, the obtained information from a particular material is mainly related to its crystalline structure rather than other factors. But, XRD investigation offers a whole range of detailed information about crystal structure, average crystalline, orientation and the stress in material. When a crystalline material is hit by a beam of X-rays, the electrons in the region of the atoms in the material oscillate with the same frequency of the incoming X-ray beam. The atoms are normally arranged in a regular pattern in a crystal lattice, causing a few constructive interferences along their directions. A precise x-ray beam departing from the sample to various directions and the wave are in the same phase, although a diffracted beam consisting of scattered rays are mutually reinforcing one another [3.11]. Meanwhile, the diffraction effect is as result of scattering from the periodic atomic arrays, the scattering characterised in terms of sample expression which is refers to as the Bragg's Law. It is the fundamental law concerned in the diffraction method of structured analysis sandwiched between the scattering angle, the spacing between the plane of atoms and the

wavelength of the radiation. However, the distance between the atomic planes are reliant on the size, distribution of atoms and the structure of the material [3.10, 3.11].

Fig. 3.7: A pictorial representation of the PANalytical Empyrean diffractometer used in this work.

In this study, grazing incidence X-ray diffraction (GIXRD) patterns were recorded using a PANalytical Empyrean diffractometer with CuKα radiation (λ=1.5406A˚) as X-ray source, operated at 45 kV, 40 mA. The incident beam was kept at 0.4 degrees with respect to the substrate, with a 2θ range from 10 to 90 degrees (0.02 degrees step size at 2 seconds per step). The incident beam optics comprised of a parabolic mirror, 4 mm mask, 1/16 divergence and 0.04 radians Soller slit; the diffracted beam optics included a parallel plate collimator slit, 0.04 Soller collected by a PIXcel3D 55 μm2 (256 x 256 pixels) x-ray detector. To correct for the instrument broadening and peak position calibration, a large area LaB_6 standard was used. This system is shown in Fig. 3.7 and is hosted by the Surface Characterisation Unit of the Metrology Institute of South Africa, Pretoria. The GIXRD technique was used because the conventional XRD experimental θ/2θ set-up yielded a week signal from the TiO_2 and ZnO NW films and an intense signal from the substrate. GIXRD is a proven technique to avoid intense signal from the substrate and is performed by a 2θ scan with a fixed grazing angle of

incidence. The fixed angle is chosen to be slightly above the critical angle for total reflection of the film material; in this study this was determined at 0.4 degrees to the TCO substrate.

3.2.2 Theory. In crystalline material, the atoms are arranged in three-dimensional ways called the crystal lattices. A crystalline can be understood to be made up of a number of crystal planes. An X-ray beam is incident on a surface crystal, the atoms of the crystal occupying definite positions in the crystal lattice act as a scattering X-ray centre. Thus, X-rays being scattered from different atoms reinforce each other underneath certain conditions and scattered X-rays come out different directions. These scattered waves can be regarded as reflected or diffracted wave. Furthermore, certain crystal planes in the atoms will be rich and from these crystal planes we obtain scattered waves of large intensities. Considering a crystal were the crystal planes are at a distance 'd' apart as presented in Fig. 3.8. The parallel X-rays beams are incident on the crystal surface at 'θ' angle. We obtain scattered wave BC corresponding to the incident wave AB, where the wavelength of X-ray 'λ' and the inter-planar distance is 'd'. Fig. 3.8 presents the illustration of Bragg's diffraction.

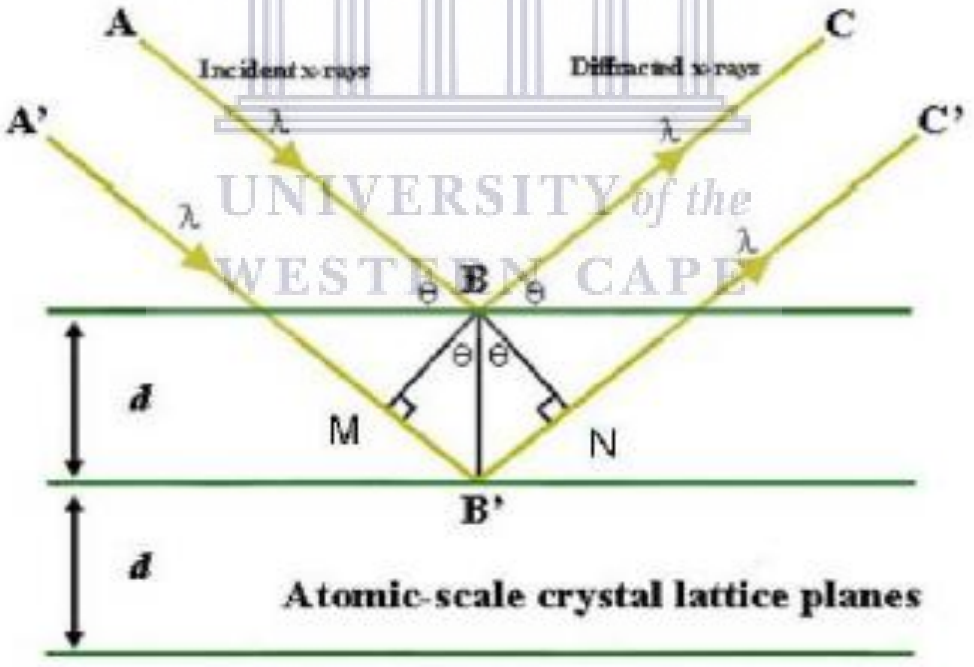

Fig. 3.8: llustration of Bragg's diffraction [3.11].

But a different wave along different wave along A′ B′ is incident on the next layer of atoms and is scattered along B′ C′. In addition, both reflected waves BC and B′ C′ support each other to produce a tough reflected X-ray, however the path difference between then is

equivalent to the product of wavelength of X-ray and an integer 'n' (n. λ). To get the path divergence draw BM and BN. Thus the path divergence sandwiched between BC and B′ C′ is MB′ +B′ N.

For triangle BB′ M

$$\frac{MB'}{BB'} = Sin\ \theta \qquad (3.6)$$

Therefore $MB' = BB'\sin\theta = d\sin\theta$, since BB' is the interplanar spacing, d. Likewise from triangle BB′N, $B'N = d'\sin\theta$. Thus, for reinforcement or to generate a reflected X-ray beam,

$$d\sin\theta + d\sin\theta = n\lambda, \text{ or}$$

$$2\,d\sin\theta = n\lambda \qquad (3.7)$$

Equation 3.7 is known as Bragg's Law of diffraction. The diffraction patterns obtained experimentally of samples are compared with those of the standard powder diffraction files published by the Joint Committee on Powder Diffraction Studies (JCPDS).

3.2.3 Scherrer Formulation for the Determination of Crystallite Sizes. An essential analytical instrument of XRD is its capacity to determine the crystal size of small crystallites, through analysing the width and intensity of a diffracted X-ray peak. The Bragg's Law of equation of 3.8 is made based on the assumption that the incident-ray beam consists of perfectly monochromatic and parallel radiation, which is rarely the case in reality. Supposing that the crystal has a thickness, t, measured in a direction perpendicular to a particular set of reflecting planes and have (m + 1) planes as shown in Fig. 3.9 below.

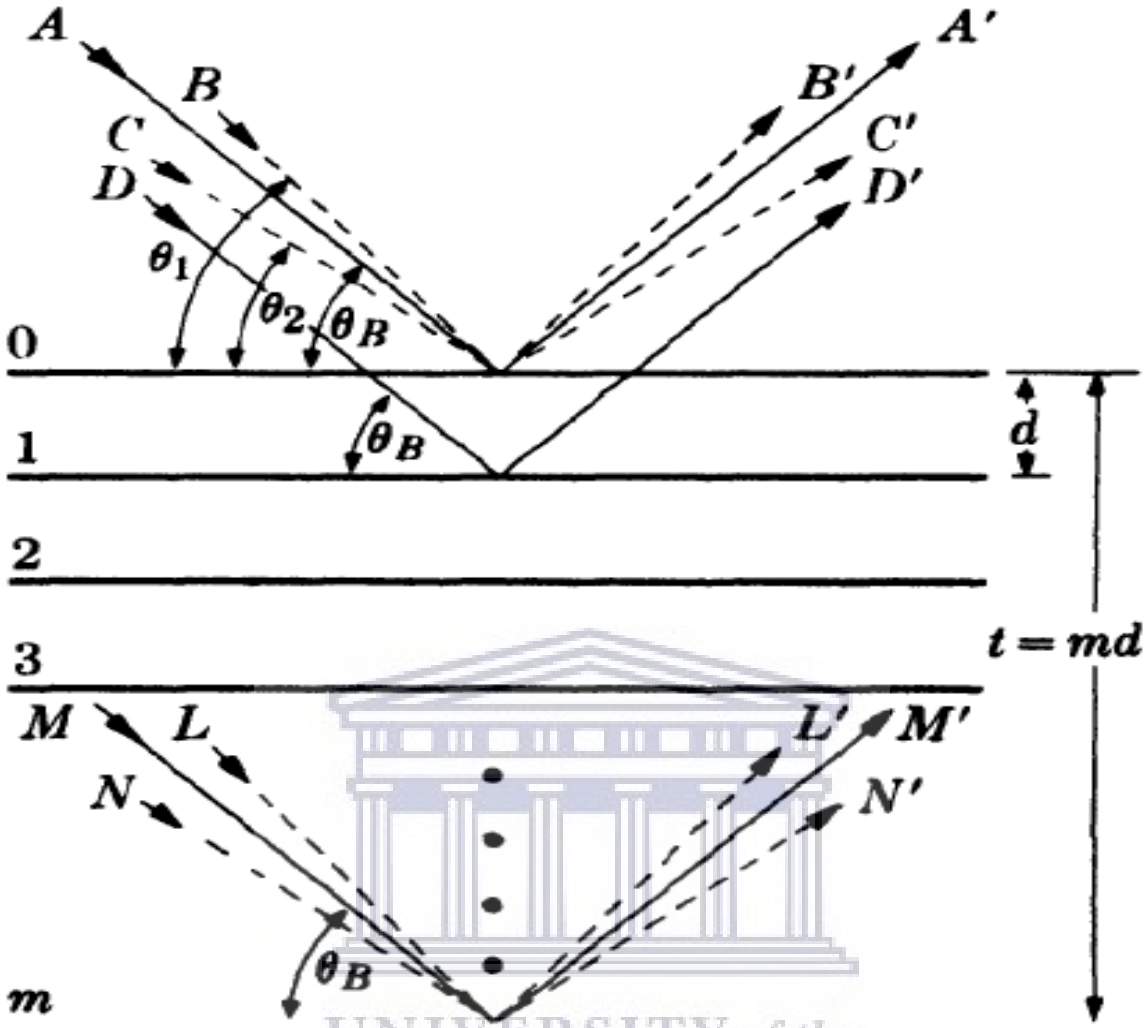

Fig. 3.9: Effects of crystal size on diffraction [3.12]

When the rays **A**, **D**,..., **M** are incident to the reflecting planes at angle θ_B of the crystal, then the scattering of the incident rays with the crystal planes takes place, with ray **D'** which is due to the scattering of ray **D** by the first plane below the surface. Thus this means that ray **D'** is one wavelength out of phase with ray A' and that ray M' that is scattered by the m^{th} plane below the surface is m wavelengths out of phase with A'. Hence, at the diffraction angle $2\theta_B$, the rays A', D',..., M' are totally in phase and interfere constructively to form a diffraction of maximum amplitude, i.e. a beam of maximum intensity, since the intensity is directly proportional to the square of the amplitude. But, when one considers incident X-rays at a little different angles from θ_B, it is found that destructive interference is not total. For instance, when the ray **B** make a little larger angle θ_1, such that ray **L'** that is scattered by the m^{th} plane below the surface is (m + 1) wavelengths out of phase with **B'**. Thus this means that

midway in the crystal there is a plane that scatters a ray that is half a wavelength out of phase with ray **B'**. Then, these planes cancel each other out and so do the other rays from similar pairs of planes throughout the crystal. Therefore the net effect is that, rays scattered by the top half of the crystal annul those scattered by the bottom half. The intensity of the beam diffracted at an angle $2\theta_1$ is however zero. It is also zero at an angle $2\theta_2$ where θ_2 is such that ray N' scattered by the m^{th} plane below the surface is (m – 1) wavelengths out of phase with ray C' from the surface plane. Therefore, it follows that the diffracted intensity at angles close to $2\theta_B$, and not more than $2\theta_1$ or less than $2\theta_2$ is not zero, but has an intermediate value between zero and the maximum intensity of the beam diffracted at an angle $2\theta_B$. Fig. 3.10 illustrates this relationship between the diffracted intensity and $2\theta_B$, and contrasts it to the ideal diffraction condition implied by Bragg's Law.

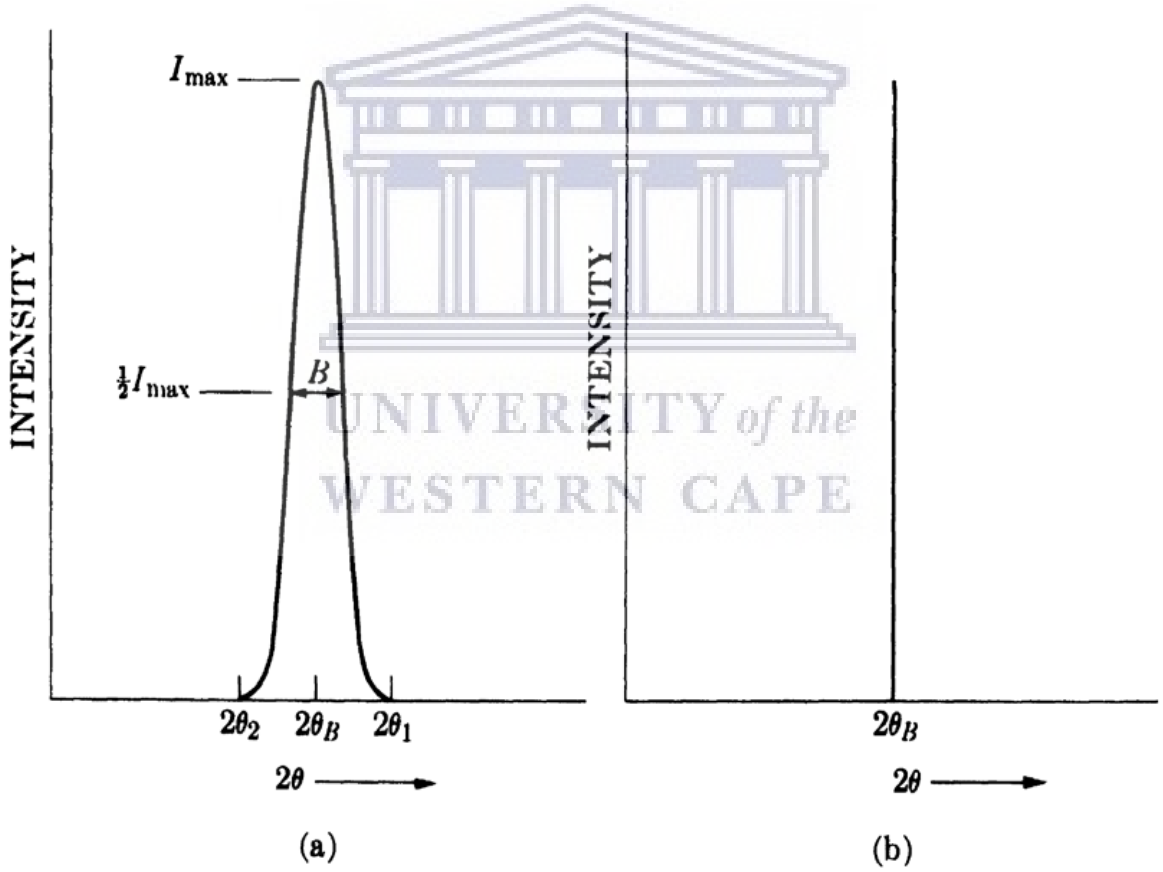

Fig. 3.10: Effect of crystal size on the diffraction curve under (a) real conditions and (b) ideal Bragg conditions [3.12]

Furthermore, the width of the diffraction curve of Fig. 3.8 (a) increases as the thickness of the crystal decreases. And the width B is typically measured in radians, at an intensity equal to

half the maximum intensity. As a rough measure of B, one can take half the difference between the two extreme angles at which the intensity is zero, i.e.:

$$B = \frac{1}{2}(2\theta_1 - 2\theta_2) = \theta_1 - \theta_2 \quad (3.8)$$

The path difference requirements from Bragg's law for these two angles indicates that

$$2t\sin(\theta_1) = (m+1)\lambda$$

$$2t\sin(\theta_2) = (m-1)\lambda \quad (3.9)$$

Subtracting the equations in from each other 3.9 gives

$$t(\sin(\theta_1 - \sin(\theta_2))) = \lambda \quad (3.10)$$

When trigonometric identities are used, equation 3.10 can be rewritten as

$$2t\cos\left(\frac{\theta_1+\theta_2}{2}\right)\sin\left(\frac{\theta_1-\theta_2}{2}\right) = \lambda \quad (3.11)$$

But, θ_1 and θ_2 are both very close to θ_B, and that means that $\theta_1 + \theta_2 = 2\theta_B$. So, by small angle approximation, $\sin\frac{\theta_1+\theta_2}{2} = \frac{\theta_1+\theta_2}{2}$ and this means that 3.11 can be rewritten as

$$2t\left(\frac{\theta_1+\theta_2}{2}\right)\cos(\theta_B)=\lambda \quad (3.12)$$

$\beta_{obs} = \frac{\theta_1-\theta_2}{2}$ can be assigned as the observed full-width half maximum intensity of the diffraction curve measured in radians. Note, thus far, the formulation of Scherrer equation assumes that observed peak broadening is only due to the crystallite size. In fact, that is not the case. An observed broadening of the diffraction peak consists of both the instrumental broadening (β_{instr}) and the crystallite size broadening (β_{Size}). To decouple these contributions, it is necessary to collect diffraction pattern from a line broadening of a known standard material such as silicon. When assuming a Lorentzian shape of the diffraction peak, the size broadening can be computed as

$$\beta_{Size} = \{\beta_{obs} - \beta_{inst}\} \quad (3.13)$$

Combining (3.12) and (3.13) results in the well know Scherrer formula (3.14) that is used to determine the crystallite size,

$$t = \frac{k\lambda}{\beta_{Size\cos(\theta\beta)}} \quad (3.14)$$

where t is the crystallite size, *k* the shape constant normally assumed to be 1, and λ the wavelength of the Cu Kα radiation [3.12].

3.2.4 Williamson-Hall Analysis for the Determination of Crystal Size and Strain. As a result of Scherrer's famous equation (3.14), Wilson and Stokes noticed that the strained or imperfect crystals contains line broadening of a different sort to that of crystallite size and that the strain-related broadening is given by

$$\varepsilon_{str} = \frac{\beta_{str}}{4\tan(\theta\beta)} \quad (3.15)$$

where ε_{str} is the average strain and β_{str} strain related broadening (measured in radians 2θ). Again, for accurate determination of the crystallite size and strain, one must account for the line broadening contributions. In Lorentzian shape

$$\beta_{obs} - \beta_{inst} = \beta_{Size} + \beta_{str} \quad (3.16)$$

In 1953, Williamson and Hall proposed a method of deconvoluting the size and strain by looking at the peak width as function of 2θ. Substituting (3.14) and (3.15) it can be deduced that:

$$\beta_{obs} - \beta_{inst} = \frac{k\lambda}{t\cos(\theta\beta)} + 4\varepsilon_{str}\tan(\theta\beta) \quad (3.17)$$

Rearranging (3.17), results (3.18):

$$\{\beta_{obs} + \beta_{inst}\}\cos(\theta\beta) = \frac{k\lambda}{t} + 4\varepsilon_{str}\sin(\theta\beta) \quad (3.18)$$

Equation (3.18) is known as the Williamson-Hall simplified integral breadth method that is used to determine the crystallite size and strain from the y-intercept and the slope of the straight-line fit to the obtained data points. To obtain a Williamson-Hall plot, one should plot $\cos(\theta\beta)$ in the y-axis and $4\sin(\theta\beta)$ on the x-axis [3.13-3.14]. The intercept with y, i.e. when $x = 4\sin(\theta\beta) = 0$, yields the crystallite size according to:

$$\tau = \frac{k\lambda}{y(x=0)} \quad (3.19)$$

whereas the slope of the linear fit yields the lattice strain, ε_{str} , within the film of nanowires.

3.3 Structural Characterisation - Scanning Electron Microscopy

3.3.1 Working Principle. The study of the morphology and fine structures of ZnO and TiO_2 NWs films was achieved using a field emission scanning electron microscopy (FESEM). In FESEM the primary electrons are produced with an electric field during operation, unlike the conventional SEM where a filament is heated. The electron source is a really thin sharp mono-crystalline tungsten crystal (tip radius of between 10 and 100 nm) at the centre of the FESEM instrument, which produces a coherent electron beam of about 1000 times smaller than the conventional SEM. This smaller beam diameter is responsible for the greater resolution yield obtained by an FESEM, than what is obtainable in conventional SEM microscopy; the resolution is as low as 1nm. A basic field emission system comprises of a primary and secondary anode, with the crystal functioning as a cathode. A voltage is generated over the cathode and anode generated is in the range between 0.5 and 2 kV under a high vacuum in the order of 10^{-7} to 10^{-9} mbar [3.15, 3.16] to extract electrons from the tungsten crystal. The crystal emitted electrons, which are known as primary electrons, are focused and reflected by electromagnetic lenses and coils to generate an extremely narrow beam, focused at the sample object. As the beam irradiates the samples, secondary electrons are emitted from each atom of the sample that are exposed to the beam. The secondary electrons generated by the specimen are detected by a detector called the Everhart-Thornley

detector, with a Robinson type detector detecting the back-scattered primary electrons. The collected electrons are then amplified and converted into a magnified digital image through a digital camera system connected to the detectors. By scanning the electron beam across the sample surface, a topographical representation of the sample surface is acquired and analysed in real time on a computer screen of a desktop computer connected to the digital system [3.16]. Fig. 3.10 shows a schematic representation a typical electron column of a scanning electron microscope.

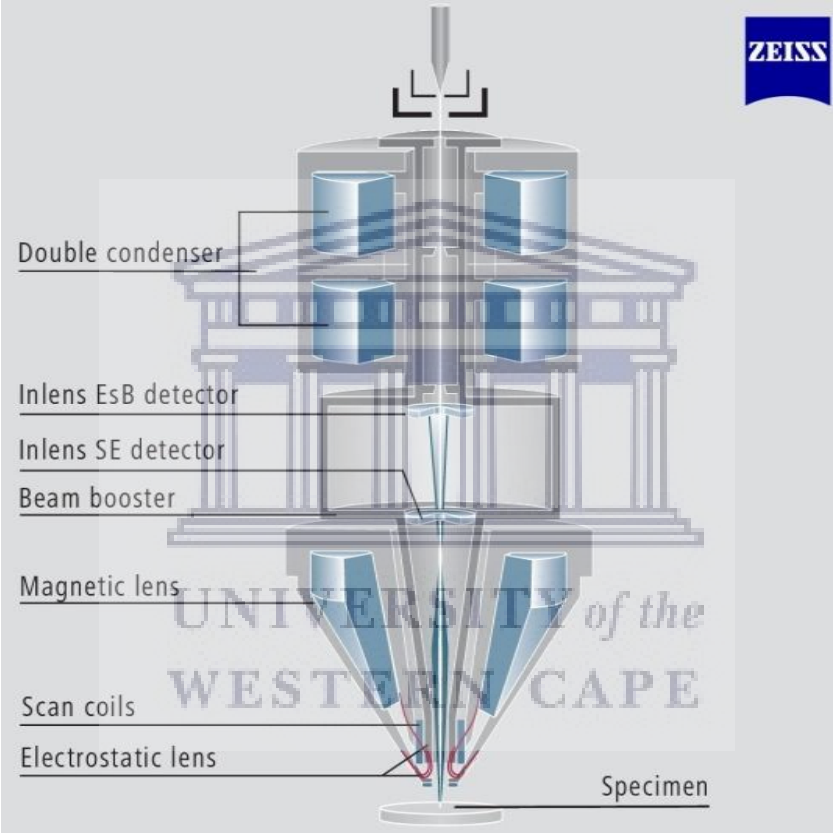

Fig. 3.11: Schematic representation of the components of a FESEM electron column [3.16]

In this work a Zeiss Auriga field emission SEM (FESEM) was used to investigate the structure of the both TiO_2 and ZnO NWs films. The electron beam energies of between 1 and 10 kV was used in to operate the microscope. The cross-section of the Nanowires for both TiO_2 and ZnO NWs films were viewed by pre-cutting the FTO/ITO glasses into 1 by 1 cm^2 in order to measure the growth length of the NWs. Thus, the pre-cracking or pre- cutting of the synthesis TiO_2 and ZnO NWs films FTO/ITO before FESEM analysis does give an approximately exact or accurate growth length of the NWs layer, this process do not cause

any damage to both TiO_2 and ZnO NWs films. Fig. 3.12 shows the Zeiss Auriga FESEM used in this study, hosted by the Electron Microscope Unit, University of the Western Cape, Cape Town.

Fig. 3.12: Zeiss Auriga FESEM hosted at the University of the Western Cape; the major detectors used are as indicated.

3.3.2 Characteristic X-ray Detection and Energy Dispersive Spectroscopy. X-ray signals are produced in larger depths of the interaction volume due to excitation of atoms deepest electrons upon receiving sufficient energy from the incident primary electrons. Considering the schematic diagram of energy levels of atoms around the nucleus also referred to as electron shells labelled K, L, M, as shown in Fig. 3.13. The specimen atoms interaction with the high energetic primary electrons gives increased probability of the innermost electrons, usually for the K-shell, to be extricated into higher energy states creating a vacancy in the K-

shell behind. The electrons in higher energy state are assumed to be in an *excited state*. Meanwhile, the electrons in surrounding shells can jump to fill the vacancy left by the excited electron, thus emitting a photon of characteristic short wavelength referred to as x-rays. For instance, when an electron from L-shell fills the vacancy left in the K-shell, the kind of radiation created would be the Kα radiation, whereas a transition from M to K produces the K_β radiation. Related nomenclature is applied when an electron in the outer shells has been removed.

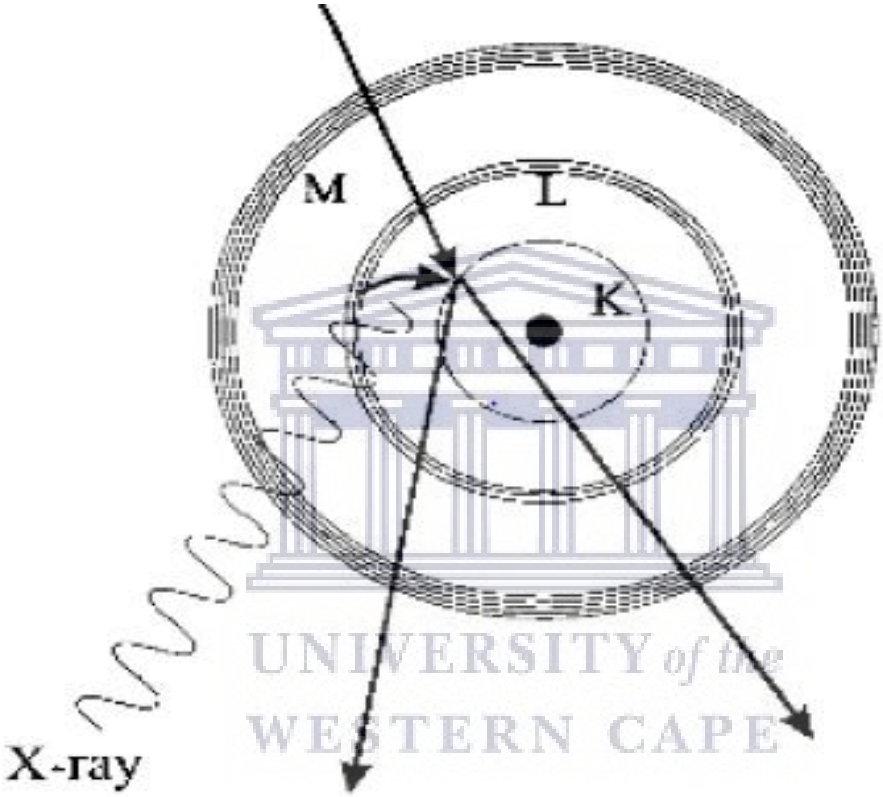

Fig. 3.13: Schematic diagram of inner electron shells of atoms [3.20]

The energy levels of each individual atom are decided by its atomic number, the characteristic energy of the x-ray is distinctive for every element; therefore, the x-ray signal collected can be applied for elemental analysis during energy dispersive x-ray spectroscopy (EDS). Because of the scintillation damage upon impingement of x-rays on their surface, a semiconductor detector is used preferably for the detection of x-rays, as it also helps in dispersing the x-rays according to their energies. A classic semiconductor detector used for this interference, has a beam and is made of semiconductor crystals like Si or germanium

(Ge), the purpose is normally in the form of a thin plate, which is built on the objective aperture, which does not have a beryllium (Be) window.

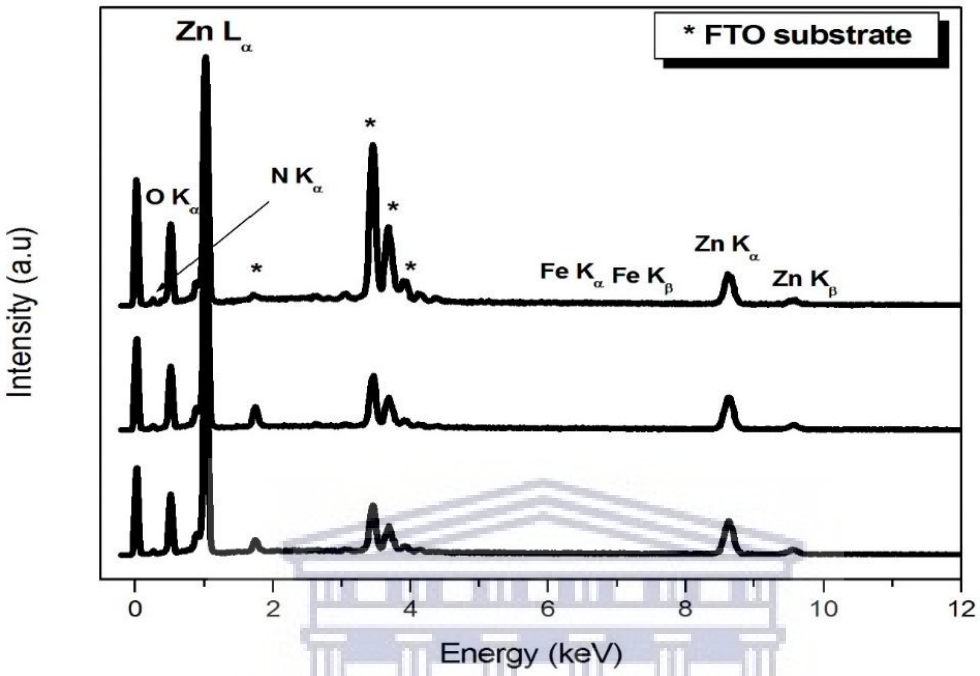

Fig. 3.14: EDX elemental spectra showing all elements present in the three different samples.

As soon as the X-rays strike the surface of the semiconductor crystal, the electrons in the crystal absorbs the X-ray energy, which is enough to overcome the energy-gap (E_g). They are therefore excited from the valence band to the conduction band with the number of excited electrons proportional to the X-ray energy. The recombination of the electron-hole pairs is restricted with the presence of an electric field in the depleted region known as the p-n junction in the semiconductor crystal used. Although, because of the dominant absorption of X-rays by the Be-window, the elements lighter than sodium (Na) cannot be detected. Hence, for analysis of light elements, one needs a dedicated technique [3.20]. The electric current formed during this process is then contacted to a thin gold (Au) layer and to an amplifier, where it is amplified into electric pulses. However, an analogue-to-digital converter (ADC), is mounted in to a multichannel analyser (MCA), digitalises the amplified signal into electric pulses, which are then sorted according to their energy, by the MCA. Furthermore, the MCA counts the number of X-rays striking the semiconductor crystal at every energy level, thus producing an intensity distribution, which can then be used to plot a normal EDS spectrum. Fig. 3.14 shows an example of and EDS spectrum collected in this study, using an Oxford

Instruments X-MAX solid-state drift detector installed on the Zeiss Auriga FESEM as shown in Fig. 3.12; each spectrum is usually collected for a minimum of 30 seconds.

3.4 Structural Characterisation - Transmission Electron Microscopy

3.4.1 Working Principle. The internal structure of the TiO_2 and ZnO nanowires was studied with transmission electron microscopy (TEM). There is a clear distinction between the working principles of this technique from the SEM. In this case the primary electron beam is transmitted through the specimen instead of being back scattered or knocking out secondary electrons in the specimen sample as the case in SEM. As a result, increasing the accelerating potential of the electrons to 50kV, then the electron wavelength contracts to about 5pm in agreement with De Broglie's relationship [3.21] and these higher-energy electrons can penetrate distances of several microns (μm) into a solid. But if it's a solid crystal, the electrons are diffracted by atomic planes inside the material, producing a transmission electron diffraction pattern. Due to very small wavelengths of the transmitted electrons, the specimen can be imaged at a spatial resolution much greater than is the case of SEM [3.21, 3.22]. The present TEMs function properly with electron accelerating voltages between 100 and 300 kV, accomplishing spectral resolution of 0.1 nm (one Angstrom) with regularity. During TEM imaging, the image formation can be said to be occurring in two stages. The incident electrons and the atoms of the specimen undergo interactions with each other, resulting in elastic and inelastic scattering processes. The electron wave function that leaves the exit surface of the specimen is transmitted through the objective lens, and subsequent intermediate lenses of the electron microscope to form the final enlarged image as shown in the ray diagram of Fig. 3.15.

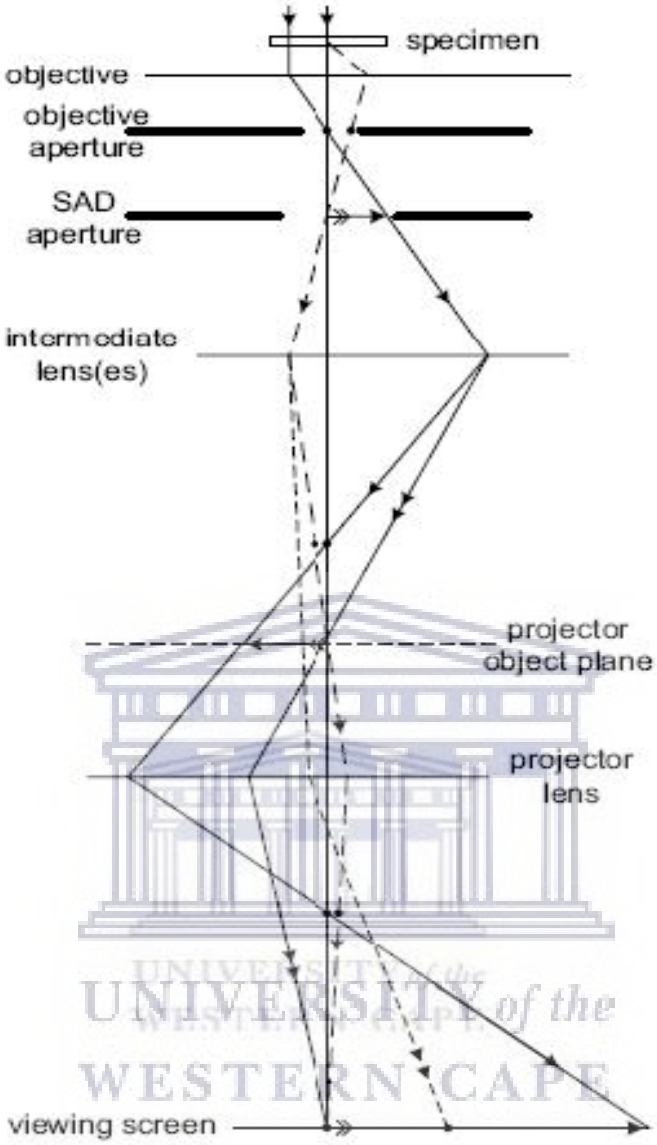

Fig. 3.15: Thin-lens ray diagram of the imaging system of a TEM [3.22]

Elastically scattered electrons contribute to the high resolution TEM image, whereas the inelastically scattered electrons are detected and recorded to yield valuable elemental information about the specimen during electron energy loss spectroscopy [3.22, 3.23]. The examination of the internal structure of the samples was done with FEI Tecnai $G^2$20 high resolution TEM, operated at 200 kV. The TEM samples were prepared by scratching the surface of the as-synthesised TiO_2 and ZnO NWs films into ethanol, followed by ultra-sonication for 3 minutes and finally drop platting on a holey-carbon copper grid and dried at ambient condition. The Tecnai TEM, hosted by the Electron Microscope Unit, University of

the Western Cape, Cape Town is shown in Fig. 3.16 with the major detector systems indicated.

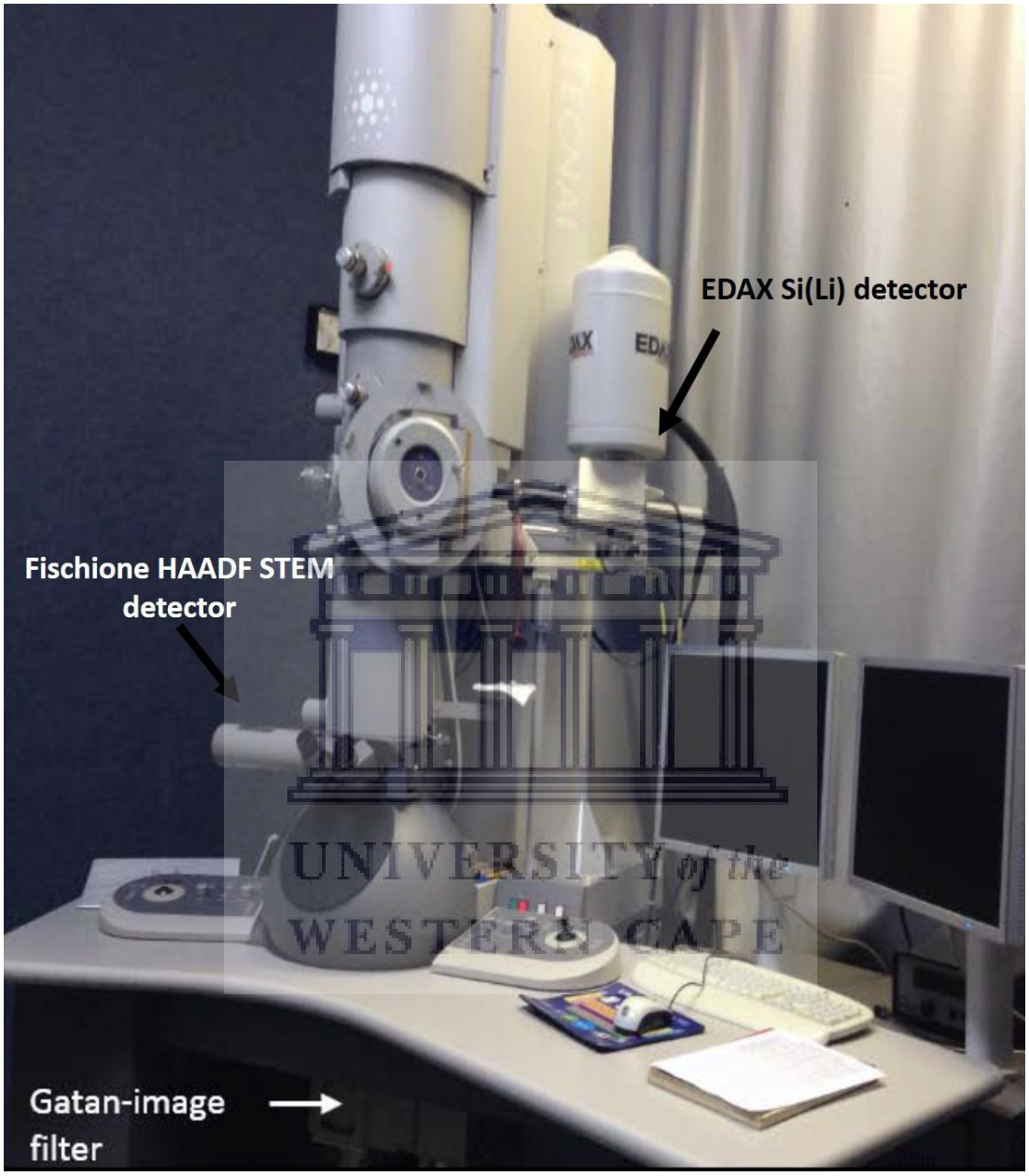

Fig. 3.16: A pictorial representation of the Tecnai $G^2$20 field-emission gun TEM used in this study

3.4.2 Scanning Transmission Electron Microscopy. When a fine electron probe is used to form scanning transmission electron microscopy (STEM) images, the objective-lens optics are a little more complex than in conventional TEM. The key feature to remember is that the scanning beam must not change direction, as the beam is scanned, unlike in an SEM where

the scanning beam easily pivots about a point above the specimen. However, if the incident direction varies then the electron scattering (particularly the diffraction) processes changed as the beam intercepts the specimen at different angles. As a result, interpreting the image contrast would be rather difficult, to say the least [3.29].

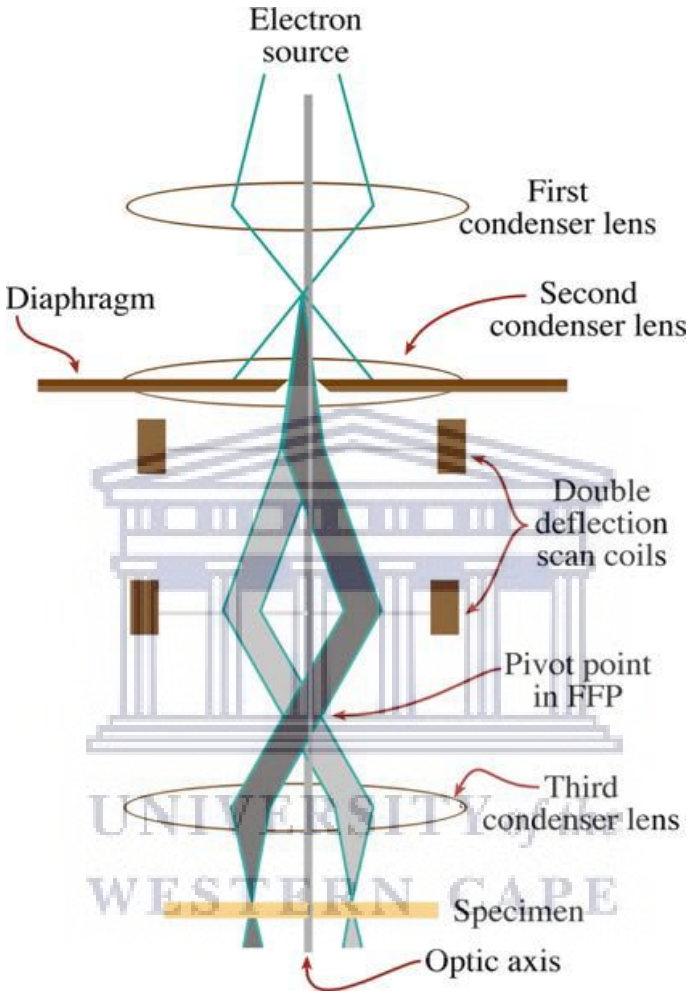

Fig. 3.17: Schematic illustration of a convergent probe scanned over a specimen for STEM image formation [3.30]

The electron beam has to scan parallel to the optic axis at all times, so that it copies the parallel beam in a TEM even though it is scanning. As illustrated in Fig. 3.17, to achieve parallel configuration upon incidence, two pairs of scan coils are used to pivot the beam about the front focal plane (FFP) of the upper objective (C3) pole piece. The C3 lens ensures that all electrons emanating from the pivot point are brought parallel to the optic axis; additionally, an image of the C1 lens crossover in the specimen plane is formed. If the

objective lens is symmetrical and the lower objective pole piece is equally strong, then a stationary diffraction pattern is formed in the back-focal plane (BFP). This pattern does not move, even though the beam is scanning, as it is conjugate with the FFP, as illustrated in Fig. 3.17. If the beam is stopped from scanning, then we have a condensed beam electron diffraction (CBED) pattern in the BFP that can be projected onto the viewing screen.

The STEM image quality exclusively depends on the probe. The probe has aberrations because of the lens used to form it. Therefore, the STEM image quality does depend on a lens and not just on an imaging lens [3.29]. STEM imaging, as is the case in the SEM, does not need to employ the use of lenses to form an image. As such, the defect in the imaging lenses has no effect on the image resolution; however, the resolution is limited by the beam dimensions. For this reason, the chromatic aberration which can seriously limit TEM image resolution is not present in STEM images. This is advantageous when dealing with a thick specimen. For this reason, STEM images are not widely used especially for crystalline specimens because of the difficulty in focusing such a very small probe onto the specimen [3.30].

3.4.3 Bright-Field STEM Images. The use of scanning mode in formation of the image is fundamentally different to the use of a static-beam for TEM image formation. TEM imaging is a portion of the electrons emanating from an area of the given specimen, which is selected and their distribution projected onto the screen. The principle of scanning-image formation is illustrated in Fig. 3.19. The scanning of the beam on the specimen is done by adjusting the scan coils; while these same coils are used to scan the computer display synchronously. Meanwhile, the electron detector acts as the interface connecting the electrons coming from the specimen and the viewed image on the display screen. Because it takes up to 2048 scan lines to build up an image on the recording screen, the entire process of creating a STEM image is much slower compared to TEM imaging: since it's serial recording instead of parallel recording [3.30].

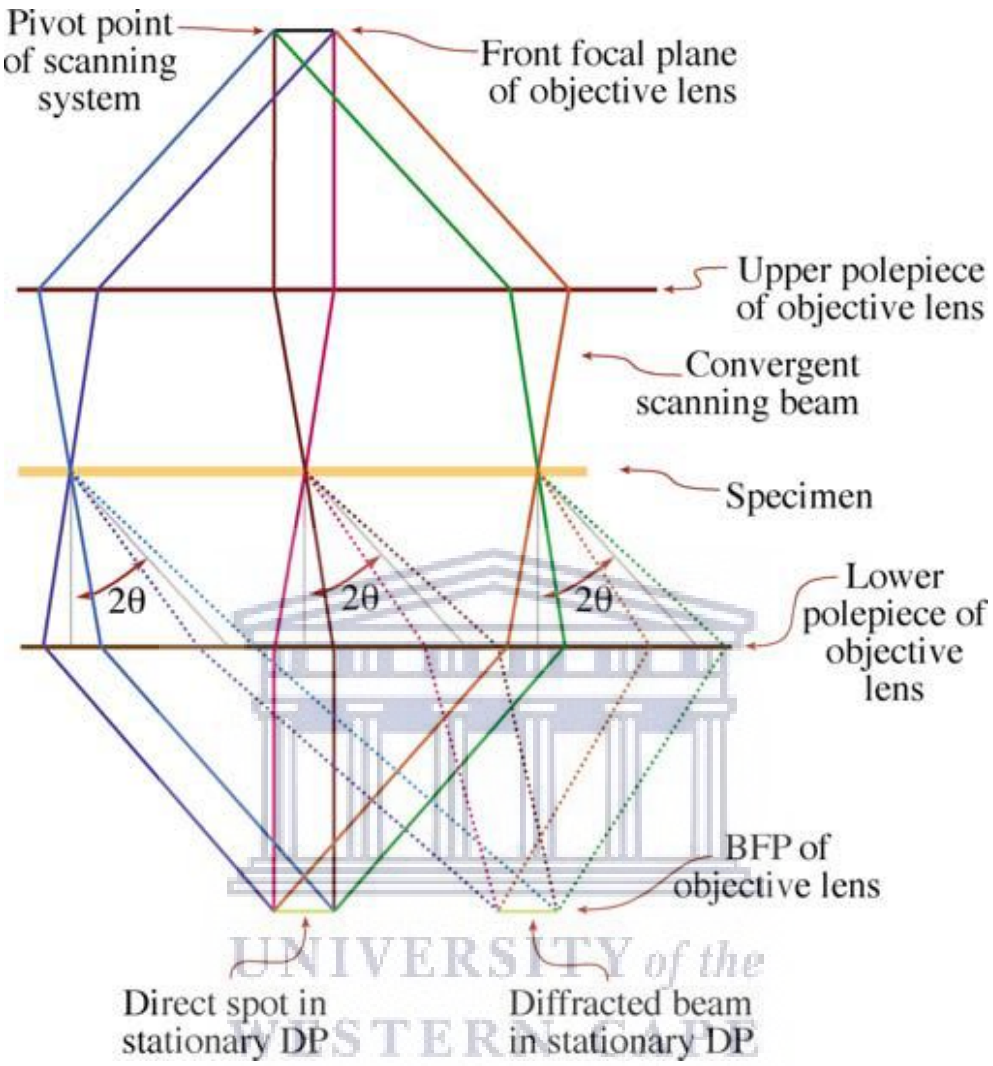

Fig. 3.18: Schematic illustration of a stationary CBED pattern in the BFP of the objective lens; a necessary prerequisite for STEM imaging [3.24].

As shown in Fig. 3.19, no lenses are required to form the image. The signal is generated at a point on the specimen, detected, amplified, and an equivalent signal displaced at a corresponding point on the computer display. This process is precisely the same principle as used in any scanning-beam instrument such as a scanning-tunnelling microscope or an SEM (discussed in Chapter 3.3). To form a TEM bright field (BF) image, an aperture is inserted into the plane of the TEM DP, which allows only the direct electrons through into the imaging system. Similarly, in the STEM mode an electron detector is used, in exactly the

same way the aperture is used: allowing only the electrons that can contribute to the image to hit the detector. So a BF detector (in practice, either a scintillator or semiconductor based) is inserted in the axis of the microscope and intercepts the direct-beam electrons no matter where the beam is scanning on the specimen, as illustrated in Fig. 3.19 (a).

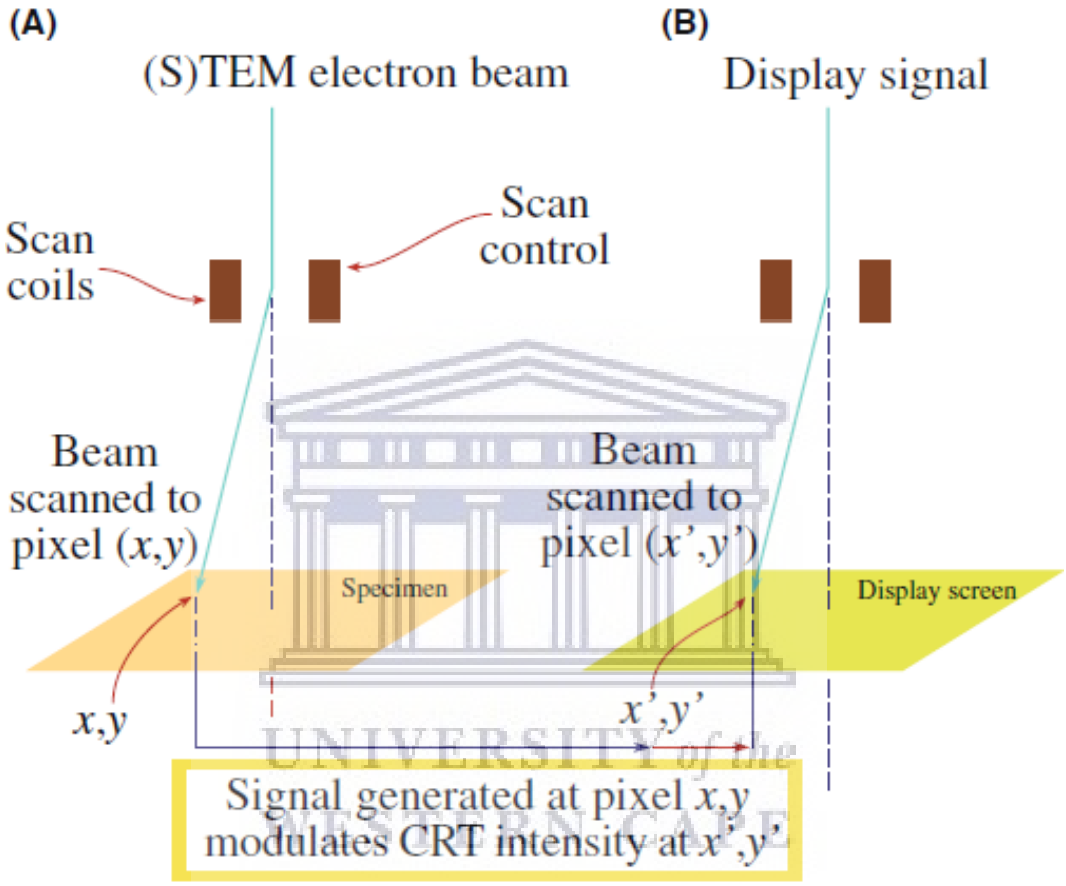

Fig. 3.19: The principle of forming a scanning image; scan coils in the microscope control (A) the beam-scan on the specimen and (B) the beam-scan on the computer display screen of the STEM [3.24].

A variable, direct-beam signal travels from the detector via an amplification system to modulate the signal on a computer display, building up a BF image as shown in Fig. 3.20 (d). The BF detector picks up the direct beam which varies in intensity depending on the specific point on the specimen illuminated by the probe at that specific time [3.31]. However, in the TEM the detector can't physically be placed in the BFP of the objective lens to form a STEM image, because it would interfere with the objective aperture. Therefore, a detector usually

inserted into a conjugate plane to the stationary DP. So when a STEM image is formed in a TEM, the TEM is operated in diffraction mode and a detector inserted into the viewing chamber of the TEM, either above or below (in which case you raise) the screen. The stationary DP falls on the detector and the signal goes to the display. [3.29, 3.31].

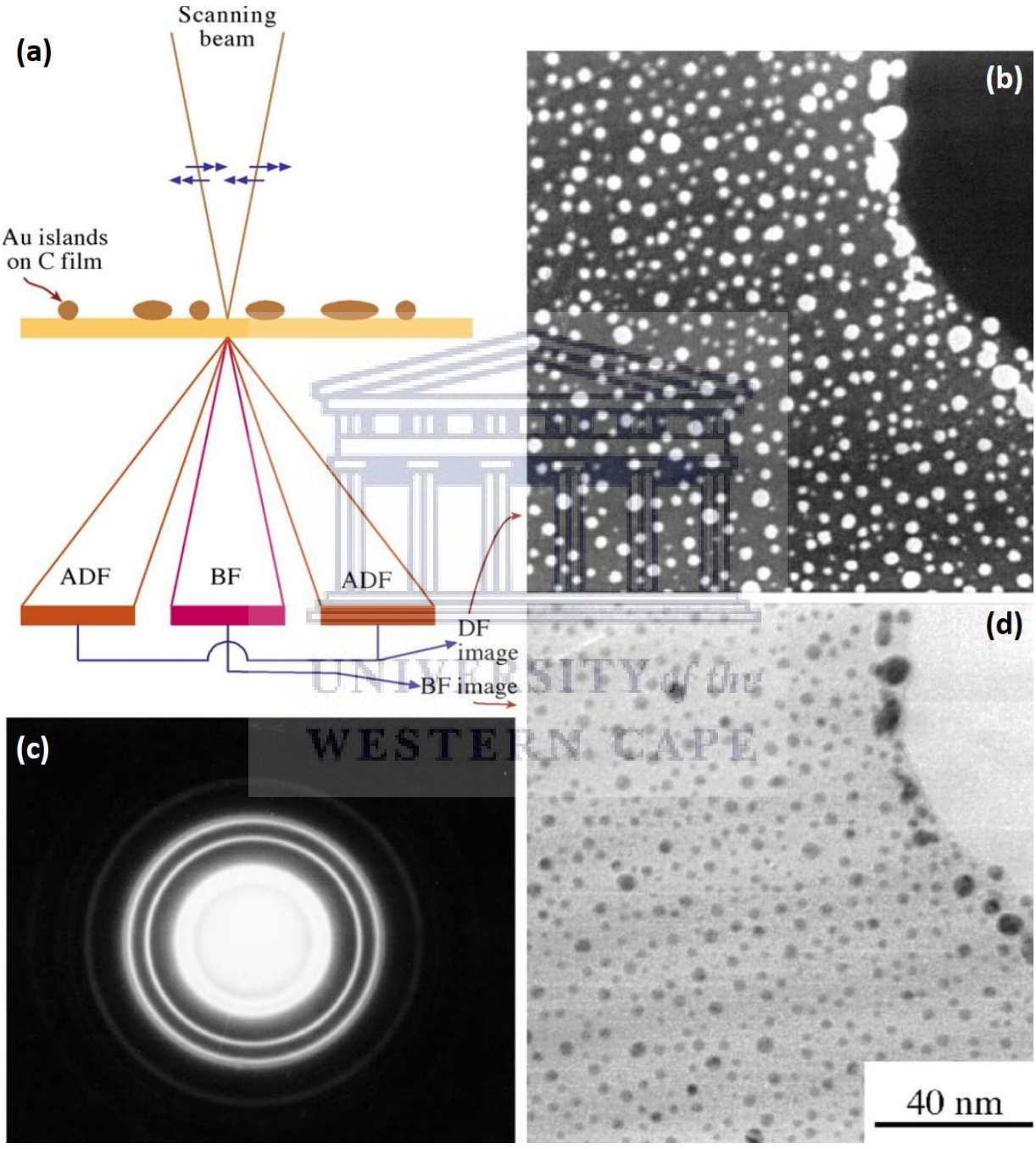

Fig. 3.20: STEM image formation: ABF detector is placed in a conjugate plane to the BFP to intercept the direct beam (A) and a concentric annular DF detector intercepts the diffracted electrons whose distribution is shown in the SAD pattern in (B). The signals from either

detector are amplified and modulate the STEM computer display. The specimen (Au islands on a C film) gives complementary ADF (C) and BF (D) images [3.24].

3.4.4 Dark-Field STEM Images. The approach is very similar to that of TEM image formation in that the DF image is formed by selecting any or all of the scattered electrons, instead of the direct-beam electrons. In a TEM an incident beam titled so that the scattered electrons that form the image travel down the optic axis and are selected by the objective aperture. In a STEM, it differs such that if a specific beam of scattered electrons is required to fall on the BF detector, the stationary DP can simply be shifted, such that the scattered beam is on the optic axis and hits the BF detector. It's simple to do this with the DP centring controls or by displacing the C2 aperture. The former is to be preferred since doing the latter misaligns the illumination system [3.31].

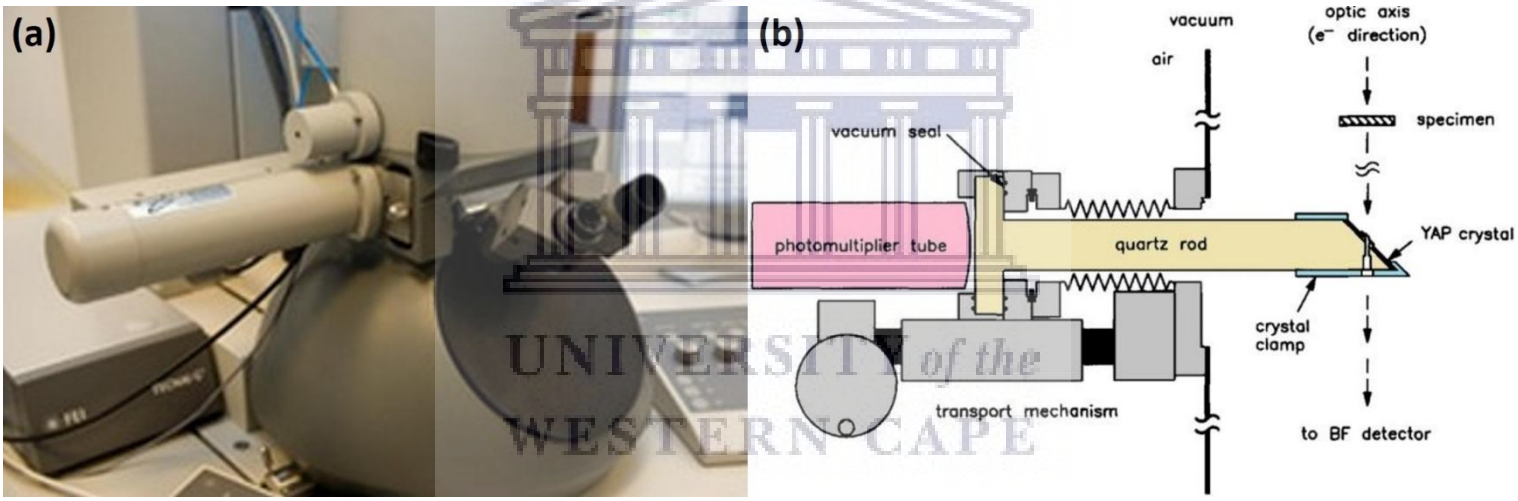

Fig. 3.21: (a) Fischione HAADF detector installed on the Tecnai $G^2$20 200kV TEM; (b) schematic of a typical ADF detector

3.4.5 Annular Dark-Field Images. Instead of using the BF detector for DF imaging, an annular detector used, usually surrounds the BF detector, so that all the scattered electrons fall onto that detector. This process is called annular dark-field (ADF) imaging and it has certain advantages, depending on the contrast mechanism operating in the specimen. As illustrated in Fig. 3.20 (a), the ADF detector is centred on the optic axis and has a hole in the middle were the BF detector sits. A resultant ADF image is shown in the Fig. 3.20 (c), which is complementary to the more common BF image in Fig. 3.20 (d). Another annular detector

can be inserted around the ADF to pick up the electrons scattered about high angles, forming so-called high-angle annular dark-field (HAADF, or Z-contrast) images in which Rutherford-scattering effects are maximised and diffraction-contrast effects smoothed out. Fig. 3.21 (a) shows the HAADF detector used in this study to collect DF images of the nanowire structures, installed on the Tecnai TEM; Fig 3.21 (b) shows a schematic with all the components of a typical annular DF detector system [3.32].

3.5 Structural Characterisation – X Ray Imaging and Mapping

3.5.1 Overview. The use of mapping or compositional imaging for analysis is rarely used in the analytical electron microscopy (AEM), due to the low X-ray count rate because of the small probe currents and collection angles [3.33]. In order to collect a map with sufficient X-ray counts to draw any conclusions about the variations in the physics of the thin film, a particular area of interest must be scanned over an extended period of time. During this time, specimen drift, damage or contamination would occur resulting in compromised results. With improvements in field emission electron sources, drift correction software, detectors with higher collection efficiency, cleaner stage vacuums and the introduction of aberration correctors, it is nowadays possible on the best AEMs, to collect quantitative X-ray maps in a matter of minutes. This said, these instruments are very expensive and access to them extremely limited. As such, a simpler approach followed by many researchers is to combine x-ray spectrum collection with STEM image formation to form a first step to obtaining elemental information of specific areas within the specimen, as shown in Fig. 3.20. In the figure, a line-scan in performed across a grain boundary of Mo_xNi_y allow (Fig. 3.22 (a)), with an EDS spectrum collected at multiple spots on this line and stacked to show which areas are Mo and Ni rich, respectively; see Fig 3.22 (b) [3.34].

3.5.2 Digital Mapping. With advent of computers it has become possible and easier to gather X-rays from multiple channels or windows and therefore acquiring several maps simultaneously [3.24, 3.37]. Hunneyball *et al* [3.38] collected the first successful digital thin-foil X-ray maps. Back then it was only feasible to build up pixel images of 128 X 128 with 256 X-ray counts at each pixel using a 100 nm probe with 5 nA of probe current over 200s. The maps, however, were fully quantitative and had the effects of foil-thickness variation

removed, while revealing relatively small composition discrepancies around grain boundaries in aged Al alloys; as shown in Fig. 3.22 (a).

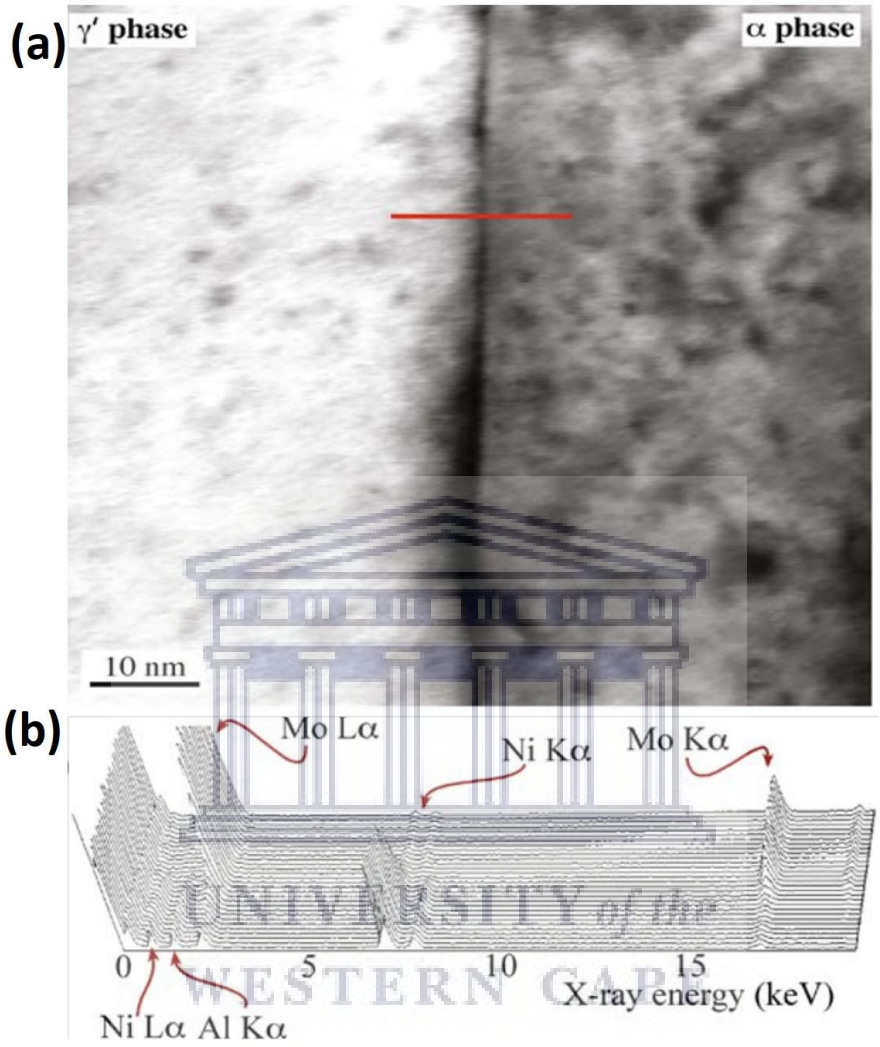

Fig. 3.22: (a) STEM image of an interface in a Ni base super alloy with a line showing from where X-ray spectra were obtained. (b) A spectrum-line profile taken along the line in (a) showing clearly the change in Ni and Mo composition across the interface [3.24].

Due to the central role the computer plays in the acquisition, this approach has the advantage of comparing different quantification routines and post-acquisition processing. Furthermore, after acquisition it is possible to make use of such processing techniques as false colouring, scatter diagrams, computerised image overlays, etc. [3.39]. Each and every one of these advantages are combined together to make digital imaging a most attractive approach for displaying EDS data. An instance from such an AEM is illustrated in Fig. 3.23 (b), which is

256 X 256 pixels and acquired with a 1-nm probe with 0.9 nA of current for 5400 s. Comparing Fig. 3.23 (a) and (b) is instructive and illustrates the vast progress made in both the quality of mapping and the spatial resolution.

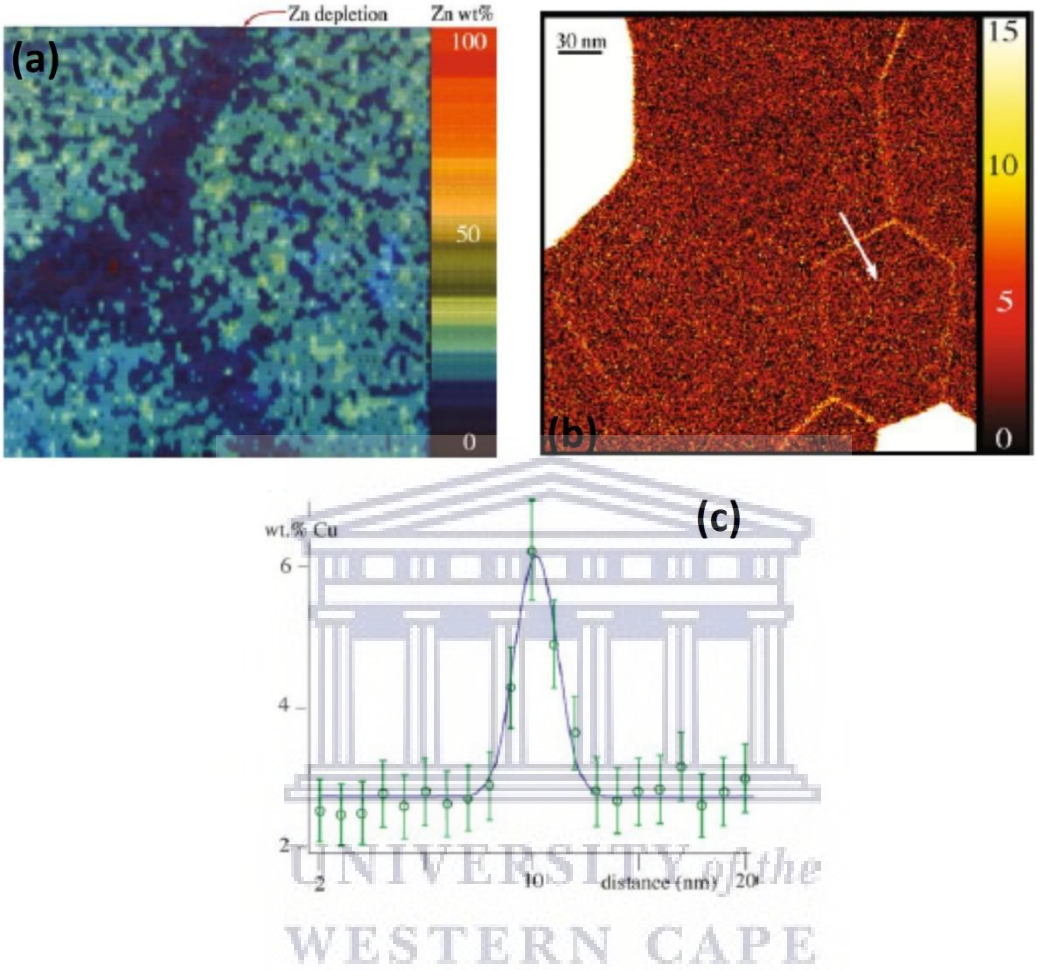

Fig. 3.23: (a) the first quantitative digital map (128 X 128 pixels) obtained in an old thermionic-source AEM generating a low count rate. (b) More recent digital map from a 300-kV FEG AEM showing enrichment of Al at grain boundaries in an electro-migrated specimen of Al-4% Cu. (c) Quantitative Cu line profile taken across a grain boundary, indicated in (b), by arrow [3.24].

With digital map such as this, one can extract quantitative data from any part of section of the map, for example the line profile taken across the grain boundary in Fig. 3.23 (c). However, a window or peak has to be selected in the spectrum that has been mapped, therefore introducing a bias in terms of what is to be expected in the specimen. Also, once the map is recorded and stored, it is not possible to return to re-check the data, or even map another element from the same region, because all the other information in the spectrum has been

lost. Similarly, unless the image is stored from the mapped area, it cannot be re-examined. So this technique is very time consuming and sensitive, with expertise crucial. To overcome this, newer techniques make use of spectrum imaging as will be discussed below [3.37].

3.5.3 Spectrum Imaging. As the term entails, spectrum imaging (SI) gathers a full spectrum at each pixel in the digital image, so this can only be done in STEM mode, though there are analogue versions in energy-filtered TEM, which will not be discussed in this thesis. The result of the SI process is a 3 dimensional data cube, as illustrated in Fig. 3.24 (a), with the electron image comprising the x–y plane, while all the EDS spectra are contained in the z direction. In the late 1980s the term SI was first used for electron energy loss spectroscopy (EELS, to be discussed below). It was only much later that SI became possible for X-ray mapping, even though it is now common enough to be employed in materials problem solving [3.40]. The SI methods have been practiced in other fields, like radio astronomy for several decades [3.41].

The data are collected on a magnetic tape and afterward reconstructed into a 3D file. The benefit of the SI technique is that, once this data cube is stored, one can go back to it at any time, recheck the data, repeat any analysis and also search for other spectral features that might not originally have thought present or important, look at different images at different energies, and yet always have the original image and spectra at our disposal. Consider the diagram in Fig. 3.24 (a), it can be observed that there are many ways to slice and dice the data cube to reproduce all the other methods of analysis that have been described. If a single pixel is selected in the x–y (image) plane, then there will be a full spectrum attached to it and so, a set of individual pixels can be selected to do as many spot analyses as desired. Similarly, a line of pixels can be selected in the image, effectively slicing the cube along the x–z, y–z, or some arrangement of these directions and as a result produce spectrum-line profiles. It's possible (and this is where it really gets useful) to slice the cube at any plane in the z (labelled E for energy) direction and, all planes get different images consisting of X-rays of that very particular energy. Planes can be added, subtracted, and image pixels summed in certain features only (e.g., along a boundary plane or a strangely shaped precipitate). Consider a 1k X 1k pixel image with a 2048-channel spectrum at each pixel, the data cube is about 2GB in size. In gathering such huge amounts of data cubes, the challenge is finding ways to search this enormous database efficiently and extracting meaningful data.

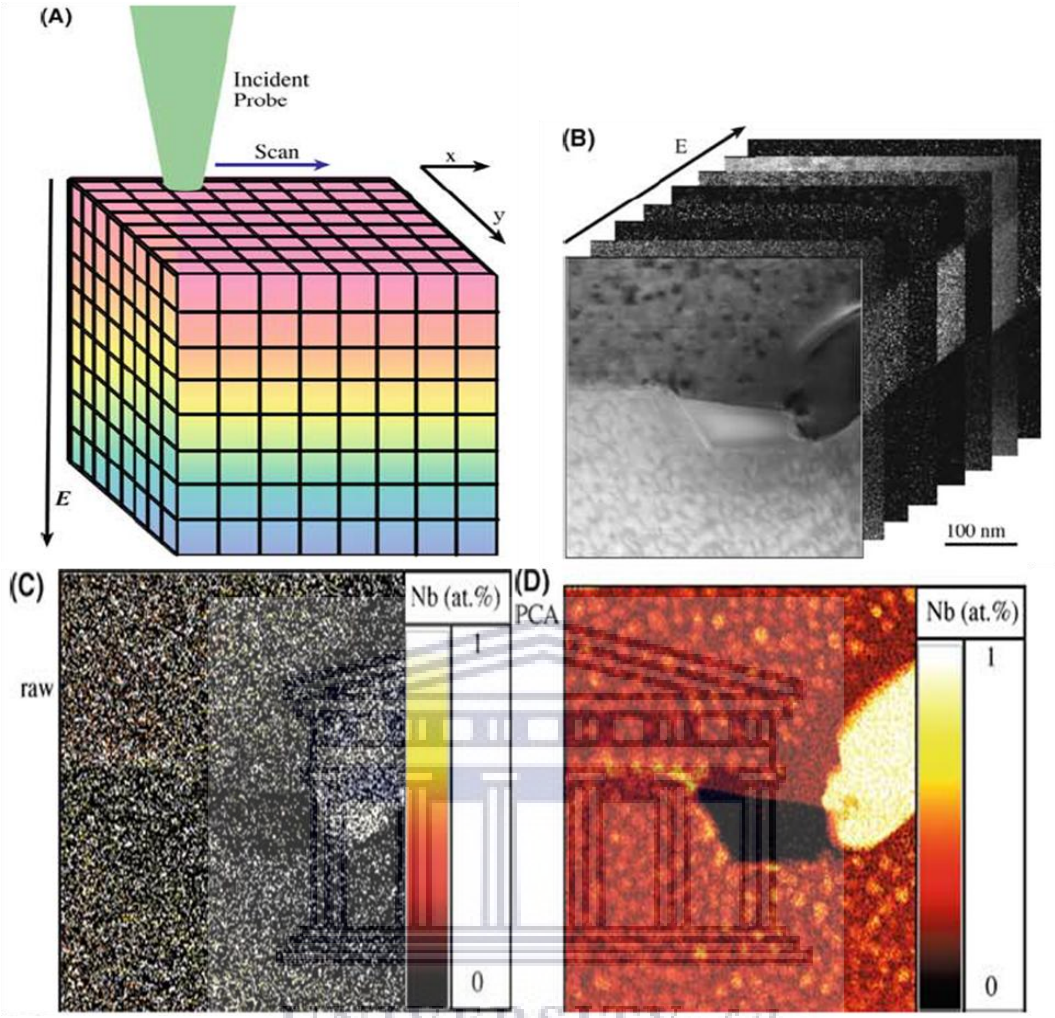

Fig. 3.24: (a) Schematic SI data cube showing how as the beam stops at each pixel in the x–y plane as it is creating a STEM image; a full X-ray spectrum is gathered at each pixel. The different colors at different energy (z) values indicate different signals from different elements that appear at different energies. (b) A series of X-ray maps of a grain boundary region in a Ni-base super alloy taken at specific energies from an SI data cube. (c) An example of a map from a single channel in the X-ray spectrum in the SI in (b) coinciding with the Nb K_α peak energy. (d) The application of multivariate statistical analysis and principal component analysis to remove noise and enhance the Nb signal [3.24].

A variety of advanced software methods, such as multivariate statistical analysis, maximum-pixel spectrum analysis and principal-component analysis are all available to remove noise and extract rare events from the data cube. However, such processes are closely related to the parameterizing of HRTEM images. To give a hint of what can be done, Fig. 3.24 (b)

illustrates a series of X-ray images cutting the x–y plane at different energy values, displayed 'behind' the original STEM (E = 0) image. If a single x–y plane is selected such as that at the Nb K_α line energy (Fig. 3.24 (c)), that image is very noisy because of the limited signal captured in that one plane. But, sophisticated software can be used to remove all the noise components in the plane and furthermore add in all the other Nb signals from other energy planes to produce the image illustrating the Nb distribution (Fig. 3.24 (d)). However, before one think that such a surprising change is unreasonable and that information is being created where it did not exist, compare the processed image (D) with the original STEM electron image (the top slice in B). Clearly the small matrix precipitates that are imaged in (A) are also mapped in (D). Extracting information like this from the SI data cube tells you how much more powerful the SI approach is compared with spot or line profile analyses. Now it is routine to gather both EDS and EELS SI simultaneously, thus completely optimising the acquisition of analytical data [3.36, 3.37].

3.6 Elemental and Doping Characterisation - Electron Energy Loss Spectroscopy

3.6.1 Overview. Electron energy loss spectroscopy is a technique mostly used by material scientists to study the electronic structure and chemistry of the specimen, that consecutively reveals detailed information about the bonding of atoms in the specimen, atomic structure (or crystal structure) and the energy band-gap of semiconducting specimens [3.24, 3.25]. Modern advances in monochromators for electron guns joined with availability of lenses with corrected spherical and chromatic aberrations has facilitated the performance of EELS studies at energy resolution of less than 100 meV [3.24]. Therefore, this makes EELS a preferred microanalytical technique, employed in studying both heavy and light elements efficiently compared to EDS which cannot be employed to study elements lighter than sodium [3.22]. However, when the monochromatic electron beam interacts with the specimen, a range of signals (elastic and inelastic scattered electrons) is created in the interaction volume. Of particular interest to the EELS technique are the inelastically scattered electrons who suffer detectable energy loss (ΔE) upon their interaction with atoms of the specimen. Inelastically scattered electrons lose their energy in four different ways, which include energy loss of: (i) less than 1 eV by excitation of phonon vibration in solids; (ii) about 1 eV because of single

excitation from the valence band (VB) to higher energy states in the conduction band (CB); (iii) 30 – 50 eV by combined excitation of electrons from VB into CB in semiconductor material or by plasmon excitations; and (iv) few hundreds or thousands of eV by excitation of inner-shell electrons as mentioned in Chapter 3.3.2 [3.22, 3.24-3.28]. The signals emanating the specimen are detected and dispersed by way of post or an in-column magnetic prism spectrometer to generate EELS spectra, which are recorded by means of a photodiode array (PDA) or CCD [3.24]. However, for the purpose of this study, the TEM instrument used for characterisation of TiO_2 and ZnO NWs is well equipped with post-column Gatan-Image Filter (GIF, model GIF-2001) spectrometer. Therefore, only the operation principle of post-column GIFs will be discussed in the next section.

3.6.2 Acquisition of EELS spectra using Magnetic Prism. The post-column Gatan-Image Filter employed for the acquisition of EELS is made up of (i) an entrance aperture, (ii) focusing or alignment coils, (iii) a magnetic prism with magnetically isolated drift tube, (iv) multipole system, and (v) the detection system in the form of a CCD array or PDA, as shown in Fig. 3.25 [3.24]. The diverging electrons originating at the back of the specimen, enters the spectrometer through the entrance aperture, and are converged by the alignment coils towards the central axis (axis of the incident beam) prior to entering the magnetic prism [3.25]. Though inside the prism, there exists a uniform magnetic field in the direction perpendicular to the velocity of the incoming beam of electrons.

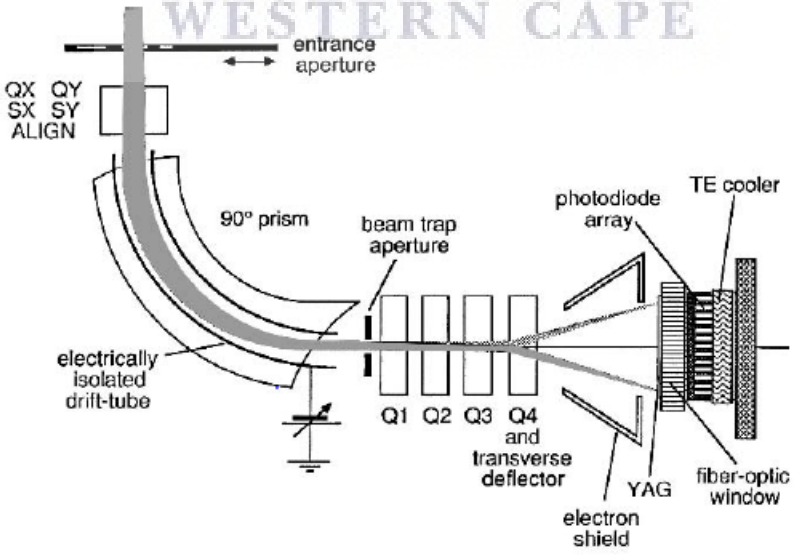

Fig. 3.25: Schematic of typical Gatan image filtering spectrometer used for acquisition of EELS spectra [3.25].

However, the electrons entering the magnetic prism move through a circular orbit, with radius of curvature given by equation (3.20), proportional to both the velocity of the electrons and the intensity of the magnetic field

$$R = \left({}^{\gamma m_o}/_{eB}\right)V \qquad (3.20)$$

Where $\gamma = \left(1 - \frac{V^2}{C^2}\right)^{\frac{1}{2}}$ is the relativistic factor, m_o the rest mass of an electron, e the electron charge, B and v the magnitude of the magnetic field intensity and speed of electrons, respectively [3.26]. Equation (3.20) reveals that electrons which have lost energy during their interaction with specimen atoms will have lower velocities, Hence smaller curvature radius compared to the elastically scattered (zero-loss) electrons, whose radius of curvature will be larger as a result of their high velocities, which is equivalent to the velocity of the primary electrons as shown in Fig. 3.26 below.

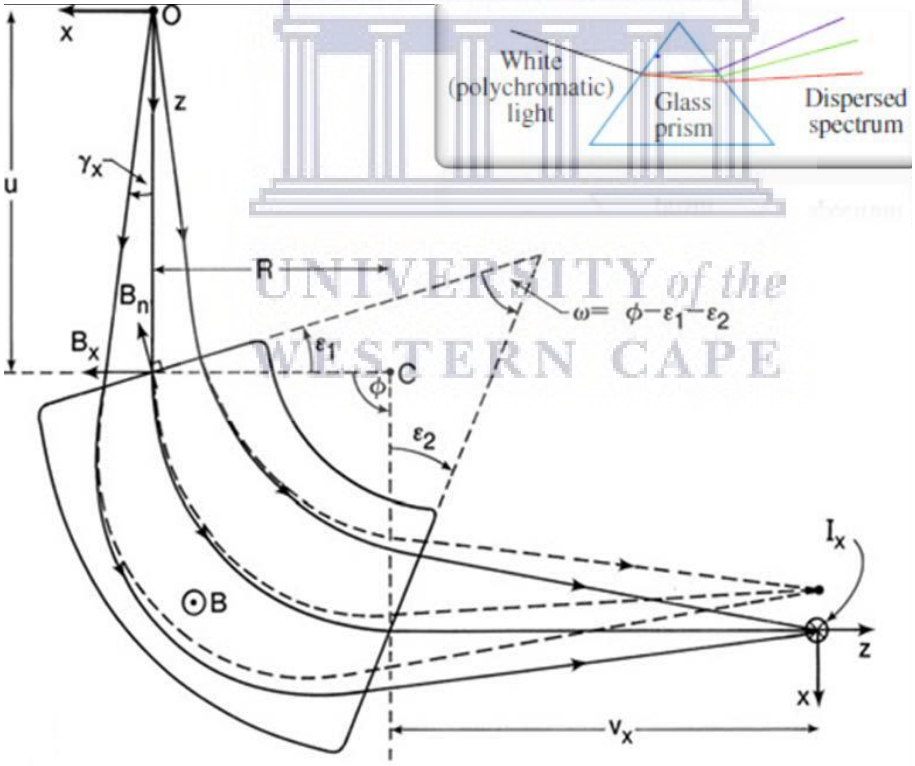

Fig. 3.26: Working principle of magnetic prism to disperse electrons according to their energy loss during acquisition of EELS spectra [3.26]

The deflection of electrons inside the magnetic prism according to their energy loss, thereby resulting in energy dispersion, is analogous to the principle of the glass prism shown in the inset of Fig. 3.26, where the polychromatic light entering the prism is dispersed into light of different wavelengths (colours) [3.24]. But, in the magnetic prism the dispersed electrons exiting the prism are focused to the dispersion/image plane *Ix*, as shown in Fig. 3.26, meanwhile this focusing is not observed in a glass prism. The focusing in the magnetic prism occurs due to electrons with positive γx (measured radially) travel greater distances in the magnetic field, thus experiencing larger deflection compared to electrons, which have negative γx which travel shorter distances, as shown with dashed lines in Fig. 3.26 [3.24,3.26, 3.27].

Prior to the acquisition of EELS spectra, a series of quadrupoles, shown in Fig. 3.25, are employed for magnification and further focusing of the electron dispersion prior to recording on the PDA or CCD, placed at the dispersion plane. The modern instruments make use of CCD arrays for acquisition of EELS spectra over PDA, because of the improved resolution, better photon sensitivity, high dynamic range and straight forward recording offered by CCDs. Meanwhile EELS spectra compose of wide energy range of electrons, both PDA and CCD are coupled with an yttrium aluminium garnet (YAG) scintillator that converts electrons into photons that are proportional to the incident radiation to reduce the radiation damage possibilities [3.24, 3.27]. However, when photons from the scintillator falls onto the CCD detector with 100 × 1340 arrays of 25 μm pixels, a full frame transfer of the array permits efficient collection of EELS spectra with good resolution over a short exposure periods compared to multiple integration in PDAs as a result of its saturation at counts of approximately 16 000 electrons. Additionally, in the presence of beam a trap aperture (Fig. 3.25), the electrons from the optical axis are filtered, therefore allowing simultaneous recording of selected EELS and the performance of energy filtered TEM (EFTEM) imaging [3.24]. The resulting EELS spectra recorded by CCD detector has two dominant artefacts namely; dark current and the ghost peak. Dark-current artefacts form as result of background noise in detectors while the ghost peaks arise as result of overexposing the YAG scintillator to the high energy radiation such as the zero-loss electrons. The former can be minimised by subtracting the pre-recorded spectrum in the absence of electrons from the gathered EELS data, whereas the later can be minimised by subtraction of the extrapolated data using a decay power law, as the ghost peaks decay over exposure times. Therefore, the resulting EELS

spectrum reveals true proportionality of the intensity and the energy loss, thus enabling extraction of meaningful information about the specimen [3.24, 3.26-3.28].

3.6.3 Characteristics of an Electron Energy Loss Spectrum. An EELS spectrum is usually categorised into two parts namely the *low-loss* and the *core-loss* sections, as presented in the schematic of Fig. 3.27. The low-loss part is made up of the zero-loss peak (ZLP) which is the most intense peak and consists primarily of elastically scattered electrons (no energy loss) and many number of plasmon peaks (even though the schematic show only one peak). Meanwhile the core-loss part consists of only ionisation peaks or sometimes referred to as the edges. The *low-loss* and *core-loss* occur as a result of the processes described in Chapter 3.5.2 [3.22, 3.24 – 3.27].

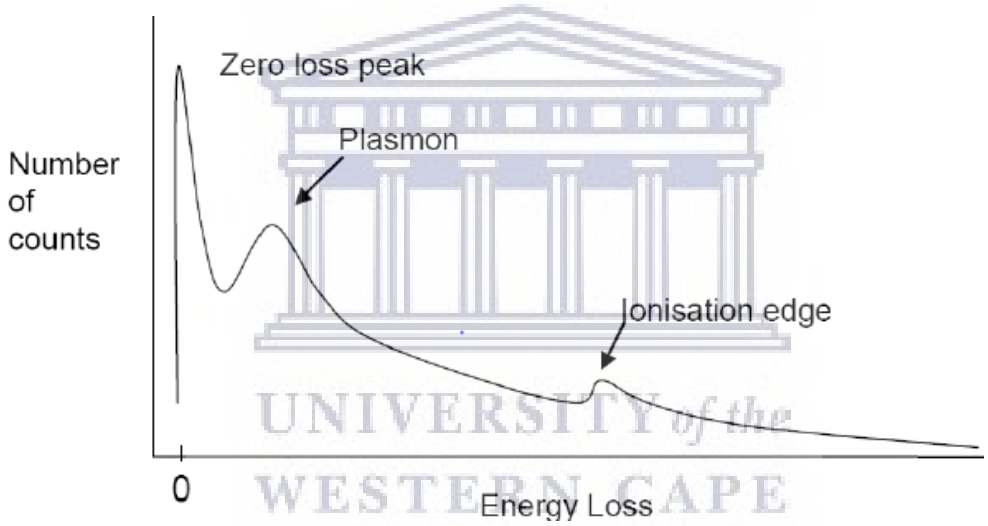

Fig. 3.27: Schematic of a typical EELS spectrum with exaggerated peak broadening [3.27].

In theory, the width of the ZLP is supposed to be zero, but because of broadening effects, caused by the electron source and the nature of the instrumentation used, the electron energy spread is observed as a normal distribution and is measurable. The result in Fig. 3.25 is exaggerated to highlight this phenomenon [3.22, 3.24]. However, for the purpose of micro-analytical studies, the ZLP is of no significance as it provides no useful information about the specimen. Nonetheless, the microscopist use this peak when making instrument calibrations due to its known centre and measurable full-width half maximum (FWHM) that permits performance of beam alignment and in determination of instrument resolution, respectively

[3.22, 3.25]. Numerous number of plasmon peaks with intensities that get progressively weaker towards higher energy losses are also not often employed for microanalysis, as their occurrence is very similar for all elements. Hence, the ionisation edges which are observed at higher energy losses between 100 eV and 2000 eV [3.22] are the frequently used peaks as they are characteristic for each element and allow identification of elements present in the specimen. For instance, the ionisation edge experienced from 456 eV to just about 465 eV can only be that of Ti-$L_{3,2}$ edges as illustrated in Fig. 3.28 (a) and those experienced from 520 eV to roughly 540 eV can only be ionisation edges of oxygen's K edge (O-K). Furthermore, the quantitative analysis is also performed utilising this region since the edge size is proportional to the number of atoms present in the specimen, thus enabling determination of exact elemental concentration [3.22, 3.25-3.28].

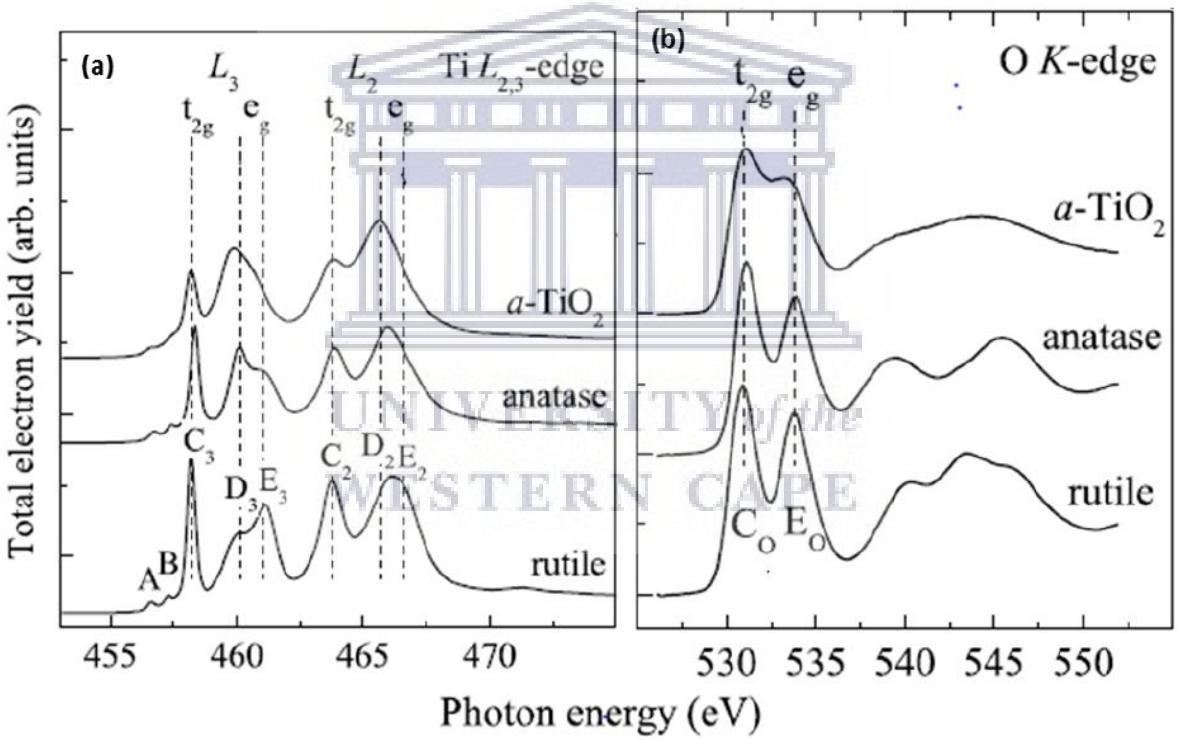

Fig. 3.28: Ionisation edges of different TiO_2 polymorphs showing (a) Ti $L_{3,2}$ and (b) O K-edge of amorphous, rutile and anatase phases of TiO_2 [3.43, 3.44].

Fig. 3.29 shows energy spectra and their first derivative of the O-K edge, while Fig. 3.30 presents Zn L_3 edge for three different ZnO samples [4.45]. As will be discussed in later chapters, the fine structure features in the spectra are washed out in both O K and Zn L_3 with

increasing oxygen vacancy in the lattice structure. Other appreciable differences in the spectra are labeled. Although in the O K spectra, there are no appreciable changes at pre-edge features as a function of O vacancies, but smearing of the fine features is observed. The absence of prominent pre edge peaks may be due to the fact that the O atoms come only in the second coordination shell of any O vacancy. On the contrary, there are clear pre-edge features for the three samples in the Zn L_3 spectra. The four main expected peaks of ZnO are labeled A, E, T, and TT in Fig. 3.30. The relative peak height of b to a is increasing with oxygen vacancy concentrations. There are also extra peaks like c, d, etc. that come up at higher oxygen deficiencies. The change in the pre edge structure can be made more pronounced from the first derivative spectra. The ratio of b to a increases slightly (0.23 – 0.5) with increasing concentrations of oxygen deficiencies [3.45].

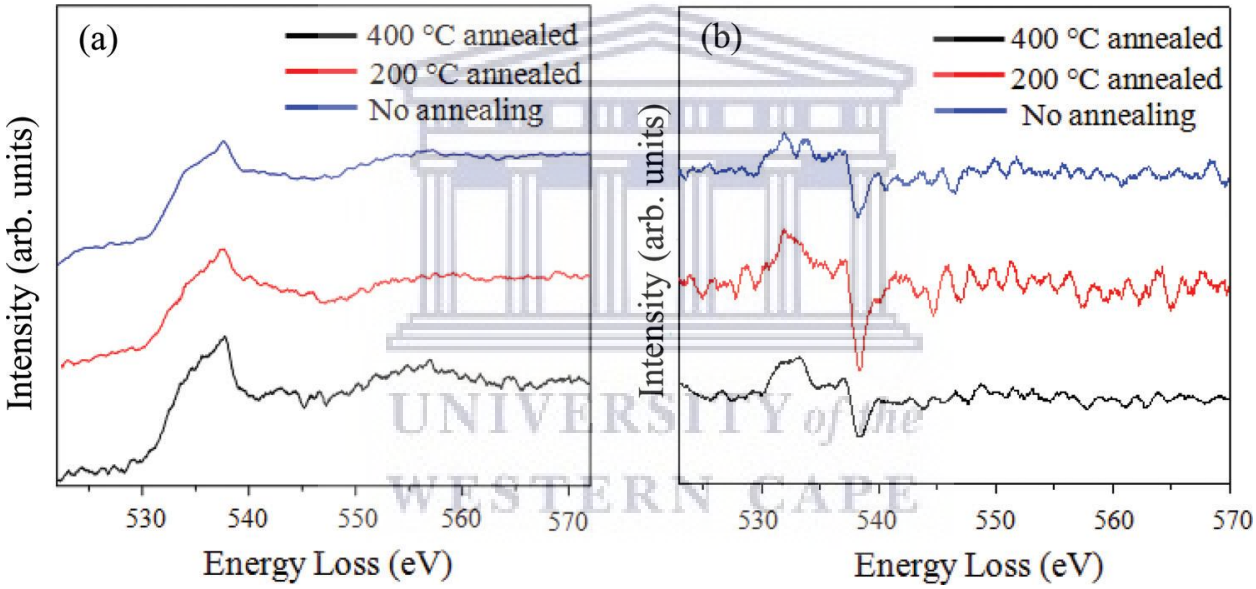

Fig. 3.29: (a) Experimental O K edge ELNES and (b) its first derivative. The pre-edge features are not clear in this case [4.45].

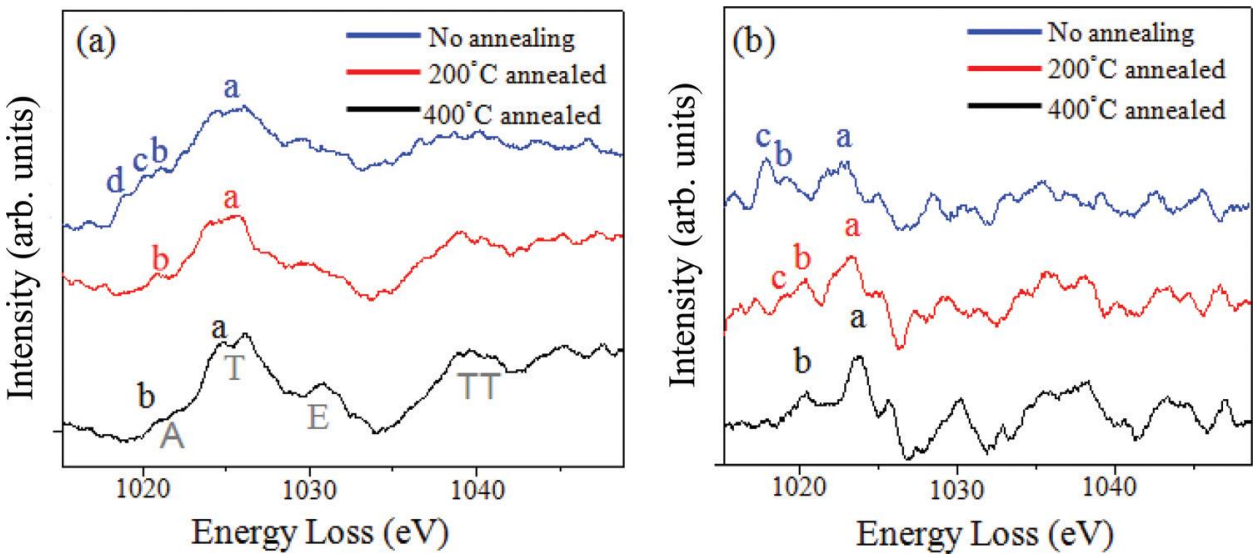

Fig. 3.30: (a) Experimental Zn L_3 edge ELNES and (b) its first derivative. The pre-edge features are labeled [3.45].

3.7 Elemental and Doping Characterisation - X-ray Photoelectron Spectroscopy

3.7.1 Overview. The X-ray photoelectron spectroscopy (XPS) technique is one of the most responsive analytical techniques employed for the measurement of surface properties such as electronic state and oxidation state, the chemical environment of an element contained within a sample usually to a depth of approximately 10 nm (Ray *et al* [3.46]). The XPS profile of a sample can be acquired through bombarding the synthesised material with an X-ray beam causing the emission of the core-level electrons from the sample, often localised at a specific binding energy position under high or ultra-high vacuum (~10-8 or < 10-9 mbar). In this study, XPS was used to study the electronic structure of the Ti and Zn 2p, O 1s and N 1s. The Ti 2p spectrum of TiO_2 NWs has two major peaks at 458 and 464 eV attributed to the binding energy of the $2p_{3/2}$ and $2p_{1/2}$ electronic shells, respectively. The ZnO has two main peaks positions at Zn 2p at 1022 eV and O 1s at 531 eV. The Zn 2p spectrum of ZnO has two major peaks at Zn $2p_{3/2}$ line located at 1022.34 eV and the Zn $2p_{1/2}$ peak at 1045.45 eV which was also studied respectively. The signals of the differently synthesised and plasma treated TiO_2 and ZnO NWs structures were collected with a Thermo ESCAlab 250Xi spectrometer using

monochromatic aluminium Kα x-rays (1486.7 eV) at a probe spot size of 900 µm and high resolution spectral energy resolution of 20 eV. This instrument is shown in Fig. 3.31 below and is hosted by The National Metrology Institute, Pretoria. The C 1s peak was used as energy scale calibration throughout all experiments and the linearity of the scan was adjusted to measure the presence of core-level Fe 2p at approximately 708 eV in the Fe:ZnO material, as well as both core-level Fe 2p and N 1s in the plasma exposed N_2 – Fe:ZnO NWs, in addition to the Zn 2p at 1022 eV and O 1s at 531 Ev. Also the C 1s species was observed at 285 eV emanate from hydrocarbon contamination, and it is assumed to be a common phenomenon for samples exposed for prolonged periods to air. The various XPS signals were plotted as a function of the measured photoelectron intensity versus the binding energy.

Fig. 3.31: Thermo ESCAlab 250Xi XPS spectrometer used in this study

3.7.2 Theory. The analysis in a few nm of surface layers of chemical state of a given metal is achieved via X-ray Photoelectron Spectroscopy (XPS). The emission of electron is done with the help of homogeneous light that been applied on the material by the photoelectric effect. The measuring method of intensity distribution and electron energy is called XPS method.

$$E_{kin}^{v} = hv - E_b - \emptyset \tag{3.21}$$

where E_{kin}^{v}, hv, E_b and $\emptyset$ are the kinetic energy of the liberated photoelectron. If hv is constant, then the binding energy can be acquire by measuring the kinetic energy of electron emitted, however the identification of element is easily possible by measuring E_{kin}^{v} because the binding energy of each electron orbit is different. Alternatively, the binding energy of same orbit of a particular element is changed a little with the influence atomic surrounding state and the environment. However, the state analysis of element is achievable by measuring this change variation known as chemical shift. Furthermore, the mean free path of electron is not so long due to the absorption and scattering process of electron in solid glass. Consequently, because XPS method can detect only the surface of nm order, then it is very suitable for thin film evaluation. Fig. 3.32 shows typical spectra for the Ti and Zn 2p electronic shells produced in this study; to be discussed in more detail in the ensuing Results and Discussion chapters.

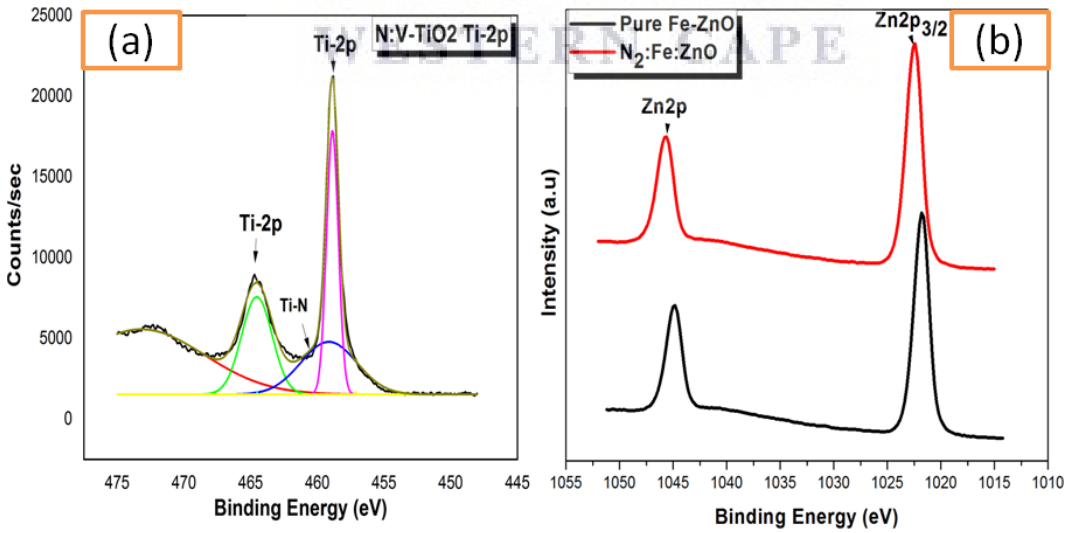

Fig. 3.32: (a) An example of TiO_2 and (b) ZnO XPS spectra.

3.7.2 Sample Preparation. The C specimen holders were cleaned with alcohol and dried with nitrogen gas. The glass samples of as synthesised TiO_2 s and ZnO nanowires were mounted separately on top of C specimen holders. While the treated TiO_2 and ZnO nanowires were mounted on carbon tape with the same type of C specimen holder used for TiO_2 s and ZnO nanowires. Prior to that, to prevent further oxidation samples were dried in a nitrogen-purged container at room temperature and then mounted into the sample cell directly. The instrumental operating conditions are given for Thermo ESCAlab 250Xi operating conditions with instrumental parameters conditions are as follows:

- Irradiation type Non-monochromatized Al Kα source
- Energy 1486.6 Ev
- Power (voltage, current) 300 W (15 keV, 30 mA)
- Scan rate 400 ms/step for 0.125 eV step-size
- Hemispherical sector energy Analyser (CHA) 178.95 eV, 0.5 eV/step and 100 ms/step
- Vacuum chamber < 10-9 mbar

3.8 Solar Cell Current-Voltage Performance Testing

Fig. 3.33 shows the Ossila T111 manual current-voltage testing system, coupled to a standard Sciencetech Solar Simulator, used to test the performance of the manufactured solar cells. The 8-pixel test board (bottom left in Fig 3.33) allows the 8-pixel substrate manufactured devices, as shown in Fig. 2.19, to be tested at 8 different regions on the substrate. This allows for an averaged data collection and reporting. The design also allows for maximum shunt current resistance and minimum series losses. The source and measure unit (SMU) allows for characterising current responses ranging from 10 µA up to 100 mA.

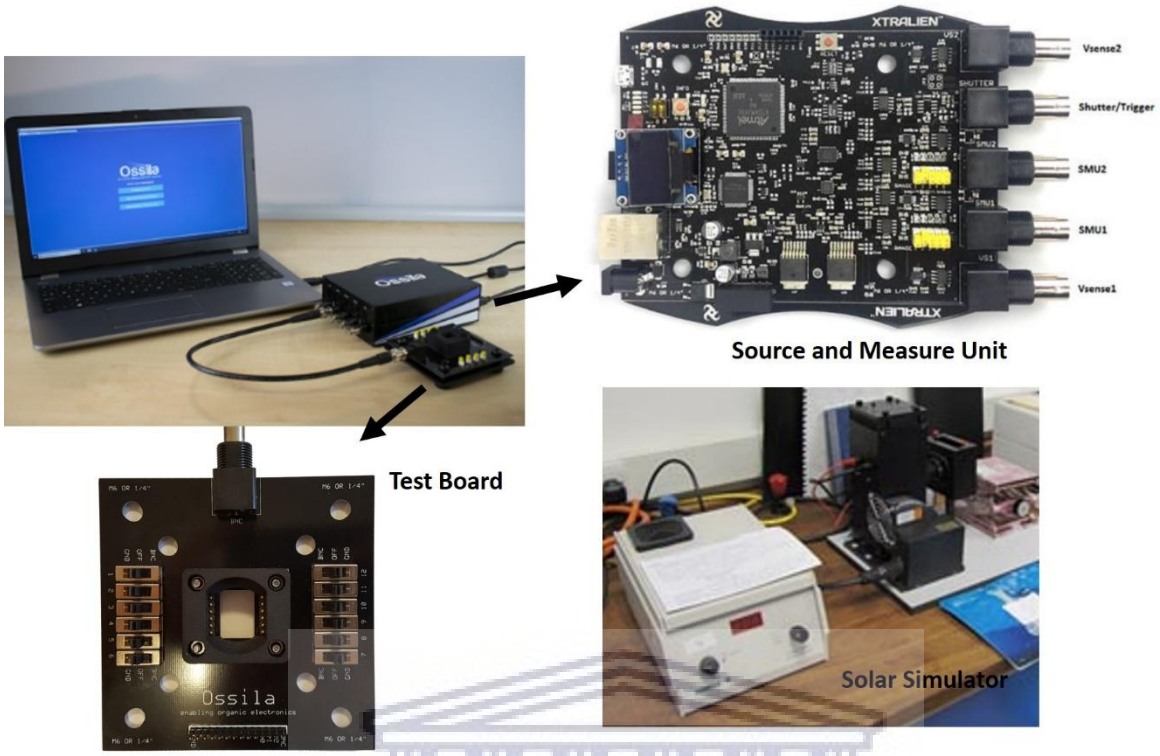

Fig. 3.33: Ossila T111 I-V curve testing kit, with the solar cell test board and the SMU enlarged; (bottom right) Solartech solar simulator used as illumination source during testing

References

[3.1] M. Fox, Optical Properties of Solids, Oxford University Press, New York USA (2001).

[3.2] R.C. Denney, R. Sinclair, D. Mowthorpe, Visible and ultraviolet spectroscopy: Published on behalf *of ACOL*, Thames Polytechnic, London, by John Wiley, *1987*.

[3.3] S. Aydogu, O. Sendil, M.B. Coban, Chinese Journal of Physics 50 (2012) 89-100.

[3.4] B.M. Weckhuysen, In situ spectroscopy of catalysts, American Scientific Publishers Stevenson Ranch (2004) 255.

[3.5] Z.M. Khoshhesab, Infrared spectroscopy-materials science, engineering and technology, 11 (2012) 233-244.

[3.6] V. Barron, J. Torrent, M.P. Morales, C.J. Serna, J.F. Boily, Q. Liu, Methods of soil analysis, 5 (2008) 367-387.

[3.7] A.D. McNaught, A. Wilkinson, Compendium of Chemical Terminology (The Gold Book), International Union of Pure and Applied chemistry (IUPAC), Second Edition (1997). Online corrected version.

[3.8] G.R. Hayes, B. Deveaud *Physica Status Solidi* 190 (2002) 637.

[3.9] R. Kellner, J.M. Mernet, M. Otto, H.M Widmer, Book of Analytical Chemistry 1st Edition. Hardcover: 942 pages, Publisher: Wiley-VCH. (March 9, *1998*).

[3.10] F.R. Cummings, Hot-Wire Chemical Vapour Deposition of Carbon Nanotubes, University of the Western Cape, Cape Town South Africa (M.Sc. Thesis 2007).

[3.11] B.D. Cullity, Elements of X-Ray Diffraction. 2nd Edition, *Addison-Wesley Publishing Company* Inc., Phillippines (1978).

[3.12] V.K. Peacharasky, P.Y. Zavalij, In Fundamentals of Powder Diffraction and Structural Characterization of Materials Publisher: Kluwer January 2003.

[3.13] P.P Ewald, Fifty years of X-Ray Diffraction, International Union of Crystallography,= Springer – Springer Netherlands 1962. (www.springer.com › book)

[3.14] G.K. Williamson, W.H. Hall. Acta Metall. 1 (1953) 22.

[3.15] A. Tolvanen, Dye-sensitized solar cells on alternative substrates-core, Helsinki University of Technology, Helsinki Finland, (M.Sc. Thesis 2003).

[3.16] P.J. Goodhew, F. J. Humphreys, Electron Microscopy and Analysis, 2nd edn Publishers: Taylor & Francis, London (1988).

[3.17] N. Yao, Focused Ion Beam Systems Basics and Applications, Cambridge University Press, New York USA, 67 – 86 (2007).

[3.18] N. Yao, Z.L. Wang, Electronics and Electron Physics, Supplement 20, Kluwer *Academic* Publishers, Boston (2005).

[3.19] T. M. Poster, S. K. Howard, A. H Johnson, K. L. McMichael, Scanning. Electron Microscope, Ladd Research Industries. United States of America 2001.

[3.20] J. Goldstein, D.E Newbury, P. Echlin, D.C. Joy, A.D. Romig Jr, C.E. Lyman, C. Fiori, E. Lifshin, Scanning Electron Microscopy and X-Ray Microanalysis, Springer US 1992.

[3.21] R.F. Egerton, Physical Principles of Electron Microscopy. An Introduction to TEM, SEM, and AEM. Authors: Springer, USA (2005).

[3.22] J.I. Godstein, H.Yakowitz, D.E Newbury, E. Lifshin, J.W. Colby, J.R Coleman, Practical Scanning Electron Microscopy, Electron and Ion Microprobe Analysis, First Edition, Plenum Press, New York 1975

[3.23] K.S. Birdi, Handbook of Surface and Colloid Chemistry, CRC Press LLC, Florida USA (2003).

[3.24] D. B. William, B. C. Carter, Transmission Electron Microscopy- A textbook for material science, Springer Science + Business Media LLC, United States of America

[3.25] J. Palisaitis, Valence electron energy loss spectroscopy of III-Nitrate of Semiconductors, Linkoping University, Sweden 2012.

[3.26] R. F. Egerton, Electron Energy-Loss Spectroscopy in the Electron Microscope Springer, United States of America (1996).

[3.27] K. Jorissen, The improvement of calculations of Electron energy loss spectroscopy, University Antwerpen, Netherlands (Unpublished PhD thesis) (2007).

[3.28] C.C. Ahned, Transmission electron energy loss spectrometry in Material science and the EELS atlas, 2nd Edition, Wiley-VCH, California, United States of America (2004).

[3.29] J.I. Goldstein, D.E. Newbury, D.C. Joy, C.E Lyman, P. Echlin, E. Lifshin, L.C. Sawyer, J.R. Michael, Scanning Electron Microscopy and X-ray Microanalysis 3rd Ed, Kluwer New York (2003).

[3.30] K.K. Christenson, J.A. Eades, Ultramicroscopy 26 (1988)113–132

[3.31] J.P. McCaffrey, J.M Baribeau, Microsc. Res. Tech. 32 (1995) 449–454.

[3.32] R.J Keyse, A.J. Garratt-Reed, P.J Goodhew, G.W Lorimer, Introduction to Scanning Transmission Electron Microscopy Royal Microscopical Society Handbook No. 39 Bios Scientific Publishers Oxford. Basic (1997).

[3.33] A.J. Garrett-Reed, D.C. Bell, Energy-dispersive X-ray Analysis in the Electron Microscope Royal Microsc. Soc. Oxford UK (2003).

[3.34] C.E. Lyman, D.E. Newbury, J.I. Goldstein, D.B. Williams, A.D. Romig Jr, J.T. Armstrong, P.E. Echlin, C.E. Fiori, D. Joy, E. Lifshin, K.R. Peters, Scanning Electron Microscopy, X-Ray Microanalysis and Analytical Electron Microscopy; A Laboratory Workbook, Plenum Press New York 1990.

[3.35] V.E. Cosslett, P. Duncumb, Flying-spot X-ray Method Nature 177 (1956)1172–1173.

[3.36] J.J Friel, C.E Lyman, Tutorial Review: X-ray Mapping in Electron-Beam Instruments, Published online by Cambridge University Press: 24 January 12 (2006)2–25.

[3.37] D.B. Williams, J.I Goldstein, D.E. Newbury, X-Ray Spectrometry in Electron Beam Instruments Plenum Press New York (1995).

[3.38] P.D. Hunneyball, M.H. Jacobs, T.J. Law, The Metals Society London (1981) 195–202.

[3.39] D.S. Bright, D.E Newbury, Concentration Histogram Imaging Analytical Chemistry 63 (1991) 243A–250A.

[3.40] J.E Wittig, J.F. Al-Sharaba, M. Doerner, X. Bian, J. Bentley, N.D. Evans, Scripta Mater. 48 (2003) 943–948.

[3.41] G.J.F. Legge, I. Hammond, J. Microsc. 117 (1979) 201–210.

[3.42] R.B. Mott, J.J. Friel, J. Microsc. 193 (1999) 2–14.

[3.43] R. Brydson. J. Phys.Condens. Matter 1 (1989) 797

[3.44] R. Brydson J. Phys.Condens. Matter 4 (1994) 3429

[3.45] K. Dileep, L.S. Panchakarla, K. Balasubramanian, U.V. Waghmare, R. Datta, Journal of Applied Physics 109 (2011) 063523.

[3.46] S. Ray, A.G. Shard, Analytical Chemistry, 22 (2011) 8659-8666.

CHAPTER FOUR

RESULTS AND DISCUSSION

The results of this chapter have been published in *Bello Ladan Muhammad and Franscious Cummings, "Nitrogen plasma treatment of ZnO and TiO_2 nanowire arrays for polymer photovoltaic applications" Surfaces and Interfaces 17 (2019) 100382*
https://doi.org/10.1016/j.surfin.2019.100382

4.1 Overview

The work reports on the simple, yet unique approach to improving the opto-electronic properties of vertically-aligned arrays of rutile TiO_2 and Wurzite ZnO nanowires by means of controlled nitrogen doping during exposure to highly kinetic radio-frequency generated N_2 plasma radicals. Morphologically, the plasma treatment causes a distortion of the vertical alignment of the nanowires due to a dissociation of the weak Van der Waals force clustering the nanowires. Optical spectroscopy show that plasma treatment increases the light transmission of TiO_2 arrays from 48% to 90%, with the ZnO arrays exhibiting an increase from 70% to 90% in the visible to UV range. The as-synthesised TiO_2 array has an indirect band gap of 3.13 eV, which reduces to 3.03 eV after N_2 treatment, with the ZnO equivalent decreasing from 3.20 to 3.17 eV post plasma exposure. A study of the 3d transition metal near edge fine structure of both Ti and Zn show that the N_2 plasma treatment of the nanowires results in nitrogen doping of both TiO_2 and ZnO lattices; this is confirmed by scanning transmission electron microscopy coupled with energy dispersive spectroscopy x-ray maps collected of single nanowires, which show a clear distribution of nitrogen throughout the metal-oxide. Application of these structures in P3HT:PCBM polymer blends shows progressive improvement in the photoluminescence quenching of the photoactive layer when incorporating both undoped and nitrogen-doped nanowires.

4.2 Morphology

Fig. 4.1 (a, c and b, d) show the micrographs of the top and cross-sectional views of the TiO_2 and N-TiO_2 NWs, respectively, whereas Fig. 4.1 (e, f and g, h) contain the micrographs of the top and cross-sectional views of the ZnO and N-ZnO NW films, respectively. These images clearly indicate that entire surface of the FTO substrates are covered uniformly and densely with vertically oriented TiO_2 and ZnO NWs. Furthermore, the TiO_2 NWs are tetragonal in shape with square top facets, which is the typical growth mechanism for tetragonal TiO_2 crystal structures [4.1]; the ZnO nanowires, in contrast, exhibit a needle-shape structure as discussed by Yhimura *et al* [4.2] and Baruah *et al* [4.3]. Moreover, it is also noticeable that the diameter of the ZnO NWs slightly increases after the plasma treatment while the vertical alignment of the nanowires, for both TiO_2 and ZnO become distorted, as can be seen from the cross-sectional images.

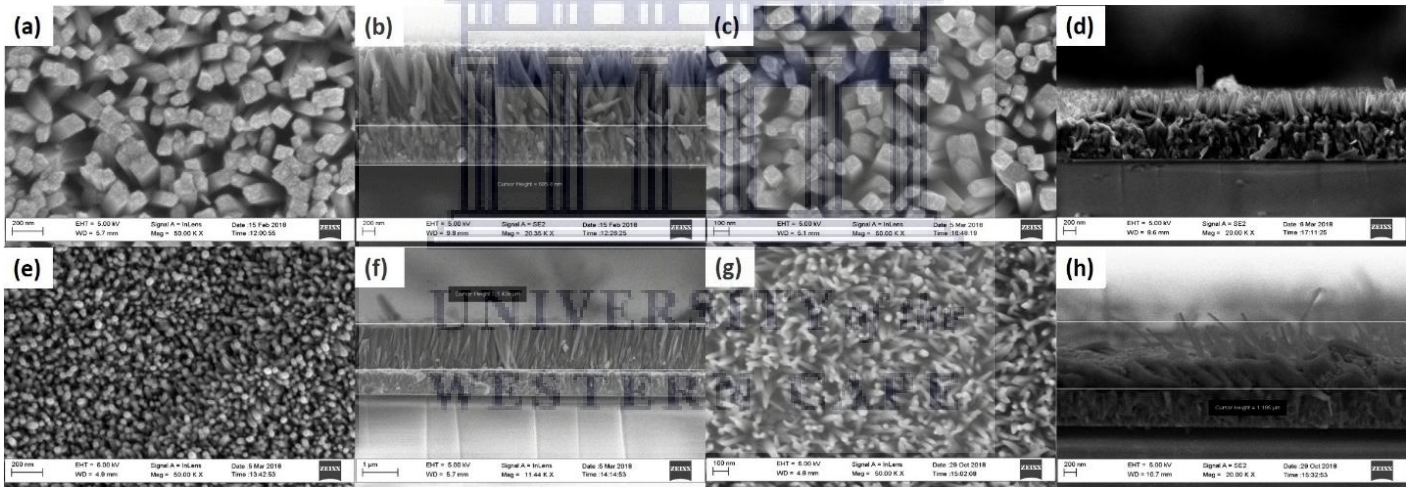

Fig. 4.1: Respective plan and cross-sectional SEM micrographs of (a, b) TiO_2; (c, d) N-TiO_2 (e, f) ZnO and (g, h) N-ZnO nanowires

The untreated TiO_2 NWs have an average diameter of 112.17 ± 29.3 nm and length of 1.391 ± 0.051 µm, while the N-TiO_2 nanowires have an average diameter of 110.9 ± 10.3 nm and length of 453.04 ± 49.2 nm. It must be noted that variance in length must be accounted for due to the error in measurement in establishing the perpendicular component in the SEM micrographs as well as the three dimensional non-alignment to the FTO substrate. The images of untreated ZnO NWs have an average diameter of 39.03 ± 6.31 nm and length is 1.33 ± 0.045 µm, with N-ZnO NWs having an average diameter of 48.47 ± 11.95 nm and

length of 1.226 ± 0.142 µm. The plan-view SEM images also show that N_2 plasma treatment decreases the areal density (i.e. number of nanowires per unit area) of the nanowires at their tops. This is due to dissociation of the weak, electrostatic Van der Waals forces bunching the nanowires at their apices. Furthermore, cross-sectional SEM micrographs show the nanowire orientation is distorted post N_2 treatment for both TiO_2 and ZnO structures; this is preferable for photovoltaic material deposition and improvement of the electron-hole dissociation interface during device operation [4.1, 4.4].

Huang *et al* [4.5] reported that an increase in nitrogen plasma treatment time of TiO_2 nanotubes leads to the decrease of surface area (length) and increases the pore diameter, which was attributed to the growth of TiO_2 crystallinities during sintering. Barakat *et al* [4.6], on the other hand, performed a similar thermal-plasma treatment of TiO_2 and found that there was no significant change of surface area between the raw and treated samples at 400˚C for 60 min. A further study by Ishihara *et al* [4.7] interestingly reported that N_2 plasma surface treatment was responsible for better photocurrent density of TiO_2 nanotube arrays for samples treated from 10 to 60 minutes. It was postulated that 10 min of plasma treatment was probably too brief to induce significant N-doping in the crystalline TiO_2 structures, whereas 60 min of treatment was found to be detrimental to the TiO_2 structure as a result of induced surface defects as compared to the 20-min treatments of the samples, which was found to be optimum. At any rate, all of the samples exposed to surface treatments (10, 20 and 60 min) had superior performance in comparison with the untreated samples. Annealing of TiO_2 nanotubes at the optimum temperature in the N_2 and O_2 atmospheres is also of critical importance in order to impart high electron conductivities which lead to high photocurrent densities. Several studies [e.g. 4.8] have shown that an annealing temperature in the range of 400 – 500˚C is most effective in transforming the amorphous phase of TiO_2 to crystalline anatase with a minimal fraction in the rutile form, whereas at higher temperatures, a more polycrystalline structure is formed with increasing amounts of rutile. These results show that nitrogen introduced in the TiO_2 lattice has a direct influence on both the crystallinity and electronic properties of the material, which in effect will influence the related optical properties. Similarly, it can be anticipated that the slight morphological changes of the TiO_2 NWs shown in Fig. 4.1 (a) to (d) post N_2 plasma treatment, will have an influence on the optical properties of the material.

In the case of nitrogen plasma treated ZnO, Allami *et al* [4.9] reported the use of 100W direct-current magnetron plasma and 450V direct-current glow discharge plasma at different exposure periods of ZnO NWs and found that N incorporated in the ZnO lattice structure with multiple chemical states, including the well-screened molecular state (α-N_2), molecular nitrogen (γ-N_2) and α-N atoms occupying O sites to form Zn_3N_2 bonds. These results are in agreement with that reported by Tabet *et al* [4.10], who added that $ZnO_{1-x}N_x$ forms by the decomposition of Zn_3N_2 and the re-arrangement of N atoms in the ZnO lattice [4.10] and NO_2^- on the surface of ZnO thin films irradiated with nitrogen species during DC magnetron sputtering at low kV. Moreover, it was found that the chemical states and bonding energies of these vibrational states differ according to the plasma treatment type. In any ionizing environment, dissociation and recombination of the plasma species occur simultaneously, with the process that becomes prevalent depending on the plasma power [4.9]. This is particularly true in this study, as the high power radiofrequency plasma employed produces all three prevalent nitrogen species, namely α-N_2, γ-N_2 and atomic nitrogen. The α-N acts as an etching agent during treatment and causes the dissociation of the weak Van der Waals forces, as discussed above, leading to the disordering of the vertical alignment of both TiO_2 and ZnO nanowire arrays. The molecular nitrogen γ-N_2 in turn forms the Zn_3N_2 bond during substitutional doping of the ZnO lattice and decomposes into the $ZnO_{1-x}N_x$. Gao *et al* [4.11] reported a change of growth direction of N-doped ZnO nanowires., whereas Yuan *et al* [4.4] reported that N-doped ZnO nanowires grown at high temperature arrange along the [110] direction compared to the [001] direction for pure ZnO structures, which is ascribed to the difference in surface energy of the (100) and (110) plane densities, with the (110) facets more inclined to the incorporation of N atoms in the lattice, subsequently inhibiting the [001] growth of ZnO. Once more, as was the case for N-doped TiO_2, these studies show that the incorporation of N in the ZnO lattice causes a clear change in growth kinetics, which in turn will influence the measured crystalline and optical properties of the structures.

4.3 Crystallinity and Structural Analysis

GIXRD patterns were collected to study the incorporation of the nitrogen in the metal-oxide lattices, the results of which are shown in Fig. 4.2 (a) and (b) for the TiO_2 and ZnO NWs, respectively. From the diffraction patterns it is found that the TiO_2 NWs grow in the

tetragonal rutile phase and ZnO in the hexagonal Wurzite structure. Considering the geometry of the incident x-ray beam, i.e. parallel to the FTO/glass substrate and hence perpendicular to the growth of the nanowires, it can be seen that the TiO_2 nanowires grow predominantly along the rutile (101), whereas the ZnO stack along the (002) basal plane of the Wurzite hexagonal structure, along the length of the nanowires. From these patterns it is determined that the as-grown TiO_2 nanowire array has lattice constants a = 0.467 nm and c = 0.292 nm, which remain unchanged post N_2 plasma exposure.

The Williamson-Hall (W-H) transformation [4.12] of the GIXRD data, shown in Fig. 4.2 (c), shows that the average crystalline grain size increases from 44 nm for the TiO_2 NWs to 60.79 nm for the N-TiO_2 NWs. At the incident x-ray beam angle of 0.4˚, these grain sizes are comparable to the nanowire diameter, which was determined to be in the range of 100 nm from the SEM results of Fig. 4.1. The increase in nanowire diameter post N_2 plasma treatment is ascribed to an increase in the lattice strain, as shown in the plot, due to the passivation of the dangling of Ti bonds deep in the TiO_2 matrix, caused by the reactive nitrogen species of the plasma during doping. In the case of ZnO an average crystalline grain size of 112.68 nm and lattice strain of 2.21 x 10^{-3} are calculated from Fig. 4.2 (d) post plasma treatment compared to a grain size and strain of 76.57 nm and 1.58 x $10^{-3,}$ respectively for the as-synthesized nanowires. Once more the increase in diameter, caused by the increased lattice strain, is ascribed to the deep level doping of the ZnO lattice by the nitrogen during plasma exposure.

4.4 Optical Properties

Fig. 4.3 (a) and (b) show UV-Vis transmittance plots with a distinct improvement in light transmittance for both TiO_2 and ZnO NW arrays post N_2 plasma treatment. In particular, it can be seen that the TiO_2 array transmittance peaks at 90% at 750 nm after treatment compared to the as-synthesized structure with a low transmittance of 48% at the same wavelength. Similarly, the ZnO array transmittance increases from 70% to 90% over the same wavelength range, post plasma exposure.

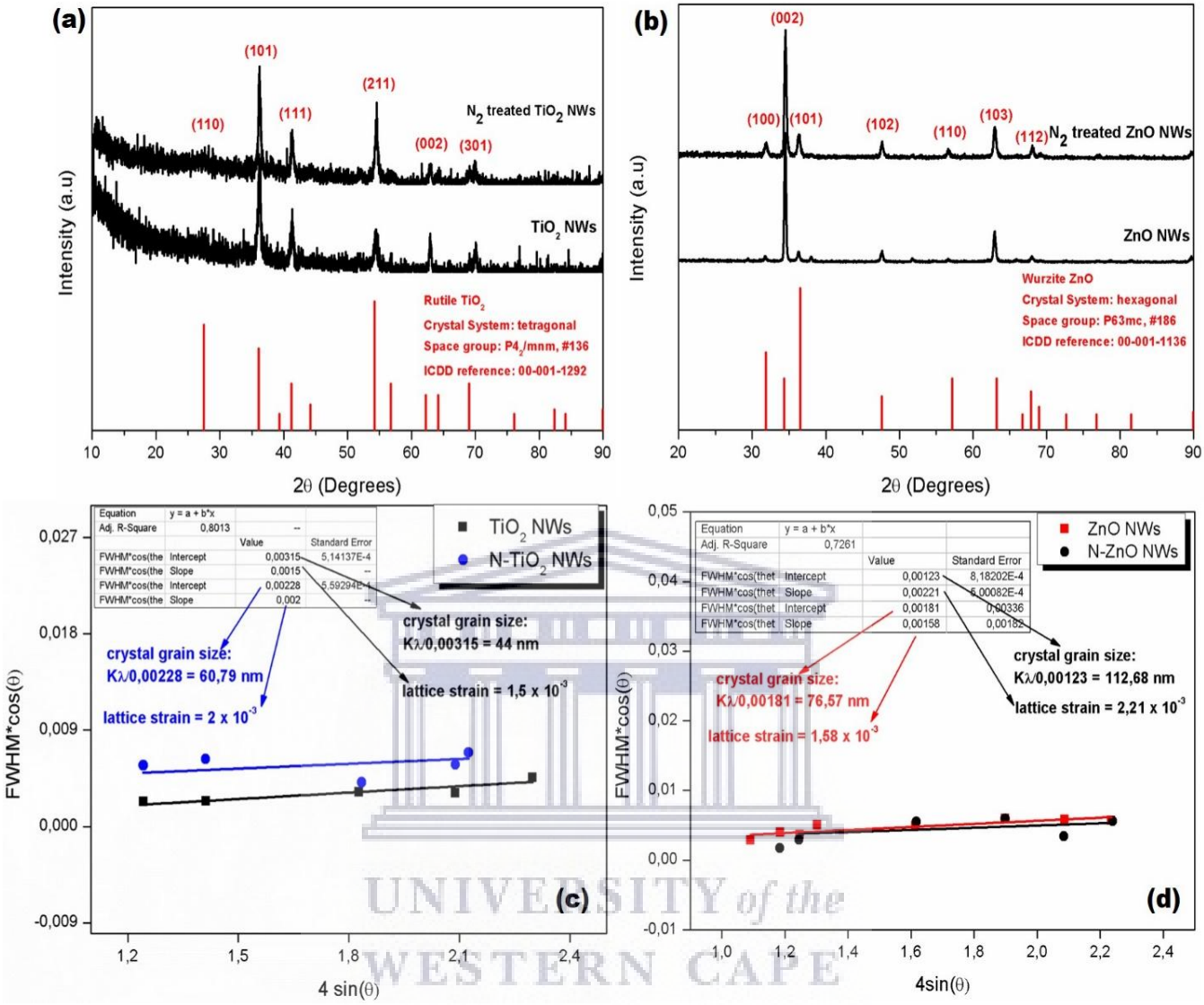

Fig. 4.2: GIXRD patterns of (a) TiO_2 and (b) ZnO NW arrays before and after N_2 plasma treatment; Williamson-Hall data of (c) TiO_2 and (d) ZnO NW arrays before and after N_2 plasma treatment.

This is a significant result considering the fact that the metal-oxide nanowire films act as electron transport layers during solar cell operation and must not impede the light penetration (when illuminated from the FTO side) of the device. The improvement in transmittance is directly attributed to the distortion of the nanowire alignment by the N_2 plasma treatment, as shown in Fig. 4.1, caused by a dissociation of the electrostatic Van Der Waals force between two adjacent, vertically-aligned nanowires. The bandgaps of both TiO_2 and ZnO before and post plasma treatment were estimated using Tauc plots. To achieve this, $(\alpha h\upsilon)^{1/2}$ versus hυ

was plotted, where α is the absorption coefficient and hυ is the photon energy. The absorption coefficient was calculated from the absorbance divided by the film thickness. The bandgap was estimated by extrapolating the linear portion of the Tauc plot of the x-axis, where value of $(\alpha\hbar\upsilon)^{1/2}$ approaches zero. The respective Tauc plots for TiO_2 and ZnO are shown in Fig. 4.3 (c) and (d).

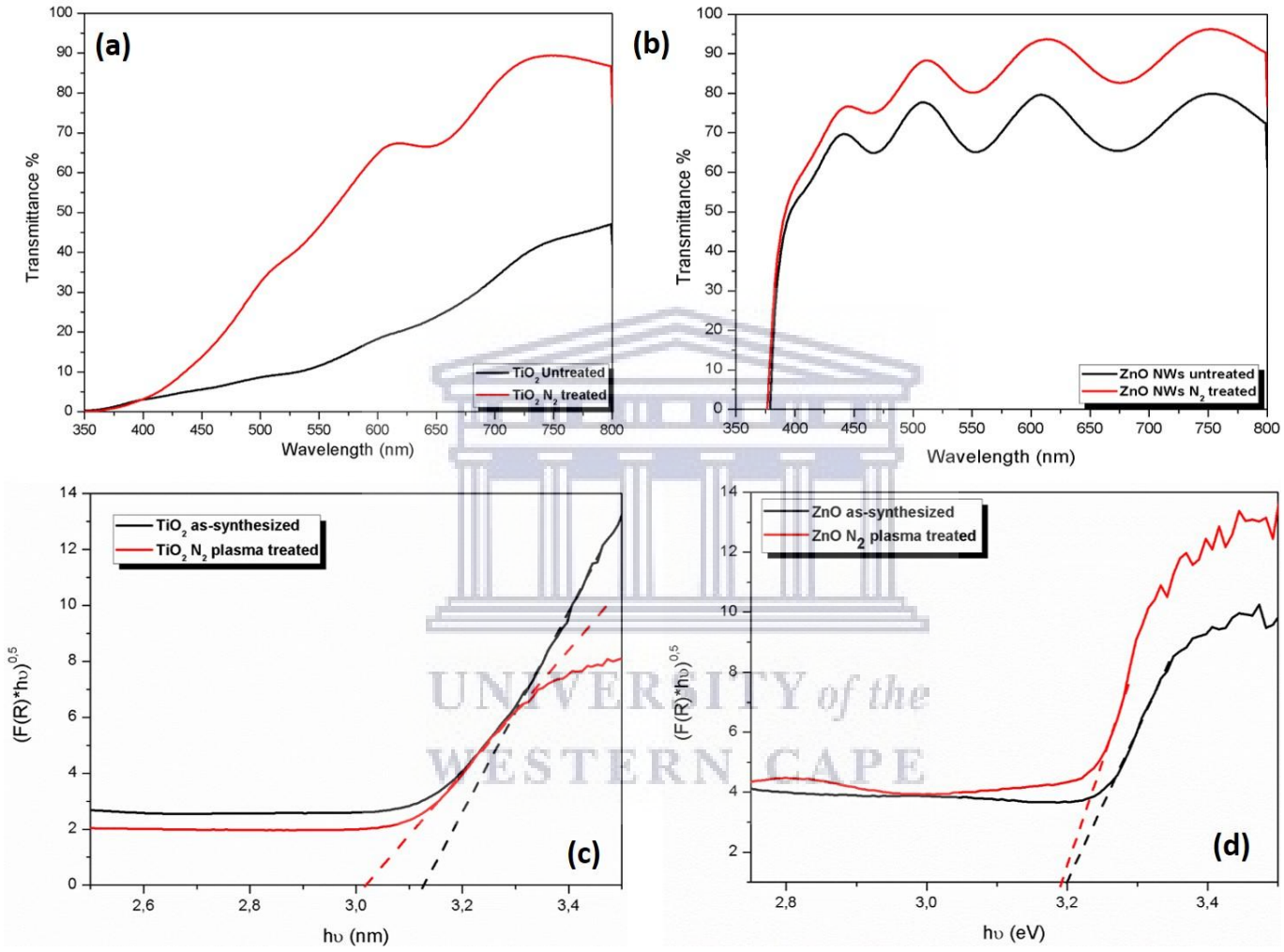

Fig. 4.3: UV-Vis transmittance plots of untreated versus N_2 plasma treated (a) TiO_2 and (b) ZnO NWs films; Tauc plots comparing the untreated and N_2 plasma treated structures of (c) TiO_2 and (d) ZnO

The band gap obtained for TiO_2 NWs is 3.13 eV before and 3.03 eV after N_2 treatment, whereas the Tauc plot band gap of ZnO NWs is 3.20 eV before and 3.17 eV post treatment. The decrease in bandgap caused by an introduction of nitrogen in the TiO_2 lattice has been

previously studied by Jinlong *et al* [4.13], who reported that nitrogen doping leads to an increase in visible light absorption, which may be attributed to the introduction of localized N 2p states, caused by atomic β-N, within the band gap. Furthermore, the reduced band gap may be due to defects (Urbach type reduction) and lattice strain. The reduction of the ZnO bandgap post N doping can similarly be explained by visiting previous literature. Reddy *et al* [4.14] reported that extensive plasma exposures increase the amount of nitrogen implanted in ZnO nanorods, with the incorporation occurring in two ways, namely by interstitial and substitutional doping. During interstitial doping, the nitrogen atoms neutralise the defect states present on the surface of ZnO materials, whereas in substitutional doping, nitrogen impurities generate interstitial defects by replacing oxygen atoms. Khranovskyy *et al* [4.15] report that, in general, the electrical conductivity of ZnO is primarily dominated by electrons generated from oxygen vacancies and zinc interstitial atoms. Various studies report that the conductivity of different types of semiconductors [4.16-4.19] reduces upon interstitial incorporation of nitrogen atoms in the lattice, diminishing the existing defect states due to passivation and subsequently minimizing the density of charge carriers. As such, the defects related absorption peak intensity strongly reduces in optical studies and may be accompanied by a decrease in band gap of ZnO since $E_g \propto n_i^{\frac{2}{3}}$, where n_i is the electron carrier density of an intrinsic semiconductor; this is also evident in Fig. 4.3 (d). Extensive literature on the structural and optical effects of nitrogen plasma treatment on ZnO nanowire arrays are not readily available. Of the few studies published, Chantarat *et al* [4.20], reported that nitrogen plasma treatment of both ZnO NWs and nanotubes causes insignificant structural damage in either structure, and noticed a reduction of the emission intensity of the deep-level donor band; this was attributed to the passivation of the surface defects, mainly oxygen vacancies, of ZnO. Elsewhere, Lin *et al* [4.21], reported that the broad emissions associated with intrinsic defects in ZnO NRs tend to disappear upon plasma treatment in NH_3 environments for 180 s, which indicates that the native defects or impurities contributing to visible transition can be greatly reduced by NH_3 plasma. However, it was observed that extensive plasma treatment can give rise to etching damage to the NR surface and results in the reduction of UV emission. These studies unanimously show that the nitrogen is introduced as a p-type dopant in the ZnO lattice during plasma treatment in a nitrogen rich environment. The dopants passivate the dangling Zn-O bond that causes oxygen vacancies, thereby slightly reducing the electron charge transport in the structure. This is accompanied by a slight decrease in the optical bandgap, but more importantly a lowering of the conduction band

minimum (E_c), which is especially important for heterojunction photovoltaic cell application, where any reduction in E_c is beneficial to the band alignment with the P3HT:PCBM blends, a final advantage of the nitrogen plasma treatment, as shown in the SEM micrographs of Fig. 4.1, extensive treatment leads to an etching effect, in accordance with [4.21], subsequently leading to lower areal density of NWs and improvement of light transmission through the nanowire array.

4.5 Polymer Photo-Electrodes Incorporating TiO_2 and ZnO NWs

Fig. 4.4 (a, b) and (c, d) show top and side-view SEM images of glass/FTO/ZnO NWs/P3HT:PCBM (1:1) and glass/FTO/N-ZnO NWs/P3HT:PCBM (1:1) photo-electrodes, respectively whereas Fig. 4.4 (e, f) and (g, h) show the SEM images of glass/FTO/TiO_2 NWs/P3HT:PCBM and glass/FTO/N-TiO_2 NWs/P3HT:PCBM (1:1), respectively. A clear distinction was observed between the untreated and treated samples of both TiO_2 and ZnO in that an increased contrast is observed as result of the N_2 treatment of P3HT:PCBM 1:1 sample on both ZnO and TiO_2 top images, as a result of the dissociation of the weak, electrostatic Van Der Waals forces on the areal density of NWs at the top, forming a less dense NW array. The cross-sectional SEM micrographs show the NW orientation is distorted after N_2 treatment for ZnO NWs, while the TiO_2 NWs remain vertically aligned to substrate, but with a lower areal density; both are recommended for photovoltaic material deposition.

HR-TEM, in combination with STEM, EDS and EELS were used to probe the internal structure, as well as the bonding and elemental concentration, as well as distribution of the N_2 treated TiO_2 and ZnO, as shown in Fig. 4.5. The analysis shows that each individual TiO_2 nanowire observed in the SEM consists of bundles of smaller nanowires (so-called fingers) having diameters ranging between of 10 and 20 nm; this is shown by the in-set of Fig. 4.5 (a) and is consistent with the structures reported by Wisnet *et al* [4.22]. In contrast, the ZnO structures primarily consist of a single structure, with a sharp, hexagonally-shaped tip, with a diameter range as determined from the SEM micrographs of Fig. 4.1; once more these are consistent with that reported previously [e.g. 4.23]. A study of the TiO_2 $L_{3,2}$ edge in the EELS spectra of Fig. 4.5 (c) shows that the ratio of the L_3 (on the lower energy side of the spectrum) to L_2 (generally referred to as white-lines) changes upon the exposure of the

nanowires to the N_2 plasma. At closer inspection, this change in ratio is found to be due to a change in the splitting of the L_3 and L_2 white-lines into respective t_{2g} and e_g sub-bands as a result of the common crystal field splitting associated with TiO_2 polymorphs [4.24, 4.25].

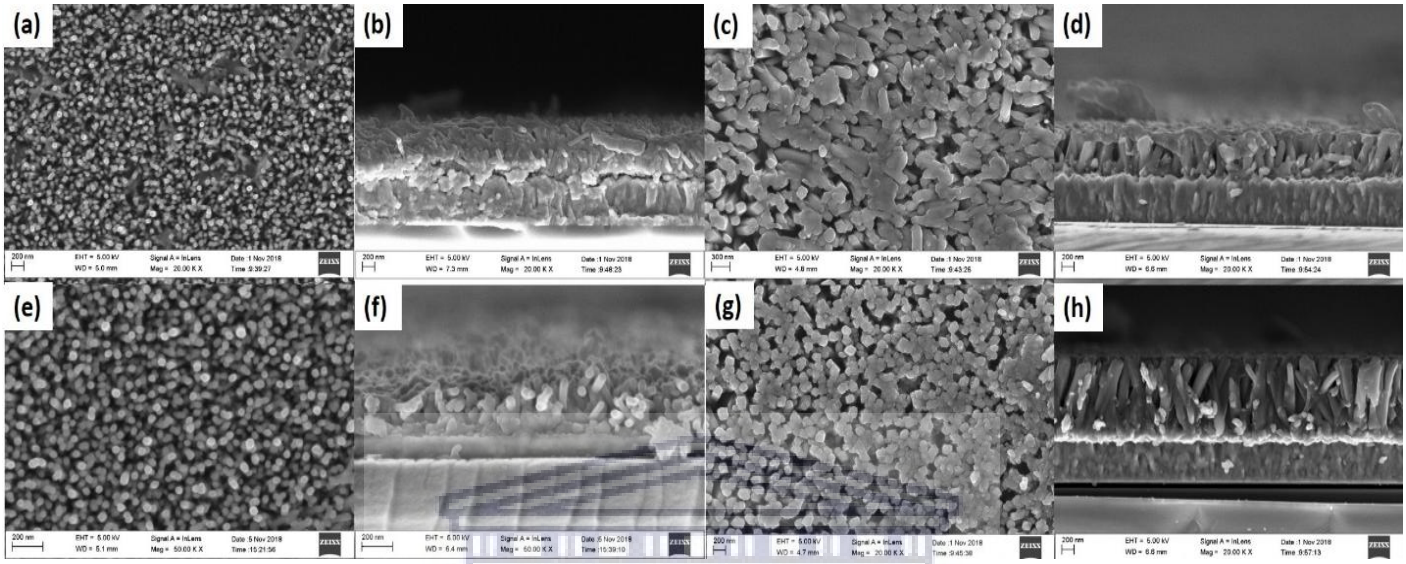

Fig. 4.4: Respective plan and cross-sectional SEM micrographs of P3HT:PCBM (1:1) spin-coated onto (a, b) TiO_2; (c, d) N-TiO_2 (e, f) ZnO and (g, h) N-ZnO nanowires

From Fig. 4.5 (c) it is found that the intensity ratio of the t_{2g} (on the low energy side of the respective L_3 and L_2 white-lines) to e_g sub-bands increases upon N_2 exposure for both the L_3 and L_2 peaks (red curve) as compared to as-synthesised TiO_2 structures (black curve). This change is indicative of the change in Ti-O $P4_2/mnm$ space group symmetry of rutile caused by the introduction of N impurity atoms in the lattice of the metal-oxide. This change in line shape, caused by the introduction of N, resembles that of other Ti_xO_y oxides, as reported previously [4.26]; in this case, however, the redistribution of the oxygen in the lattice by the N leads to the formation a Ti-N bond, thereby causing the change in symmetry. The STEM-coupled EDS spectral image (STEM-SI) collected of a single TiO_2 nanowire is shown in Fig. 4.5 (g) and the extracted elemental maps of Ti, O and N shown in colour; from these the distribution of nitrogen throughout the TiO_2 lattice is clearly observed (green colour map).

In the case of the Zn $L_{3,2}$ of Fig. 4.5 (f), the crystal field splitting leads to a sharp distinction of the L_3 and L_2 edges, post N_2 plasma treatment (red curve) compared to that found for the as-synthesized ZnO. The Zn $L_{3,2}$ edge characteristically does not split into distinct L_3 and L_2

white-lines, as in the case of TiO_2 [4.23, 4.27], and as such the presence of the sharp L_2 line at 1043 eV, is very peculiar and once more evidence that the highly kinetic N infiltrates the ZnO lattice, causing a change in the local symmetry of the Zn metal by substitutional replacement of the oxygen in the lattice.

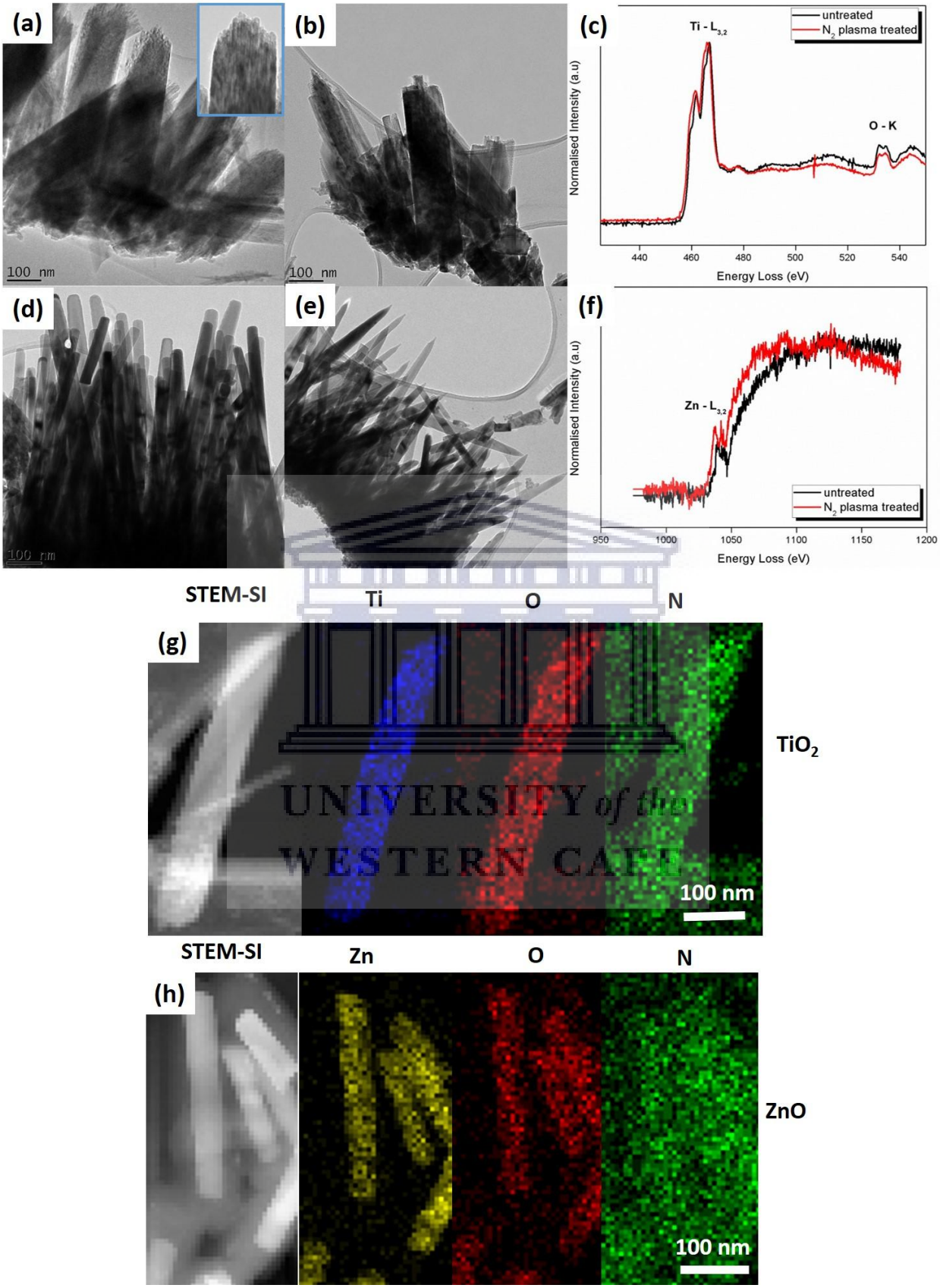

Fig. 4.5: (a, b) TEM micrographs of TiO_2 NWs and N-TiO_2 NWs, respectively; (c) electron energy loss spectra of Ti $L_{3,2}$ lineshapes before and after N_2 treatment; (d) STEM-EDS spectral image (SI) and respective elemental maps of an individual nitrogen doped TiO_2

nanowire (e, f) TEM micrographs of ZnO NWs and N-ZnO NWs, respectively; (g) EELS of Zn $L_{3,2}$ lineshapes before and after N_2 treatment; (h) STEM-SI and respective elemental maps of individual nitrogen doped ZnO nanowires

Once more, the STEM-SI map of Fig. 4.5 (h) shows the distribution of nitrogen (green map) throughout the ZnO lattice. Elemental quantification from EELS reveals that individual nanowires of TiO_2 are doped with 0.41 at% of N 100 atoms of Ti, O and N, equating to an atomic areal density of 1.86 x 10^{11} atoms/nm^2, whereas ZnO shows a N doping concentration of 0.62 at% N per 100 atoms of Zn, O and N or an areal density of 2.81 x 10^{11} atoms/nm^2. This result is in agreement with Koslowski *et al* [4.28], who reported that although an incorporation of N cannot be ruled out completely due to the EELS detection limit of around 1%, the noticeable increase in electrical properties of ZnO thin films even at low nitrogen doping levels can only be ascribed to the incorporation of the N in the ZnO lattice.

4.6 Photoluminescence Quenching

Fig. 4.6 (a) compares the PL of films of pure P3HT and P3HT:PCBM blended in 1:1 and 1:5 volume ratios, spin-coated on an FTO substrate, without the addition of an electron transport layer. As shown, in the absence of an ETL, minimal quenching of the main luminescence peak at ~ 650 nm occurs. In contrast, in Fig. 4.6 (b) an N-ZnO compact layer is added to the film arrangements of Fig. 4.6 (a) and it becomes immediately clear that exciton dissociation occurs as evidenced by the quenching of the major PL peak. When two different materials are combined, i.e P3HT:PCBM [n-type, p-type] the intensity of the PL of the pristine materials (i.e. P3HT) drops abruptly, due to the quenching behaviour of the blended mixture. This occurs due to electron transfer between the P3HT-donor and PCBM-acceptor. The drop in intensity may also be as a result of defect states present in the blended materials, which results in non-radiative recombination. Good charge separation occurs as electrons generated in conduction band of P3HT donors are completely extracted by the acceptor PCBM, these in-turn increases the charge separation and quenching intensity [4.28]. Fig. 4.6 (c) shows progressive improvement in the PL quenching of the photoactive layer, meaning the electrons and holes are effectively separated, as preferred for PV use. Similar behaviour was found for N-TiO_2 films as well as for the as synthesized NW films (not shown in the manuscript for

conciseness). The PL spectrum peaks reported are similar to the results reported in [4.29-4.32], while Omar *et al* [4.33] reported that these peaks originate from recombination of electron-hole (e-h) pairs, localized within small sp^2 carbon clusters embedded within sp^3 matrix and agglomeration phenomena. The results of Fig. 4.6 show that the plasma treated layers are suitable for application in polymer solar cell devices.

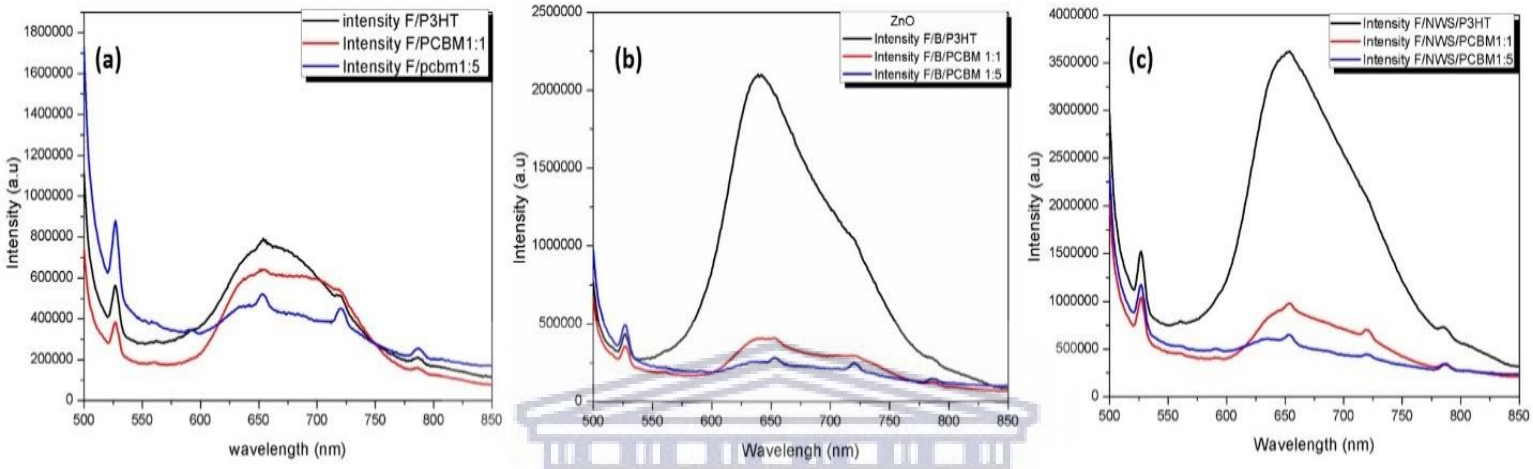

Fig. 4.6: PL comparing quenching behavior of the P3HT:PCBM blends (a) without an electron transport layer (ETL); (b) with the addition of a N-ZnO compact layer as an ETL; (c) ZnO NW array as an ETL

4.7 Conclusions

In this study the optical properties of vertically-aligned arrays of rutile TiO_2 and Wurzite ZnO nanowires were modified by the introduction of N into the respective metal-oxide host lattices, during exposure to a radio-frequency generated nitrogen plasma at a high operating power. It was found that the nitrogen doping reduces the bandgaps of both TiO_2 and ZnO, as a result of the introduction of localized N 2p states close to the metal-oxide valence caused by a β-N bonding arrangement. Moreover, it was found that the changes are caused by N doping levels of less than 1 at% in individual TiO_2 and ZnO nanowires, which changes the crystal field splitting of both Ti $L_{3,2}$ and Zn $L_{3,2}$ edges as measured by EELS. Upon application of these structures in P3HT:PCBM polymer blends the photoluminescence quenching of the photoactive layer is significantly improved for both as-prepared and nitrogen-doped nanowires, thus making it an interesting and promising architecture for overall device efficiency improvement.

References

[4.1] Z. Zhou, J. Fan, X. Wang, W. Zhou, Z. Du, S. Wu, ACS Appl. Matter Interfaces 8 (2011) 4349-4353.

[4.2] M. Yhimura, K. Byrappa, J. Material Sci. 43 (2008) 2085-2013.

[4.3] S. Baruah, J. Dutta, Sci. Technol. Adv. Mater. 10 (2009) 013001.

[4.4] G.D. Yuan, W.J. Zhang, J.S. Jie, X. Fan, J.A. Zapien, Y.H. Leung, L.B. Luo, P.F. Wang, C.S. Lee, S.T. Lee, Nano Lett.8 (2008) 2591-2597.

[4.5] C.M. Huang, L.C. Chen, K.W. Cheng, G.T. Pan, J. Mol. Catal. A. Chem. 261 (2007) 218-224.

[4.6] M.A Barakat, R. Kumar, Springer Briefs in Molecular Science. Springer, Cham. (2016) 1-29.

[4.7] H. Ishihara, J.P Bock, R. Sharma, F. Hardcastle, G.K. Kannarpady, M.K. Mazumder, A.S. Biris, Chem. Phys. Lett.489 (2010) 81-85.

[4.8] N. Martin, C. Rousselot, D. Rondot, F. Palmino, R. Mercier, Thin Solid Films 300 (1997) 113-121.

[4.9] S. Allami, Z.D.A. Ali, Y. Li, H. Hamody, B.H. Jawad, L, Liu, T. Li, Heliyon 3 (2017) e00423.

[4.10] N. Tabet, M. Faiz, A. Al-Oteibi, J. Electron. Spectrosc. Relat. Phenom. 163 (2008) 15–18.

[4.11] J. Gao, X. Zhang, Y.Sun, Q. Zhao, D.Yu, Nanotechnology 21 (2010) 245703.

[4.12] V.D. Mote, Y. Purushotham, B.N. Dole, J. Theor. Appl. Phys. 6 (2012) 6-10.

[4.13] L. Jinlong, M. Xinxin, S. Mingren, X. Li, S. Zhenlun, Thin Solid Films 519 (2010) 101-105.

[4.14] N.K. Reddy, M. Devika, Y. Hahn, Nano convergence 1 (2014) 26-31.

[4.15] V. Khranovskyy, J. Eriksson, A. Lloyd-Spetz, R. Yakimova, L. Hultman, Thin Solid Films 517 (2009) 2073-2078.

[4.16] S.Y. Myong, K.S. Lim. Journal of Applied Physics 95 (2004) 1525-1530.

[4.17] T. Mattila, S.H. Wei, A. Zunger, Phys. Rev. B 60 (1999) R11245.

[4.18] P. R. C. Kent, A. Zunger, Phys. Rev. B 64 (2001) 115208.

[4.19] D.E. Aspnes, Surf. Sci. 37 (1978) 418.

[4.20] N. Chantarat, Y. Chen, S. Chen, C. Lin, Nanotechnology 20 (2009) 395201.

[4.21] C.C. Lin, H.P. Chen, S.Y. Chen, Chem. Phys. Lett. 404 (2005) 30–34.

[4.22] A. Wisnet, S.B. Betzler, R.V. Zucker, J.A. Dorman, P. Wagatha, S. Matich, *et al.*, Crystal Growth and Design 14 (2014) 4658−4663.

[4.23] Y. Ding, Z.L. Wang, Journal of Electron Microscopy 54 (2005) 287-291.

[4.24] R.D. Leapman, L.A. Grunes, P.L. Fejes, Phys. Rev. B 26 (1982) 614 - 635.

[4.25] R. Brydson, J.M. Thomas, Solid State Commun. 64 (1987) 609-612.

[4.26] E. Stoyanov, F. Langenhorst, G. Steinle-Neumann, American Mineralogist 92 (2007) 577-586.

[4.27] Z.H. Zhang, X.Y. Qi, J. K. Jian, X.F. Duan, Micron 37 (2006) 229 – 233.

[4.28] U. Koslowski, K. Ellmer, P. Bogdanoff, T. Guminskaya, H. Tributsch, J. Vac. Sci. Technol. A. Vac. Surf. Films 24 (2006) 2199-2205.

[4.29] T.A. Chen, X. Wu, R.D. Rieke, Journal of American Chemistry Society, 117 (1995) 233-244.

[4.30] G. Janssen, A. Agurre, E.Goovaerts, P. Vanlaeke, J. Poortmans, J. Manca, Eur. Phys. J. Appl. Phys. 37 (2007) 287-290.

[4.31] H. Wang, W. Hai-yu, B. Gao, L. Wang, Z. Yang, X. Du, Q. Chen, J. Song, H. Sun, Nanoscale, 3 (2011) 2280-2285.

[4.32] P. Jorge, D.E. Tieneke, B.A. Artem, V. Loosdrecht, H.M. Paul, K. Walter, T.M. Tuan, M. Juleon, D.A.L. Siebbeles, J. Phys. C 113 (2009) 14500-14506.

[4.33] B. Omar, P.M. Nametso, M. Khenfouch, A. Bokour, M. Baitoul, M. Maaza, J.W. Venturini, Nanomater. Nanotechnol. 5 (2015) 71-76.

CHAPTER FIVE

RESULTS AND DISCUSSION

The results of this chapter have been published in B.L. Muhammad, N.V. Peterson, L. Kotsedi, F.R. Cummings, "RF nitrogen plasma irradiation of metal-doped TiO_2 nanowire arrays as an effective technique for improved light transmission and optical bandgap manipulation", Chemical Physics 538 (2020) 110922

https://doi.org/10.1016/j.chemphys.2020.110922

5.1 Overview

This chapter focuses on the effects of the addition of transition metals, as experimentally discussed in Chapter 2, on the structural and optical properties of TiO_2 NWs and is an expansion of the preliminary study done in Chapter 4. It will be shown that Sn^{4+} in the TiO_2 lattice causes defect broadening along <100> of individual nanowires causing lattice distortion, which is different to Cr^{3+} and V^{3+} doping which etch TiO_2 {110} and {111} faces, causing increases in nanowire diameter. Morphologically, nitrogen plasma exposure affects no visible change in structure, but does reduce the areal density of nanowires, subsequently yielding improved light transmission through the array. Tauc transformations of diffuse reflectance data show that the combination of metal-doping and plasma treatment decrease the optical bandgap of the TiO_2 lattice. This decrease may well be attributed to nitrogen doping occurring during plasma treatment, with the introduction of nitrogen in the metal-doped TiO_2 lattice leading to band narrowing as a result of localised N 2p states introduced by the β-N species present in the plasma.

5.2 Growth Model During In-Situ Metal Doping

Fig. 5.1 shows respective SEM top- and cross-sectional micrographs of the pristine (a, b), V doped (c, d), Cr doped (e, f) and (g, h) Sn doped TiO_2 NW arrays hydrothermally grown and subsequently exposed to the N_2 plasma. From the plan-view micrographs of Fig. 5.1, the average NW width of $TiO_2 – N_2$ is measured at 57.92 ± 6.25 nm, which increases to 61.24 ± 6.53 nm when metal-doped with V ($V:TiO_2 – N_2$) and 74.35 ± 7.54 nm for the $Cr:TiO_2 – N_2$ sample. As evident from Fig. 5.1 (g) and (h), Sn doping markedly changes the morphology of the TiO_2 NW array, with the width almost doubling due to fusing of the NWs at their tops; an average diameter of 92.58 ± 19.61 nm is determined for $Sn:TiO_2 – N_2$. From the side-view micrographs the NW array lengths are as follow: $TiO_2 – N_2$ = 457.8 nm; $V:TiO_2 – N_2$ = 453.4 nm; $Cr:TiO_2 – N_2$ = 623.7 nm and $Sn:TiO_2 – N_2$ = 740.2 nm, yielding respective aspect ratios of 7.90, 7.40, 8.39 and 7.99 when incorporating the various metal dopants.

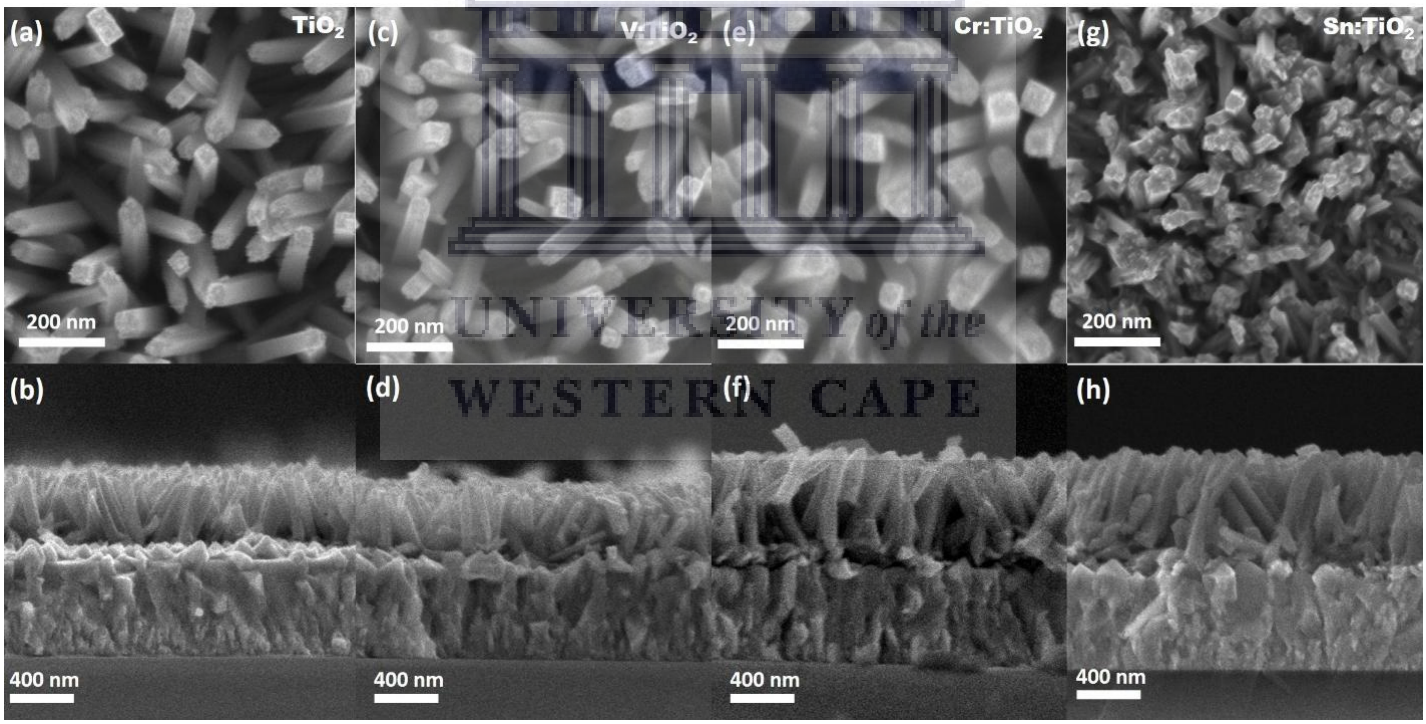

Fig. 5.1: SEM top and side views of (a, b) $TiO_2 – N_2$, (c, d) $V:TiO_2 – N_2$, (e, f) $Cr:TiO_2 – N_2$ and (g, h) $Sn:TiO_2 –N_2$

The SEM micrographs of untreated NW arrays are shown in the supplementary information of Appendix A, Fig. S1. From these images the same trends and changes in the NW diameter and length are observed when incorporating the different metal dopants into the TiO_2 matrix,

thereby implying that the N_2 plasma treatment causes no visible change in the structure of the NWs; hence the observed morphological changes are primarily due to the metal doping introduced during hydrothermal growth. This will be elaborated below when discussing the growth model of the NWs. What is noticeable, however, is a definite decrease in the areal density (i.e. number of NWs per square area) post N_2 treatment, and in particular, the detangling of the wires at their apices. This unbundling is ascribed to the weakening of the electrostatic Van der Waals forces, which are responsible for the roping of the wires at their ends, by the charged N_2 ions in the plasma. Spectral images collected during STEM-coupled EDS analysis are shown in Fig. 5.2 in which it can be seen that individual NWs contain both N_2 and the various metal dopants in their structures; a visual indication of the doped TiO_2 NWs, but lacking in-depth detail of the nature of both N_2 and metal doping. To address these issues, further structural analyses were performed, as discussed below.

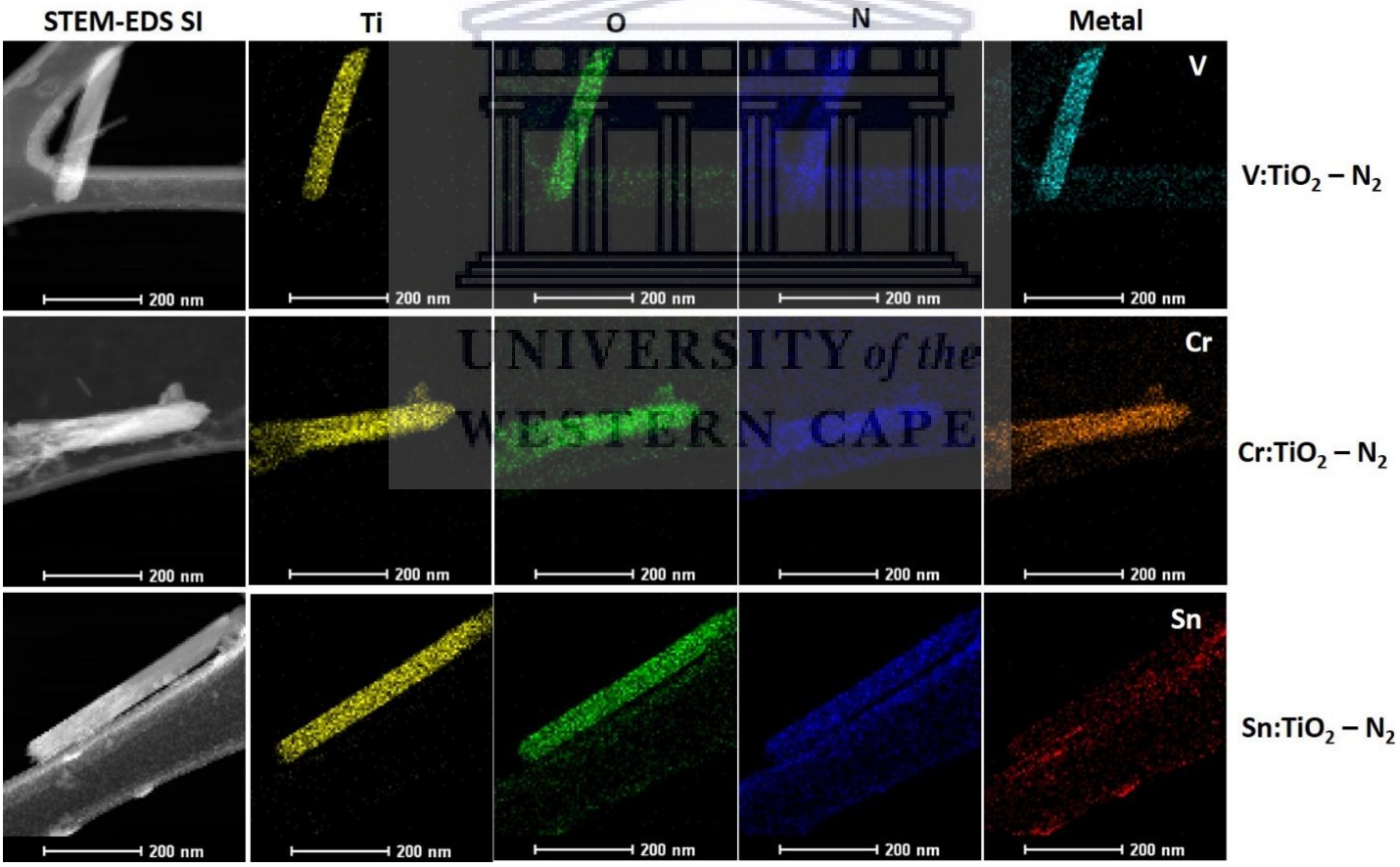

Fig. 5.2: STEM-EDS spectral images of individual metal-doped TiO_2 NWs plasma treated under N_2 plasma

The TEM bright-field (BF) micrograph of Fig. 5.3 (a) shows that the N_2 plasma treated, pure TiO_2 NWs are faceted, with clear diffraction contrast visible. Moreover, the dark contrast of the NW suggests that the predominant face orientated to the electron beam comprises of the highest electron dense set of planes of TiO_2, i.e. {111}. This is confirmed by the HR-TEM micrograph of Fig. 5.3 (b), where the lattice fringes of the {111} planes are observed. At closer inspection, growth is found to be along the NW length in the [001] direction, in accordance with previous studies [5.1]. The NWs comprise of individual *"fingers"* as shown by the BF image of Fig. 5.3 (c). The width of these structures vary between 5 and 10 nm in agreement with that noted by Wisnet et al [5.2], who proposed that the fingers are formed by V-shaped defect cascades (shown by rectangles in Fig. 5.3 (d)) which originate from the NW bottom, run along the [001] growth direction and terminate into the finger-like sub-wires at the tip of the structure. The bunched fingers, which are compacted into the block-like NW structure, can be seen in the plan-view SEM micrograph of Fig. 5.3 (d). The ascending face of a single finger is orientated in (001) as shown by the HRTEM micrograph of Fig. 5.3 (e) and blunts the tip of the finger. TEM micrographs of the metal-doped NWs are shown in Fig. S2, but for conciseness will not be discussed in detail here, as the structural features observed are similar to that noted for the non-metal-doped TiO_2 NWs of Fig. 5.3, especially for the V and Cr doped TiO_2 samples. In the case of Sn:TiO_2 – N_2 a distinct increase in the amorphous tissue is noticeable in both the TEM and SAED data of Fig. S2.

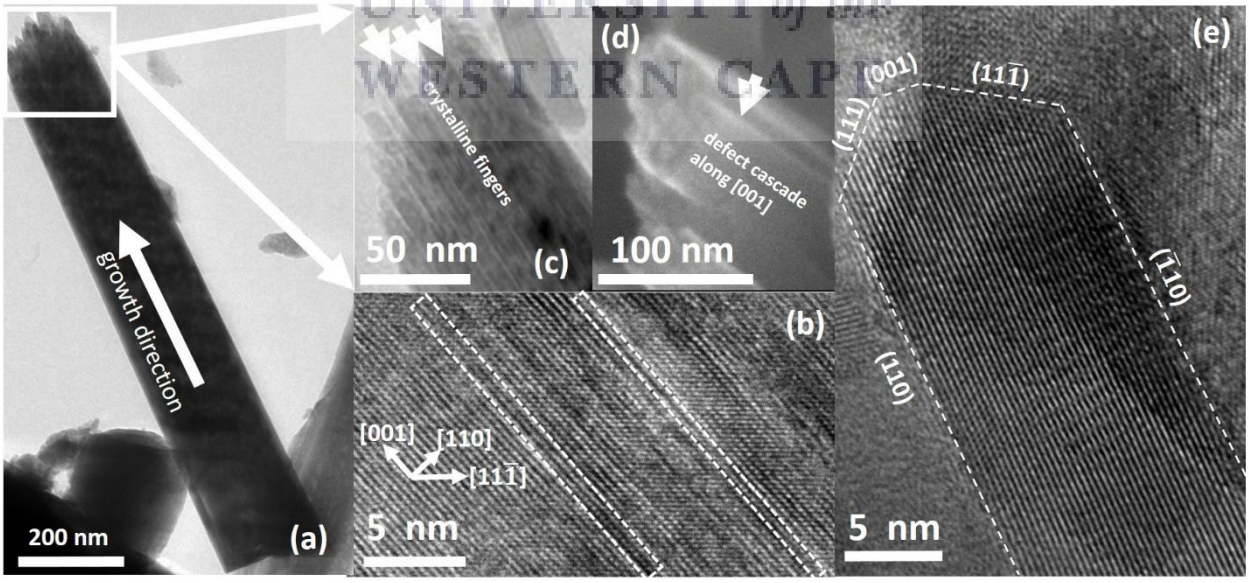

Fig. 5.3: (a) TEM bright field micrograph views of a single TiO_2 - N_2 NW; (b) HR-TEM micrograph with the defect structures along [100] indicated by rectangles; (c) and (d) respective TEM and SEM micrographs of individual TiO_2 fingers bunched together to form

the overall NW structure; (e) HR-TEM image of a single finger with the different facets indicated.

The rate determining step of TiO_2 NW growth, which primarily affects the NW width, emanates from the transformation of the $Ti(BuO)_4$ into $TiCl_4$ in solution and subsequent etching of the {111} high surface energy facets by the Cl^- ions [5.2] during the following reaction:

$$Ti(BuO)_4 + 4HCl \rightarrow TiCl_4 + 4HBuO \qquad (5.1)$$

It is suggested that NW length is terminated by the depletion of Ti in the precursor solution, as a result of NW formation as well as nanoparticle formation in solution and growth of other TiO_2 structures in the high pressure liner [5.3]. During growth, the $TiCl_4$ releases two Cl^- ions into solution and bonds to the surface hydroxyl ions at the {111} faces, subsequently leaving two dangling Cl^- ions on the {111} face. The dangling Cl^- ions are then replaced by OH^- to facilitate layer-by-layer growth on the {111} facets which also promotes the growth along the [001] axis. The {110} faces found on the side of individual fingers fuse individual NW fingers side-by-side due to their much lower surface energy compared to {111}. An increase in the size of the ions involved in the growth process significantly increases the defect density along the [100] growth direction [4.4], which explains the marked increase in diameter and change in internal structure of the NWs when incorporating $SnCl_4$ in the precursor solution during preparation of the $Sn:TiO_2 – N_2$ sample, as shown in Fig. 5.1 (g and h). The $SnCl_4$ hydrolizes and subsequently forms $Sn(OH)_4$ complexes with excess Cl^- ions in solution. The Sn hydroxyl bonds to the surface OH^- molecules, in competition with the $TiCl_4$. Steric hindrance effects on both {111} and {100} faces between the bigger $Sn(OH)_4$ hydroxyl (topological polar surface area, TPSA = $4Å^2$) and the smaller $TiCl_4$ (TPSA = $0Å^2$) result in the slowing of the Sn^{4+} incorporation into the TiO_2 lattice. The bigger, octahedrally coordinated Sn^{4+} ion, causes pronounced broadening of the defect cascades along the [100] growth direction, ultimately resulting in the disordering of the TiO_2 lattice. This is manifested by amorphous tissue observed in the TEM and SAED micrographs of Fig. S2. The excess Cl^- ions in solution leads to continued etching of the slowly growing {110} edges thereby increasing the diameter of the NW and especially the bundling of the NW fingers at the top of the NW structure as shown in Fig. 5.1 (g, h). The addition of $CrCl_3$ and VCl_3, respectively, to

the $Ti(BuO)_4$ containing precursor dissolve in water to release Cr^{3+} and V^{3+} with excess Cl^- in solution. As discussed above, these cations partake in the etching of the {110} and {111} faces, with the abundant chloride ions in solution leading to continued etching of the {110} side walls of the individual fingers thereby yielding the bigger diameters observed in Fig. 5.1 for the doped TiO_2 NWs. The non-equilibrium state of the reactants in the liner during growth leads to uncertainty in predicting the NW length. The excess Cl^- ions in solution post doping should lead to greater $TiCl_4$ formation and subsequently a faster rate of Ti depletion, thereby limiting the NW length. However, as shown in Fig. 5.1, the NW length definitely increases with an addition of Cr and Sn precursors in the reactor vessel. This suggests that the release of the excess chlorides by the V and Sn chloride precursors into solution leads to a competition between the NW diameter expansion and length contraction as suggested by the growth model and subsequently explains the wider diameters and increased lengths observed for these structures in Fig. 5.1.

5.3 Crystallinity and Structural Characteristics

The GIXRD patterns of the different NWs are shown in Fig. 5.4. From the analysis of the patterns it is found that they crystallize exclusively in the rutile polymorph of TiO_2, with no anatase phases detected. The major diffracting planes are indexed as shown, according to JCPDS #00-001-1292, with the rutile (101) Bragg peak being the most intense. Since the parallel incident x-ray beam (0.4° to the FTO surface during the GIXRD experiment) largely diffracts off the {101} family of planes, it corroborates the growth model discussed above, in that the side facets of individual NW fingers expose the (101) faces of rutile during growth. The stress induced by introduction of foreign atoms in the TiO_2 host lattice as well as its effect on the average crystalline grain sizes may be approximated by first principle Williamson-Hall (W-H) plots, as shown in Fig. S3 and tabulated in Table 5.1.

It is well known that the W-H approximation only considers the isotropic nature of the lattice, based on the assumption that the unit stress induced in the lattice is independent of the (hkl) direction along which it is measured. In nature, however, this is not always the case, and as such the anisotropic root mean square strain $<\varepsilon_{RMS}>$ formulation from W-H, as discussed in [5.6] is also considered and tabulated in Table 5.1. From this it can be seen that the

anisotropic approach yields no clear trend in the stress measured in the various (hkl) directions labelled in Fig. 5.4 when introducing the different metals, or N_2 during the in-situ doping and plasma exposure, respectively, whereas the overall lattice strain from W-H, ε_{hkl}, shows that the increase in metal diameter introduced in the TiO_2 lattice induces an incremental increase in the microstrain of the system. This also accounts for the increase in the average crystal sizes listed in Table 5.1.

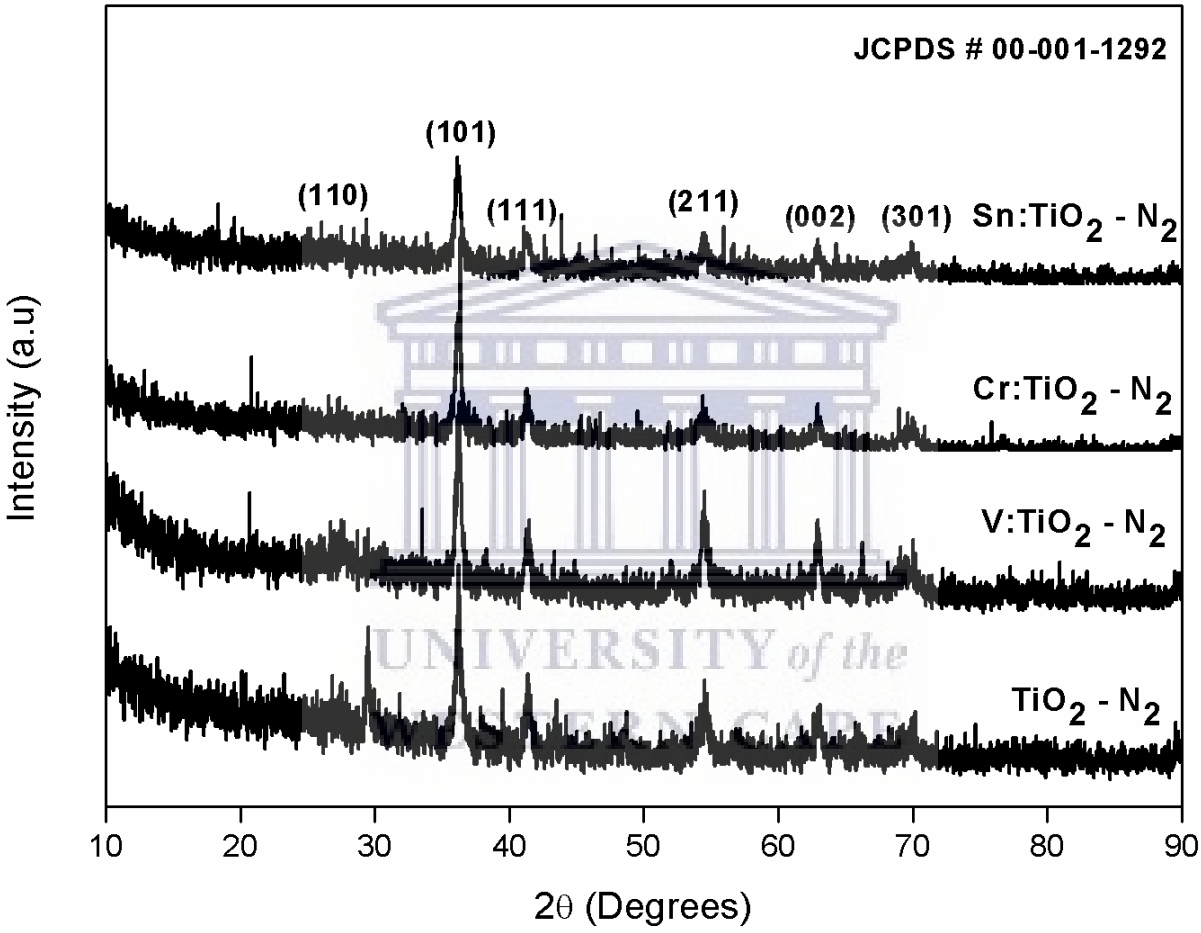

Fig. 5.4: GIXRD patterns of the un-doped and metal doped N_2 plasma treated TiO_2 NWs

Also noticeable from Table 5.1 is the insignificant change in cell volume and individual lattice constants when comparing the as-synthesised, untreated TiO_2 lattice to the N_2 plasma treated lattice prior to metal incorporation, suggesting that the N_2 is substitutionally positioned in the lattice of the unit cell of the plasma-treated doped NWs, with the Cr and Sn infused cell volumes showing a total increase of 5% compared to the as-synthesised, untreated TiO_2 lattice. A study of the individual lattice constants shows that the introduction

of V reduces the lattice constant in the <**a**> direction, but increases the volume of the unit cell in the <**c**> direction. Conversely, Cr and V doping leads to significant increase of lattice parameter, **a**, accompanied by a decrease in **c**. With these changes it can also be seen that the unit cell volumes progressively increase upon doping by the different metals. These trends may be attributed to substitutional replacement of the Ti by the bigger metallic ions in the lattice, rather than interstitial doping, since a consideration of the a/c ratio for the different doped samples shows a consistent ratio of approximately 1.6 for all three doped samples, which closely matches that of the non-metal doped, N_2 treated TiO_2 sample. From Table 5.1 it can also be seen that the average grain size is very close to the NW diameter obtained from the SEM micrographs of Fig 5.1. As shown in Fig. 5.3, individual NWs predominantly crystallise in one preferred orientation along the NW diameter, as such the average grain size obtained from the W-H data may be used as a good estimate of the NW diameter.

Table 5.1: Lattice properties obtained from Williamson-Hall and GIXRD patterns of Fig. 5.4

	SEM diameter (nm)	**W-H Crystal Grain Size (nm)**	**ε_{hkl} (x 10^{-3})**	**$<\varepsilon_{RMS}>$ (x 10^{-3})**	**Lattice Parameter a; c (nm)**	**Unit Cell Volume (x 10^3 nm^3)**
$TiO_2 - N_2$	57.92 ± 6.25	53.74	1.94	4.6	0.460; 0.294	62.18
V:$TiO_2 - N_2$	61.24 ± 6.53	66.66	1.89	3.41	0.455; 0.296	61.35
Cr:$TiO_2 - N_2$	74.35 ± 7.54	72.59	2.3	5.1	0.471; 0.290	64.40
Sn:$TiO_2 - N_2$	57.92 ± 6.25	77.46	30.8	4.04	0.469; 0.291	64.08

5.4 Nitrogen Doping by Plasma Irradiation

XPS was used to probe the nitrogen doping mechanism in both pure and metal-doped TiO_2 NWs. Fig. 5.5 (a) and (b) show high-resolution spectra of the variation in the chemical states of the titanium (Ti 2p) and oxygen (O 1s) ionic sites, respectively, whereas the individual spectra with their deconvolution data are shown in Fig. S4 and Table S1. The Ti 2p spectra show that TiO_2 NWs (black curve in Fig. 5.5 (a)) has two major peaks at 458 and 464 eV attributed to the binding energy of the $2p_{3/2}$ and $2p_{1/2}$ electronic shells, respectively. The relative quantum ratio of these two states is obtained using the formula:

$$X:Y:Z = \frac{\left(\frac{A}{f_1}\right)}{\left(\frac{A}{f_1}+\frac{B}{f_2}+\frac{C}{f_3}\right)} : \frac{\left(\frac{B}{f_2}\right)}{\left(\frac{A}{f_1}+\frac{B}{f_2}+\frac{C}{f_3}\right)} : \frac{\left(\frac{C}{f_1}\right)}{\left(\frac{A}{f_1}+\frac{B}{f_2}+\frac{C}{f_3}\right)} \quad (5.2)$$

where X, Y and Z are the elements present in the spectra, A, B and C the integrated areas under the curves of the peaks and f_1, f_2 and f_3 the sensitivity values associated with the elements X, Y and Z, respectively. From the above equation it is found that the pure TiO_2 NW structure has approximately 60:40 ratio of Ti $2p_{1/2}$ to $2p_{3/2}$ states, using a sensitivity factor of 0.6 and 1.2 respectively for the $2p_{1/2}$ and $2p_{3/2}$ states as shown in Table 5.2 below. This ratio changes considerably when subjecting the NWs to the N_2 plasma (red curve, Fig. 5.5 (a)) with the Ti $2p_{1/2}$ state now showing a density of nearly 70% with the Ti $2p_{3/2}$ state reducing to about 10%. This change in density of states is as a result of the formation of a Ti-N state, as shown by the blue curves in Fig. S4 of the supplementary information and the data captured in Table 5.2, with a density of nearly 10% as well. This Ti-N state results in the reduction in valency of the Ti^{4+} ion to Ti^{3+} [5.6] and a rearrangement of the oxygen network throughout the TiO_2 lattice.

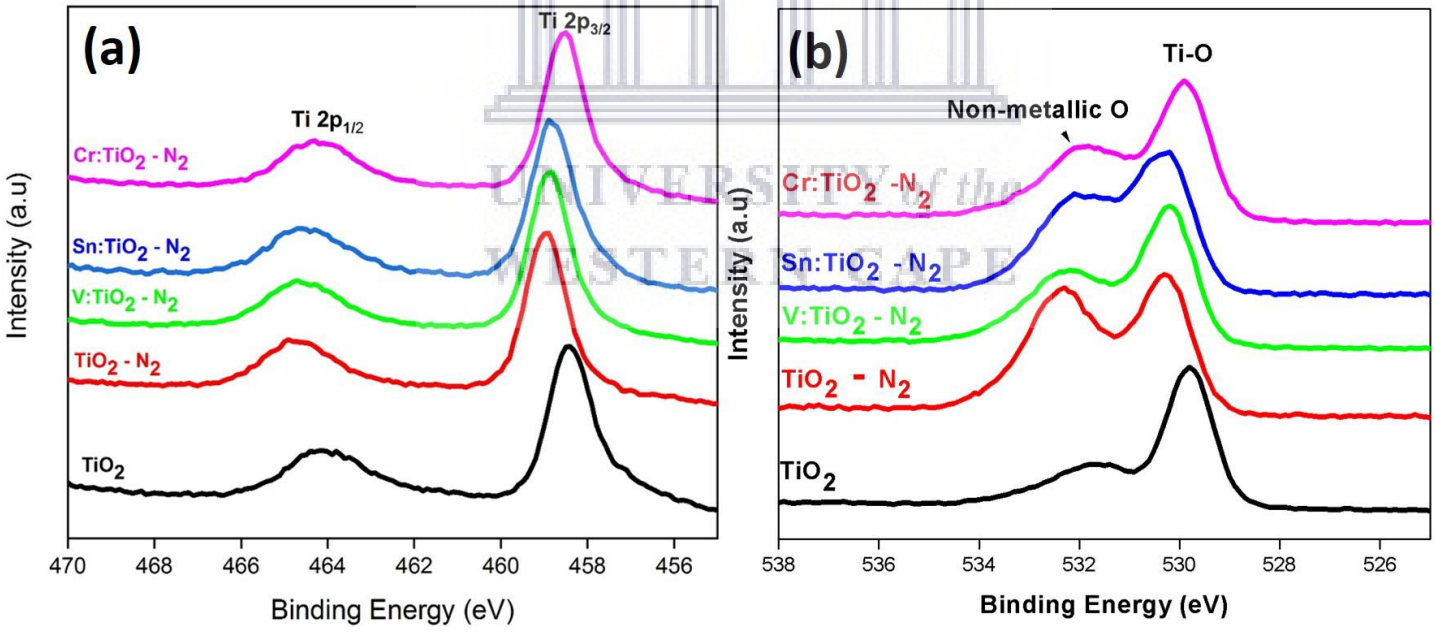

Fig. 5.5: XPS plots of (a) Ti 2p and (b) O 1s electronic structure of the various N_2 plasma treated TiO_2 NW arrays

The oxygen network rearrangement is confirmed by the formation of a N-O bond at 400.33 eV [5.7], as shown in the nitrogen (N 1s) spectra of Fig 5.6. A dominant asymmetric Ti-N

peak around 397 eV is also observed and corroborates the deconvolution results of Fig. S4 – these two peaks are created by atomic β-N species present in the plasma [5.8]. The results also confirm inferences from the XRD analyses, in that N_2 is introduced in the TiO_2 lattice substitutionally, forming a bonding network with both the Ti metal and the oxide structure. The relative quantum ratio of N 1s, using a sensitivity factor of 2 to Ti 2p (factor 1.2) yield nitrogen concentrations of 9.57, 10.05, 9.30 and 8.34 at% for the $TiO_2 – N_2$, $V:TiO_2 – N_2$, $Cr:TiO_2 – N_2$ and $Sn:TiO_2 – N_2$ samples, respectively. It must be noted that no significant signals from the metal dopants could be detected during XPS analyses, which may well be attributed to the low atomic concentration (less than 1 at% as detected by TEM-EDS), which render them below the detection limit of this surface sensitive technique.

Table 5.2: Relative Ti 2p and O 1s quantum ratios calculated for the N_2 plasma treated metal-doped NWs

Peaks (Ti 2p data)	**Sensitivity Factor (S)**	**TiO_2**	**$TiO_2 – N_2$**	**$V:TiO_2 – N_2$**	**$Cr:TiO_2 – N_2$**	**$Sn:TiO_2 – N_2$**
Ti $2p_{3/2}$ (%)	1.2	40.12	10.28	9.10	13.07	18.12
Ti $2p_{1/2}$ (%)	0.6	59.88	69.44	87.52	74.21	67.95
Ti-N $2p_{3/2}$ (%)	1.2	-	11.07	1.73	-	-
Ti-N $2p_{1/2}$ (%)	1.2	-	9.21	1.65	12.68	13.92
Total (%)		**100**	**100**	**100**	**100**	**100**

Peaks (O 1s data)	**Sensitivity Factor (S)**	**TiO_2**	**$TiO_2 – N_2$**	**$V:TiO_2 – N_2$**	**$Cr:TiO_2 – N_2$**	**$Sn:TiO_2 – N_2$**
Ti-O		88.06	75.81	80.05	80.39	77.89
Non-metallic O		11.94	24.19	19.95	19.61	22.11
Total		**100**	**100**	**100**	**100**	**100**

A discussion of the influence of the metal-dopants on the nitrogen doping is required and can be based on the Ti 2p results of Fig 5.5. From these it can be seen that the $V:TiO_2 –N_2$ sample shows a definitive decrease in density of the Ti-N $2p_{1/2}$ and Ti-N $2p_{3/2}$ states compared to the $TiO_2 – N_2$ sample whereas the $Cr:TiO_2 – N_2$ and $Sn:TiO_2 – N_2$ samples show no clear presence of the Ti-N $2p_{3/2}$ state even though the formation of the Ti-N bond is clearly detected in the N 1s high resolution spectra of Fig. 5.6. The decrease in the relative quantum ratios of the Ti-N $2p_{1/2}$ and Ti-N $2p_{3/2}$ states of the $V:TiO_2 –N_2$ sample are ascribed to the

minimal distortion of the metal-oxide lattice by the introduction of the V ion; as shown in Table 5.1, the change in unit cell volume is minimal when introducing V into the TiO_2 lattice. In the case of $Cr:TiO_2 – N_2$ and $Sn:TiO_2$ - N_2 the absence of the Ti-N $2p_{3/2}$ state is thought to be due to minimal interaction between Sn, Cr and the TiO_2 lattice, leading to partial substitutional or even complete interstitial doping, cause a change in unit cell dimensions of the TiO_2 NWs; this is especially true in the case of the $Sn:TiO_2$ - N_2 samples, which showed significant morphological changes compared to the TiO_2-N_2 sample, as shown in Figs. 5.1 and S1.

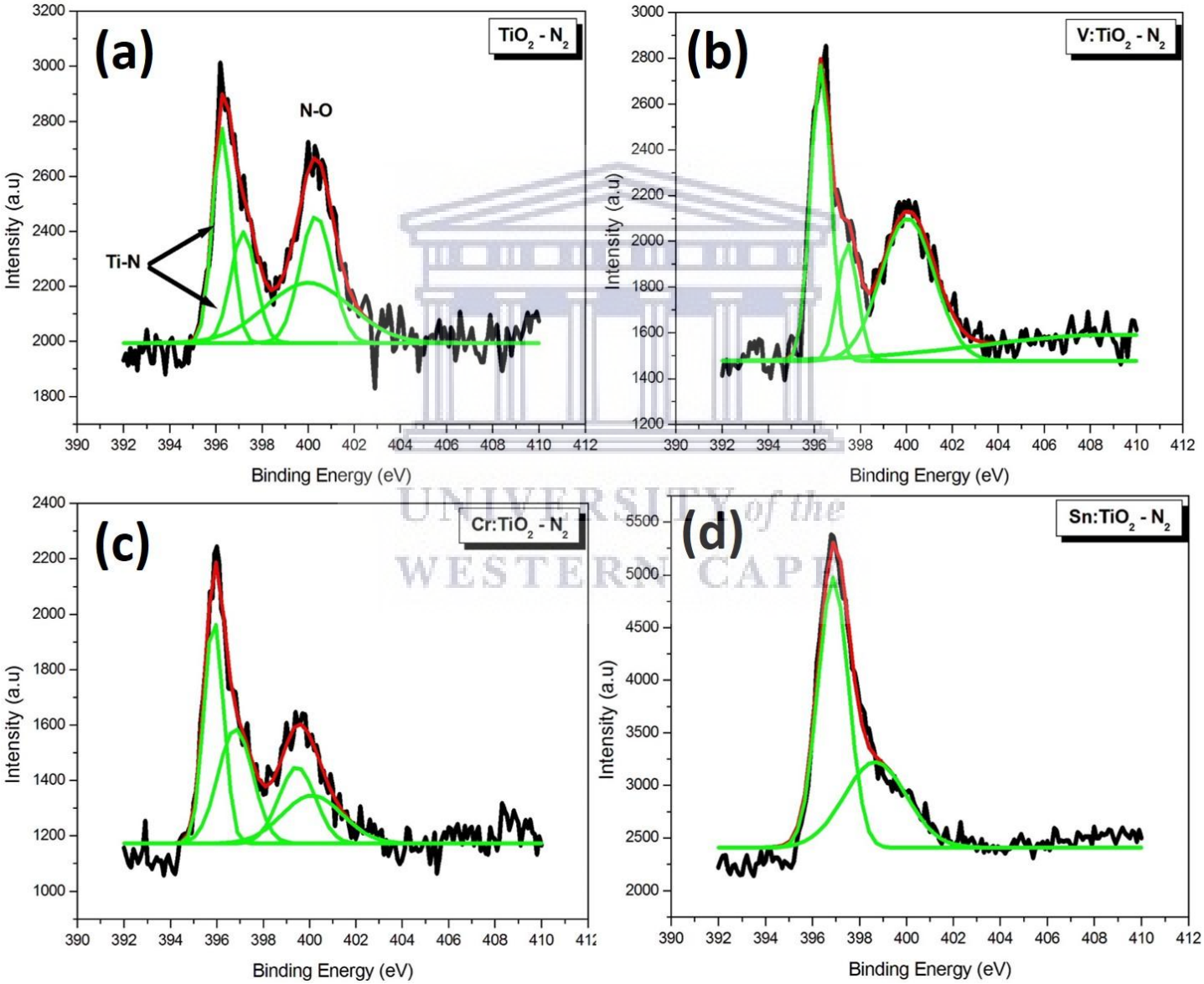

Fig. 5.6: Nitrogen 1s core level spectra of (a) $TiO_2 – N_2$; (b) $V:TiO_2 – N_2$; (c) $Cr:TiO_2 – N_2$ and $Sn:TiO_2 – N_2$

5.5 Optical Properties of Metal-Doped and Nitrogen Irradiated Metal-Doped TiO_2 NWs

The optical behaviour of the in-situ doped and plasma irradiated samples are shown in the transmittance and diffuse reflectance spectra of Fig. 5.7. The specular component of reflectance yielded negligible data due to the high roughness of the film architecture and as such is omitted. As can be observed in Fig. 5.7 (a) and (c), doping the pristine TiO_2 NWs by different metals results in a progressive increase in transmission over the visible range between 400 and 800 nm with the reflectance decreasing correspondingly - blue shift of the transmission in Fig. 5.7 (a) is observed when doping with the different metals, with V:TiO_2 – N_2 showing the most significant shift. Post N_2 plasma treatment, Fig. 5.7 (b) and (d), it is found that the transmission increases on average by 20%, for the TiO_2, and between 5 and 10 % for the three different metal-doped TiO_2 samples as shown. V:TiO_2 – N_2 once again shows the most significant blue shift, but in addition, clear blue shift of the N_2 doped TiO_2 curve is also noted. As expected, the corresponding diffuse reflectance spectra of the N_2 treated TiO_2 in Fig. 5.7 (d) now shows a decrease between 400 and 800 nm compared to untreated sample due to the increase in transmittance. What is also interesting is the similarities in optical curves of the Cr and Sn doped TiO_2 samples, even though their morphologies differed noticeably as shown in Fig. 5.1.

The Tauc plots of the untreated and N_2 plasma treated spectra are plotted in Fig. 5.7 (e) and (f), respectively. As shown, the optical bandgap of the as-prepared, undoped TiO_2 NW arrays is 3.13 eV (dashed black extrapolation line of Fig. 5.7 (f)). This value decreases to 3.01 eV post N_2 plasma treatment, as shown by the black dashed line in Fig. 5.7 (g). Doping the TiO_2 NWs with V, Cr and Sn, without exposure to plasma, decreases the bandgap to 3.00, 3.04 and 3.05 eV, respectively, whereas post N_2 plasma treatment further reduction in bandgap for the doped TiO_2 NWs is noted, with values of 2.98, 3.02 and 3.01 eV determined for the V:TiO_2 – N_2, Cr:TiO_2 – N_2 and Sn:TiO_2 – N_2 samples, respectively. The trends in the band gap values obtained in Fig. 5.7 are in agreement with that noted by Islam *et al* [5.9], who observed that N_2 plasma treatment of pure anatase TiO_2 reduces the band gap from 3.5 to 3.0 eV, as well as Kimigar and Mohammadizadeh [5.10], who reported improvement of the light absorption of N-TiO_2 as a result of the energy band reduction of rutile TiO_2 from; it also noted that doping

the TiO_2 thin films with nitrogen causes the generation of oxygen vacancies, thereby making a contribution to the visible light response.

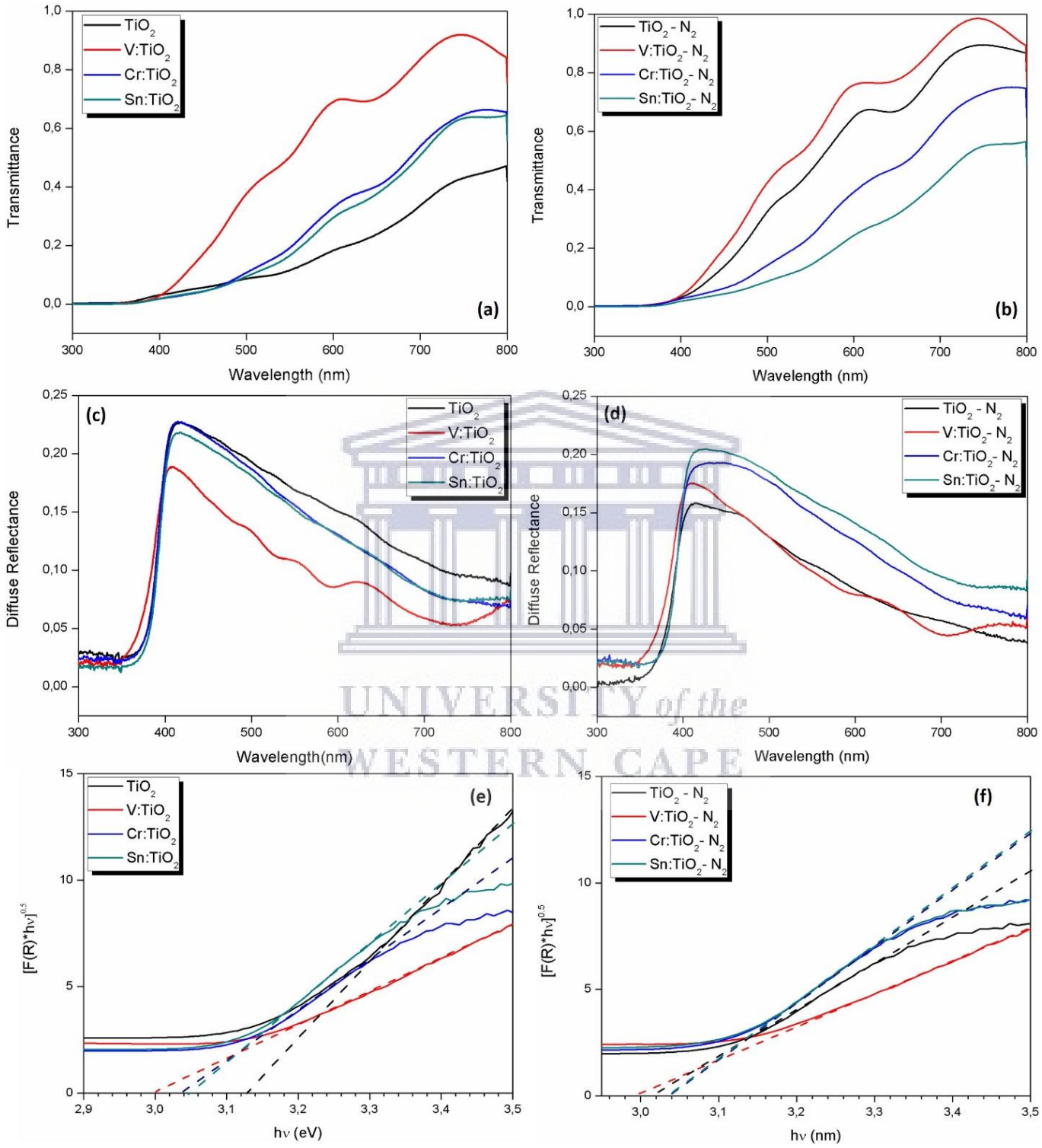

Fig. 5.7: UV-Vis transmittance spectra of (a) untreated and (b) N_2 plasma treated TiO_2 NWs; diffuse reflectance spectra of (c) untreated and (d) N_2 plasma treated TiO_2 NWs; Tauc plots of (e) untreated and (f) N_2 plasma treated TiO_2 NWs

To compare the noted decrease in bandgaps post-metal doping shown in Fig. 5.7, the band gap obtained for the Cr-TiO_2 of 3.0 eV is in agreement with that of Hajjaji *et al* [5.11], who reported a change in band gap from 3.3 to 3.0 eV after Cr doping. In the case of V doped TiO_2, Lu *et al* [5.12] similarly reported a decrease in value from 3.04 eV to 2.96 eV post doping, whereas research on Sn doped TiO_2 show a decrease to 3.04 eV for Sn:TiO_2 thin films [5.13]. It must be noted, however, that all these studies referenced, primarily focused on doping thin films of TiO_2 and do not consider the co-doping of N_2, as is the focus of this study. The 1D nature of the TiO_2 NWs, with their denser concentration of oxygen vacancies, especially surface vacancies owing to the greater surface-to-volume ratio compared to thin films, offer a different architecture that is not present in more compact layers of TiO_2. The high concentration of nitrogen passivates the dangling Ti bonds and promotes visible light absorption due to band gap narrowing. Moreover, the alteration of the optical properties of Fig. 5.7 can be summarised as a result of the introduction of anti-bonding states less than 1 eV below the conduction band by the metal dopants [5.14] and the introduction of localised N 2p states induced by atomic β-N present during plasma irradiation [5.15].

5.6 Conclusions

Facile post-synthesis RF plasma irradiation of hydrothermally grown, vertically aligned TiO_2 NW arrays doped with V, Cr and Sn metals were investigated for improvement in the optical transmission and reduction of bandgap of the underlying TiO_2 lattice. The addition of $SnCl_4$ to the precursor solution resulted in octahedrally coordinated Sn^{4+} incorporation in the TiO_2 lattice causing pronounced broadening of the defect cascade density along the [100] growth direction and subsequent disordering of the TiO_2 lattice, which were manifested by the presence of amorphous tissue in TEM micrographs and a broadening of the NW diameter as shown by SEM images. In contrast, the presence of $CrCl_3$ and VCl_3 in the hydrothermal bath did not significantly distort the NW morphology, but rather dissolved to form Cr^{3+} and V^{3+} cations, respectively, with excess Cl^- anions present in the hydrothermal reactor, which partake in etching of the TiO_2 {110} and {111} faces thereby causing the small increase in NW diameter. Morphologically, the N_2 plasma treatment caused no change in the structural features of the metal-doped TiO_2 NWs, but rather changed the areal density of NWs, which

led to improved light transmission through the array film. Optical studies showed that the combination of metal-doping along with the post-synthesis plasma irradiation, not only improves light transmission, but also the optical absorption as a result of a decrease in bandgap, which was attributed to the dual introduction of occupied anti-bonding levels below the conduction band edge of the by the metal dopants, as well as band narrowing caused by localised N 2p states introduced by the β-N bonding with Ti and O ions in the lattice.

References

[5.1] X. Feng, K. Shankar, O.K. Varghese, M. Paulose, T.J. Latempa, C.A. Grimes, Nano Lett. 8 (2008) 3781−3786.

[5.2] A. Wisnet, S.B. Betzler, R.V. Zucker, J.A. Dorman, P. Wagatha, S. Matich, E. Okunishi, L. Schmidt-Mende, C. Scheu, Cryst. Growth Des. 14 (2014) 4658−4663.

[5.3] X. Huang, C.J. Pan, Cryst. Growth 306 (2007) 117−122.

[5.4] A. Wisnet, K. Bader, S.B. Betzler, Advanced Functional Materials 17(2015) 2601-2608.

[5.5] V.D. Mote, Y. Purushotham, B.N. Dole, J. Theor. Appl. Phys. 6 (2012) 6-11.

[5.6] X. Li, J. Zhao, S. Sun, L. Huang, Z. Qiu, P. Dong, Y. Zhang, Electrochimica Acta. 211 (2016) 395–403.

[5.7] D. Jaeger, J. Patscheider, J. Electron Spectrosc. Relat. Phenom. 185 (2012) 523-534.

[5.8] S.Z. Islam, A. Reed, D.Y. Kim, S.E. Rankin, Microporous Mesoporous Mater. 220 (2016) 120−128.

[5.9] L. Jinlong, M. Xinxin, S. Mingren, X. Li, S. Zhenlun, Thin Solid Films 519 (2010) 101−105.

[5.10] S. Kimiagar, M.R. Mohammadizadeh, Eur. Phys. J. Appl. Phys. 61 (2013) 10303.

[5.11] A. Hajjaji, M. Gaidi, B. Bessai, M.A. El Khakan, J. Appl Surf Sci. 257 (2011) 10351-10357.

[5.12] D. Lu, M. Zhang, Z. Zhang, Q. Li, X. Wang, J. Yang, Nanoscale Research Letters 9 (2014) 272.

[5.13] X. Zhu, S. Han, W. Feng, Q. Kong, Z. Dong, C. Wang, J. Lei, Q. Yia, RSC Adv. 8 (2018) 14249-14257.

[5.14] T. Umebayashi, T. Yamaki, H. Itoh, K. Asai, J. Phys. Chem. Solid. 63 (2002) 1909.

[5.15] S.Z. Islam, A. Reed, D.Y. Kim, S.E. Rankin, Microporous Mesoporous Mater. 220 (2016) 120−128.

CHAPTER SIX

RESULTS AND DISCUSSION

The results of this chapter have been published in Bello Ladan Muhammad and Franscious Cummings, "Nitrogen plasma irradiation of Fe doped ZnO nanowire arrays for improved optical properties", Materials Today: Proceedings (2020), Article In Press https://doi.org/10.1016/j.matpr.2020.04.684.

6.1 Overview

In this chapter an in-depth study will be presented on the ability to improve the optical properties of in-situ Fe doped ZnO nanowires using the RF plasma irradiation technique. The results are an extension of the data presented in Chapter 4. Unlike the case of TiO_2, which have various candidate transition metals than can be used as dopants during growth, the more complex Wurtzite crystal structure of ZnO has been proven to be suitable for Fe incorporation. The morphology, structural and optical properties of ZnO, Fe:ZnO NWs and N_2 treated Fe:ZnO NWs are studied by scanning electron microscopy, grazing incidence x-ray diffraction and UV-visible spectroscopy, respectively, whereas elemental doping of the nanostructures are investigated by means of x-ray photo-electron spectroscopy. It will be shown that no discernible morphological differences between the ZnO, Fe:ZnO NWs and N_2-Fe:ZnO NWs result during treatment, however a clear increase in light transmission over the visible to UV range, accompanied by a decrease in optical band gap of 3.261 eV for ZnO NWs to 3.255 eV for Fe:ZnO NWs and ultimately 3.250 eV for N_2 treated Fe:ZnO nanowires are observed. This band gap reduction is ascribed to the presence of a high density of shallow donor states in the bandgap of the ZnO lattice, subsequently causing an overall reshaping of the conduction band minimum, caused by filling of oxygen vacancies and substitutional replacement of lattice oxygen by the highly kinetic α-N species during oxynitride, O-Zn-N bond formation. The results suggest that nitrogen doping during plasma irradiation provides a controlled method of deep lattice nitrogen doping that is favourable for improved photo-electrochemical, photovoltaic and photo-response applications of ZnO nanowires.

6.2 Morphology

Fig. 6.1 shows SEM micrographs of the top and cross-sectional views of the ZnO, Fe:ZnO and N_2-Fe:ZnO NW samples. The images indicate that the entire surface of the FTO substrate is covered uniformly and densely with vertically oriented nanowires, thereby forming an arrayed architecture. As shown by the top-view micrographs, both ZnO (Fig. 6.1 (a)) and Fe-ZnO nanowires (Fig. 6.1 (c)) exhibit a hexagonally shaped structure as discussed by Yhimura *et al* [6.1] and Baruah *et al* [6.2]. The nanowire diameter and length of the pure ZnO structures are 34.69 ± 4.81 nm and 1.14 ± 0.24 µm, respectively, which change slightly to 35.85 ± 6.21 nm and 1.04 ± 0.07 µm for the Fe:ZnO NW structures.

The nitrogen plasma treated structures of Fig. 6.1 (e, f) show no change in the hexagonal shape observed in Fig. 6.1 (a,b) and (c,d); the diameter and length of the varies slightly compared to the preceding structures with diameter of 37.62 ± 1.83 nm and length of 707.26 ± 42.67 nm recorded; the only noticeable observation is the dispersion of the nanowires (i.e. decrease in the areal density or nanowires per unit area) after plasma exposure, which is ascribed to the dissociation of the weak Van Der Waals electrostatic force which bundles the nanowires together, as shown in Fig. 6.1 (a). It must be highlighted that a discussion on the nanowire diameter or length, based on the SEM micrographs presented in Fig. 6.1 is factually flawed as any discrepancy in these values must be ascribed to the non-repeatability of the hydrothermal process (a well-known fact), rather than the effective Fe introduction in the autoclave liner or post synthesis N_2 treatment. This said, the unaffected structural features, coupled with the nanowire orientation distortion are potentially preferable for light transmission promotion in these array architectures.

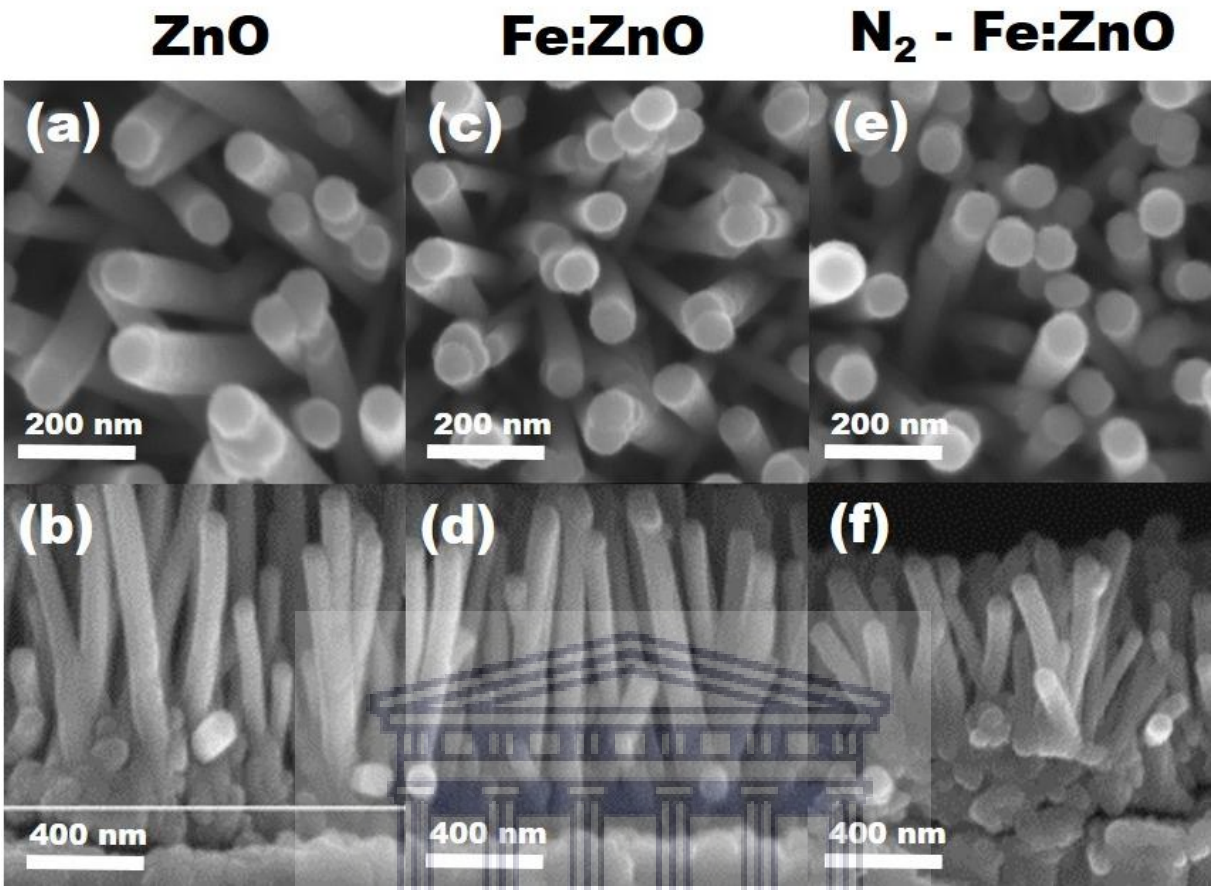

Fig. 6.1: Top and cross-section SEM micrographs of (a, b) ZnO; (c, d) Fe:ZnO and (e, f) N2–Fe:ZnO nanowires.

The EDS quantification, summarised in Fig 6.2 and Table 6.1, shows that both ZnO and Fe:ZnO NWs contain no nitrogen, whereas it can be seen that the in-situ doping of the ZnO lattice with Fe yields nanowires with 0.28 and 0.22 at% of Fe in the Fe:ZnO and N_2-Fe:ZnO, respectively. Moreover, the elemental analysis shows that the plasma irradiation produces nanowires with a significant nitrogen concentration of 6.37 at%. The results presented in the EDS data of Fig 6.2 and Table 6.1 were averaged over several different regions within the sample, with a very narrow standard deviation (< 0.05 at%), which shows the homogenous incorporation of the various dopants in the lattice.

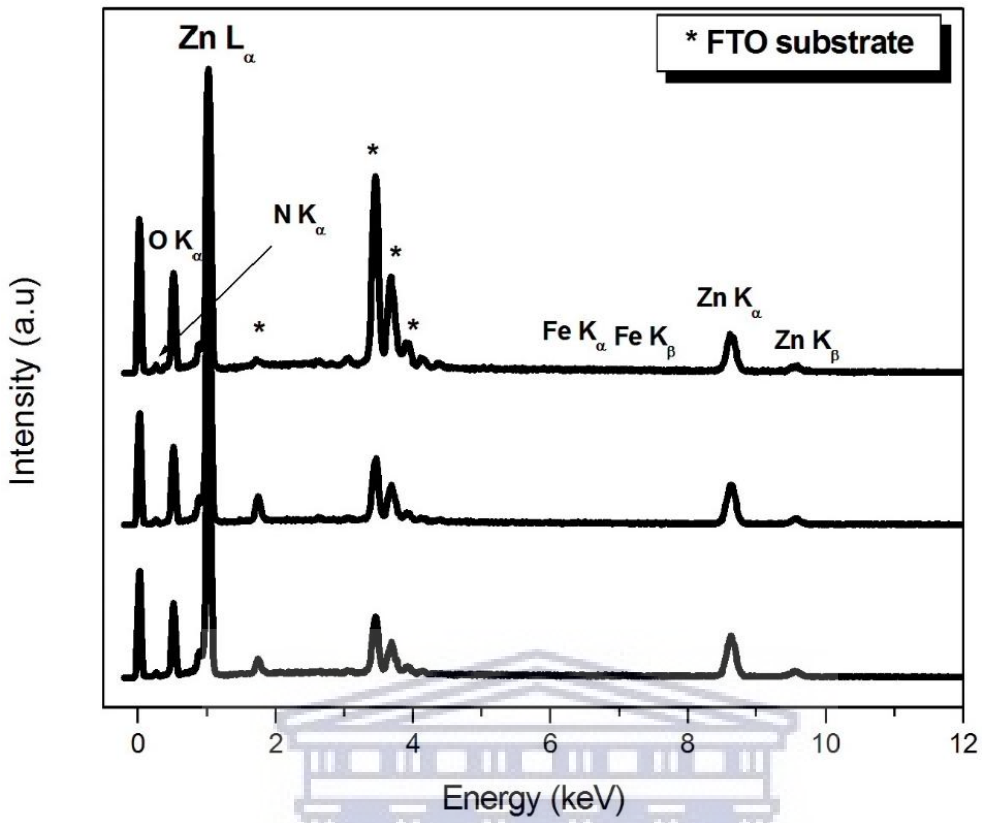

Fig. 6.2: EDS elemental spectra showing all elements present in the three different samples.

Table 6.1: Summary of the major elemental composition of the ZnO, Fe:ZnO and N_2-Fe:ZnO samples

	Elements in atomic %			
	N	**O**	**Fe**	**Zn**
ZnO	**0.00**	**58.56**	**0.00**	**41.44**
Fe:ZnO	**0.00**	**59.92**	**0.28**	**39.81**
N_2-Fe:ZnO	**6.37**	**66.90**	**0.22**	**26.51**

6.3 Crystallinity and Structural Analysis

The GIXRD patterns were collected to investigate the structural effects of the Fe and N doping in the metal-oxide lattices, the results of which are presented in Fig. 6.3. As was the case in the SEM micrographs of Fig .1, no significant changes in diffraction patterns of ZnO, Fe:ZnO or N_2-Fe:ZnO can be observed in Fig. 6.3. The ZnO nanowires grow in the wurtzite hexagonal phase with a preferred growth orientation resulting from stacking in the (002) Basal plane. The lattice constants of all three samples were calculated from the two most dominating crystalline orientations, i.e. (002) and (103) as shown in Fig.6. 3, with values of a = 0.324 and c = 0.518 nm determined, yielding a c/a ratio of 1.599, which closely resembles the theoretical value of 1.633.

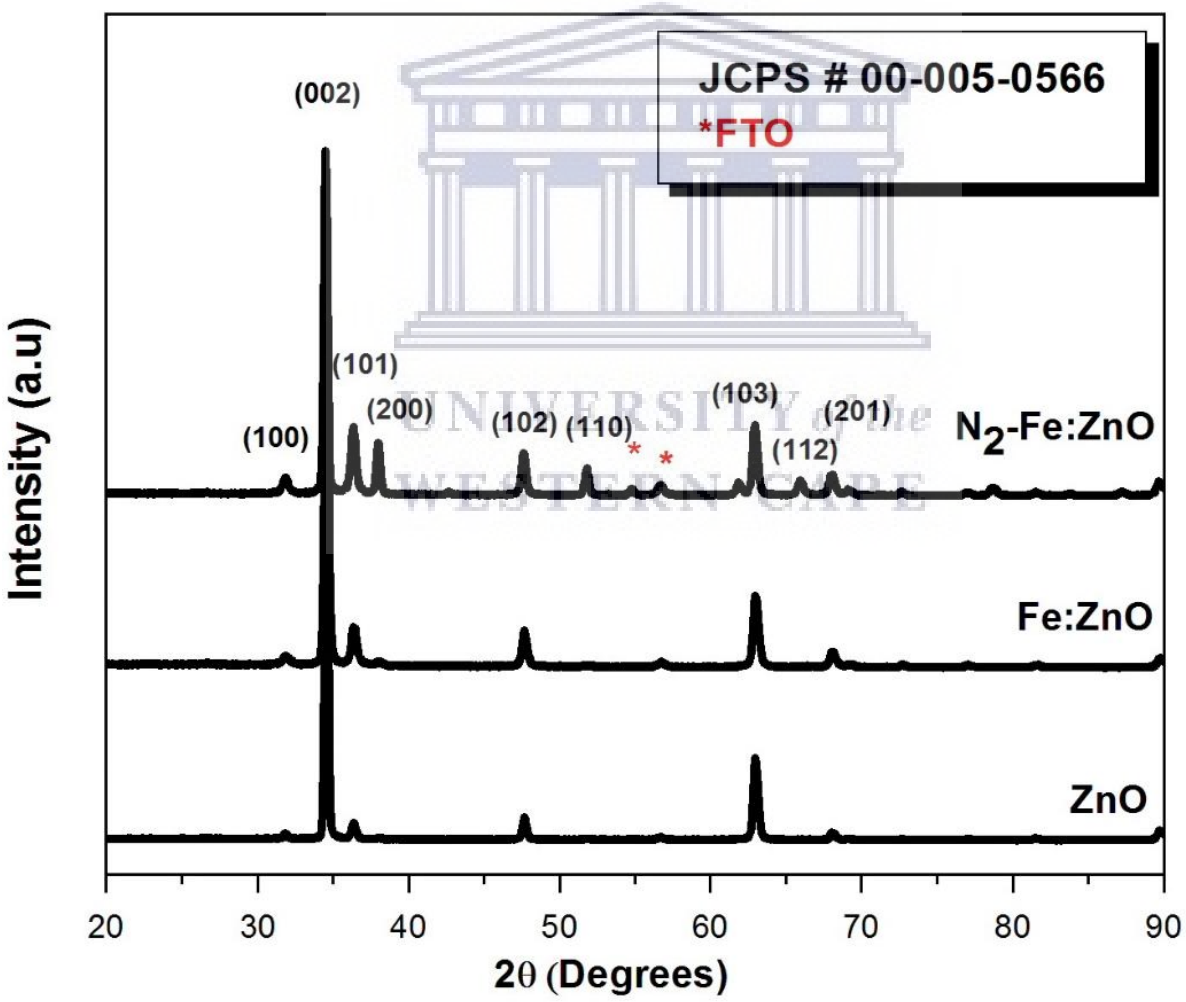

Fig. 6.3: GIXRD patterns of ZnO, Fe-ZnO and N_2- Fe:ZnO NWs

The deviation from theory is a result of intrinsic compressive strain in the lattice at room temperature and/or the presence of defect structures throughout the crystal. The presence of Fe in the lattice further increases this compressive strain, as discussed by Wang *et al* [6.3] whereas the introduction of nitrogen ions in the lattice causes minimal structural distortion [6.2]. In addition, taking the geometry of the incident x-ray beam into consideration, i.e. is parallel to the FTO/glass substrate and therefore perpendicular to the growth of the nanowires, it can be concluded that the nanowires grow predominantly along the c-axis (002) basal plane along the length of the nanowires, which is known to be polar with the non-polar lateral crystal facets along [100], [110] and [010] on the hexagonally shaped wires also visible in the diffraction pattern.

6.4 Optical Characterisation

Fig. 6.4 shows UV-Vis transmittance plots with a distinct improvement in light transmittance of the ZnO NW layer after both Fe and N introduction in the lattice. In particular, it can be seen that the N_2-Fe:ZnO array transmittance peaks at 63% at 750 nm after treatment compared to the doped Fe:ZnO with 53%, while the as-synthesised structure with a low transmittance of 37% at the same wavelength. This is an important result bearing in mind the fact that the metal-oxide nanowire films function during solar cell operation as electron transport layers must not impede the light infiltration (when illuminated from the FTO side) of the device. The enhancement in transmittance is directly attributed to the distortion of the nanowire alignment by the N_2 plasma irradiation, as shown in Fig. 6.1 which results from dissociation of the electrostatic Van der Waals force between two adjacent, vertically-aligned nanowires. The diffuse reflectance spectra of Fig. 6.4 (b) were converted by Kubelka-Munk transformations into pseudo absorbance spectra (F(R)), which were then used in Tauc plots to obtain the respective optical bandgaps, as shown in Fig. 6.4 (c). From this it can be seen that the bandgap decreases from 3.261 eV for ZnO to 3.255 eV for Fe:ZnO, with the exposure to the nitrogen plasma causing a further decrease in bandgap to 3.250 eV. The decrease in band gap caused by Fe doing of the ZnO lattice is discussed in various literatures and is well-known [6.4 – 6.7]. However, the further reduction in bandgap caused by the introduction of nitrogen in the Fe:ZnO lattice is not reported. The work by Jinlong *et al* [6.8], who reported that nitrogen doping results to an increase in visible light absorption, which may be ascribed

to the introduction of localised N 2p states, caused by atomic β-N, within the band gap is of relevance; the doping by nitrogen is confirmed by in the XPS data of Fig 6.5, as will be discussed in this section.

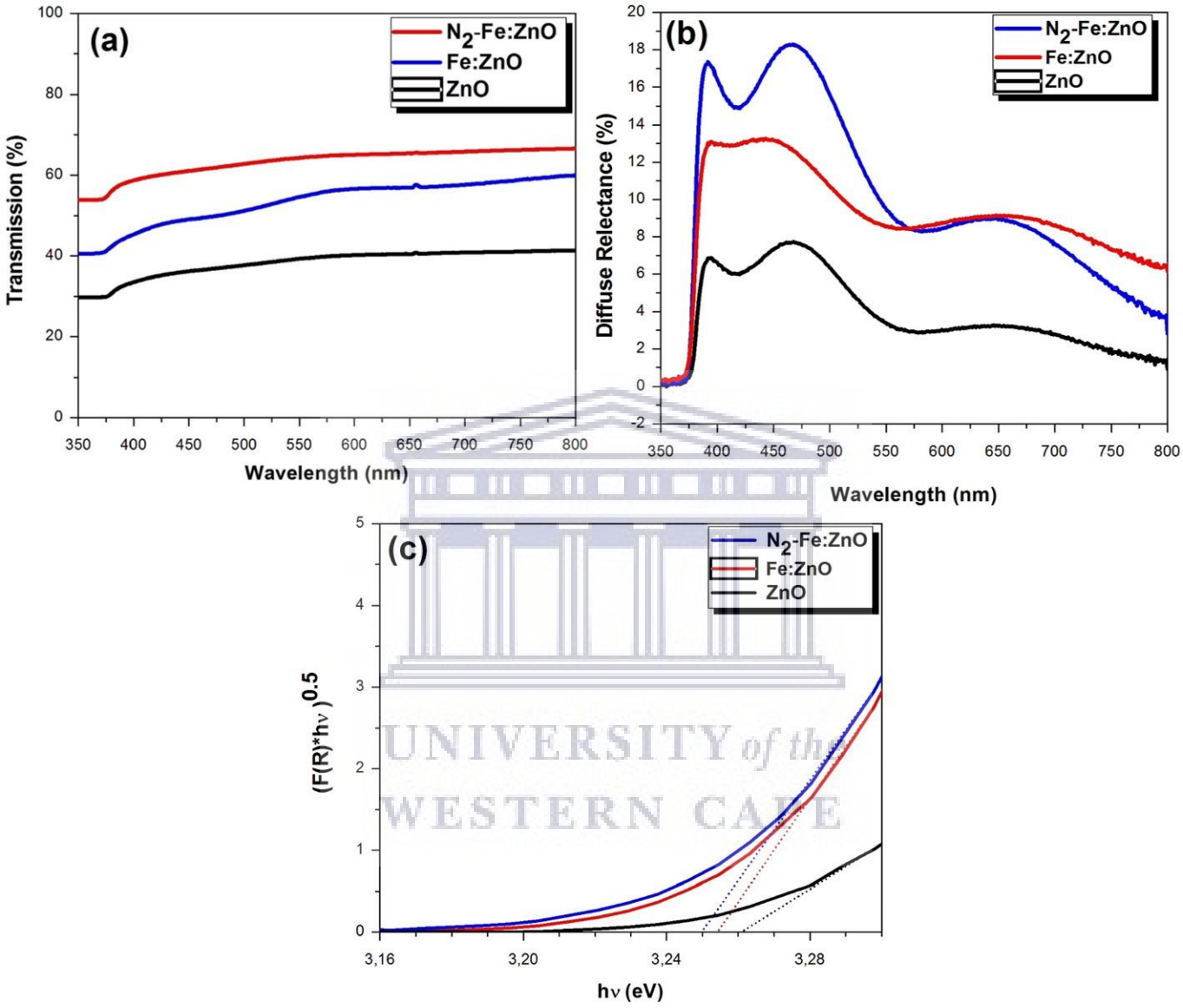

Fig. 6.4: UV-Vis (a) transmission, (b) diffuse reflectance and (c) Tauc plots comparing the ZnO, Fe:ZnO and N_2-Fe:ZnO NWs

The highly kinetic nature of the plasma species is expected to lead to elevated levels of both surface and deep lattice nitrogen introduction in individual ZnO nanowires, with the integration taking place in two ways, namely substitutional and/or interstitial, as reported by Reddy *et al* [6.9]. For the substitutional doping, the nitrogen impurities create interstitial defects through replacement of oxygen atoms, while interstitial doping leads to the

neutralisation of the defect states on the surface of ZnO materials by nitrogen. Generally, the electrical conductivity of ZnO is dominated by electrons created from oxygen vacancies and interstitial atoms of zinc, as reported by Khranovskyy *et al* [6.10]. Some studies also report that the conductivity of diverse types of semiconductors [6.11-6.14], upon interstitial incorporation of nitrogen atoms in the lattice, reduce or even entirely diminish the existing defect states in their structures, due to passivation. As a consequence, the often observed defects related absorption peak intensity readily reduces during optical studies and can be accompanied by a decrease in band gap of ZnO given that $E_g \propto n_i^{\frac{2}{3}}$, where n_i is the electron carrier density of an intrinsic semiconductor; as shown in Fig. 6.4 (c). As such, the reduction of the bandgap is readily attributed to interstitial doping of Fe of the pure ZnO lattice and subsequent replacement of oxygen, as well as passivation of dangling Zn atoms by nitrogen during plasma exposure.

6.5 Nitrogen Doping During Plasma Irradiation

The XPS survey scans of Fig. 6.5 (a) confirm the presence of core-level Fe 2p at approximately 708 eV in the Fe:ZnO material, as well as both core-level Fe 2p and N 1s in the plasma exposed N_2 – Fe:ZnO NWs, in addition to the Zn 2p at 1022 eV and O 1s at 531 eV. The C 1s species observed at 285 eV emanate from hydrocarbon contamination, and is a common phenomenon for samples exposed for prolonged periods to air [6.15]. The C 1s peak was used as energy scale calibration throughout all experiments. Quantitative analysis from the low resolution survey data reveals a very low Fe concentration of 0,19 at%. Due to the low signal-to-noise ratio in the high resolution scan, the Fe 2p spectra is omitted from this contribution., as no feasible data analysis could be extracted from it. As shown in Fig. 6.5 (b), the Zn $2p_{3/2}$ and Zn $2p_{1/2}$ core lines of the pure ZnO nanowire structures are located at 1021.78 and 1044.89 eV, respectively, which shift by 0.62 eV for Fe:ZnO, to be located at 1022.4 and 1045.58, respectively. This chemical shift due to the presence of Fe^{2+} as well as Fe^{3+} has been reported previously [6.16] and is direct evidence of low level substitutional Fe doping in the ZnO lattice. No significant chemical shift of the Zn 2p line is observed after N_2 plasma exposure as shown in Fig. 6.5 (b) with the Zn $2p_{3/2}$ line located at 1022.34 eV and the Zn $2p_{1/2}$ peak at 1045.45 eV for N_2-Fe:ZnO. Figs. 6.5 (c) to (e) show the deconvolution of the oxygen 1s core spectra of the ZnO, Fe:ZnO and N_2- Fe:ZnO, respectively. A study of the

core-line spectrum of the pure ZnO shows the presence of three constituent peaks – the main peak at 529.64 eV is attributed to the lattice oxides [6.17], with a second major peak of broader width at 531.66 eV emanating from hydrocarbon surface contamination as identified in the survey scans of Fig. 6.5 (a).

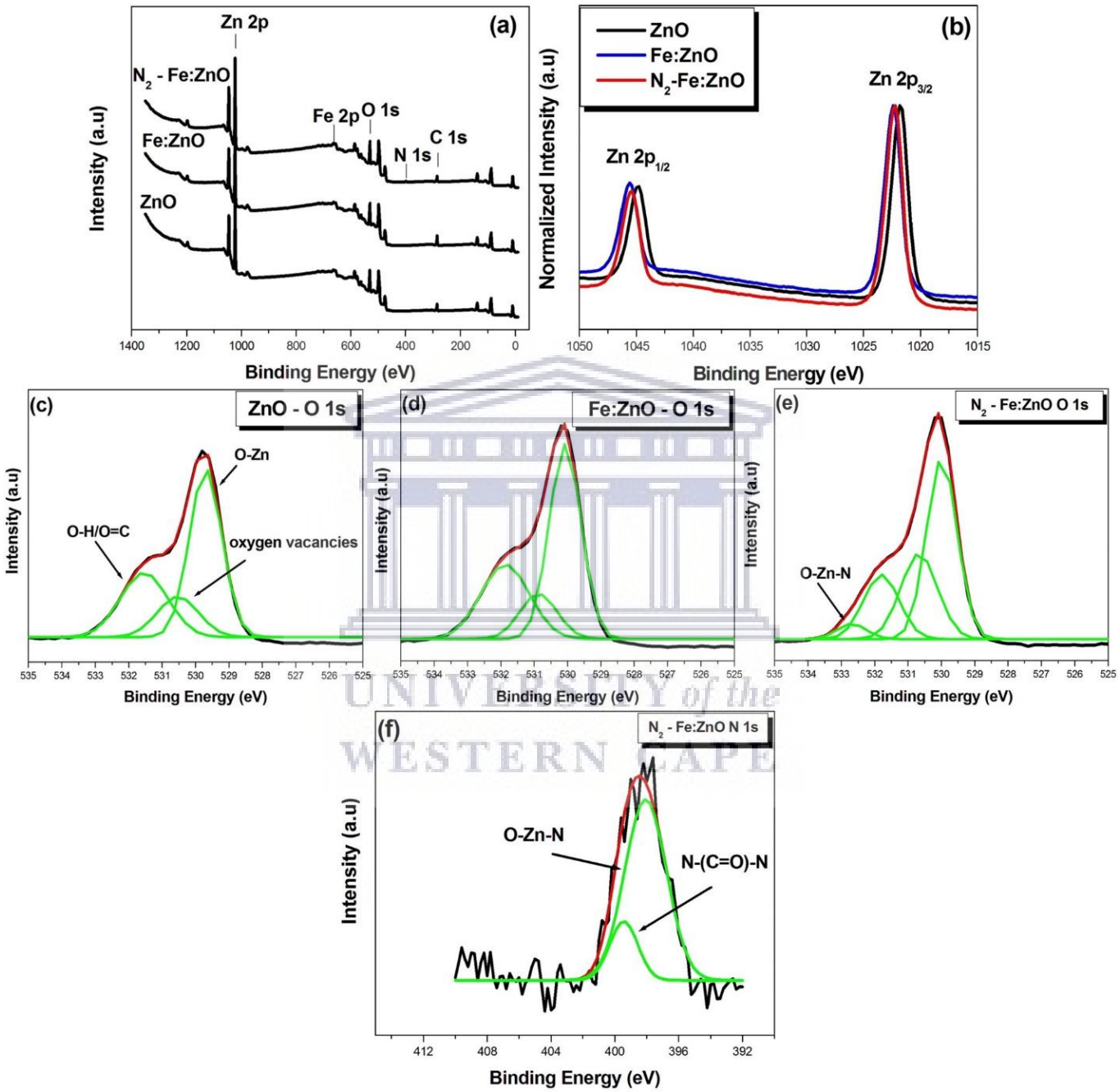

Fig. 6.5: (a) Low resolution XPS survey scan, (b) Zn 2p and (c – e) O 1s high resolution spectra of the three different samples and (f) N 1s high resolution scan of N_2 – Fe:ZnO

What is interesting is the significant contribution of a defective oxide peak [6.18, 6.19] at 530.63 eV which is assigned to oxygen vacancies, which is common in nanostructured metal-oxides [6.20]. As shown in Fig. 6.5 (d), the introduction of Fe^{2+} in the lattice reduces the relative ratio of oxygen vacancies to lattice oxides and carbon-oxide species, which is attributed to the rearrangement of the oxides to accommodate the Fe and possible Fe-O-Zn bond formation. The exposure to N_2 plasma reduces the surface hydrocarbon contamination, with a decrease in the carbon-oxide peak intensity at 531.66 eV noted. This decrease is accompanied by an increase in the oxygen vacancies peak at 530.63 eV and another peak forming at 532.72 eV, which is assigned to O-Zn-N bond formation as shown in Fig. 6.5 (e). This is direct evidence of the dual interaction of the nitrogen plasma – the highly kinetic nitrogen species dislodge lattice oxides thereby causing greater concentration of oxygen vacancies, whereas reactive species in the nitrogen plasma cause deep lattice nitrogen doping [6.21, 6.22]. To confirm this, the N 1s spectrum of Fig. 6.5 (f) shows the presence of two major peaks at 398.07 eV and 399.44 eV which are assigned to the O-Zn-N [6.23, 6.24] formation and surface organic compound contamination [6.25].

For plasma irradiated nitrogen ZnO, Allami *et al* [6.21] described the use of direct-current magnetron plasma of 1000W and 400V direct-current glow discharge plasma at multiple exposure time of ZnO NWs and established that N incorporated in the ZnO lattice structure by means of different chemical states, together with well-screened molecular state (α-N_2), α-N atoms occupying O sites to form Zn_3N_2 bonds and molecular nitrogen (γ-N_2). Thus, these results are in conformity with the reports of Tabet *et al* [6.22] who added that $ZnO_{1-x}N_x$ made by disintegration of Zn_3N_2 and the reshuffling of N atoms in the ZnO lattice and NO^{2-} on the surface of ZnO thin films irradiated with nitrogen species during DC magnetron sputtering at low kV. Furthermore, it was established that the chemical states and bonding energies of these vibrational states vary according to the type plasma irradiation. In any ionising situation, recombination and dissociation of the plasma species happen simultaneously, with the process depending on the plasma power [6.21]. This is especially true in this study, as the high power radiofrequency plasma used produces all three dominate nitrogen species, namely atomic nitrogen and α-N_2, γ-N_2. The α-N_2 acts as an etching agent in plasma irradiation and cause the dissociation of the weak Van der Waals forces, as discussed above, resulting to the disordering of the vertical alignment of Fe:ZnO nanowire arrays. During the substitutional

doping of ZnO lattice, the molecular nitrogen γ-N_2 in turn forms the Zn_3N_2 bond and then decomposes into the $ZnO_{1-x}N_x$.

6.6 Conclusions

Hydrothermally grown, vertically aligned ZnO nanowire arrays were in-situ doped with low concentration of Fe and subsequently exposed to a high-powered plasma of N_2 to improve the optical properties of the ZnO structure. The addition of Fe causes a decrease in defective oxygen sites and a shift of the core-level Zn 2p states to higher binding energies, as a result of the formation of a Fe-O-Zn network. The doping causes a slight decrease in bandgap from 3.261 eV for ZnO NWs to 3.255 eV for Fe:ZnO NWs. Exposure to nitrogen plasma creates nitrogen co-doped Fe:ZnO NW structures with an even smaller bandgap of 3.250 eV, which is ascribed to the presence of a high density of shallow donor states in the bandgap of the ZnO lattice, which causes a reshape of the conduction band minimum, due to by filling of oxygen vacancies and substitutional replacement of lattice oxygen by the highly kinetic α-N species during oxynitride, O-Zn-N bond formation. Structurally, the Fe doping causes no discernible change in morphology of crystalline structure of the ZnO lattice, whereas the plasma radicals cause a dissociation of the weakly bonded nanowires, and as such a decrease in the nanowire areal density of the N_2-Fe:ZnO sample.

References

[6.1] L.C. Chao, Y.R. Shih, Y.K. Li, J.W. Chen, J.D. Wu, C.H. Ho, Appl. Surf. Sci. 256 (2010) 4153–4156.

[6.2] S. Das, S. Patra, J.P. Kar, A. Roy, A. Ray, J.M. Myoung, Mater. Lett. 161 (2015) 701–704.

[6.3] C. Wang, Z. Chen, Y. He, L. Li, D. Zhang, Appl. Surf. Sci. 255 (2009) 6881–6887.

[6.4] I. Soumahoro, R. Moubah, G. Schmerber, S. Colis, A. Mait, M. Abd-Lefdil, Thin Solid Films 528 (2010) 4593-4599.

[6.5] B. Aleman, Y. Ortega, J.A. Garca, P. Fernandez, J. Piqueras, J. Appl. Phys. 110 (2011) 014317.

[6.6] B.L. Muhammad, F. Cummings, Surfaces and Interfaces 17 (2019) 100382.

[6.7] S. Baruah, J. Dutta, Sci. Technol. Adv. Mater. 10 (2009) 013001.

[6.8] L. Jinlong, M. Xinxin, S. Mingren, X. Li, S. Zhenlun, Thin Solid Films 519 (2010) 101-105.

[6.9] N.K. Reddy, M. Devika, Y. Hahn, Nano Convergence 1 (2014) 26-31.

[6.10] V. Khranovskyy, J. Eriksson, A. Lloyd-Spetz, R. Yakimova, L. Hultman, Thin Solid Films 517 (2009) 2073-2078.

[6.11] S.Y. Myong, K.S. Lim, J. Appl. Phys. 95 (2004) 1525-1530.

[6.12] T. Mattila, S.-H. Wei, and A. Zunger, Phys. Rev. B 60 (1999) R11245.

[6.13] P.R.C. Kent and A. Zunger, Phys. Rev. B 64 (2001) 115208.

[6.14] D.E. Aspnes, Surf. Sci. 37 (1973) 418- 442.

[6.15] M.B. Haider, Nanoscale Research Letters 12 (2017) 5-9.

[6.16] S. Bai, T. Guo, Y. Zhao, J. Sun, D. Li, A. Chen, C. Liu, Sensors and Actuators B: Chemical 195 (2014) 657-666.

[6.17] M.C. Biesinger, L.W.M. Lau, A.R. Gerson, R.St.C. Smart, Appl. Surf. Sci. 257 (2010) 887-898.

[6.18] H.A.E. Hagelin-Weaver, J.F. Weaver, G.B. Hoflund, G.N.Salaita, J. Electron Spec. Rel. Phenom. 134 (2004) 139 – 171.

[6.19] P.R. Norton, G.L. Tapping, J.W. Goodale, Surf. Sci. 65 (1977) 13-36.

[6.20] H.B. Fan, S.Y. Yang, P.F. Zhang, *et al.*, Chinese Physics Letters 24 (2007) 2108-2111.

[6.21] S. Allami, Z.D.A. Ali, Y. Li, H. Hamody, B.H. Jawad, L. Liu, T. Li, Heliyon 3 (2017) e00423.

[6.22] N. Tabet, M. Faiz, A. Al-Oteibi, J. Electron. Spectrosc. Relat. Phenom. 163 (2008) 15–18.

[6.23] C.L. Perkins, S.H. Lee, X. Li, S.E. Asher, T.J. Coutts, J. Appl. Phys. 97 (2005) 034907.

[6.24] X. Yang, A. Wolcott, G. Wang, *et al*., Nano Lett., 9 (2009) 2331-2336.

[6.25] C.D. Wagner, A.V. Naumkin, A. Kraut-Vass, J.W. Allison, C.J. Powell, J.R.Jr. Rumble, NIST Standard Reference Database 20, Version 3.4 (web version) (http:/srdata.nist.gov/xsps/) 2003.

CHAPTER SEVEN

RESULTS AND DISCUSSION

This chapter will discuss the photovoltaic performance of the plasma treated TiO_2 and ZnO NWs as electron transport layers in hybrid organic photovoltaics.

The solar cell I-V characterisation with TiO_2 and ZnO NWs as ETLs are shown in Fig. 7.1 and 7.2, respectively. A device active area of 0.0256 cm^2, as determined by the 8-pixel device architecture discussed in Chapter 2, was characterised using intensity of 100 mW/cm^2 under simulated AM of 1.5 with a solar simulator (see Chapter 3 for full details). In each case, more than one active area was characterised to give a more accurate representation of the overall device efficiency. As shown, the devices with ZnO NWs as ETL and P3HT:PCBM in a 1:1 weight ratio as active layer, MoO_3 as HTL and Ag as top contact show little photo-response, possibly because the of the length of ZnO NWs, which was in the range of 900 nm - 1μm. This likely results in diffusing of the P3HT:PCBM and MoO_3 in between the porous holes of lengthy wires. Another possible reason may be the fact that MoO_3 HTL is thermally deposited, which makes it difficult for a solid layer to form on top of the active layer of P3HT:PCBM. Furthermore, when the top contact of Ag is thermally deposited on the device possible diffusion of the Ag ion and oxygen into the active layer may occur, or possibly electron extraction through the ZnO NWs ETL to the anode, therefore causing short-circuiting of the device as can be seen in the I-V curves in Fig. 7.1.

However, that was not case when the TiO_2 NWs ETL/P3HT:PCBM/MoO_3 HTL/Ag was characterised, as shown in Fig. 7.2. In this case, a much better photoactive response was observed. The MoO_3 film acts as a good electron blocking layer to isolate the Ag anode from the P3HT:PCBM active layer, improving the quality of the interface and reducing recombination probabilities. In addition, it eases hole transport to the Ag anode while providing blockage to the flow of electrons towards the anode. Additionally, the thin layer provides a barrier which effectively prevents diffusion of the Ag anode into the polymer

active layer and protecting the active layer from being damaged during deposition of Ag as can be seen in Fig. 7.2.

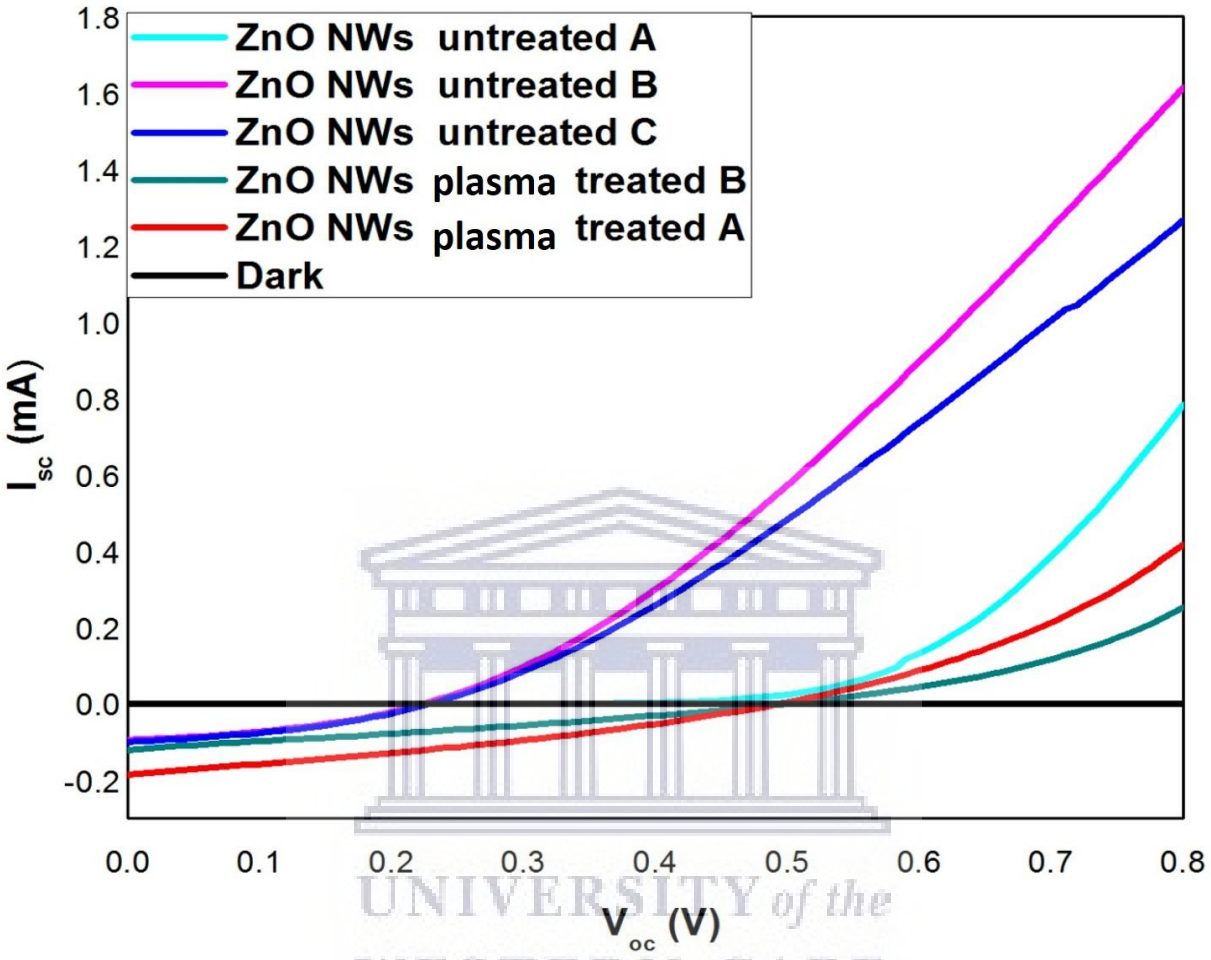

Fig. 7.1: Current-voltage curves of ZnO ETLs of untreated and N_2 plasma treated devices with thermal evaporated MoO_3 HTL under illumination.

Tables 7.1 and 7.2 present a summary of the device performance parameters for the TiO2 and ZnO NWs as ETLs, respectively. The nitrogen plasma treatment on the NWs plays an important role in the transportation of the charge carriers for both TiO_2 and ZnO devices. Moreover, the NWs N_2 treated ETLs may also well enhance the exciton dissociation at the polymer-blend ETL interface by increasing the number of excitons between acceptor and donor materials which leads to improved open-circuit voltage (V_{oc}), since the photon-to-current conversion efficiency (PCE) is guided by the number of the charge carriers produced and those that get through to the electrodes. Furthermore, the N_2 plasma treatment of NWs

help to effectively reduce the length of NWs, by reducing areal density of the nanowire arrays, as shown from in Chapters 4 to 6, leading to an improvement in the optical transmittance as observed for the treated device over the untreated device [7.1 - 7.5]. And above all, the band gap reduction was justified in our published works [7.6 - 7.12]. These reduce the recombination time and improved the e-h transports within the devices, thereby increasing the PCE of the devices over the conventional untreated devices [7.13 – 7.17].

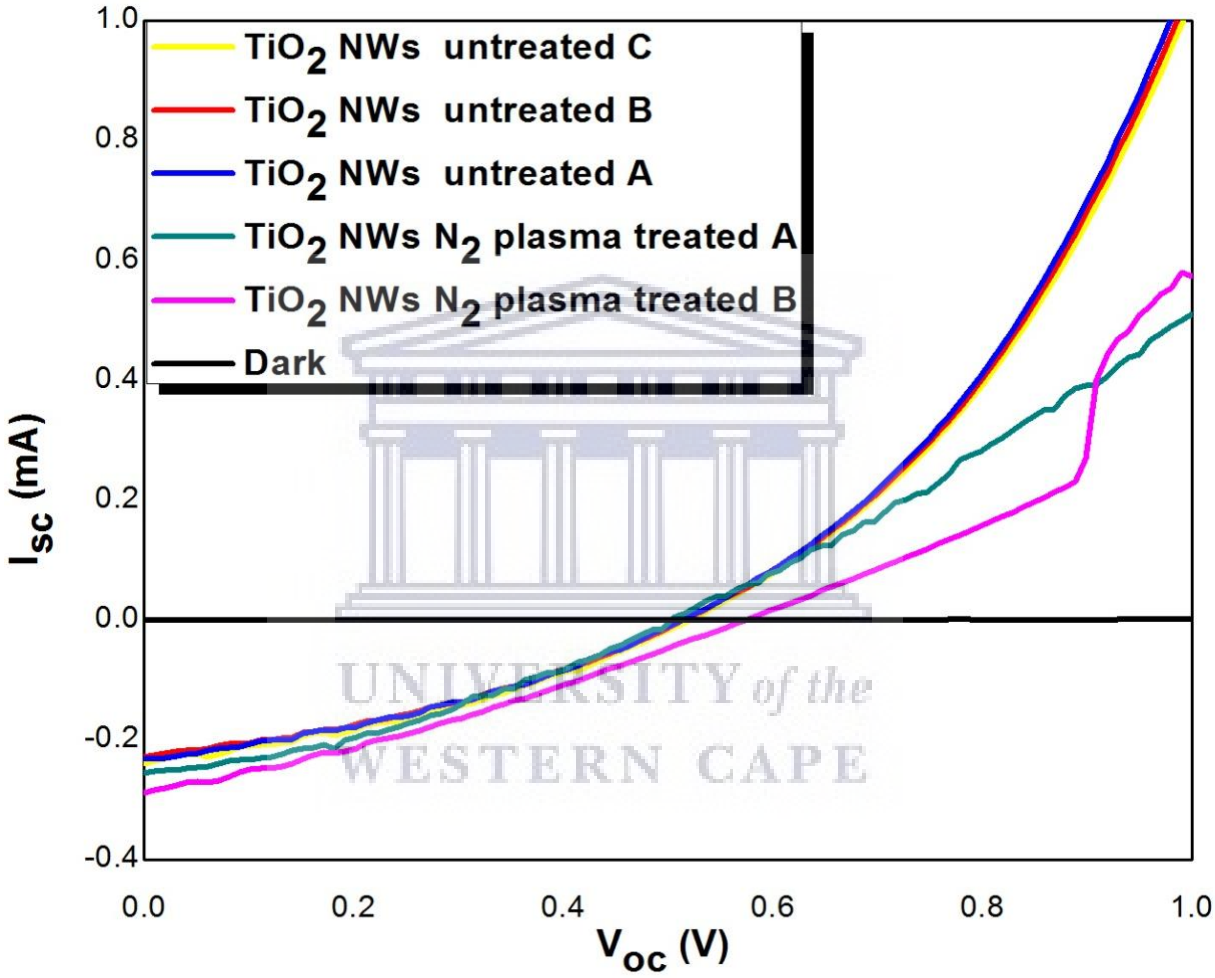

Fig. 7.2: Current-voltage curves of TiO_2 ETLs of untreated and N_2 plasma treated devices with thermal evaporated MoO_3 HTL under illumination.

When the TiO_2 ETL is treated with N_2 plasma device efficiencies of 1.73 and 1.95% are recorded, whereas the untreated TiO_2 ETLs device has a PCE of 1.63, 1.64 and 1.70%, as shown in Table 7.1. This distinction could be due to a decrease of the fill factor (FF) from 0.3490 of the untreated to 0.3030 for the treated sample. The small change in the current

value from 0.5210 mA for the untreated to 0.5740 for the treated TiO_2 NWs device samples is actually responsible for the change in the PCE between the untreated and treated TiO_2 ETLs. Also similar distinction was observed with the ZnO ETLs when treated with N_2 plasma, the device PCEs of 0.5660 and 0.3350 are recorded; with the untreated ZnO NWs ETL device has PCEs of 0.0087, 0.1580 and 0.1667%, as shown in Table 7.2. These could be due to a small change in the fill factor (FF) from 0.2460 of the untreated to 0.3150 for the treated sample. The small change in the current value from 0.0185 mA for the untreated to 0.4930 mA for the treated ZnO NWs device samples is actually responsible for the change in the PCE between the untreated and treated ZnO ETLs. The enhancement in performance of the device can also be attributed to the lower leakage of current due to improvement in hole blocking and electron collecting capabilities of the N_2 plasma treated TiO_2 NWs and ZnO NWs ETLs. However, because the conditions of the top electrode, namely the MoO_3 HTL and Ag top contact are kept the same throughout, the performance of the devices can be attributed solely to the ETL differences, with the N_2 plasma treated ETLs performing better than the conventional untreated ETL.

Table 7.1: Performance parameters of inverted OSCs with untreated TiO_2 NWs and N_2 plasma treated TiO_2 NWs as ETLs.

DEVICE	V_{oc} (V)	I_{sc} (mA)	FF	PCE (%)
TiO_2 NW untreated A	0.5090	0.2326	0.3469	1.630
TiO_2 NW untreated B	0.5130	0.2340	0.3490	1.640
TiO_2 NW untreated C	0.5210	0.2365	0.3040	1.700
TiO_2 NW N_2 plasma treated A	0.5030	0.2557	0.3440	1.730
TiO_2 NW N_2 plasma treated B	0.5740	0.2867	0.3030	1.950

To explain the device performances further, the N_2 plasma ETLs show reduced length and shorter recombination time for an improved charge extraction, whereas the reduced band gap and PCE which are correlated, result in faster electron movement within the NWs compared

to small mesoporous TiO_2 and ZnO NWs [7.4]. These compacted ETLs provide an increased contact area with the photoactive layer, thereby reducing photo-carrier recombination during electron transport [7.15 – 7.19]. The excitons created in the photoactive layers during light absorption can more efficiently be separated by increasing the contact area between the ETLs and photoactive layer, with further increased light scattering provided N_2 plasma treated NWs thin films. This makes enhanced photon absorption into the device possible. The overall photovoltaic performances of these devices are consequently improved, similar to previously reported experiments [7.20 – 7.24].

Table 7.2: Performance parameters of inverted OSCs with untreated ZnO NWs and N_2 plasma treated ZnO NWs as ETLs.

DEVICE	**V_{oc} (V)**	**I_{sc} (mA)**	**FF**	**PCE (%)**
ZnO NW untreated A	0.0185	0.0543	0.2460	0.0087
ZnO NW untreated B	0.2237	0.0383	0.3762	0.1580
ZnO NW untreated C	0.2292	0.0397	0.3752	0.1667
ZnO NW N_2 plasma treated A	0.4990	0.0727	0.2850	0.3350
ZnO NW N_2 plasma treated B	0.4930	0.11059	0.3150	0.5660

References

[7.1] X. Feng, K. Shankar, O.K. Varghese, M. Paulose, T.J. Latempa, C.A. Grime, Nano Lett. 8 (2008) 3781-3786.

[7.2] G.D. Yuan, W.J. Zhang, J.S. Jie, X. Fan, J.A. Zapien, Y.H. Leung, L.B. Luo, P.F. Wang, C.S. Lee, S.T. Lee, P-type ZnO nanowire arrays, Nano Lett. 8 (2008) 2591-2597.

[7.3] B.L. Muhammad, F. Cummings, Surfaces and Interfaces 17 (2019) 100382.

[7.4] B.L. Muhammad, N.V. Peterson, L. Kotsedi, F.R. Cummings, Chemical Physics 538 (2020) 110922.

[7.5] B.L. Muhammad, F. Cummings, Materials Today Proceedinings (2020) (Article in Press).

[7.6] L. Jinlong, M. Xinxin, S. Mingren, X. Li, S. Zhenlun, Thin Solid Films 519 (2010) 101-105.

[7.7] N.K. Reddy, M. Devika, Y. Hahn, Nano convergence 1 (2014) 26-31.

[7.8] V. Khranovskyy, J. Eriksson, A. Lloyd-Spetz, R. Yakimova, L. Hultman, Thin Solid Films 517 (2009) 2073-2078.

[7.9] S.Y. Myong, K.S. Li, Journal of Applied Physics 95 (2004) 1525-1530.

[7.10] T. Mattila, S.H. Wei, A. Zunger, Phys. Rev. B 60 (1999) R11245.

[7.11] P.R.C. Kent, A. Zunger, Phys. Rev. B 64 (2001) 115208.

[7.12] D. E. Aspnes, Surf. Sci. 37 (1978) 418.

[7.13] T. A. Chen, X. Wu, R.D. Rieke, Journal of American Chemistry Society 117 (1995) 233-244.

[7.14] G. Janssen, A. Agurre, E. Goovaerts, P. Vanlaeke, J. Poortmans, J. Manca, Eur. Phys. J. Appl. Phys. 37 (2007) 287-290.

[7.15] H. Wang, W. Hai-yu, B. Gao, L. Wang, Z. Yang, X. Du, Q. Chen, J. Song, H. Sun, Nanoscale 3 (2011) 2280-2285.

[7.16] P. Jorge, D. E. Tieneke, B. A. Artem, V. Loosdrecht, H.M. Paul, K. Walter, T.M. Tuan, M. Juleon, D.A.L. Siebbeles, J. Phys. C 113 (2009) 14500-14506.

[7.17] B. Omar, P.M. Nametso, M. Khenfouch, A. Bokour, M. Baitoul, M. Maaza, J.W. Venturini, Nanomater. Nanotechnol., 5 (2015) 71-76.

[7.18] X.B Chen, Chinese Journal of Catalysis 30 (2009) 839-851

[7.19] A.V Emeline, V.N Kuznetsov, V.K Rybchuk, N. Serpone, International Journal of Photoenergy (2008) https://doi.org/10.1155/2008/258394.

[7.20] W. Guo, Y.H. Shen, G. Boschloo, A. Hagfeldt, T.L. Ma, Electrochimica Acta 56 (2011) 4611-4617.

[7.21] W. Guo, L.Q. Wu, Z. Chen, G. Boschloo, A. Hagfeldt, T.L. Ma, Journal of Photochemistry and Photobiology a-Chemistry 219 (2011) 180-187.

[7.22] S.H. Kang, H.S Kim, J.Y. Kim, Y.E. Sung, Materials Chemistry and Physics, 124 (2010), 422-426.

[7.23] H.J. Tian, L.H. Hu, C.N. Zhang, W.Q. Liu, Y, Huang, L. Mo, L. Guo, J. Sheng, S.Y. Dai, J. Phys. Chem. C 114 (2010) 1627-1632

[7.24] S.M. Yang, H.B. Xue, H.J. Wang, H.Z. Kou, J.C. Wang, G.H. Zhu, Journal of Physics and Chemistry of Solids 73 (2012) 911-916.

SUMMARY and FUTURE WORK

This thesis investigated the distinction between as-synthesised and plasma treated NWs used as ETLs in organic solar cells. The use of high powered RF N_2 plasma on TiO_2 and ZnO NWs ETLs have been brought together for the first time during this study, subsequently leading to the publication of three manuscripts. In summary, the study focused predominantly on the structure-optical property relationship of vertically-aligned arrays of rutile TiO_2 and Wurzite ZnO nanowires, which were modified by doing by transition metals such Fe, V, Cr and Sn prior to the introduction of N into the respective metal-oxide host lattices, during plasma exposure. It was found that the nitrogen doping reduces the bandgaps of TiO_2, ZnO and Fe-ZnO as a result of the introduction of localized N 2p states close to the metal-oxide valence caused by a β-N bonding arrangement. Moreover, it was found that the changes are caused by N doping levels of less than 1 at% in individual TiO_2 and ZnO nanowires, which changes the crystal field splitting of both Ti $L_{3,2}$ and Zn $L_{3,2}$ edges as measured by EELS. SEM results show that clear distinction between the untreated and N_2 plasma treated ETLs can be observed in terms of their areal density, whereas UV-Vis results confirm a distinctive optical improvement between untreated and treated samples. In particular, it could be observed that the TiO_2 array transmittance peaks at 90% at 750 nm after treatment compared to the as-synthesized structure with a low transmittance of 48% at the same wavelength. Similarly, the ZnO array transmittance increases from 70% to 90% over the same wavelength range, post plasma exposure. This is a significant result considering the fact that the metal-oxide nanowire films act as electron transport layers during solar cell operation and must not impede the light penetration (when illuminated from the FTO side) of the device. Upon application of these structures in P3HT:PCBM polymer blends the photoluminescence quenching of the photoactive layer is significantly improved for both as-prepared and nitrogen-doped nanowires, thus making it an interesting and promising architecture for overall device efficiency improvement. The heterojunction photovoltaic performance showed that short-circuit current and overall PCE of the device increased upon reduction in the ETLs length which was due to the 10 minutes high plasma on the NWs ETLs with the PCVD. The maximum current and PCE of 5.21×10^{-1} mA and 1.95% were respectively obtained for plasma treated TiO_2 ETLs, whereas the ZnO NWs exhibited a maximum photo-current and PCE of 1.1059×10^{-1} mA and 0.57%, respectively. Upon further investigation, it was noticed

that the dark current curves exhibit pure diode behviour meaning the electrons and holes were not properly separated. This said, there is good correspondence between the optical and the electrical properties of both ZnO and TiO2 post N_2 plasma, definitive improvements in device performance noticed. Thus, it can confidently be claimed that with improvements of more than 43% for TiO_2 and 73% for ZnO based devices post N_2 plasma irradiation, this technique indeed holds great promise as a simple method for overall organic solar cell device performance.

The promising PV performance results upon application in organic solar cells has led to an expansion of this study to kesterites (by co-evaporation) and chalcopyrite (by flash evaporation techniques) as absorber layers in inorganic solar cells. Appendix B shows some of the work recently completed, which will form the basis of the future research. Notwithstanding this, more work is currently underway to improve the overall organic solar cell performance with the nitrogen doped nanowire structures, as well.

APPENDIX A

SUPPLEMENTARY INFORMATION

RF nitrogen plasma irradiation of metal-doped TiO_2 nanowire arrays as an effective technique for improved light transmission and optical bandgap manipulation

B.L. Muhammad[1,3], N.V. Peterson[1,2], L. Kotsedi[4] and F.R. Cummings[2,*]

[1]Department of Physics and Astronomy, University of the Western Cape, Private Bag X17, Bellville 7535, South Africa.

[2]Electron Microscope Unit, University of the Western Cape, Private Bag X17, Bellville 7535, South Africa.

[3]Department of Physics, Ibrahim Badamasi Babagida University P.M.B 11 Lapai, Niger State Nigeria.

[4]Materials Research Group, iThemba LABS, Faure 7130, South Africa

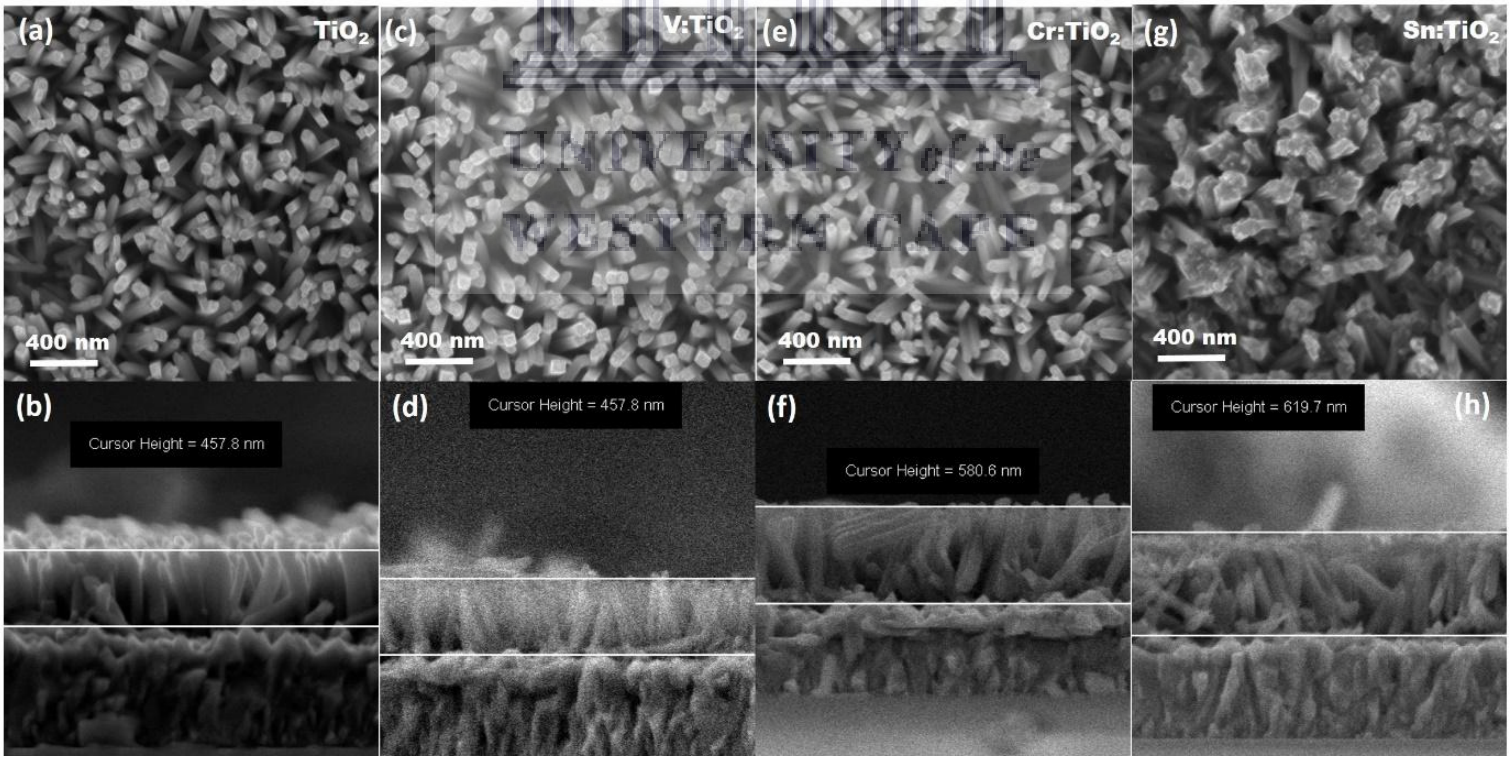

Fig. S1: SEM top and side views of the as-prepared nanowires of (a, b) pure TiO_2, (c,d) V:TiO_2, (e, f) Cr:TiO_2 and (g, h) Sn:TiO_2 NWs

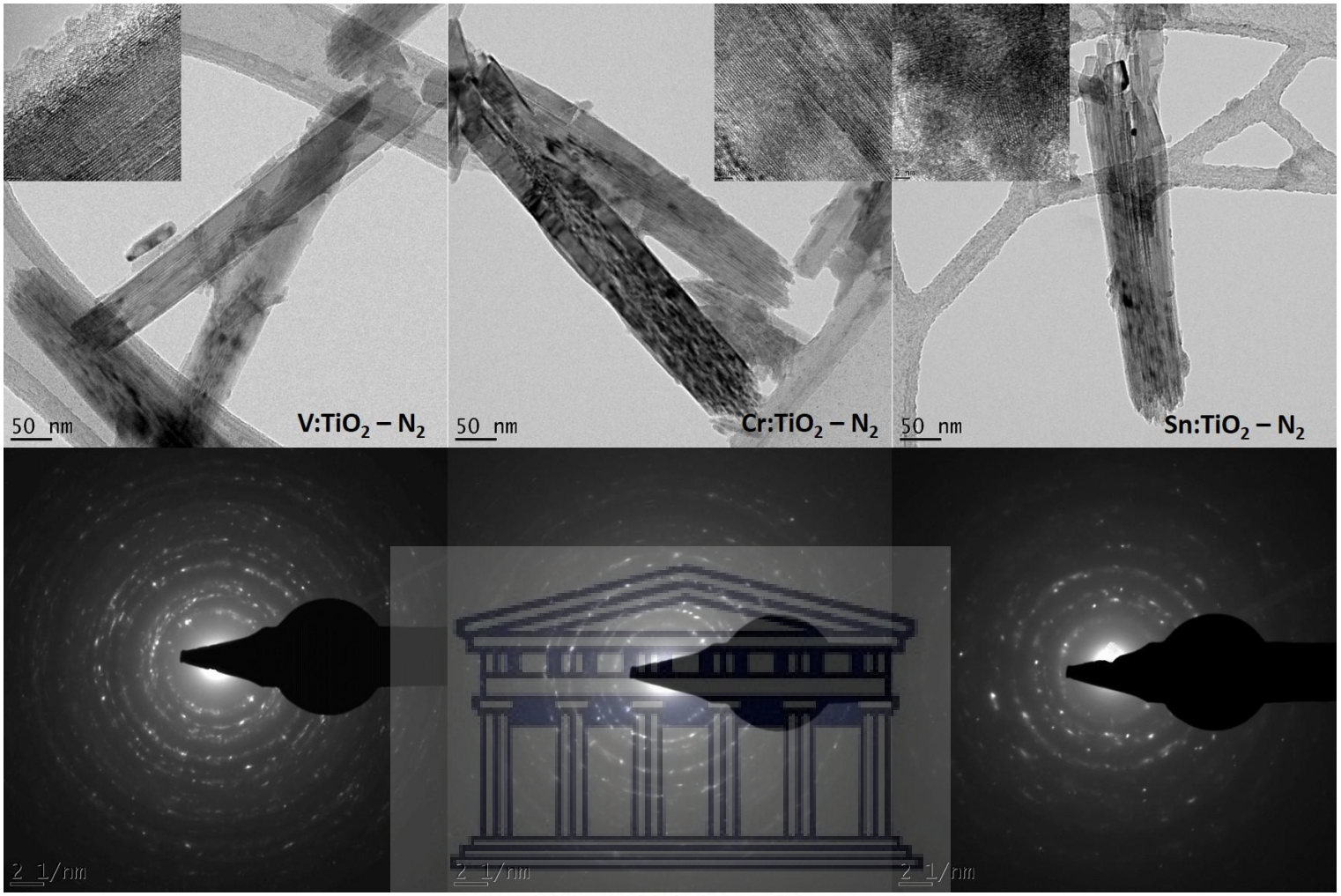

Fig. S2: TEM and SAED micrographs of nitrogen treated metal-doped TiO_2 NWs.

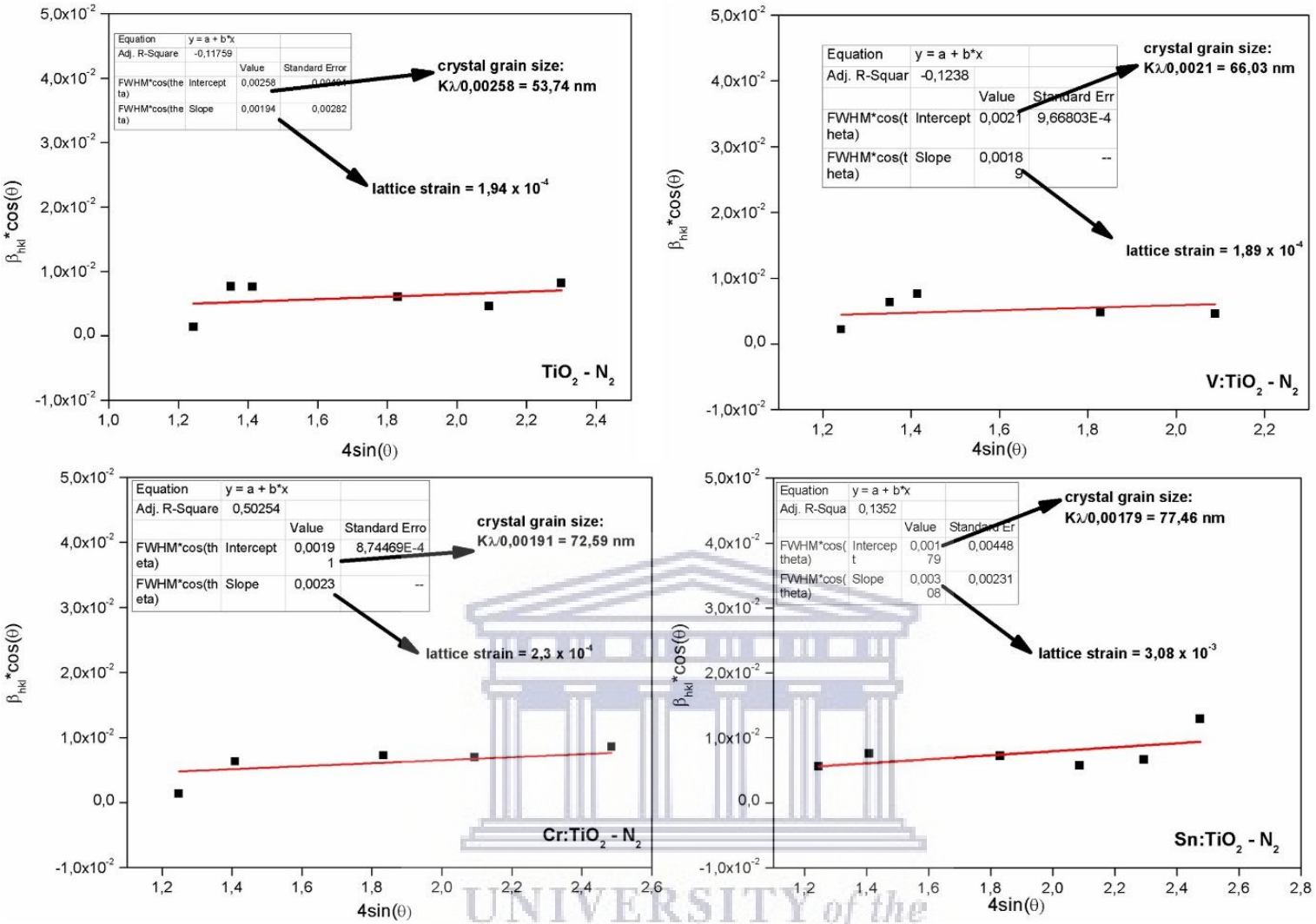

Fig. S3: Williamson-Hall data of the TiO_2 nanowires doped with the different metals and exposed to the N_2 plasma

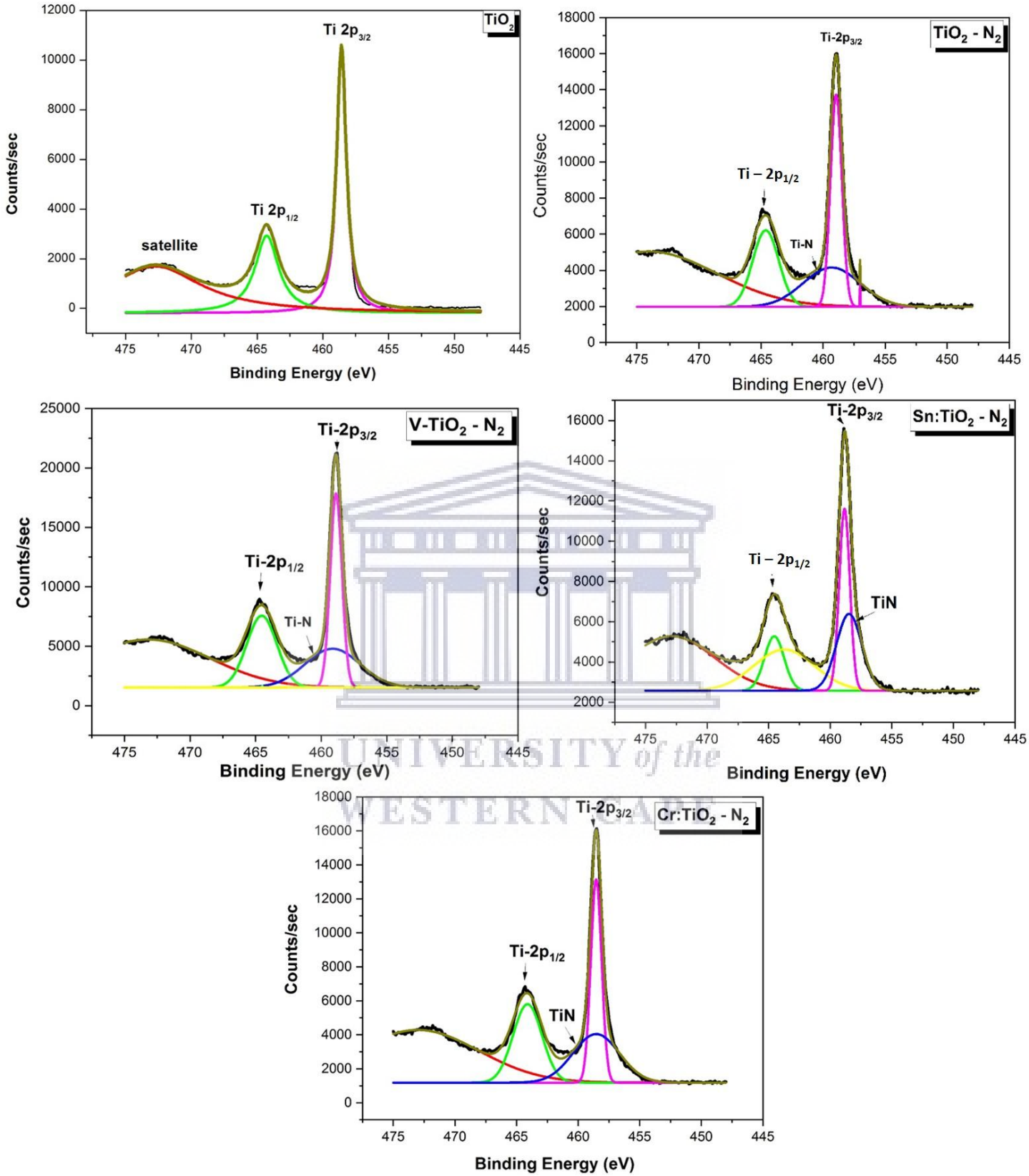

Fig. S4: XPS plots of Ti 2p electronic structure showing the deconvolution results of the individual Ti data for each of the differently doped and treated TiO_2 NW arrays

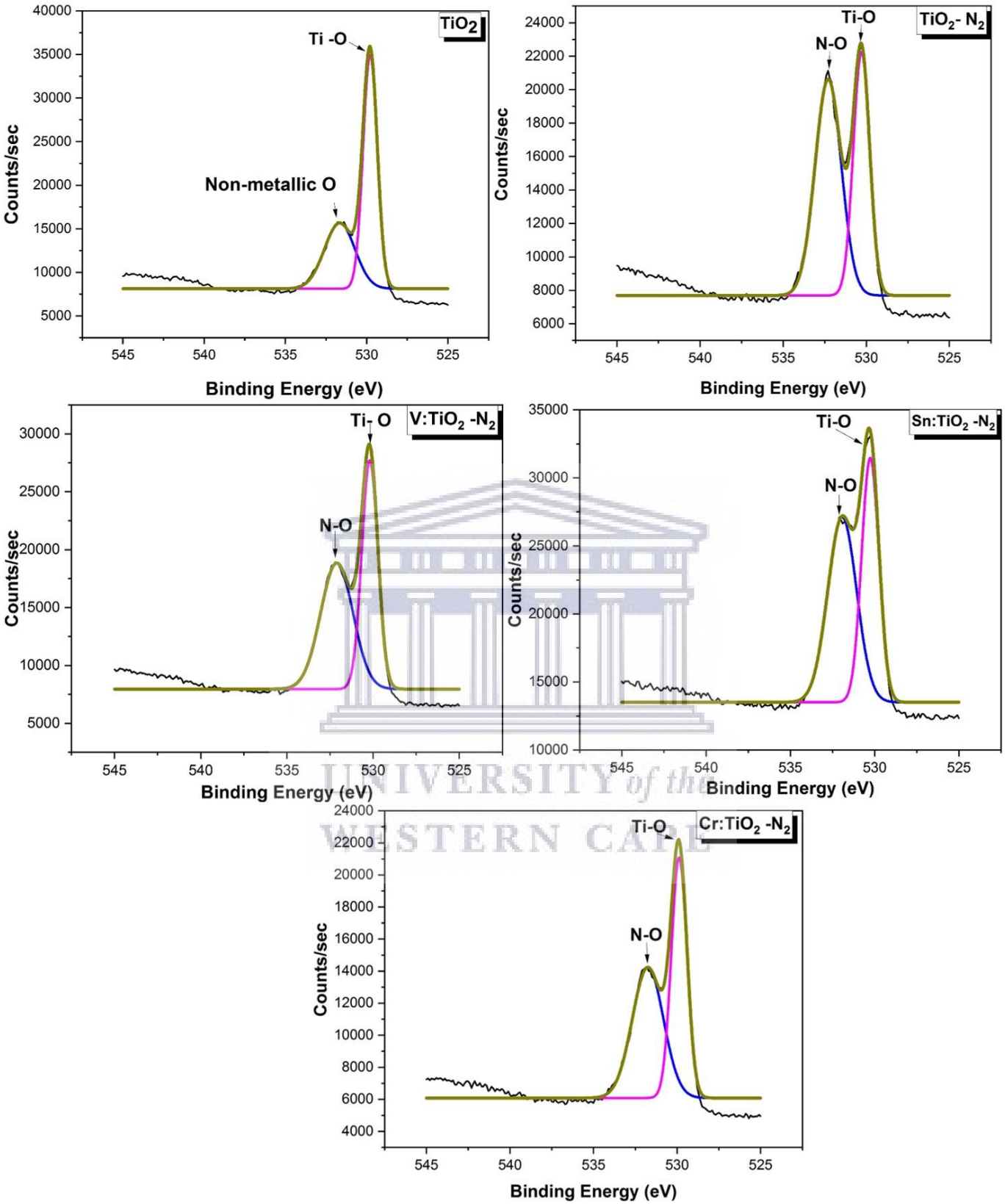

Fig. S5: XPS plots of O 1s electronic structure showing the deconvolution results of the individual Ti data for each of the differently doped and treated TiO_2 NW arrays

Table S1: Peak parameter data obtained from the deconvolution of the Ti 2p and O 1s peaks of Figs. S4 and S5.

Peaks	Parameters	TiO_2	$TiO_2 – N_2$	$V:TiO_2 – N_2$	$Cr:TiO_2 – N_2$	$Sn:TiO_2 – N_2$
	Position (eV)	458.57	458.95	458.87	458.54	458.47
Ti $2p_{3/2}$	Area (a.u)	12113.09	12455.65	17351.69	13148.85	9728.19
	FWHM (eV)	1.78	5.37	1.05	1.03	1.01
	Position (eV)	464.28	464.62	464.53	464.11	464.54
Ti $2p_{1/2}$	Area (a.u)	9040.64	42059.30	921603.46	38481.31	23723.25
	FWHM (eV)	4.23	12.89	11.16	11.65	8.23
	Position (eV)	-	456.98	457.09	-	-
Ti-N $2p_{3/2}$	Area (a.u)	-	13413.15	18189.21	-	-
	FWHM (eV)	-	1.07	1.05	-	-
	Position (eV)	-	459.31	459.13	459.00	459.00
Ti-N $2p_{1/2}$	Area (a.u)	-	11152.57	47923.75	13592.51	12651.34
	FWHM (eV)	-	2.47	2.70	2.77	5.81
	Position (eV)	529.78	530.29	530.19	530.26	529.88
Ti-O	Area (a.u)	29347.28	18006.59	23107.96	23070.05	17559.07
	FWHM (eV)	1.03	1.16	1.10	1.21	1.10
	Position (eV)	531.66	532.29	532.11	531.93	531.75
Non-metallic O/N-O	Area (a.u)	17657.50	25514.06	25562.54	29079.16	19016.30
	FWHM (eV)	2.02	1.85	2.21	2.01	2.19

APPENDIX B

FUTURE WORK: KESTERITE PHOTOVOLTAIC RESEARCH

During the latter stages of my PhD studies, I spent three months at University Autonoma de Madrid (UAM) in Spain as part of the EU RISE INFINITE CELL Project between South Africa and host countries in Europe. My primary objective was to grow films of kesterites by co-evaporation and chalcopyrite by flash evaporation techniques as absorber layers, incorporating the ZnO NWs as electron mediating layer in inorganic solar cells. Surface and device characterisation included SEM, UV-vis, XRD and device performance measurements by means of I-V characterisation. Nanowires, 600 nm in length were used as ETLs in the devices, with active layers of approximately 1 µm deposited via the respective evaporation technique. Solar cells of 2 x 3 cm^2 active area were specially designed for the purpose of the study. The co-evaporation of kesterite based layers involved the evaporation of seven different metals, namely, Cu, Ge, Zn, SnSe alloy, Na and ZnSe alloy at different rates to form a dense, uniform layer. The deposition process lasts between 4 to 5 hours, with the substrates heated to 270˚C. One micrometer thick layers of CuGeZnSe and CuSnZnSe were successfully deposited directly onto the glass/ITO/ZnO/ZnO NW substrates, and then left overnight to allow for full sulphurisation - a process of placing the samples in an aluminium box with 30 mg of sulphur at 480˚C for 1 hour and allowing for cooling to room temperature. After each successful process of the experiment the samples were taken for EDX and XRD measurements to determine the composition and the crystal structure respectively. The composition studies assist in determining whether the layers were copper-rich or copper-poor, with the aim of achieving a low atomic percentage of copper in the layer. The actual device fabrication and testing were done at the Energy Research Institute of Catalonia (IREC), Barcelona.

During flash evaporation, chalcopyrite powders ($Cu(Ga,In)Se_2$) were mixed together in different ratios to form the chalcopyrite film at evaporation temperatures ranging between 210 and 250˚C. The chalcopyrite thicknesses were varied between 1-1.5µm (through a manual operation process of film deposition) for all the different experiments, taking between 5 and 6 hours to finish depending on the desired thickness. Devices were made on both FTO

and ITO substrates containing ZnO NWs as the ETLs. The glass/TCO/ZnO/ZnO NWs/chalcopyrite samples were then selenised by annealing at 450 ˚C for 1 hour to increase the band gap of the material through and allowed to cool to room temperature. Once more, the half cells were sent to IREC for the device fabrication and IV testing. Some results are

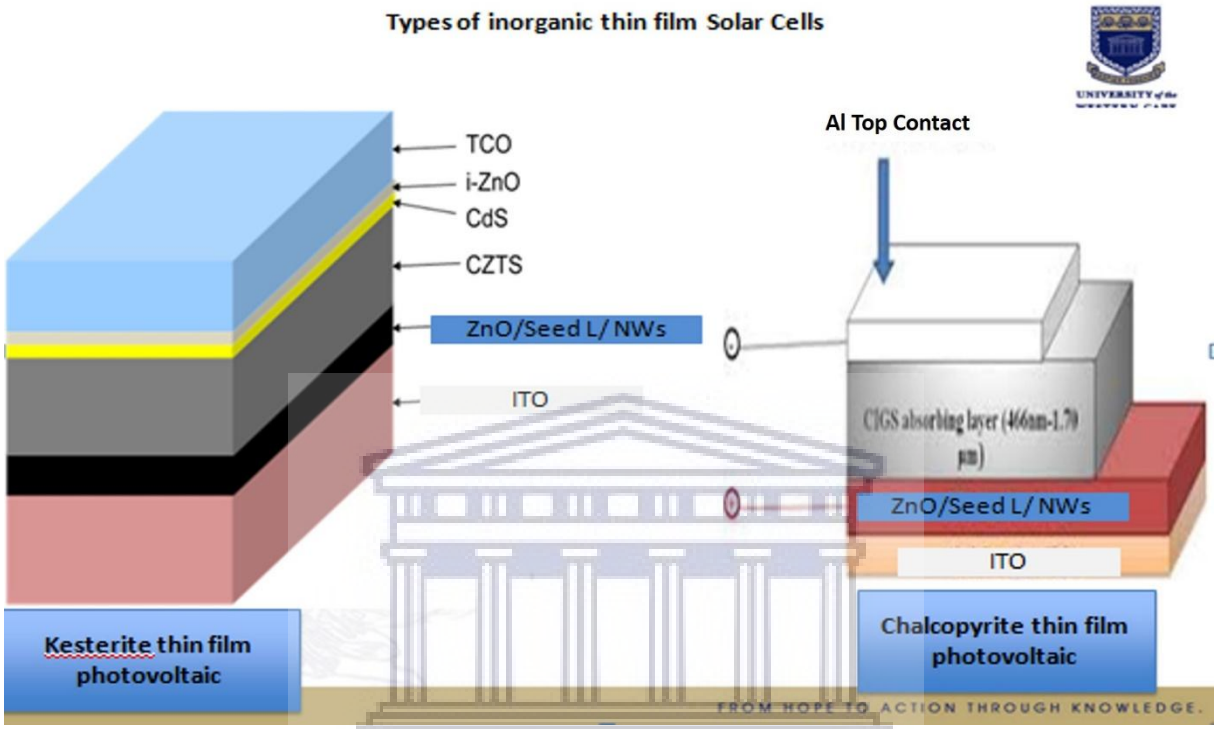

shown below, that are ongoing and will form the basis for future research between the different institutions.

Fig. T1: Schematics of the kesterite and chalcopyrite based inorganic solar cell designs investigated

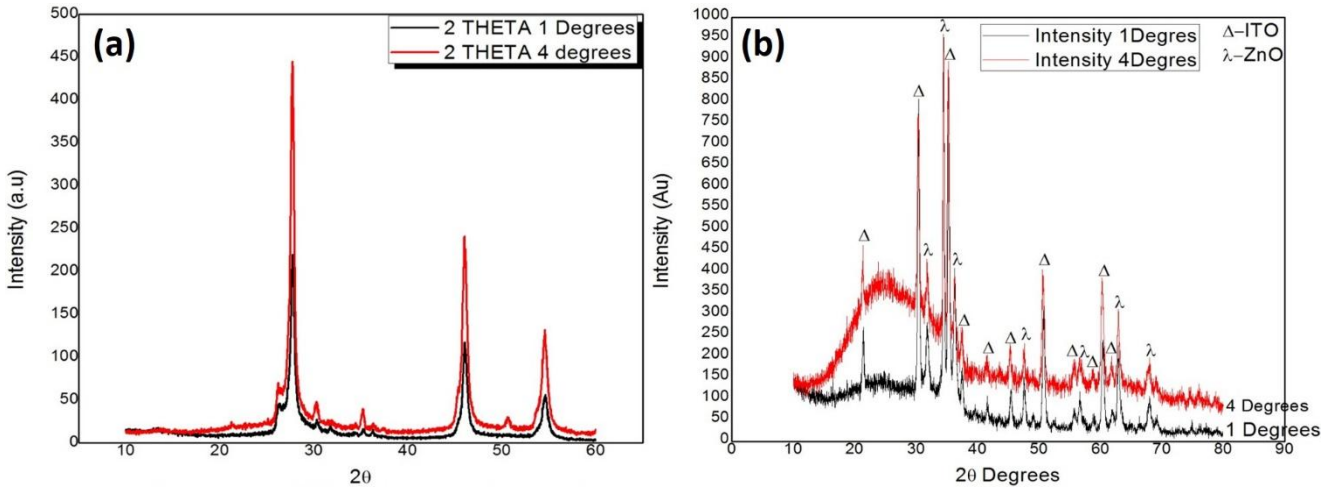

Fig. T2: GIXRD of (a) kesterite and (b) chalcopyrite layers deposited onto ZnO NW at grazing angles of 1 and 4 degrees

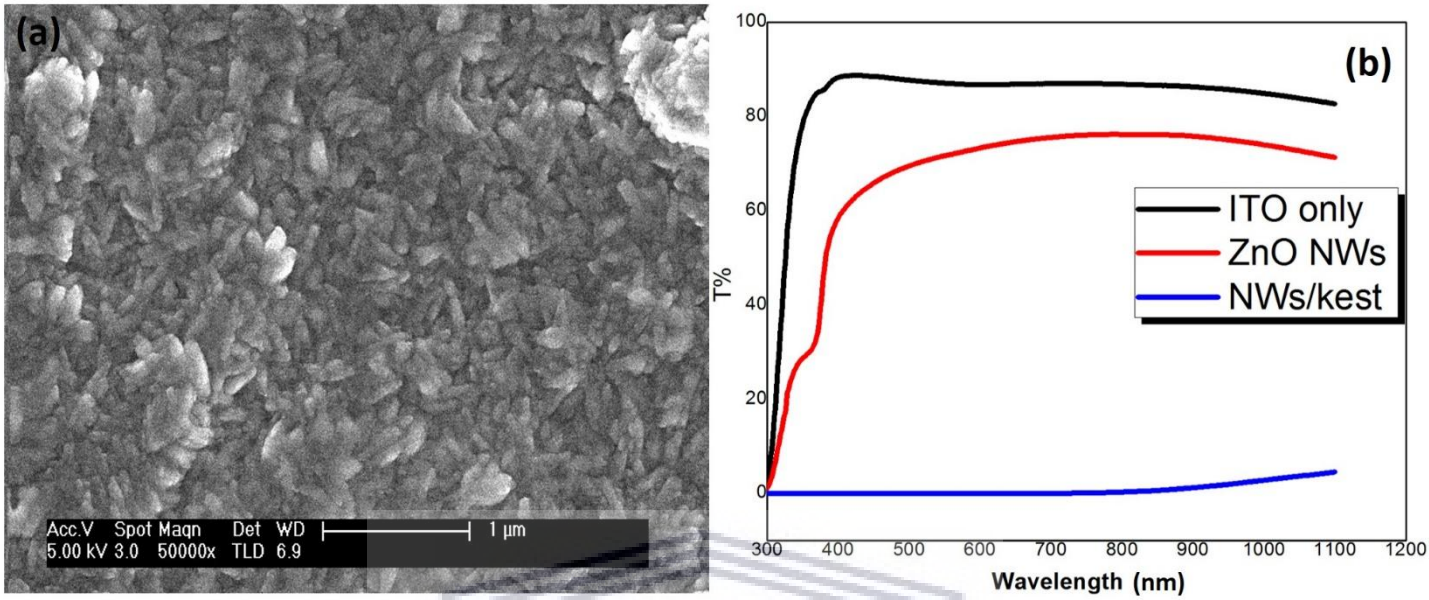

Fig. T3: (a) SEM micrograph of the kesterite layer and (b) transmittance measurements

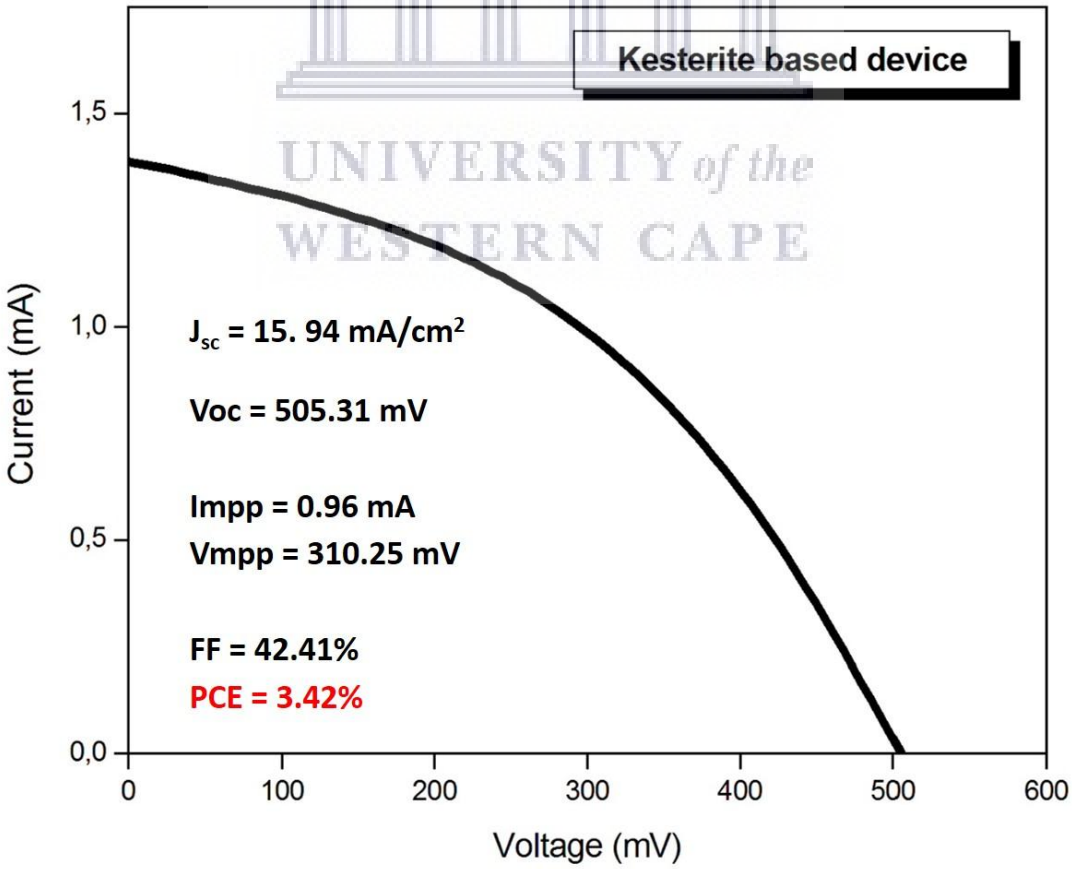

Fig. T4: I-V performance of a kesterite based solar cell incorporating ZnO NWs

APPENDIX C

PUBLISHED ARTICLES

Surfaces and Interfaces 17 (2019) 100382

Contents lists available at ScienceDirect

Surfaces and Interfaces

journal homepage: www.elsevier.com/locate/surfin

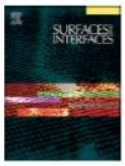

Nitrogen plasma treatment of ZnO and TiO_2 nanowire arrays for polymer photovoltaic applications

Bello Ladan Muhammad[a,c], Franscious Cummings[b,*]

[a] Department of Physics and Astronomy, University of the Western Cape, Private Bag X17, Bellville 7535, South Africa
[b] Electron Microscope Unit, University of the Western Cape, Private Bag X17, Bellville 7535, South Africa
[c] Department of Physics, Ibrahim Badamasi Babagida University, P.M.B 11 Lapai, Niger State, Nigeria

ARTICLE INFO

Keywords:
Hydrothermal synthesis
One-dimensional nanowire arrays
RF plasma nitrogen doping
Electron energy loss spectroscopy

ABSTRACT

This work reports on a simple, yet unique approach to improving the opto-electronic properties of vertically-aligned arrays of rutile TiO_2 and Wurzite ZnO nanowires by means of controlled nitrogen doping during exposure to highly kinetic radio-frequency generated N_2 plasma radicals. Morphologically, the plasma treatment causes a distortion of the vertical alignment of the nanowires due to a dissociation of the weak Van der Waals force clustering the nanowires. Optical spectroscopy show that plasma treatment increases the light transmission of TiO_2 arrays from 48% to 90%, with the ZnO arrays exhibiting an increase from 70% to 90% in the visible to UV range. The as-synthesized TiO_2 array has an indirect band gap of 3.13 eV, which reduces to 3.03 eV after N_2 treatment, with the ZnO equivalent decreasing from 3.20 to 3.17 eV post plasma exposure. A study of the 3d transition metal near edge fine structure of both Ti and Zn show that the N_2 plasma treatment of the nanowires results in nitrogen doping of both TiO_2 and ZnO lattices; this is confirmed by scanning transmission electron microscopy coupled with energy dispersive spectroscopy x-ray maps collected of single nanowires, which show a clear distribution of nitrogen throughout the metal-oxide. Application of these structures in P3HT:PCBM polymer blends shows progressive improvement in the photoluminescence quenching of the photoactive layer when incorporating both undoped and nitrogen-doped nanowires.

1. Introduction

An attractive approach to improve efficiency and reduce costs of modern hybrid photovoltaics such as polymer, perovskite and radial junction p-n type silicon cells, is the application of one-dimensional (1D) metal-oxides such as TiO_2 [1], ZnO as well as their nanocomposite forms [2–4]. The n-type nature of these materials has been widely exploited for use as an electron transport layer in these devices. However, this n-type character originates from the large density of oxygen vacancies generally detected on the surface of these 1D materials. In turn, these vacancies lead to electron trap-sites, causing electron–hole recombination during operation of the device. In addition, the presence of vacancies also changes the material's chemical reactivity and stability [5–9]. To overcome this constraint, nitrogen doping has been the preferred method, with various approaches employed, such as chemical doping during synthesis [10], high temperature annealing in a nitrogen ambient [11], ion implantation [12] and cathode magnetron sputtering [13]. Considering the above approaches, radio frequency (RF) plasma generation of highly reactive nitrogen species for substitutional nitrogen doping in both TiO_2 [14] and ZnO [15], unlike chemical, in-situ or high temperature annealing approaches, allows for better control of the dopant flux, depth and concentration [16] by altering the plasma power, exposure time and temperature of the treated material. Dopants such as nitrogen and carbon generally serve as electron donors in metal-oxides [17–19], with the dopants introducing impurity states at various positions in the band gaps of both TiO_2 and ZnO, leading to different degrees of modification in electrical conductivity [20,21]; oxygen vacancies, on the other hand, are known to be shallow donors for TiO_2 and ZnO, with relatively low formation energies [22]. This study aims to contribute to this broad body of literature by showing that radiating TiO_2 and ZnO lattices with highly kinetic nitrogen plasma species has a unique, two-fold lattice effect: (1) passivation of the dangling Ti^{2+} and Zn^{2+} ionic species on the surface of the nanowire and (2) creation of deep-lying ionic bonds in the lattice leading to an increase in both electron conductivity and alteration of the optical behavior of the material. TiO_2 and ZnO NWs films are hydrothermally grown on fluorine-doped tin-oxide (FTO) substrates using well-known synthesis protocols [23,24], followed by plasma exposure for 10 min at

* Corresponding author.
E-mail address: fcummings@uwc.ac.za (F. Cummings).

https://doi.org/10.1016/j.surfin.2019.100382
Received 7 June 2019; Received in revised form 8 September 2019; Accepted 9 September 2019
Available online 10 September 2019
2468-0230/

Chemical Physics 538 (2020) 110922

Contents lists available at ScienceDirect

Chemical Physics

journal homepage: www.elsevier.com/locate/chemphys

RF nitrogen plasma irradiation of metal-doped TiO_2 nanowire arrays as an effective technique for improved light transmission and optical bandgap manipulation

B.L. Muhammad[a,c], N.V. Peterson[a], L. Kotsedi[d], F.R. Cummings[b,*]

[a] Department of Physics and Astronomy, University of the Western Cape, Private Bag X17, Bellville 7535, South Africa
[b] Electron Microscope Unit, University of the Western Cape, Private Bag X17, Bellville 7535, South Africa
[c] Department of Physics, Ibrahim Badamasi Babagida University, P.M.B 11 Lapai, Niger State, Nigeria
[d] Materials Research Group, iThemba LABS, Faure 7130, South Africa

ARTICLE INFO

Keywords:
Hydrothermal synthesis
One-dimensional nanowire arrays
Radio-frequency plasma
Nitrogen doping
Opto-electronic properties

ABSTRACT

TiO_2 NWs doped with V, Cr and Sn ions are subjected to RF generated nitrogen plasma and characterized for variance in light transmission and optical bandgap. Structurally, the introduction of Sn^{4+} in the TiO_2 lattice causes defect broadening along the ⟨100⟩ direction of individual nanowires, causing lattice distortion. This is different to Cr^{3+} and V^{3+} doping, which etch TiO_2 {110} and {111} faces, causing increases in nanowire diameter. Nitrogen plasma irradiation affects no visible change in structure, but does reduce the areal density of the nanowires, subsequently yielding improved light transmission through the array. Tauc transformations of diffuse reflectance data show that the combination of metal-doping and plasma irradiation induce a decrease of the optical bandgap of the TiO_2 structures. This bandgap decrease is mainly attributed to deep-lattice nitrogen doping, resulting in optical band narrowing by localized N 2p states, created by β-N species present in the plasma.

1. Introduction

The favourable electronic and optical properties of arrays of one-dimensional (1D) TiO_2 arrays, grown atop conductive substrates, have seen it widely applied in photovoltaics (PVs) as electron transport and light trapping media [1], as well as water splitting [2,3] and purification applications [4,5] as photocatalysts. Being a wide-bandgap semiconductor with an optical bandgap of 3.3 eV implies that TiO_2 requires ultraviolet radiation for electron-hole pair generation during photocatalytic experiments [6,7], whereas their low electron conductivity and oxygen vacancies often result in electron-hole recombination when used in PVs [5,8,9]. Doping TiO_2 with particular metallic [10,11] and/or non-metallic ions [11,12] not only improves the photo-catalytic activity of the material [6,7], but also improves the electronic conductivity and optical bandgap of the TiO_2 host matrix under certain doping conditions. Metal-doped TiO_2 nanowire (NW) arrays, in particular, have received considerable research focus over the last 10 years due to the clear improvement in opto-electronic properties induced by the foreign metal ions. Dopants introduced during synthesis (in-situ) or under post-synthesis treatment (ex-situ) create inter-bandgap donor or acceptor levels, also called trap states, that enhance the probability of recombination of photo-generated electron-hole pairs; however, this is obviously undesirable for application as electron transport media in PVs. To overcome this disadvantage, post-synthesis treatment by either heat [13–17] or chemical means [18–22] are common approaches to improving both optical and electrical properties.

In this contribution, metal-doped (V, Cr and Sn) TiO_2 NW arrays are in-situ doped during hydrothermal synthesis and subjected to highly kinetic, radio-frequency (RF) generated N_2 plasma radicals for precise control of the nitrogen dopant species compared to more common post-synthesis approaches. Doping TiO_2 with nitrogen is found to be particularly effective because favourable bandgap narrowing is induced during mixing of N 2p and O 2p states [23–25]. RF plasma irradiation also produces higher nitrogen doping concentrations compared to post-synthesis nitrogen annealing and chemical treatment methods, which often fail to produce concentrations greater than 5 at%, considered a critical value for obtaining significant shift in optical response and effective lowering of trap-sites [25]. At the time of writing, RF plasma irradiation of hydrothermally synthesized metal-doped TiO_2 NW arrays with nitrogen is unprecedented, with no prior literature available.

* Corresponding author.
E-mail address: fcummings@uwc.ac.za (F.R. Cummings).

https://doi.org/10.1016/j.chemphys.2020.110922
Received 7 April 2020; Received in revised form 15 June 2020; Accepted 6 July 2020
Available online 09 July 2020

ARTICLE IN PRESS

Materials Today: Proceedings xxx (xxxx) xxx

Contents lists available at ScienceDirect

Materials Today: Proceedings

journal homepage: www.elsevier.com/locate/matpr

Nitrogen plasma irradiation of Fe doped ZnO nanowire arrays for improved optical properties

Bello Ladan Muhammad [a,c], Franscious Cummings [b,*]

[a] Department of Physics and Astronomy, University of the Western Cape, Private Bag X17, Bellville 7535, South Africa
[b] Electron Microscope Unit, University of the Western Cape, Private Bag X17, Bellville 7535, South Africa
[c] Department of Physics, Ibrahim Badamasi Babagida University, P.M.B 11 Lapai, Niger State, Nigeria

ARTICLE INFO

Article history:
Received 23 March 2020
Received in revised form 22 April 2020
Accepted 23 April 2020
Available online xxxx

Keywords:
ZnO nanowires
Bandgap
Radio-frequency plasma
Diffraction
Doping
X-ray photo-electron spectroscopy

ABSTRACT

This work reports on the ability to improve the optical properties of hydrothermally grown, vertically-aligned arrays of wurzite ZnO and Fe doped ZnO nanowires by means of nitrogen doping during high-powered plasma irradiation. The morphology, structural and optical properties of ZnO, Fe:ZnO NWs and N_2 – Fe:ZnO NWs are studied by scanning electron microscopy, grazing incidence X-ray diffraction and UV–visible spectroscopy, respectively, whereas elemental doping of the nanostructures are investigated by means of X-ray photo-electron spectroscopy. SEM micrographs show no discernible morphological differences between the ZnO, Fe:ZnO NWs and N_2-Fe:ZnO NWs, however a clear increase in light transmission over the visible to UV range, accompanied by a decrease in optical band gap of 3.261 eV for ZnO NWs to 3.255 eV for Fe:ZnO NWs and ultimately 3.250 eV for N_2-Fe:ZnO nanowires is observed. This band gap reduction is ascribed to the presence of a high density of shallow donor states in the band-gap of the ZnO lattice, subsequently causing an overall reshape of the conduction band minimum, caused by filling of oxygen vacancies and substitutional replacement of lattice oxygen by the highly kinetic α-N species during oxynitride, O-Zn-N bond formation. The results suggest that nitrogen doping during plasma irradiation provides a controlled method of deep lattice nitrogen doping that is favorable for improved photo-electrochemical, photovoltaic and photo-response applications of ZnO nanowires.

Selection and peer-review under responsibility of the scientific committee of the NANOSMATAFRICA-2018.

1. Introduction

ZnO has a wide band gap of 3.37 eV and 60 meV exciton binding energy, which allow for very effective excitonic emissions [1]. These characteristics make the material an important component in different functional systems such as visible light emitting diodes [2,3], ultraviolet laser diodes, photocatalysts [4,5], sensors [6,7] and solar cells [8,9]. During application in solar cells ZnO has proven to be an excellent transparent conducting electrode, but is also a promising material for next generation electronic and optoelectronic applications due to its unique charge transport properties [10–12]. The optoelectronic properties of ZnO, especially, are known to depend on the material's structural morphology [1], doping elements and concentration [13], as well as fabrication technique [14]. Since the turn of the century, nano-structured ZnO such as nano-combs [15], belts [16], helixes/springs [17], rods [18], nanotubes [19] and nanowires [20] doped with various metallic [21] and non-metallic [22] elements have been intensely researched because of the enhancement in opto-electronic and photochemical properties offered by the different nano-architectures during doping. The similarities in ionic radius between O, Fe and N make the latter two elements especially suitable doping candidates in ZnO lattices. Fe and N are known to behave as p-type dopants in group II–VI semiconductors [23,24], whereas Fe and N impurities behave as donors and acceptors, respectively or can be employed as co-dopants, thus acting as shallow donors to enhance the electrical properties in ZnO thin films [14,25,26].

N doped ZnO (N:ZnO) thin films are traditionally synthesized using high vacuum systems during metal–organic chemical vapour deposition [27], discharged pulsed laser deposition [28], polymeric precursor methods [29], laser irradiation [30], successive ionic layer adsorption and reaction [31], modified aqueous chemical growth [32], ion implantation [33,34] and high-powered radio frequency sputter deposition [35]. These layers typically display

* Corresponding author.
E-mail address: fcummings@uwc.ac.za (F. Cummings).

https://doi.org/10.1016/j.matpr.2020.04.684
2214-7853/
Selection and peer-review under responsibility of the scientific committee of the NANOSMATAFRICA-2018.

Please cite this article as: B. Ladan Muhammad and F. Cummings, Nitrogen plasma irradiation of Fe doped ZnO nanowire arrays for improved optical properties, Materials Today: Proceedings, https://doi.org/10.1016/j.matpr.2020.04.684